Studies of Turbulent Round Jets Through Experimentation, Simulation, and Modeling

Ryan Keedy

A dissertation
submitted in partial fulfillment of the
requirements for the degree of

Doctor of Philosophy

University of Washington

2013

Reading Committee:

Alberto Aliseda, Chair

James Riley

John Kramlich

Program Authorized to Offer Degree:
Mechanical Engineering

University of Washington

Abstract

Studies of Turbulent Round Jets Through Experimentation, Simulation, and Modeling

Ryan Keedy

Chair of the Supervisory Committee:
Associate Professor Alberto Aliseda
Mechanical Engineering

This thesis studies the physics of the turbulent round jet. In particular, it focuses on three different problems that have the turbulent round jet as their base flow.

The first part of this thesis examines a compressible turbulent round jet at its sonic condition. We investigate the shearing effect such a jet has when impinging on a solid surface that is perpendicular to the flow direction. We report on experiments to evaluate the jet's ability to remove different types of explosive particles from a glass surface. Theoretical analysis revealed trends and enabled modeling to improve the predictability of particle removal for various jet conditions.

The second part of thesis aims at developing a non-intrusive measurement technique for free-shear turbulent flows in nature. Most turbulent jet investigations in the literature, both in the laboratory and in the field, required specialized intrusive instrumentation and/or complex optical setups. There are many situations in naturally-occurring flows where the environment may prove too hostile or remote for existing instrumentation. We have developed a methodology for analyzing video of the exterior of a naturally-occurring flow and calculating the flow velocity. We found that the presence of viscosity gradients affects the velocity analysis. While these effects produce consistent, predictable changes, we became interested in the mechanism by which the viscosity gradients affect the mixing and development of the turbulent round jet. We conducted a stability analysis of the axisymmetric jet when a viscosity gradient is present.

Finally, the third problem addressed in this thesis is the growth of liquid droplets by condensation in a turbulent round jet. A vapor-saturated turbulent jet issues into a cold, dry environment. The resulting mixing produces highly inhomogeneous regions of supersaturation, where droplets grow and evaporate. Non-linear interactions between the droplet growth rate and the supersaturation field make analysis computationally taxing. A Probability Density Function (PDF) model for the concentration of scalars, as well as for the droplet number in different diameter-size bins, is developed. The distribution of droplets as they evolve along the jet, for different downstream and radial positions, compared favorably with experimental measurements in the literature. We utilized a graphical processing unit with the PDF method to more efficiently compute the statistics of the droplet diameter in the non-uniform supersaturation field.

TABLE OF CONTENTS

Page

List of Figures v

Chapter 1: Introduction 1

Chapter 2: Particle Removal with a Sonic, Turbulent Jet 4
2.1 Nomenclature 4
2.2 Background 4
2.3 Experimental Procedure 7
2.3.1 Ceramic Micropheres 9
2.3.2 Explosives 11
2.4 Modeling 15
2.4.1 Removal Modeling 18
2.5 Experimental Data 20
2.5.1 Microsphere Particles 20
2.5.2 Explosive Particles 20
2.6 Summary 22

Chapter 3: Multi-component Turbulent Jet 25
3.1 Nomenclature 25
3.2 Background 26
3.3 Experimental Setup 29
3.3.1 Fluids Equipment 29
3.3.2 Imaging Setup 35
3.3.3 Visualization Techniques 38
3.3.3.1 Seeded Flow Imaging 39
3.3.3.2 Rhodamine-B 41
3.3.4 Fluids 43
3.3.4.1 Water-Water 43
3.3.4.2 Water-Hot Water 43

3.3.4.3 Water-Glycerol . . . 44
3.4 Particle Image Velocimetry . . . 44
3.4.1 PIV Methodology . . . 44
3.4.2 Image Processing . . . 48
3.4.3 PIV Analysis . . . 50
3.4.4 Statistical Treatment of the PIV Measurements . . . 52
3.5 Results . . . 53
3.5.1 Flow Velocity across the Jet . . . 53
3.5.2 Flow Turbulent/Non-Turbulent Interface . . . 56
3.5.2.1 Reynolds Number . . . 59
3.5.2.2 Inter-Frame Time Delay . . . 60
3.5.2.3 Jet Initial Conditions . . . 62
3.5.2.4 Buoyancy . . . 63
3.5.2.5 Viscosity . . . 66
3.5.3 Signal to Noise Ratio (SNR) . . . 67
3.6 Conclusions . . . 73
3.7 Future Work . . . 75

Chapter 4: Round Jet Stability . . . 80
4.1 Nomenclature . . . 80
4.2 Background . . . 81
4.2.1 Velocity Profiles . . . 83
4.3 Derivation . . . 85
4.3.1 Boundary Conditions . . . 90
4.3.2 Method of Solution . . . 94
4.3.3 Identifying the Most Unstable Mode . . . 96
4.3.3.1 Inverse Iteration Method . . . 96
4.4 Validation . . . 97
4.4.1 Resolution Study . . . 99
4.5 Results . . . 100
4.5.1 Concentration Gradient . . . 102
4.5.2 Reynolds Number . . . 103
4.5.3 Viscosity Ratio . . . 106
4.5.4 Viscosity/Concentration Relationship . . . 108
4.5.4.1 High Viscosity Jet . . . 108

4.5.4.2 Low Viscosity Jet . . . 109
4.5.5 Velocity Profile . . . 110
4.5.6 Asymmetric Instability Mode . . . 114
4.6 Experiments . . . 114
4.6.1 Experimental Setup . . . 114
4.6.2 Reynolds Number Variation . . . 119
4.6.3 Viscosity Ratio Variation . . . 119
4.7 Discussion . . . 122
4.8 Future Work . . . 123

Chapter 5: Condensation at the edge of a Turbulent Jet . . . 125
5.1 Nomenclature . . . 125
5.2 Background . . . 126
5.2.1 Momentum-Dominated Turbulent Jet . . . 126
5.2.2 Condensation Mixing Model . . . 127
5.3 An Improved Axisymmetric, Two-Dimensional CSTR Model . . . 129
5.3.1 Description . . . 129
5.3.2 Implementation . . . 132
5.3.3 Comparison with Experiments from Literature . . . 136
5.4 PDF-Based Model . . . 143
5.4.1 Model Overview . . . 146
5.4.1.1 Computational Domain . . . 146
5.4.1.2 Initial Conditions . . . 148
5.4.1.3 Boundary Conditions . . . 148
5.4.2 Model Time Stepping . . . 149
5.4.2.1 Advection Model . . . 149
5.4.2.2 Cell Balancing . . . 149
5.4.2.3 Reaction Model . . . 150
5.4.2.4 Mixing Model . . . 151
5.4.3 RANS Simulation . . . 152
5.4.4 PDF Implementation . . . 157
5.4.4.1 Time-Stepping . . . 158
5.4.4.2 Diameter Distribution . . . 158
5.4.4.3 Reaction Model . . . 158
5.4.4.4 Boundary Conditions . . . 159

5.4.4.5 Cell Balancing . . . 159
5.4.4.6 Cell Integration and Advection . . . 160
5.4.5 Validation . . . 161
5.4.6 Comparison to Experiments from Literature . . . 165
5.4.6.1 Effect of Aerosol/Droplet Concentration . . . 170
5.4.6.2 Effect of Computational Particle Concentration . . . 173
5.4.6.3 Effect of Diameter Bin Size . . . 174
5.5 Conclusions . . . 175
5.6 Future Work . . . 176

Appendix A: Derivation of Viscosity-Dependent Stability Equations . . . 177
A.1 Navier-Stokes (Cylindrical Coordinates) . . . 177
A.2 Decomposition (Mean and Fluctuating Parts) . . . 180
A.3 Free Shear Approximation . . . 182
A.4 Assumed Form of Fluctuating Parts . . . 187
A.5 Linearization in α . . . 189
A.6 Non-dimensionalization . . . 192
A.7 Matrix Form . . . 194

LIST OF FIGURES

Figure Number — Page

2.1 Cartoons of the three different removal mechanisms identified by Wang (1990): (a) lift-off, (b) sliding, and (c) rolling . . . 6
2.2 Diagram of the air jet interrogation experimental setup . . . 7
2.3 Volume of air ejected from a 4.5 mm nozzle as a function of reservoir pressure and pulse duration . . . 8
2.4 Ceramic microsphere removal for jet bursts of different duration (2.5 mm nozzle diameter, 276 kPa reservoir pressure, 152 mm stand-off distance) . . . 9
2.5 Microscope images of ceramic microspheres on glass, both before and after interrogation by an air jet pulse (2.5 mm diameter nozzle, 207 kPa reservoir pressure, 152 mm stand-off distance) . . . 10
2.6 Ceramic microsphere removal for jet bursts with varying reservoir pressures (2.5 mm diameter nozzle, 152 mm stand-off distance) . . . 12
2.7 Microscopic images of TNT before and after transfer. (a) Solid TNT nugget (5 μm) resulting from desiccation. (b) TNT particles after transfer . . . 13
2.8 Microscope images of TNT on glass, both before and after interrogation by an air jet pulse (4.75 mm diameter nozzle, 655 kPa reservoir pressure, 47 mm stand-off distance) . . . 14
2.9 Histograms of particle size for the four types of particles in our study . . . 15
2.10 Diagram of dimensions used for analysis . . . 17
2.11 Contours of $\frac{U}{U_0}$ versus back-pressure and $\frac{z}{d}$ . . . 18
2.12 Plot of experimental data for ceramic microsphere particle diameter experiencing 50% removal at various ζ; data is fit with the curve from equation 2.15, $K = 1.35\ \mu m^{6/7}$ . . . 21
2.13 Plot of removal versus ζ for three explosives and ceramic microspheres (experimental results as points; curve fits from eq. 2.16 as lines) . . . 23

3.1 Plot of velocity measurements ranging from z/d values of 40 to 97.5 reported in Wygnanski & Fiedler (1969) . . . 28
3.2 Graphs from Hussein et al. (1994) showing results for Reynolds stresses collected via SHW, FHW, and LDA . . . 29
3.3 Graph from Hussein et al. (1994) showing centerline velocity ratio collected via SHW and LDA . . . 30

3.4 A drawing of our octagonal tank, seen from different perspectives 32
3.5 CAD drawing of a converging nozzle with a 2 mm diameter 34
3.6 Cartoon of the flow experiment plumbing 35
3.7 Relative positions and configuration of the laser and camera for imaging of the jet interior (top) and exterior (bottom) 37
3.8 Image of the nozzle with the calibrated scale in place 38
3.9 Stokes number as a function of downstream distance 41
3.10 Photograph of a Rhodamine-dyed water jet 42
3.11 Interrogations areas from a pair of particle-seeded images; (a) M=N=32 pixel square area from first image, (b) 64 pixel square area from second image . . . 46
3.12 Contours of the computed cross-correlation function plotted on the first image from Figure 3.11; arrow indicates displacement of the covariance peak from the image center 47
3.13 Filled contour of the displaced interrogation area (from image 1) plotted on image 2 (see Figure 3.11), with squares showing original and displaced locations 48
3.14 Interrogations areas from a pair of opaque turbulent/non-turbulent interface images; (a) M=N=32 pixel square area from the first image, (b) 64 pixel square area from the second image 48
3.15 Contours of the computed cross-correlation function plotted on the first image from Figure 3.14; arrow indicates displacement of the covariance peak from the image center 49
3.16 Filled contour of the displaced interrogation area (from image 1) plotted on image 2 (see Figure 3.14), with squares showing original and displaced locations 50
3.17 Image pairs ($\delta t = 20\ \mu s$) of illuminated lycopodium particles within a water jet ($Re = 25,000$) interior both before (top) and after (bottom) contrast normalization via ImageJ 51
3.18 Calculated velocity vector field of the image pair from Figure 3.17; vectors are colored by magnitude 52
3.19 Velocity field calculated by averaging 1300+ image pairs from the same experiment as Figure 3.18 53
3.20 Normalized plots of axial velocity profiles, demonstrating the self-similarity of the flow measured with PIV (4 mm nozzle, $Re = 50,000$) 55
3.21 Plots of Reynolds stresses measured with PIV for flow through a 4 mm nozzle 55
3.22 PIV results of the centerline velocity ratio decay for flow through a 4 mm nozzle 56
3.23 Image pairs ($\delta t = 120\ \mu s$) of an illuminated Rhodamine-dyed water jet ($Re = 50,000$) interface both before (top) and after (bottom) contrast normalization via ImageJ 57

3.24 Calculated velocity vector field of the image pair from Figure 3.23; vectors are colored by magnitude 58
3.25 Velocity field calculated by averaging 380+ image pairs from the same experiment as Figure 3.24 59
3.26 Plot of the exterior jet velocity ratio (at $z/d = 1.5$) versus Reynolds number for many experiments (uniform fluid properties) 60
3.27 Plot of the exterior jet velocity ratio (at $z/d = 1.5$) versus Reynolds number colored by various values of $\hat{\tau}$ 61
3.28 Plot of experimental data comparing the effect of $\hat{\tau}$ on $\hat{U}$ at 1.5 diameters downstream distance 62
3.29 Images of free, turbulent jet exteriors at $Re = 50,000$ 64
3.30 Plots the minimum non-dimensional velocity ($U_j(gd)^{-1/2}$) required for $P > 1$ as a function of the jet density ratio (ρ_j/ρ_a) 65
3.31 Images of jets issuing from a 4 mm convergent nozzle at 12.6 m/s; the jet viscosity is (left to right) 0.5 cP, 1 cP, 2 cP, 10 cP, 100 cP 66
3.32 Images of three jets issuing from a 4 mm convergent nozzle; the left-most jet is 1 cP and has a velocity of 12.6 m/s ($Re = 50,000$); the middle jet is 2 cP and has a velocity of 12.6 m/s ($Re = 25,000$); the right-most jet is 1 cP and has a velocity of 6.3 m/s ($Re = 25,000$) 67
3.33 Plot of the velocity ratio (U_e/U_J) versus the time ratio ($\hat{\tau}$) measured at $1.5d$ for jets (converging nozzle) of several different viscosities 68
3.34 Plot of the velocity ratio (U_e/U_J) as a function of downstream distance for jets of several different viscosities ($\hat{\tau} = 0.25$) 69
3.35 Plot of the SNR versus time ratio for several jet viscosities 71
3.36 Plot of the velocity ratio versus SNR for several jet viscosities 72
3.37 Plot of the experimental data velocity ratios versus the time ratio scaled by the viscosity ratio ($\hat{\tau}\mu_r$) 74
3.38 Illuminated exterior of a Rhodamine-dyed jet consisting of air and water . . . 76
3.39 Plot of the experimental data velocity ratios versus the time ratio including the jet containing air 77
3.40 Plot of the experimental data velocity ratios versus the time ratio scaled by the viscosity ratio ($\hat{\tau}\mu_r$) 78

4.1 Plots of the four velocity profiles outlined by Michalke (1984) ($\Theta/R = 0.16$) . 85
4.2 Diagram of the coordinate system and geometry of the round jet 86
4.3 Eigenfunctions corresponding to four eigenvalues identified by Morris (1976) (results are normalized such that function has the value 1 at $\hat{r} = 0$); left: original plot from Morris (1976), right: results from the current study 98

4.4 Plots of $-\hat{\alpha}_i$ corresponding to the most unstable eigenvalue for four different Reynolds numbers for velocity profile 4 (200 nodes); left: $n = 0$, right: $n = 1$; top: original plots from Morris (1976), bottom: results from the current study 100

4.5 Contour plot of the most unstable $-\hat{\alpha}_i$ versus $-\hat{\omega}$ and Re (200 nodes, $n = 1$); top: original plot from Morris (1976), bottom: results from the current study 101

4.6 Plots of $-\hat{\alpha}_i$ corresponding to the most unstable eigenvalue for four different Reynolds numbers for velocity profile 2, $\Theta/R = 0.16$, (200 nodes); left: $n = 0$, right: $n = 1$; top: original plots from Morris (1976), bottom: results from the current study 102

4.7 Graph of $-\hat{\omega}$ at which the maximum instability occurs versus the number of collocation points ($\Theta/R = 0.04$, $R_{out} = 10R$, $C_r = 1$, $n = 0$) 103

4.8 Contour plot of the most unstable eigenvalue, $-\hat{\alpha}_i$, as a function of the concentration thickness, Θ_C/R, and the frequency, $-\hat{\omega}$ ($Re_d = 5000$, $C_r = \mu_r = 2.0, \Theta/R = 0.05$) 104

4.9 Comparison of R/Θ versus downstream distance (z/d) relationships from Crighton & Gaster (1976) and Cohen & Wygnanski (1987) 105

4.10 Contour plots of the most unstable $-\hat{\alpha}_i$ versus $-\hat{\omega}$ and Re_d; dashed line indicates maximum value of $-\hat{\alpha}_i$ at a given μ_r (with points representing experimental results) 106

4.11 Contour plots of the most unstable $-\hat{\alpha}_i$ versus $-\hat{\omega}$ and Re_d (200 nodes); (a) $n = 0$, (b) $n = 1$ 107

4.12 Contour plot of $-\hat{\alpha}_i$ versus $-\hat{\omega}$ and μ_r ($Re_d = 8450$, $\Theta_c = \Theta = 0.16R$) 108

4.13 Comparison of model prediction from Cheng (2008) and experimental results of Sheely (1932) of glycerin/water mixtures at $25°C$ 110

4.14 Contour plot of $-\hat{\alpha}_i$ versus the frequency and viscosity ratio, where the concentration-viscosity relationship is defined according to equations (4.53) and (4.56) 111

4.15 Non-dimensional velocity profiles defined by equation (4.63) for various viscosity ratios, $\mu_r = \mu_a/\mu_j$ 113

4.16 Contour plot of $-\hat{\alpha}_i$ as a function of μ_r and $-\hat{\omega}$; dashed line indicates maximum value of $-\hat{\alpha}_i$ at a given μ_r (with points representing experimental results) 114

4.17 Contour plot of $\hat{\alpha}_r$ as a function of μ_r and $-\hat{\omega}$; dashed line indicates maximum value of $-\hat{\alpha}_i$ at a given μ_r 115

4.18 Plot of most unstable $\hat{\alpha}_r$ as a function of μ_r 116

4.19 Plot of $\hat{\alpha}_i$ versus μ_r for both $n = 0$ and $n = 1$ modes ($Re_d = 8450, \Theta/R = 0.16$) 117

4.20 Photograph of the laser plane generated by the continuous laser illuminating Rhodamine-dyed high-viscsity fluid above the 10 mm nozzle 117

4.21 (a) Single frame from the high-speed video of a stability experiment ($Re_d = 8450$, $C_r = 1$), showing $z/d \approx 0.5$, (b) Columns of pixels from 500 consecutive images grabbed from the indicated position from image (a) 118

4.22 Images of jets with various viscosities having Reynolds number $Re_d = 8450$; (a) $\mu_j = 0.8\ cP$ ($\mu_r = 1.2$), (b) $\mu_j = 0.5\ cP$ ($\mu_r = 2$), (c) $\mu_j = 2\ cP$ ($\mu_r = 0.5$) 120

4.23 Standard deviation plot of jets with various viscosities having Reynolds number $Re_d = 8450$; (a) $\mu_j = 0.8\ cP$ ($\mu_r = 1.2$), (b) $\mu_j = 0.5\ cP$ ($\mu_r = 2$), (c) $\mu_j = 2\ cP$ ($\mu_r = 0.5$) 121

4.24 Plot of momentum-conserving velocity profiles for various viscosity ratios ($\Theta_j/R \approx 0.1$) 124

5.1 Graph of the radial variation concentration fluctuation intensity from Panchapakesan & Lumley (1993b) 128

5.2 Figure from Strum & Toor (1992) illustrating the continual stirred-tank reactor used in the condensation mixing model 129

5.3 Figure from Villermaux & Innocenti (1999) illustrating Reynolds number independence of iso-concentration regions; the upper image is of a jet with half the Reynolds number of the jet in the lower image 131

5.4 Graph of normalized proportion of scalar bin $dF = 0.03$ as a function of F value and η 133

5.5 Illustration of the computational domain decomposition 134

5.6 Comparison of experimental and model results of droplet diameter, D_{30}, at the jet centerline as a function of downstream distance for a saturated 62 $^\circ C$ jet 138

5.7 Comparison of experimental and model results of droplet diameter, D_{30}, at the jet centerline as a function of downstream distance for a saturated 85 $^\circ C$ jet 138

5.8 Comparison of experimental and model results of droplet diameter distribution at the jet centerline for various downstream positions for a saturated 62 $^\circ C$ jet 139

5.9 Comparison of experimental and model results of droplet diameter distribution at the jet centerline for various downstream positions for a saturated 85 $^\circ C$ jet 140

5.10 Comparison of experimental and model results of droplet diameter distribution at various radial positions at a downstream distance of $z/d = 1.7$ for a saturated 85 $^\circ C$ jet 141

5.11 Comparison of experimental and model results of droplet diameter distribution at various radial positions at a downstream distance of $z/d = 15$ for a saturated 85 $^\circ C$ jet 142

5.12 PDF particle field (particles colored by passive scalar) overlaid with the PDF computational grid (top) and CFD computational grid (bottom) 147
5.13 CFD results from `OpenFOAM` showing velocity contours 154
5.14 Plot of normalized jet velocity as a function of η at various downstream distances 154
5.15 Plot of the jet half-width as a function of downstream distance 155
5.16 Plot of the jet centerline velocity ratio $(U_j/U_c(z))$ as a function of non-dimensional downstream distance (z/d) 155
5.17 Plot of the jet centerline velocity ratio $(U_j/U_c(z))$ as a function of non-dimensional downstream distance (z/d) for the low-density, 85 $^\circ C$ jet 157
5.18 Plot the density discrepancies between the PDF and CFD simulations both (a) with and (b) without velocity corrections 160
5.19 Plot of computational particles colored with scalar value 161
5.20 Plot of the non-dimensionalized centerline concentration decay 162
5.21 Plot of the non-dimensionalized concentration profiles 163
5.22 Plot of the non-dimensionalized concentration profiles 164
5.23 Contour plot of D_{10} values predicted by PDF for the 85 $^\circ C$ jet 165
5.24 Time-lapse photo of a condensing jet illuminated by a laser sweeping along the jet axis 166
5.25 Plot of the diameter distribution of the centerline of the 85 $^\circ C$ jet at various downstream distances 168
5.26 Plot of the diameter distribution of the centerline of the 62 $^\circ C$ jet at various downstream distances 169
5.27 Plot of the diameter distribution for the 85 $^\circ C$ jet at $z/d = 15$ at various radial distances 169
5.28 Comparison plot of D_{30} versus downstream distance for the 85 $^\circ C$ jet, both seeded and unseeded 171
5.29 Comparison plot of D_{30} versus downstream distance for the 62 $^\circ C$ jet, both seeded and unseeded 172
5.30 Plot of the typical particle concentration throughout the domain 173
5.31 Plot of D_{30} along the jet centerline for two particle density cases 174
5.32 Plot of D_{30} along the jet centerline for two diameter bin discretizations 175

ACKNOWLEDGMENTS

I would like to express sincere appreciation to the University of Washington, where I have had the opportunity to work. Seattle has been a fantastic city to spend the last four years in no small part due to UW. My appreciation extends to the ME department and the support staff. I also owe a debt of gratitude to Rice University, where I earned my B.S. and M.S. degrees. Specifically, Dr. Tezduyar, for whom I did research as an undergraduate, for being my first graduate adviser and helping me earn my master's degree.

Thanks to Igor, Evan, Michelle, and everyone at Enertechnix. Besides keeping me funded with an interesting project at the beginning of my graduate student career, they were all instrumental in helping me publish my first paper as a first author.

Thanks go out to all of my lab-mates and classmates, past and present, for all of their support. Special thanks go to Chin for being my partner in engineering for the octagonal jet experiments. He might be the only person I can think of who could work so closely with me for so long without complaining. It was my privilege to work with him for much of my time at UW. Thanks to Colin, who was very accommodating as we continually disrupted his lab space with our large-scale experiment, and for taking the initiative on the lab camping trip every year. Thanks to Teymour, who helped me survive quals, and Grant, Cheri, and Vara for helping me remember what I forgot about mechanics of materials. I still owe Sam for mitigating the damage done by the violent water leak I may or may not have been responsible for. Thanks to Danny for helping me navigate the confusing waters of running on a GPU in Linux. Thanks to Pat and Danny for showing me it is possible to graduate when I was beginning to have my doubts. Thanks to Michael for getting me back on-line when the computer I needed to run stability simulations on quit ignominiously. I am grateful to Leo, who machined the nozzle calibration stand.

A number of people/organizations have made it possible for me to eat three square meals

a day during my time at the University. I am grateful for their assistance: Funding for the work on explosive particle removal modeling was provided by the Department of Homeland Security, Science and Technology Directorate. The physics department kept me gainfully employed as a teaching assistant in between research assistant opportunities. Dr. Keith Holsapple was gracious to have me as a research assistant in between opportunities that directly funded my thesis research. Funding for the work on turbulent jet exterior PIV was provided by the Department of Justice. Sandia National Laboratories interviewed and hired me before I defended.

Thanks to my committee members for their time and expertise. Special thanks to Dr. Alberto Aliseda for bringing me into his laboratory group sight unseen. His tirelessness never ceases to amaze me, and his knowledge and advice have been invaluable. The adviser you end up working with is probably the most important thing that happens to you in graduate school, and I got very lucky, indeed, to partner with Alberto. I could not have navigated the ins and outs and highs and lows of graduate school without him.

Of course, my family and friends deserve on-going thanks. In particular, enormous thanks go to my wife, Jackie. She encouraged me in my decision to go back to school and has supported me throughout. Best of all, she brought our daughter into the world and has done more than her fair share of parenting as I have spent numerous weekends and evenings working on my dissertation. I look forward to making it up to her for the rest of my life.

DEDICATION

To my wife Jackie, who will always be the real doctor in our family

Chapter 1

INTRODUCTION

The true logic of this world is in the calculus of probabilities.

– James Clerk Maxwell

The single component, single phase, turbulent round free jet has been studied for many years by a number of researchers. It has been examined successfully by use of computational fluid dynamics (CFD), experimentation, and analytic analysis using first principles. The simplicity of its description (as few as two parameters: initial velocity and nozzle diameter), combined with the complexity inherent to any turbulent flow makes it a tempting target of investigation. It may also serve as a fluid dynamicist's "spherical cow": a simple, well-studied surrogate used as a foundation to help understand more complex flows that share some of the same features.

Despite its apparent simplicity, the turbulent round jet still offers a rich field to study. Even the basic momentum-dominated turbulent round jet still has unanswered questions concerning, for instance, the effect of initial conditions, or the cause of the mixing transition (Dimotakis, 2005). Deviations from the simplest case add layers of complexity that still await investigation.

The nature of turbulence is sufficiently chaotic that when quantitative predictions are made about its behavior, they are only made in a statistical sense; that self-similarity emerges and applies to many aspects of the flow (e.g. mean and standard deviations of velocity) is of great utility. Because turbulence is so complex, much of the useful modeling cannot be derived from first principles, and understanding must rely on empirical data.

The behavior of the turbulent round jet in most applications emanates from the simplest, canonical behavior. In order to extend specific experimental findings to other scenarios that are either too numerous or exotic for the laboratory, modeling (either analytical or computational) must be applied. Detailed modeling can be used to help understand observed

phenomena; on the other hand, experimental observations can be used to support the appropriateness of certain physics-based models. In this way, sufficient understanding of such flows can only be achieved by leveraging all of the tools in the engineer's arsenal: modeling, simulation, and experimentation.

The first part of our investigation (Chapter 2) examines a sonic turbulent round jet. It does not satisfy the typical assumption of incompressibility because it emerges underexpanded from the nozzle, with a higher than ambient density. Given enough time/space, such jets eventually expand sufficiently to assume the self-similar behavior associated with the canonical, incompressible jet. We investigate the shearing effect such a jet has when impinging on a solid surface that is perpendicular to the flow direction. We conducted experiments to evaluate the jet's ability to remove different types of explosive particles from a glass surface. Analysis revealed trends that improve the predictability of particle removal for various jet conditions. The results of this research were published in Keedy et al. (2012).

In previous jet investigations, numerous methods have been employed to analyze the jet velocity profile and its associated statistics. Most if not all of these analyses require specialized equipment either in the form of in-situ instrumentation (e.g. hot wire) or illumination (e.g. lasers for particle image velocimetry). There are many situations where environments may prove too hostile or remote for the desired instrumentation. In Chapter 3, we develop a methodology for analyzing video of the exterior of such a naturally-occurring flow.

As part of the remote-sensing velocity measurements methodology, we found that the presence of viscosity gradients affects the velocity analysis. While these effects produce consistent, predictable changes, we are interested in the mechanism by which the viscosity gradients affect the mixing and development of the turbulent round jet. Since our velocity analysis methodology relies on the visualization of the turbulent/non-turbulent interface, we suspect that the viscosity gradient is influencing the interface behavior. To further explore this possibility, in Chapter 4 we conduct a stability analysis of the axisymmetric jet when a viscosity gradient is present.

Finally, we investigate another rich area of turbulence research: multi-phase flow. Specifically, in Chapter 5 we look at how droplet growth rates and turbulent convection affect the diameter distribution of condensing water droplets in a supersaturated turbulent jet. Non-

linear interactions between the droplet growth rate and the supersaturation field make analysis computationally taxing. Our investigation is entirely numerical, although we validate our results against experiments from the literature. We utilize a graphical processing unit to more efficiently make statistical predictions of the spatially-varying diameter distribution of the condensing droplets.

Chapter 2

PARTICLE REMOVAL WITH A SONIC, TURBULENT JET

2.1 Nomenclature

d_p	Particle diameter
z	Nozzle stand-off distance
z_0	Downstream distance of virtual origin
z^*	Virtual downstream distance $(z - z_0)$
d	Nozzle diameter
P_0	Reservoir (supply) pressure for jet
U_0	Jet exit velocity, eq. (2.5)
d_e	Effective nozzle diameter, eq. (2.4)
U_e	Effective jet exit velocity, eq. (2.5)
ε_{rem}	particle removal efficiency (by area)
$\hat{z}$	Dimensionless downstream distance (z/d)
ζ	Effective virtual downstream dist, eq. (2.3)
ζ_{50}	Value of ζ corresponding to 50% removal

2.2 Background

The removal of small solid particles from solid surfaces is a ubiquitous problem in material processing. While most of these applications rely on liquid solvents to extract the solid residue from a process surface, there are many cases in which a non-intrusive clean up process is preferable to reduce cost and limit the possible damage or contamination of the surface.

In addition, there is a need for non-invasive sampling and inspection of contaminating residues that may indicate chemical, radiological, or biological hazards. Fine particulates of explosives may be dislodged during the bomb making or handling process and may adhere

to available surfaces. Bender et al. (1992) observed that low volatility explosive vapors tend to adsorb onto surfaces or dust particles which may settle on the surface. Davidson & Scott (2002) noted that this presents an opportunity for several explosive detection schemes based on particulate sampling. A recommendation of the recently released report of the National Research Council on Existing and Potential Standoff Explosives Detection Techniques calls for "the use of convective streams with or without airborne adsorbing particles to gather chemical samples" (NRC 2004). This advocates the approach of dislodging molecular vapors and particles containing traces of explosives from the surface and near-surface boundary layer by increasing convective mass transfer, which would allow them to be captured and analyzed.

Particle removal depends on particle, surface, and jet properties. A high-speed gas jet impinging on a solid surface sets up a tangential flow with a thin boundary layer, thereby producing high shear stresses on the surface. This exerts a force on the particles that can potentially overcome the adhesive forces binding the particles to the surface as well as their own weight, and suspend them in the gas stream. The gas stream can then be sampled by a detector designed to collect and analyze the suspended particles.

Ranade (1987) noted that particle-surface interactions are determined by a wide variety of particle and surface properties, in addition to the particles' shape, size, and distribution. He listed molecular interactions, electrostatic interactions, liquid bridges, double-layer repulsion and chemical bonds among the influences that conspire to attach a particle to a surface. There is a paucity of data relating these properties or specific molecular traits of the surface to measurements of particle adhesion. The aim of this investigation was to take a more holistic approach; we seek to evaluate removal rates of three types of explosives, and compare their removal efficiency to that of benchmark ceramic microspheres. Because various types of microspheres are easy to obtain in a range of sizes and their regularity is conducive to modeling, they can be useful surrogates for explosive particles.

Several researchers have used microspheres as surrogates for explosive particles to study non-invasive removal. Fletcher et al. (2008) examined particle removal by air jets from filter and cloth surfaces. Polycarbonate spheres of several sizes were used as surrogates for explosive particles; the smallest microspheres were shown to be significantly more resistant

to resuspension than larger ones. In another removal study, Phares et al. (2000c) simulated explosives by creating spherical mono-disperse polystyrene particles laced with TNT. They observed the smaller particles to be more resistant to resuspension, however, once resuspended, they were easier to collect than their larger counterparts.

There are a number of theories on particle detachment. Wang (1990) suggested three mechanisms of removal of a single particle: lift-off, sliding, and rolling (see Figure 2.1). Ibrahim et al. (2003) concluded that rolling is likely the primary driver of detachment caused by forced air. However, they cited particle-particle interactions to be a potentially important secondary cause of particle detachment. For the purposes of this analysis, we will assume in our analysis and quantitative model that rolling is the dominant mechanism for resuspension. This is a conservative estimate of particle removal, and secondary mechanisms such as particle-particle collisions can be added later.

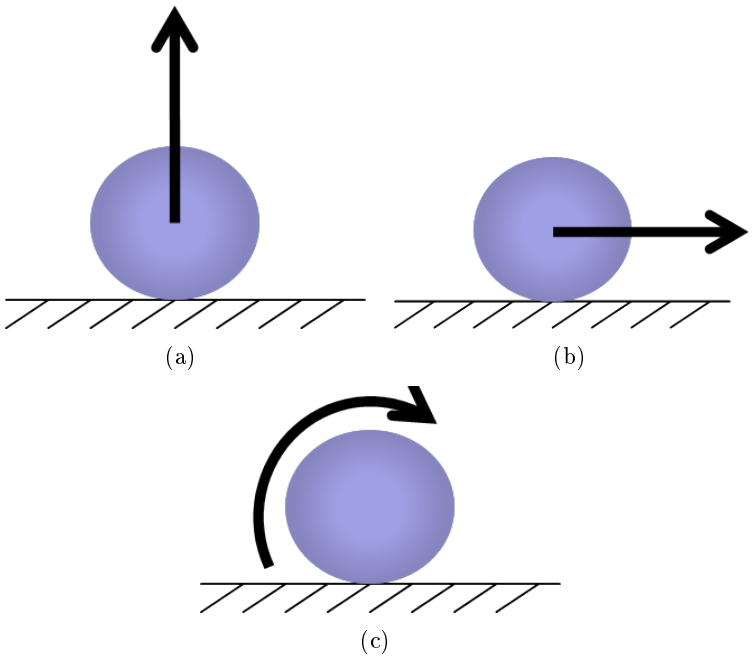

Figure 2.1: Cartoons of the three different removal mechanisms identified by Wang (1990): (a) lift-off, (b) sliding, and (c) rolling

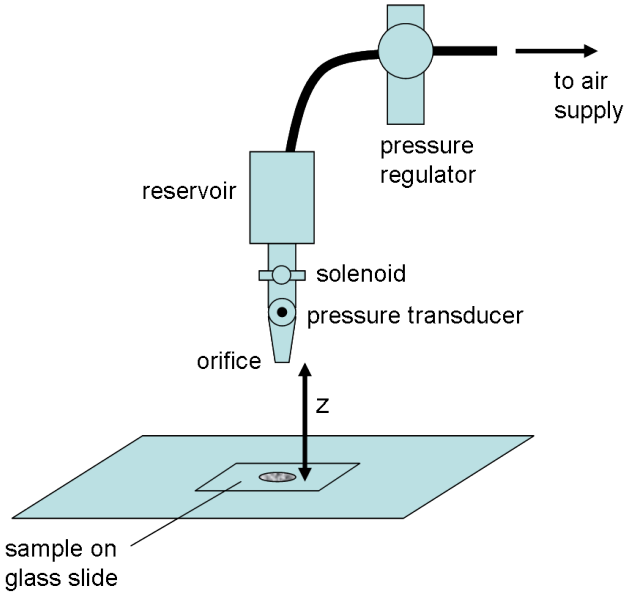

Figure 2.2: Diagram of the air jet interrogation experimental setup

2.3 Experimental Procedure

Both ceramic microspheres and explosive particles were interrogated with the same air jet experimental setup. Figure 2.2 shows a sketch of the experimental layout. The experiments involving the ceramic microspheres were all conducted with a jet issuing from a convergent nozzle of diameter 2.5 mm. However, in order to remove explosive particles at reasonable rates, we found it necessary to increase the nozzle diameter, testing nozzles up to 4.75 mm in diameter. Analyses described in section 2.4 allow for quantitative comparisons to be made across a range of nozzle diameters.

All particles were deposited onto a VWR VistaVision^{TM} glass slide prior to being interrogated with the air jet. Before deposition, the glass slides were cleaned in an ultrasonic bath and dried. Each prepared glass slide was subjected to a single air pulse. Most tests involved a pulse of approximately 20 ms in duration, although some tests involved longer duration pulses in order to evaluate the effect of pulse duration. Masuda et al. (1994) observed that the duration of the jet, as well as the number of jet pulses used are both known to affect removal rates. All of our experiments, however, used a single jet burst; we did not notice

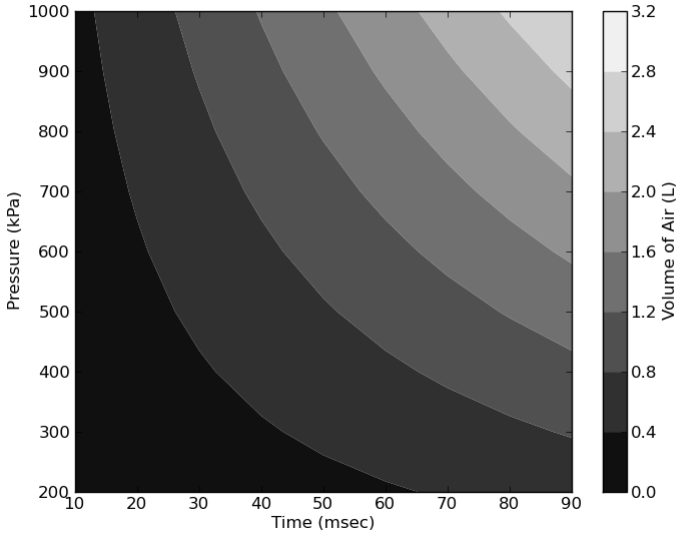

Figure 2.3: Volume of air ejected from a 4.5 mm nozzle as a function of reservoir pressure and pulse duration

a strong effect due to varying the jet duration from $25 - 100$ ms (see Figure 2.4). For the eventual purpose of collecting the removed particles for analysis, a shorter pulse length reduces the dilution of the air to be sampled; therefore, the interrogation of explosive particles was done with air jets on the order of 20 ms (significantly smaller pulses being challenging in practice due to solenoid valve limitations). Figure 2.3 illustrates the resulting volume of air ejected from a 4.5 mm nozzle, as a function of reservoir pressure and pulse duration.

An ASCO® Red-Hat II fast-acting solenoid valve controlled the length of the pulse. Supply pressures ranged from 138 to 965 kPa above atmospheric; a reservoir was used upstream of the solenoid to help maintain a constant jet back-pressure for the duration of the pulse.

For the values of reservoir pressure tested, the air jet emerges sonically from the nozzle as an under-expanded jet. Humidity was controlled in the lab, maintaining a value of 30-50%. This is an important consideration, as previous experiments, notably Corn & Stein (1965), have noted that removal efficiency drops significantly at high humidity levels.

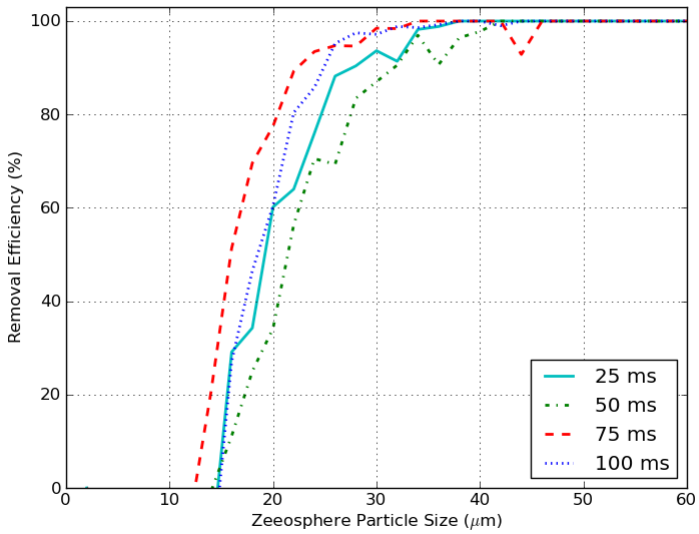

Figure 2.4: Ceramic microsphere removal for jet bursts of different duration (2.5 mm nozzle diameter, 276 kPa reservoir pressure, 152 mm stand-off distance)

2.3.1 Ceramic Microspheres

We tested removal of polydisperse ceramic spheres, as a benchmark against which to compare the explosive particles. The particles were Zeeosphere™ ceramic microspheres G-850 (Zeeospheres Ceramics, LLC, Lockport, LA). According to the documentation, the mean particle diameter ranges in size between 35 and 60 microns, with a 50 micron mean being reported as typical. Verkouteren (2007) suggests this is within the range of explosive particle sizes that should be targeted for sampling.

The particles were gravity-deposited directly onto the glass slides (dry transfer via Bytac® strip was not used in these experiments) and interrogated at least 24 hours later. We expect this method of deposition yield approximately equivalent removal results to our experiments using explosives (where particles were forcibly applied). Otani et al. (1995) performed experiments showing that a single jet pulse removed particles at comparable rates whether they were deposited by inertial impaction or gravitational settling followed by a waiting period.

For these experiments with ceramic spheres, air supply pressure ranged from 138 to 483 kPa above atmospheric. Stand-off distance was varied from 25 to 229 mm ($\hat{z} = 10$ to 92)

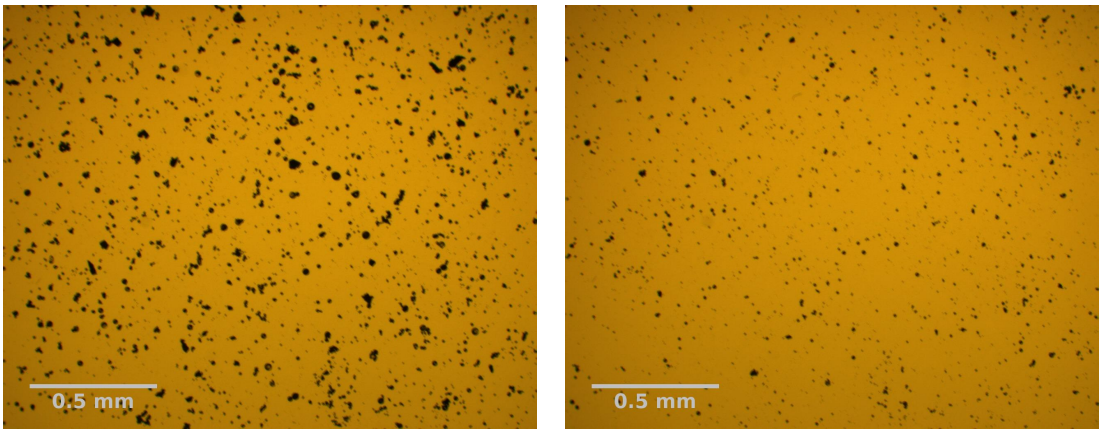

(a) Ceramic microspheres before air jet interrogation

(b) Ceramic microspheres after air jet interrogation

Figure 2.5: Microscope images of ceramic microspheres on glass, both before and after interrogation by an air jet pulse (2.5 mm diameter nozzle, 207 kPa reservoir pressure, 152 mm stand-off distance)

Pictures of the slides were taken under microscopic magnification both before and after interrogation (see Figure 2.5). ImageJ (NIH, Rasband 1997–2011) was used to analyze the microscopy images before and after interrogation in two different ways. If only the the coverage area was necessary, the a converted binary image was examined, and the number of dark and light pixels were recorded. The number of black pixels in both the before and after the air jet interrogation were recorded as coverage areas. In this manner, removal efficiency was calculated simply as

$$\varepsilon_{rem} = \frac{A_{before} - A_{after}}{A_{before}}. \tag{2.1}$$

Notice that this surface area removal metric assumes that the mass of explosive is deposited in a single layer with uniform thickness. This is an approximation that, by being used consistently across the experiments described in this study, allows for quantitative comparisons to be made.

In addition to making a coverage area measurement, the processed, binary image can

be used to determine the size distribution of the particles. An ImageJ macro is used to distinguish individual particles that may be close enough to touch after thresholding, but are separate physically. This histogram procedure is most effective when analyzing ceramic spheres. In addition to the ceramic spheres being more clearly distinct than the explosive particles, because the ceramic particles are spherical, a histogram of particles, binned by diameter can be determined from the images.

The particle size which experienced 50% removal was determined by analysis of various particle size bins both before and after interrogation by the air jet. The ratio of the particle count before and after removal was converted to a percentage removal for each particle diameter range. Plotting the data as a function of diameter, we expect the curves of removal (one curve for each experiment) to cross the 50% removal level at the relevant particle diameter.

One drawback of this approach is that if multiple particles are deposited adjacent to each other, the software may incorrectly account for them as a single large particle instead of several small particles. Additionally, the number of particles necessary for reliable analysis may challenge the approximation we are making that particle-to-particle interactions are not a main driver of particle removal.

Figure 2.6 shows removal efficiency data as a function of particle diameter for several experiments varying the supply pressure. The data tend to become noisier at larger particle diameters because they occur with less frequency than the smaller particles; the relatively small number of particles before interrogation leads to removal rates calculated using relatively small sample sizes. Despite challenges with the sample sizes, there is a clear trend that particle removal efficiency depends strongly on the jet reservoir pressure.

2.3.2 Explosives

Chamberlain (2002) has outlined a procedure for preparing explosives for sampling, which we used in these experiments. C-4, TNT and RDX were obtained as solutions in acetonitrile at known concentrations. In order to prepare a sample, a volume of the solution, proportional to the mass of explosive desired (typically 5 μg), was deposited onto a 1"x 1" Bytac®

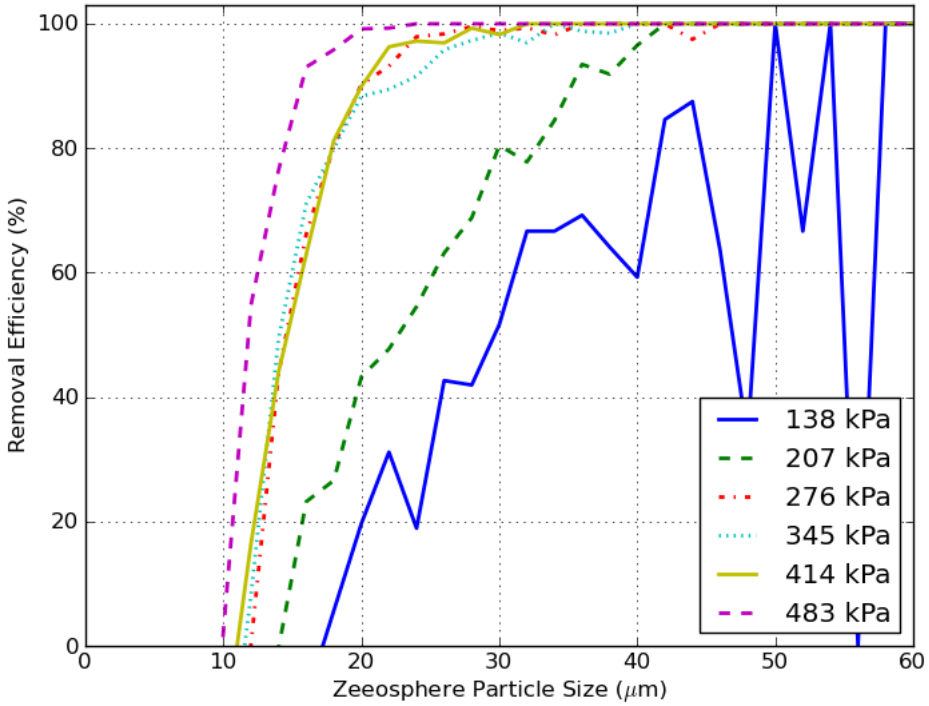

Figure 2.6: Ceramic microsphere removal for jet bursts with varying reservoir pressures (2.5 mm diameter nozzle, 152 mm stand-off distance)

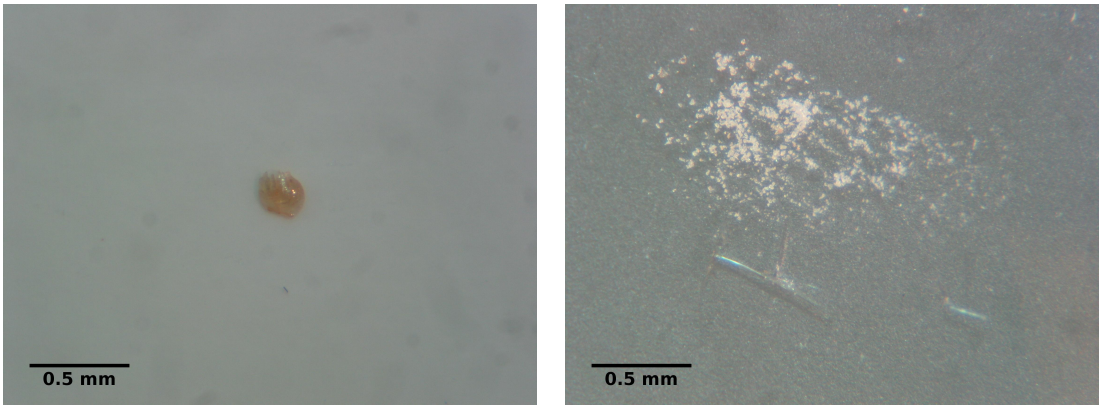

(a) (b)

Figure 2.7: Microscopic images of TNT before and after transfer. (a) Solid TNT nugget (5 μm) resulting from desiccation. (b) TNT particles after transfer

coupon. A drying chamber was used to speed up evaporation of the acetonitrile, resulting in the formation of crystal structures of trace explosive. The relatively low volatility of the explosive ($\mathcal{O}$ 0.01 Pa versus $\mathcal{O}$ 10 Pa for acetonitrile) allowed us to predict that the mass of the explosive was conserved during the drying process.

The explosives were then applied to glass slides by rubbing the coupon back and forth several times against the surface. This transfer was performed (as opposed to directly depositing the explosive solution onto the slide) in order to ensure repeatability and to remain consistent with the procedure outlines by Chamberlain (2002). Had the explosive particles been wet-deposited onto the glass surface, work from Bhattacharya & Mittal (1978) suggests that the particles would adhere much more strongly than in these experiments that use dry deposition. Furthermore, the transfer allowed the homogenous, condensed explosive to be broken up into smaller particles upon transfer. TNT was particularly prone to form a single solid structure upon evaporation of the acetone; applying the transfer technique described by Chamberlain allowed it to break up into many smaller particles (Figure 2.7).

The glass slides were interrogated shortly (less than 5 minutes) after application. The experimental setup for trace explosives removal was identical to the one used for ceramic spheres, shown in Figure 2.2. The pressure regulator was varied to establish the supply

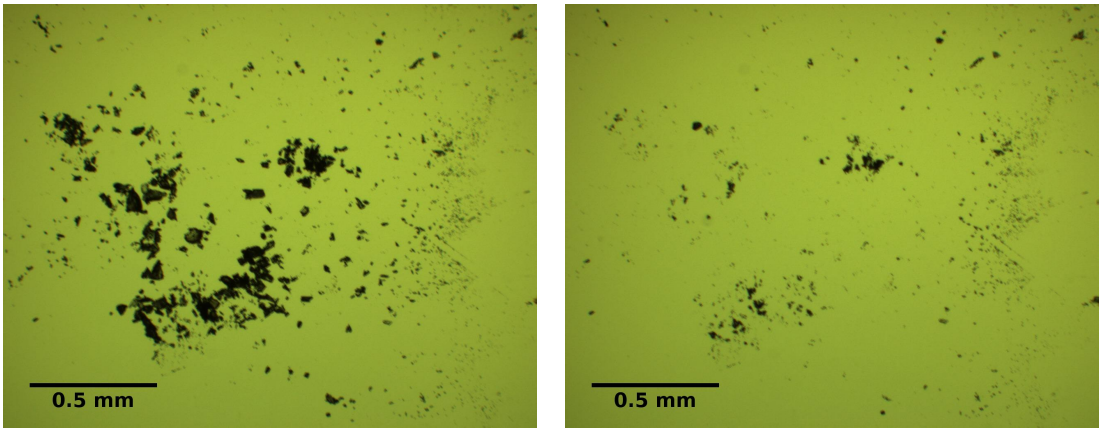

(a) TNT before air jet interrogation (b) TNT after air jet interrogation

Figure 2.8: Microscope images of TNT on glass, both before and after interrogation by an air jet pulse (4.75 mm diameter nozzle, 655 kPa reservoir pressure, 47 mm stand-off distance)

pressure to between 172 and 965 kPa. We measured the pressure and pulse duration just upstream of the nozzle using an SSI MediaSensor^{TM}P51 pressure transducer. The nozzle diameters tested were 2.5, 4.0, 4.5 and 4.75 mm. Vertical stand-off from the nozzle to the glass slide spanned 25 to 152 mm.

Because the explosive particles' shape and size distribution are irregular, options for evaluating removal are limited. The masses involved are too small to be weighed reliably ($\leq$ 5 μg). Also, individual particles sometimes cannot be optically resolved due to their proximity to each other. Even if the individual particles could be resolved, their irregular shapes would make the determination of their volume (and therefore their mass) subjective. Instead, we chose to measure the area covered by particles before and after interrogation, and compare them to determine removal efficiency (neglecting thickness of deposition).

Photographs were taken while examining the slides under a microscope both before and after the test (see Figure 2.8). ImageJ was used to analyze the images, calculating the area covered before and after the air jet interrogation, and removal efficiency was computed as defined in equation 2.1.

In addition, particle size analysis was conducted in the same manner as it was done for the Zeeospheres, though the uncertainty is higher due to the inability to identify inter-

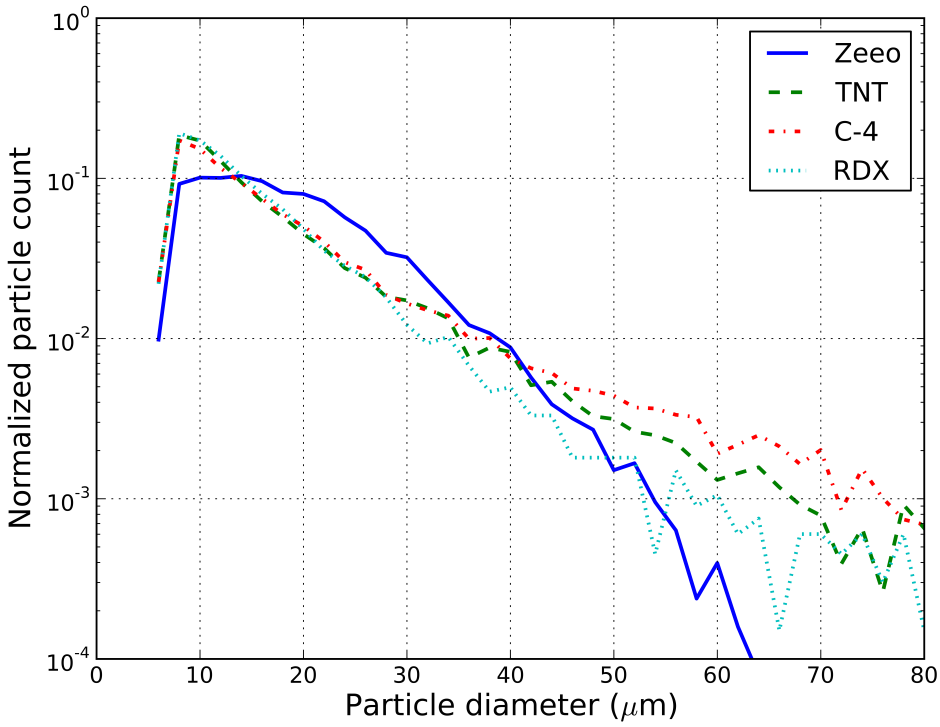

Figure 2.9: Histograms of particle size for the four types of particles in our study

nal boundaries of large explosive deposits. Figure 2.9 compares the results of histograms compiled from microscope images of the various particle types. Note that the three types of explosives exhibit the most similarity in particle size distributions, all of them having a wider distribution of particle sizes than the ceramic microspheres. However, Table 2.1 shows that for various particle distribution metrics, the four particles are quantitatively similar.

2.4 Modeling

For a choked, under-expanded gas jet, Birch et al. (1987) established that in the developed region,

$$\frac{1}{U_c} \propto \zeta, \tag{2.2}$$

	Zeeospheres	TNT	C-4	RDX
Median d_p (μm)	16	12	13	12
D_{10} (μm)	18	16	18	15
σ_d (μm)	9	13	16	11
D_{20} (μm)	20	21	24	18

Table 2.1: Particle size distribution properties

where the value ζ is a non-dimensional downstream distance that incorporates the effect of the jet reservoir pressure, stand-off distance and nozzle diameter. Due to the different experimental conditions used, ζ is an important non-dimensional variable that enables the comparison of different results across experiments. Birch determined the non-dimensionalized axial downstream distance of an under-expanded air jet by defining an effective jet diameter (d_e) and virtual origin (z_0) that are functions of the jet reservoir pressure. Plotted against this non-dimensional distance, the inverse of the jet velocity along the centerline collapses to a single, linear profile (outside of the development region).

The non-dimensional distance, ζ, is defined as

$$\zeta = \frac{z^*}{d_e} \tag{2.3}$$

where d_e is the effective diameter and z^* is the adjusted downstream distance, accounting for the virtual origin. Specifically,

$$d_e = d\sqrt{\frac{P_0}{P_a}\left(\frac{2}{\gamma+1}\right)^{\frac{1}{\gamma-1}}\frac{U_0}{U_e}}. \tag{2.4}$$

where P_0 is the jet reservoir pressure (absolute), P_a is the ambient pressure, γ is the heat capacity ratio, and

$$U_e = \frac{U_0}{\gamma}\left[1+\gamma-\frac{P_a}{P_0}\left(\frac{2}{\gamma+1}\right)^{-\frac{\gamma}{\gamma-1}}\right]. \tag{2.5}$$

The coordinate for downstream distance, z^*, is defined simply as $z^* = z - z_0$ where z_0 is the virtual origin. Birch provides an empirical relationship for z_0 versus reservoir pressure.

Hence, ζ is a function of z, d, P_a, and P_0. Figure 2.10 provides an illustration of the

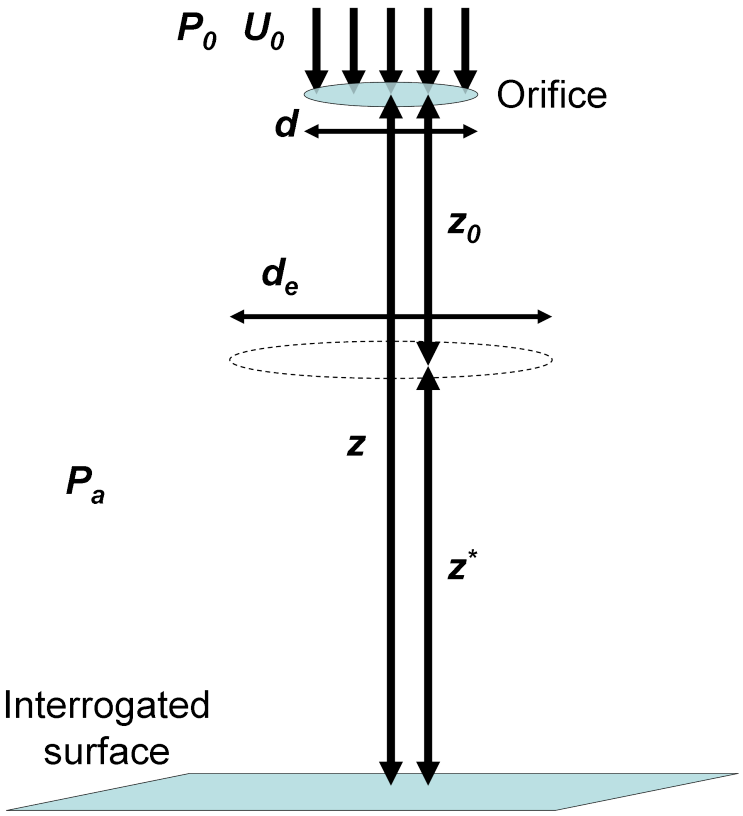

Figure 2.10: Diagram of dimensions used for analysis

various geometrical parameters used.

Figure 2.11 displays the resulting non-dimensional velocity (Mach number) contours on a pressure–$\frac{z}{d}$ plot. Note that the black line shows the boundary along which ζ equals 25. From Birch's consolidated plot of experimental data, $\zeta = 25$ appears to be the limit below which the developmental region applies and the model is not effective; therefore, we will trust predictions to the right of the line significantly more than those to the left of the line. There are reports for the development region being as small as $\frac{z}{d} = 5$, so we also included a contour of $\zeta = 5$. Alternatively, because Birch does not explicitly define the extent of the development region (and it may not correspond to one value of ζ), one may also choose an incompressibility criteria (such as $Ma < 0.3$) in order to define a region over which to apply the velocity model.

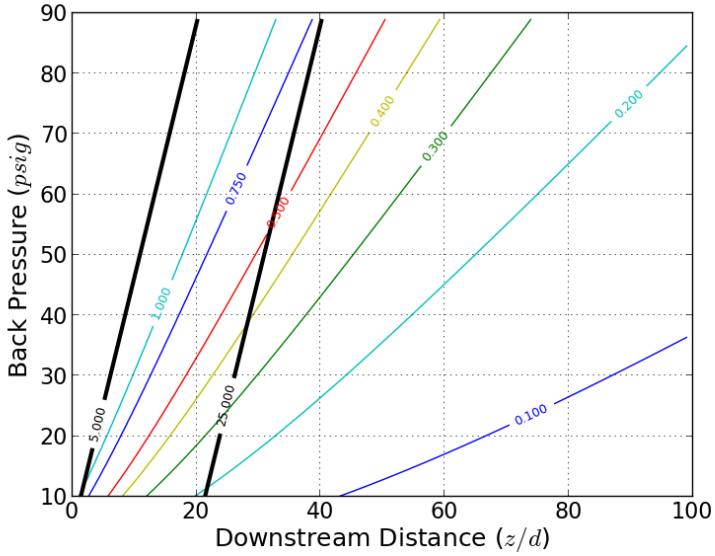

Figure 2.11: Contours of $\frac{U}{U_0}$ versus back-pressure and $\frac{z}{d}$

2.4.1 Removal Modeling

In order to remove a spherical particle from the surface by rolling, Phares et al. (2000a) proposed that the tangential drag force, applied at the particle center, must satisfy

$$F_{drag} = \frac{2aF_a}{d_p} \tag{2.6}$$

where F_a is the attachment force and a is the contact radius. Rimai et al. (1990) showed that a is proportional to the square root of the particle diameter:

$$a \propto \sqrt{d_p}. \tag{2.7}$$

and that the attachment force is proportional to a^2, which implies it is proportional to d_p:

$$F_a \propto d_p \tag{2.8}$$

That leaves the drag force to be determined. Phares also made use of the Galileo number ($Ga = C_D Re_p^2$), from which we can find a relationship between F_{drag} and d_p:

$$F_{drag} = \frac{\pi \mu^2 C_D Re_p^2}{8\rho} = \tfrac{1}{8}\pi\rho C_D d_p^2 U^2 \tag{2.9}$$

$$F_{drag} \propto d_p^2 U^2 \tag{2.10}$$

assuming C_D and ρ are constant. With the particle residing in the viscous sublayer, for a given flow intensity, we expect the velocity at the particle's centerline to be proportional to its height, d_p, and to the shear stress, τ, ($U \propto d_p \tau$) leading to

$$F_{drag} \propto d_p^4 \tau^2. \tag{2.11}$$

Thus, the condition for removal, (2.6), can be rewritten

$$d_p^{7/2} = \frac{C_1}{\tau^2} \tag{2.12}$$

where C_1 is a product of constants (and thus, a constant itself). Alternatively, and perhaps more usefully, we can determine the critical shear stress required as it relates to the particle diameter:

$$\tau = \frac{C_2}{d_p^{7/4}}. \tag{2.13}$$

The shear stress at the surface can be estimated based on analytical derivations presented in the literature. For a self-similar free jet, Phares et al. (2000b) derived a relationship indicating surface shear is proportional to $U^{1.5}$. Consolidating the constants to C_3, we can find a criterion for the removal of an individual particle using air jet velocity instead of shear stress:

$$U^{3/2} d_p^{7/4} = C_3. \tag{2.14}$$

Equation (2.2) can be used to derive a formula for ζ utilizing a new constant, K:

$$\zeta = K d_p^{7/6}. \tag{2.15}$$

2.5 Experimental Data

2.5.1 Microsphere Particles

Considering equation 2.15, K is best determined experimentally because it incorporates a number of undetermined constants. Taking into account the variability of ceramic sphere diameters, it is best to use a statistical interpretation of the deterministic model. Instead of focusing on the removal of a single particle, we will define the constant K that results in 50% removal of particles of a given diameter.

We first plot data collected from the ceramic microsphere removal tests over a range of supply pressures and stand-off distances. Figure 2.12 plots the ceramic particle diameter exhibiting 50% removal rates as a function of ζ. Because ζ is a function of the jet reservoir pressure and stand-off distance (and nozzle diameter), this allows us to overlay the results from many different experiments. A best-fit least-squares curve is also plotted, based on equation 2.15, where K was determined to be 1.35 $\mu m^{6/7}$. The data for removal of ceramic microspheres under a wide variety of experimental conditions are reasonably well described by the theoretical model.

2.5.2 Explosive Particles

After experimentally determining the ζ value corresponding to 50% removal of a particular explosive, an appropriately sized ceramic microsphere surrogate can be selected using equation 2.15. We expect such a mono-disperse surrogate to experience 50% removal under similar conditions as the explosive. However, the explosives tested all exhibited 50% removal at negative values of ζ (upstream of the virtual origin z_0). Being upstream of the self-similar region of the jet, the relationships outlined by Birch are not quantitatively accurate, and equation 2.15 does not adequately describe the relationship between downstream distance and removal. While we can no longer assume that removal will depend on ζ according to (2.15), it is reasonable to expect there will still be a similar qualitative dependency.

Quantifying explosive particle removal as a function of diameter was difficult, due to the variability in explosive particle shapes. Despite the fact that the deposition procedure was consistently followed, the explosive material was often deposited in irregular patterns with

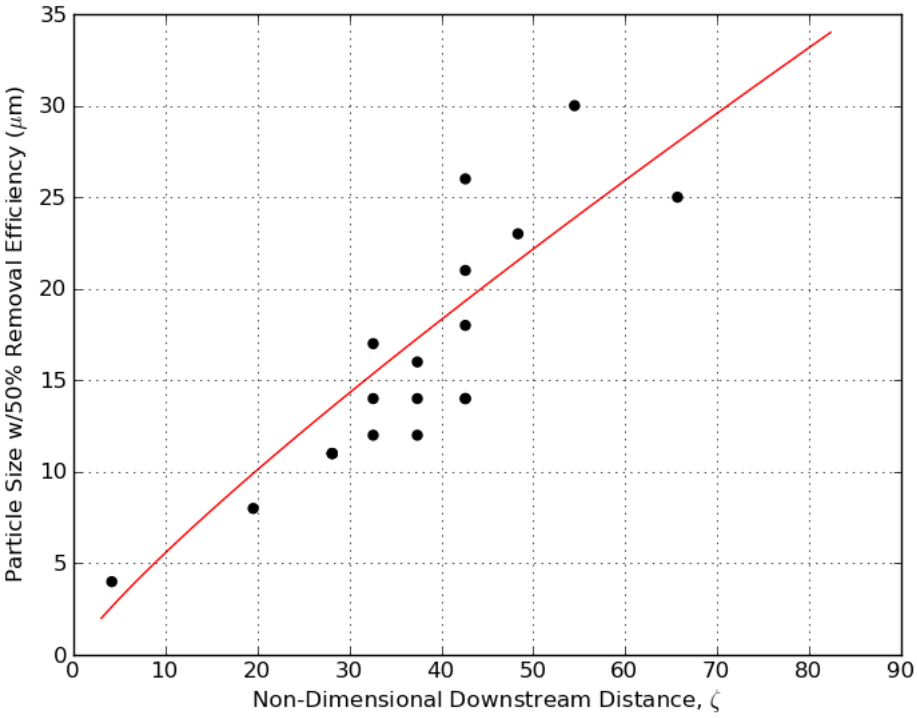

Figure 2.12: Plot of experimental data for ceramic microsphere particle diameter experiencing 50% removal at various ζ; data is fit with the curve from equation 2.15, $K = 1.35\ \mu m^{6/7}$

ill-defined internal boundaries. Because of the lack of certainty in size and shape of the particles, we chose instead to measure the explosive area removed against ζ. Figure 2.13 shows results for the three explosives tested as well as the ceramic particle tests. Although we cannot quantify the the maximum shear stress as a function of negative values of ζ, it is possible to report the value ζ_{50} that elicits 50% removal. In an effort to represent the data in a straight-forward manner with a clearly defined demarcation for 50% removal, we fitted each set of particle removal data with a sigmoid curve. The curves each had the following form

$$\varepsilon_{rem}(\zeta) = \frac{1}{1 + e^{0.12(\zeta - \zeta_{50})}} \tag{2.16}$$

where ζ is the independent variable and ζ_{50} uniquely defines the horizontal location of each curve. The coefficient 0.12 was chosen to best match the behavior of all particle types. By applying a least-squares fit criterion, ζ_{50} can be determined for each type of particle. It can be reasonably expected that under marginally different conditions the values of ζ_{50} may change, but we expect relative removal rates of the explosives to remain unchanged as long as the mechanism of particle removal from the surface remains the same.

It appears that the fit the data may be worse at higher values of ζ. We observed that occasionally the explosive transfer was not efficient in breaking up some of the larger particles. These large particles were removed at relatively high values of ζ, resulting in disproportionate coverage reduction and a high value of ε_{rem}.

C-4 proved the most difficult to remove, with a ζ_{50} value of -29. RDX was slightly easier at -23, and TNT was the easiest of the three explosives to remove at $\zeta_{50} = -11$. The ceramic microspheres on the other hand, were removed at a stand-off of $\zeta_{50} = 51$.

2.6 Summary

Explosive particles were found to be much more difficult to remove than their ceramic counterparts, despite the apparent similarity in particle size distributions. In order to achieve 50% removal, it was necessary to subject the explosives to the under-expanded, undeveloped region of the jet. This makes it difficult to quantify the shear stress needed for removal, but the non-dimensional downstream distance, ζ, may be used instead.

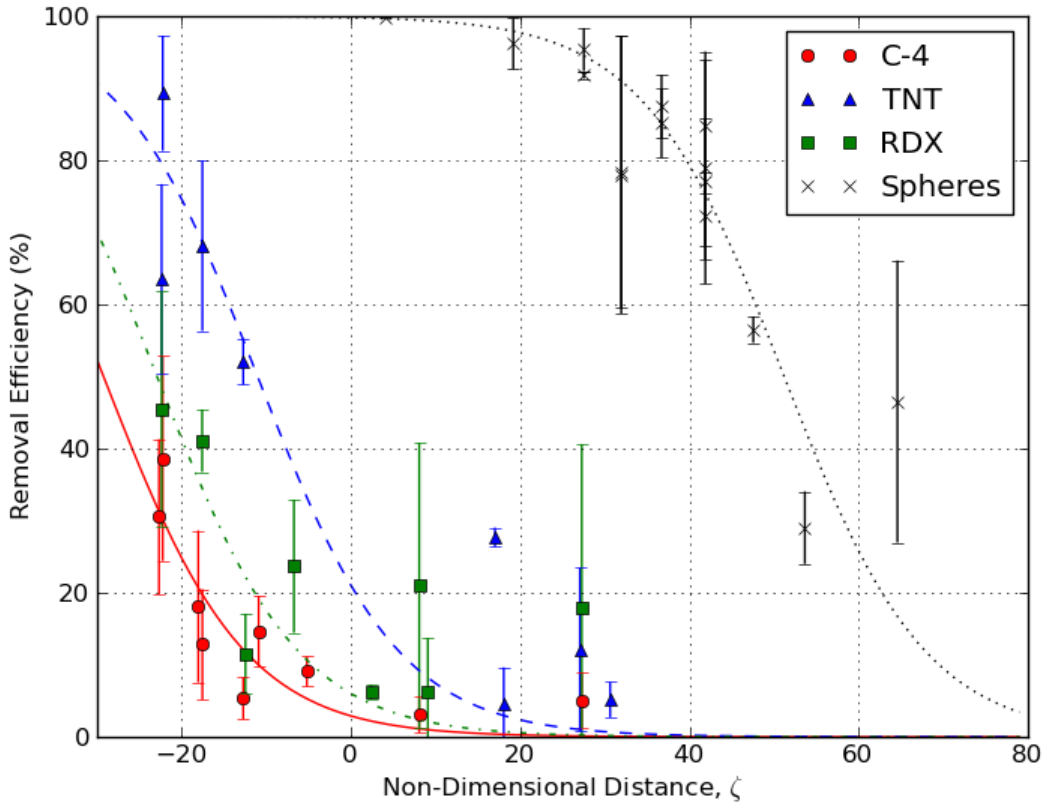

Figure 2.13: Plot of removal versus ζ for three explosives and ceramic microspheres (experimental results as points; curve fits from eq. 2.16 as lines)

The removal rate was observed to depend strongly on the type of explosive being examined, as well as being a function of ζ. There are several factors that could lead to different removal rates for different explosives. While the particle size distributions were similar among the explosives and ceramic microspheres, we have little information regarding the shapes of the explosive particles. It is reasonable to assume they are not spherical, but we cannot speculate as to whether the different explosive particles have characteristically dissimilar shapes, which would potentially result in different removal rates.

It is perhaps most natural to attribute the differences in removal rate to the chemistry of the particle and substrate involved. Since we use a glass substrate in all of our experiments, the adhesive force of each explosive can be impartially evaluated; other substrates may prove to either enhance or diminish the removal trends we observed.

The differences in ζ_{50} values indicate that TNT particles were easier than RDX to remove; C-4 particles appeared to require the highest shear stress to be resuspended. For example, given a 4.75 mm nozzle diameter, and a modest stand-off of $\hat{z} = 20$, our results from Figure 2.13 indicate 50% removal of TNT particles would require 790 kPa of supply pressure, 50% removal of RDX would require 1100 kPa, and 50% removal of C-4 would require 1300 kPa (the latter two pressures were never reached in this study). The ceramic microspheres we tested, on the other hand, should require less than 150 kPa for 50% removal. It is unclear, due to the limitations of our shear stress analysis, exactly what diameter a ceramic microsphere would need in order to behave as a surrogate for each explosive, but the typical diameter would need to be significantly smaller than 10 μm.

Chapter 3

MULTI-COMPONENT TURBULENT JET

3.1 Nomenclature

δt	Elapsed time separating PIV images in a pair
z	Nozzle stand-off distance
z_0	Downstream distance of virtual origin
z^*	Virtual downstream distance $(z - z_0)$
d	Nozzle diameter
U_j	Jet exit velocity
U_e	Jet exterior axial velocity, as measured by PIV
$U_c(z)$	Jet centerline axial velocity
d_p	Particle diameter
$\hat{U}$	Jet exit/exterior velocity ratio $\frac{U_j}{U_e}$
$\hat{\tau}$	Non-dimensional PIV time scale, eq. (3.22)
$\hat{z}$	Dimensionless downstream distance (z/d)
$\bar{z}$	Dimensionless virtual downstream distance $((z - z_0)/d)$
P	Ratio of momentum vs. buoyancy forces
ρ_a	Ambient fluid density
ρ_j	Jet fluid density
γ	Transmissivity
T	Temperature
Re	Reynolds number
μ_a	Dynamic viscosity of the ambient fluid
μ_j	Dynamic viscosity of the jet fluid

3.2 Background

The goal of this research is to enable non-intrusive velocity measurements of naturally-occurring turbulent flows, specifically flows that are opaque, cannot be seeded or are otherwise difficult to measure in-situ. In a laboratory setting there are a number of experimental techniques by which fluid velocity can be measured, for example: anemometry, hot-wire anemometry, laser Doppler anemometry (LDA), particle image velocimetry (PIV), etc. Often times, naturally-occurring turbulent flows are inappropriate candidates for such techniques, due to multiple considerations.

In some cases, the flow of interest may be difficult to access with laboratory instrumentation, such as hydrothermal vents on the ocean floor. Flows can exist in exceedingly harsh environments, such as the plumes emanating from a fire or a volcano eruption. However, a remotely operated vehicle can reach the appropriate location equipped with a video camera that can image the flow. Video cameras can capture the exterior view of hot, hazardous flows from a safe distance. Finally, some natural phenomena may be fleeting, and the most desirable instrumentation cannot be organized and set up in a timely or cost-effective manner. Video cameras, on the other hand, are nearly ubiquitous. Due to all of these considerations, it is desirable to be able to learn about such turbulent free shear flows from a series of images taken at known time intervals.

Our approach for analyzing such video will be to decompose it into consecutive image pairs and perform particle image velocimetry (PIV) analysis – in our case, perhaps the more appropriate moniker would be *pattern* image velocimetry. Typical "laboratory-grade" PIV involves a transparent flow seeded with particles. These particles are typically illuminated with powerful, brief laser bursts illuminating either a plane (for 2-D) or volume (for 3-D) within the fluid region of concern, and a specialized camera captures image pairs of the particle field with a well-controlled time separation between the two images in a pair (a more thorough discussion of PIV is included later in this chapter). Rather than predicting velocities by analyzing the movement of the particle field, our approach will deviate from traditional PIV, and analyze the movement of the patterns of turbulent structures on the jet exterior.

The effort to understand naturally-occurring flows, or to extract more information from flow visualization in the laboratory has led to multiple attempts to extend PIV techniques to non-particle flows in the literature. Aerial views of the white-caps of wind-driven deep-ocean waves have been analyzed using PIV by Melville & Matusov (2002) to determine their velocities along the ocean surface. Ryu et al. (2005) coined the term "bubble image velocimetry" in the development of a technique to obtain velocity fields inside a bubbly plume, a commonly occurring flow that presents enormous challenges to flow visualizations and direct measurements. In order to look within the flow field of a breaking wave, Rodriguez-Rodriguez et al. (2011) used the naturally entrained air bubbles to make velocity measurements. Tokumaru & Dimotakis (1995) discussed a technique for extending traditional PIV using a method called image correlation velocimetry. Through use of correlations of scalar images and global minimization, they calculate velocity and the shear field directly, most notably of Jupiter's atmosphere.

Of course, in order to develop the technique for naturally-occurring flows, we must begin in the laboratory, where we can control/measure the parameters of the flow and of the imaging system. There are several conditions for the images to make analysis more accurate. First, if the camera's position and orientation (perpendicular to the jet axis) remains steady, that will reduce the uncertainty in the optical displacement and the position of the visualized flow structures. Additionally, the laser light-source will be approximately coaxial with the camera. The flow will be momentum-dominated, and the jet flow rate will remain steady.

We base our study, and the development of this technique, on the momentum-dominated, single phase, turbulent jet. This canonical free shear flow has several advantages to serve as the theoretical basis for the study; it is a geometrically-simple flow that has been widely studied, and for which simple relationships that describe its behavior have been derived. An important characteristic is that, in the far field, the turbulent jet is known to have a self-similar velocity profile. Wygnanski & Fiedler (1969) compiled velocity measurements with a static hot-wire (SHW) anemometer at several downstream distances. By normalizing the velocity magnitude and radial distance, the curves collapse (see Figure 3.1).

Likewise, the Reynolds stresses also exhibit self-similar behavior. Hussein et al. (1994) also studied the characteristics of a momentum dominated turbulent jet using stationary

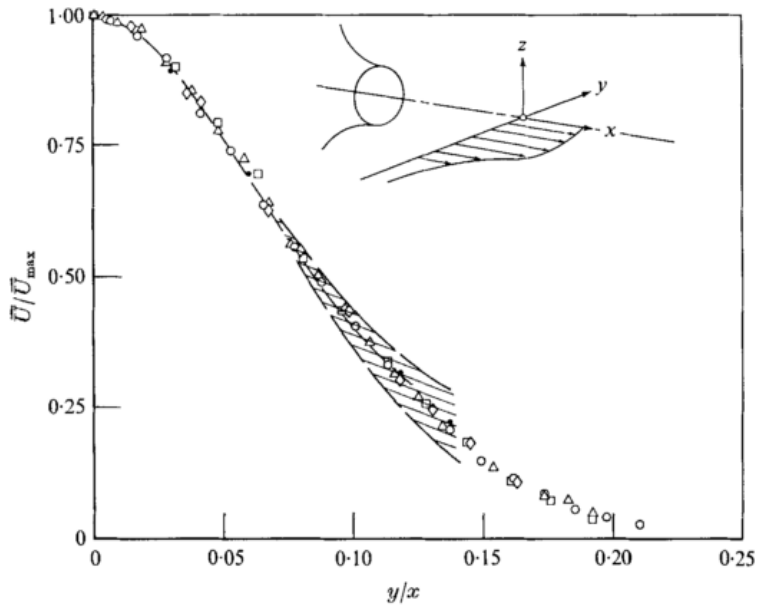

Figure 3.1: Plot of velocity measurements ranging from z/d values of 40 to 97.5 reported in Wygnanski & Fiedler (1969)

hot-wire anemometer (SHW), but supplemented the experimental data with flying hot-wire (FHW) anemometers and LDA. Figure 3.2 shows the Reynolds stresses resulting from that study.

The centerline velocity decay for a turbulent jet is, based on momentum conservation arguments:

$$\frac{U_c(z)}{U_0} = \frac{Bd}{z - z_0} = \frac{Bd}{\bar{z}} \tag{3.1}$$

where B and z_0 are both empirically determined constants (George, 1989). Hussein et al. (1994) investigated these relationships; we will use their values: $B = 5.8$ and $z_0 = 4d$. Figure 3.3 shows the favorable comparison of the model and experimental data.

These wealth of high-quality experimental data and rigorous mathematical analysis of the behavior of this flow makes it ideal to validate the experimental technique, and the ideas that it is based on, in a laboratory setting. This will allow the technique to be on solid ground to be applied in the field, where necessarily the levels of uncertainty will make the technique more complex to utilize and its results more difficult to interpret.

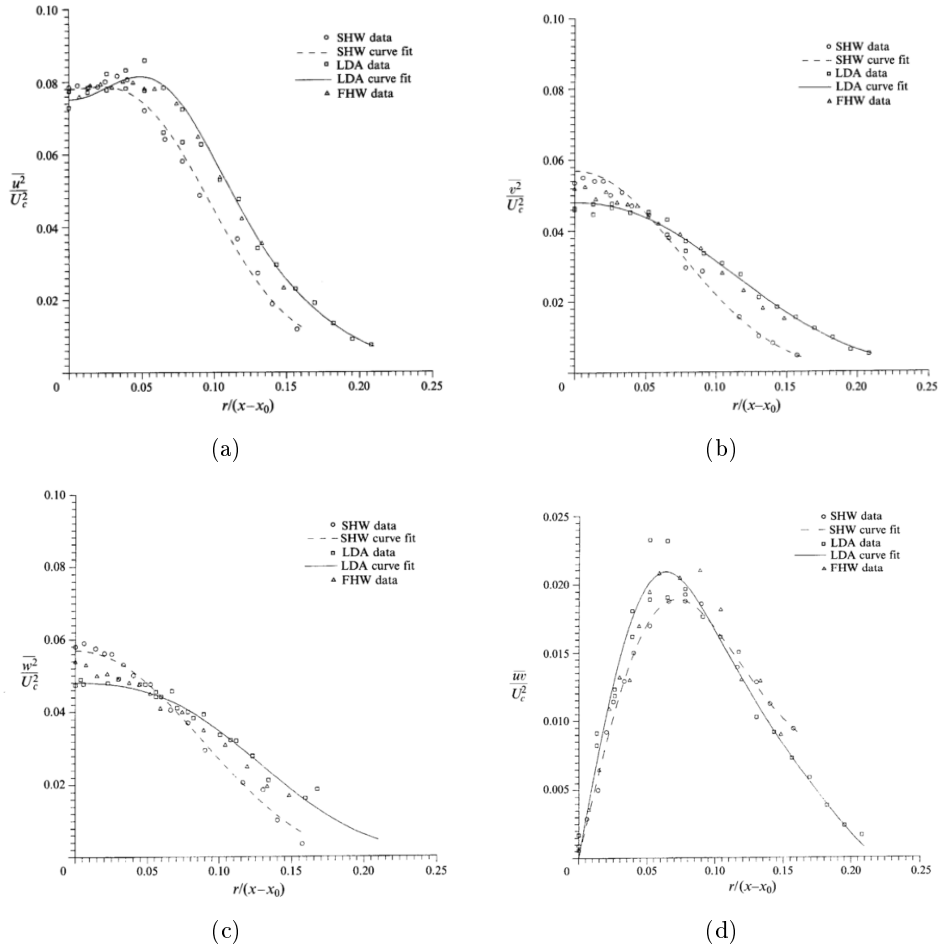

Figure 3.2: Graphs from Hussein et al. (1994) showing results for Reynolds stresses collected via SHW, FHW, and LDA

3.3 Experimental Setup

3.3.1 Fluids Equipment

We designed, built, and characterized an octagonal-prism acrylic tank to house the turbulent jet experiment. The octagonal design was chosen in order to provide a high level of flexibility to the experimental measurement techniques available for the study. In PIV measurements, it is important that both the laser and camera orientations are always perpendicular to the faces of the tank so as to avoid the complicating issues of refraction.

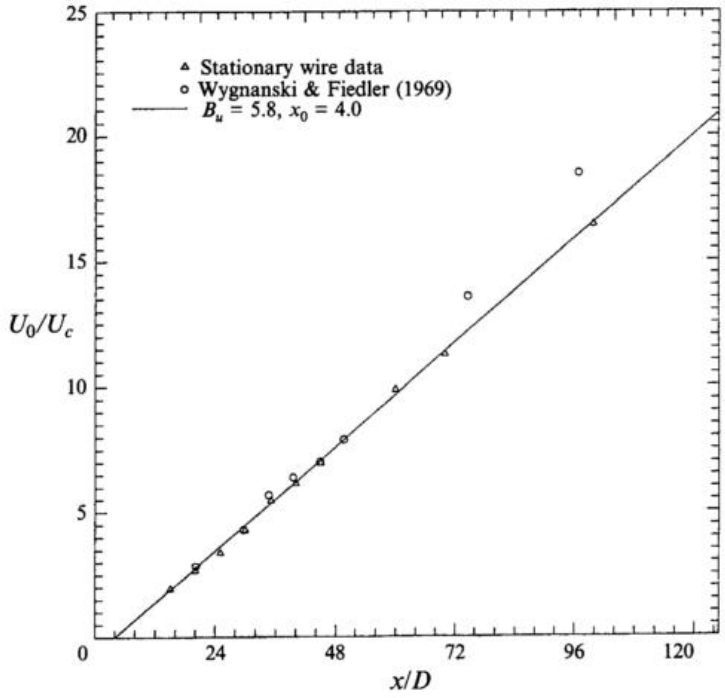

Figure 3.3: Graph from Hussein et al. (1994) showing centerline velocity ratio collected via SHW and LDA

Perpendicular face pairs of the octagon can be utilized for traditional PIV analysis. A laser sheet is cast through one side of the octagon, and the camera is oriented to look through the complimentary pane. Of course, the camera can be placed coaxial with the laser when imaging the jet exterior. While not part of this study, additional viewing angles are available for phase Doppler particle analysis (PDPA) measurements. The optimal angle between the lasers and the PDPA receiver is dependent on the particle/bubble-fluid combination. Therefore, we designed the octagon not as a regular octagon, but with several different internal angles, allowing for various PDPA setups. Specifically, we wanted to ensure there was the possibility of performing PDPA experiments at 120°, 135°, and 150°.

There are additional benefits to choosing a many-sided polygon. As the tank footprint approaches that of a circle, the boundary effects are mitigated, and the approximation of injecting fluid into an infinite reservoir is more accurate. Finally, the structural integrity is improved by reducing the stress at the joints and the deflection of the sides. The drawbacks to additional sides is complexity of construction and reducing viewing area of a given side.

Ultimately, we settled on the footprint seen in Figure 3.4, as the best compromise in flexibility of measurements and minimizing drawbacks.

The footprint is approximately 1.2 meters in each direction, and the tank is approximately 2 meters tall. The size was selected to be essentially as large as feasible, considering space, cost, and construction constraints. The motivating factor was to minimize the influence of confinement on the flow.

Hussein et al. (1994) estimated the effect of confinement by examining a momentum ratio, where a value approaching unity implies insignificant confinement effects:

$$\frac{M}{M_0} = \left[1 + \frac{16}{\pi B_m^2}\left(\frac{z}{d}\right)^2 \frac{A_0}{A_R}\right]^{-1}. \tag{3.2}$$

The value A_0 is simply the nozzle area, $\frac{1}{4}\pi d^2$. Substituting, the ratio is independent of diameter:

$$\frac{M}{M_0} = \left[1 + \frac{4}{B_m^2}\frac{z^2}{A_R}\right]^{-1} \tag{3.3}$$

where $B_m = 6.5$ and our tank has an approximate cross-sectional area: $A_R = 1\ m^2$. Thus,

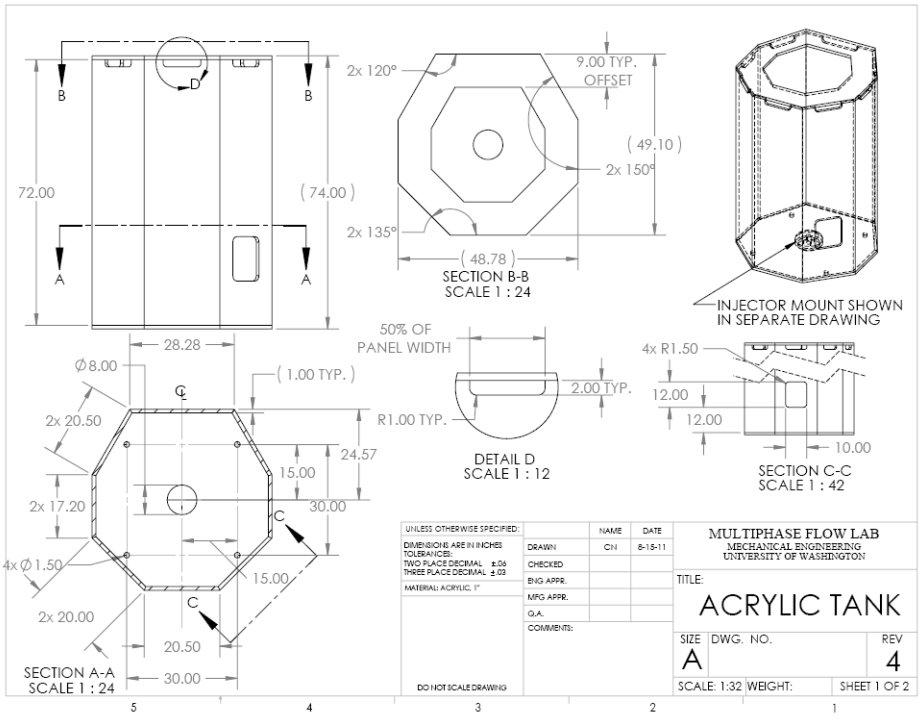

Figure 3.4: A drawing of our octagonal tank, seen from different perspectives

Nozzle Diameter (mm)	$M/M_0 > 0.99$ (z/d)	$M/M_0 > 0.95$ (z/d)
1	320	720
3	107	240
4	80	180
7	46	103
10	32	72

Table 3.1: Downstream distance for which confinement effects can be ignored in our experimental setup

the value of z below which the ratio $\frac{M}{M_0}$ remains above 0.95 can be calculated to be approximately 72 cm; for $\frac{M}{M_0}$ to remain above 0.99, the maximum downstream distance is 32 cm. Table 3.1 shows the value of $\frac{z}{d}$ for different nozzle diameters at the two different thresholds.

Overflow slots are cut near the top of the tank (see detail D in Figure 3.4) to maintain a constant level of fluid inside the tank as liquid is injected through the nozzle. An acrylic box is mounted and plumbed around each slot to divert overflowing liquid down and away to the floor drain. In this way, the ambient pressure as a function of distance from the nozzle is essentially constant over time, in an effort to further minimize the effect of the tank boundaries.

The tank is mounted on a custom-built steel table to accommodate the plumbing of the drainage/filling holes as well as the nozzle. This setup holds the tank 0.7 m above the ground in order to provide access to the jet nozzle, the underside of the tank, and flow connections associated with the experiment.

The tank has an access port on one of the lateral panes, near the base in order to manipulate the nozzle setup and allow maintenance. A transparent acrylic plate is used to cover the port; it must be manually held in place during tank filling, but once full, water pressure holds it in place, and a gasket seals it to prevent water leakage.

Convergent nozzles were designed to provide a nearly uniform velocity profile as the free jet inlet condition. We defined the interior of our nozzle shape to be identical to the optimal trinomial nozzle studied by Hussain & Ramjee (1976):

$$R = \frac{d_i}{2} - \frac{3}{2}(d_i - d_e)\left(\frac{x}{L}\right)^2 + (d_i - d_e)\left(\frac{z}{L}\right)^3. \tag{3.4}$$

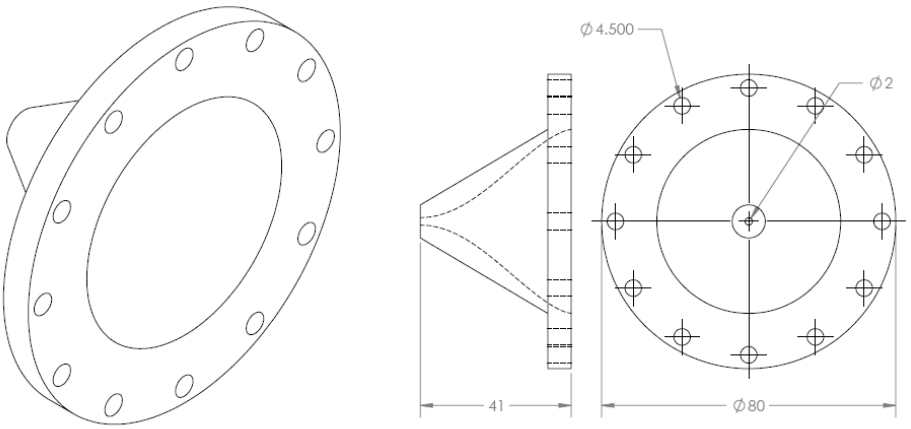

Figure 3.5: CAD drawing of a converging nozzle with a 2 mm diameter

CAD drawings for the nozzles having various exits diameters (but the same inlet diameters and lengths) were generated (see Figure 3.5); we had aluminum nozzles made and anodized for exit diameters of 1, 3, 4, 7, and 10 mm.

Fluid flow is driven by a pressurized diaphragm tank; pressure was maintained by a regulated building air supply line (regulated to approximately 600 kPa for most experiments). A Blancett Model 1110 turbine flowmeter equipped with the digital readout provided by a B2800 Series flow monitoring system was used to measure the flow rate; the digital readout (accurate to a few hundredths of a gallon per minute) is monitored during the experiments and incremental adjustments to an in-line needle valve are made to maintain a constant flow rate. The resulting average jet exit velocity depends on the diameter of the nozzle being used:

$$U_{jet} = \frac{4Q}{\pi d^2}. \tag{3.5}$$

Hot water can be injected by rerouting the water through heat-exchangers as it is injected by the pressurized tank. Two steam-powered heat exchangers are used in series to heat up the injected water to the desired level. Thermocouples are placed both in between heat exchangers and slightly upstream of the nozzle to monitor temperatures.

Figure 3.6 gives an overview of the lab equipment's organization and plumbing. The

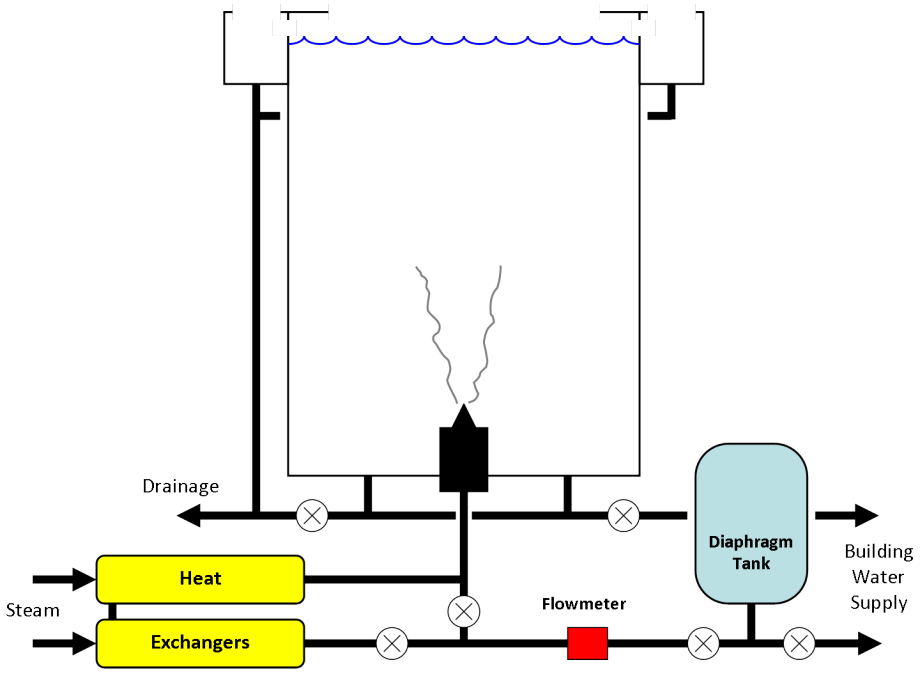

Figure 3.6: Cartoon of the flow experiment plumbing

diaphragm tank is plumbed such that it can be filled or flushed with water from the building water supply. A displacement pump is used to fill this tank with the liquid we wish to inject, whether it be Rhodamine-dyed water, or a high-viscosity glycerin solution. Due to the volume of the tubing between the diaphragm tank and the nozzle, the system must be flushed of the old injected liquid when a new type of liquid is to be used in experiments.

3.3.2 Imaging Setup

Our Solo PIV Nd:YAG Laser (New Wave Research, Portland, OR) utilizes two individual laser heads that can produce 532 nm wavelength beams with virtually any time delay between them; the pulses themselves last on the order of 5-10 nanoseconds. The lasers' power can be modulated to provide the optimum exposure for a given combination of camera distance, lens optics and flow.

A delay generator (505-8C, Berkeley Nucleonics Corporation, San Rafael, CA) is used to achieve precise, consistent timing between the two laser pulses and the camera. Five

BNC channels were used: two each for firing the lasers lamps and Q-switches, and a fifth to trigger the camera. The Q-switch delay was typically set to 200 μsec because this nominally provides for the brightest emission. However, occasionally the Q-switch interval is reduced below 200 μsec to reduce the output power in order to illuminate the jet at a level that does not saturate the camera sensor for the conditions of the experiment.

To image the interior of the jet, we use a combination of lenses to create a two-dimensional laser sheet. First, a spherical lens is used to focus the laser beam. A cylindrical lens is placed near the focal point of the spherical lens, resulting in laser light that is nearly parallel with respect to the lateral direction. The beam expands in the vertical direction past the focal point, creating a laser sheet which cuts diametrically across the nozzle in the streamwise direction of the free jet flow. The resulting laser thickness is approximately 1 mm.

When broad-area illumination is needed for visualizing the jet surface, a concave lens is used to expand the laser beam both vertically and laterally. A combination of highly reflective mirrors are used to orient the laser beam so that it is aimed at the jet exterior at an angle of less than 15°, coplanar with the camera's viewing axis. Figure 3.7 is a cartoon of the laser/camera setups illustrating the differences.

A high-resolution 4 megapixel CCD camera (MegaPlus ES4020, Princeton Instruments, Trenton, NJ) is used to capture the light scattered by the seeding particles in the flow, illuminated by the pulsed laser. The triggering signal is received by the camera controller via a BNC cable from the delay generator to start the first exposure for the camera; a time delay is set on-board the camera such that the second exposure begins immediately after the first laser pulse. Various Nikon lenses and macro extenders were used to obtain the required field of view. Data was transferred via CameraLink to a computer via a PCI frame grabber (PIXCI, EPIX Inc., Buffalo Grove, IL) and acquired by image acquisition and analysis software (XCAP, EPIX Inc., Buffalo Grove, IL).

While the elapsed time between camera exposures can be set to be very small (on the order of a few microseconds), the minimum time to reset between image pairs is on the order of a tenth of a second. This is comparable to the laser's maximum frequency, so neither the camera nor laser is severely limited by the other element in the PIV system. An image-pair acquisition frequency of approximately 10 Hz is insufficient to allow for any sort of time-

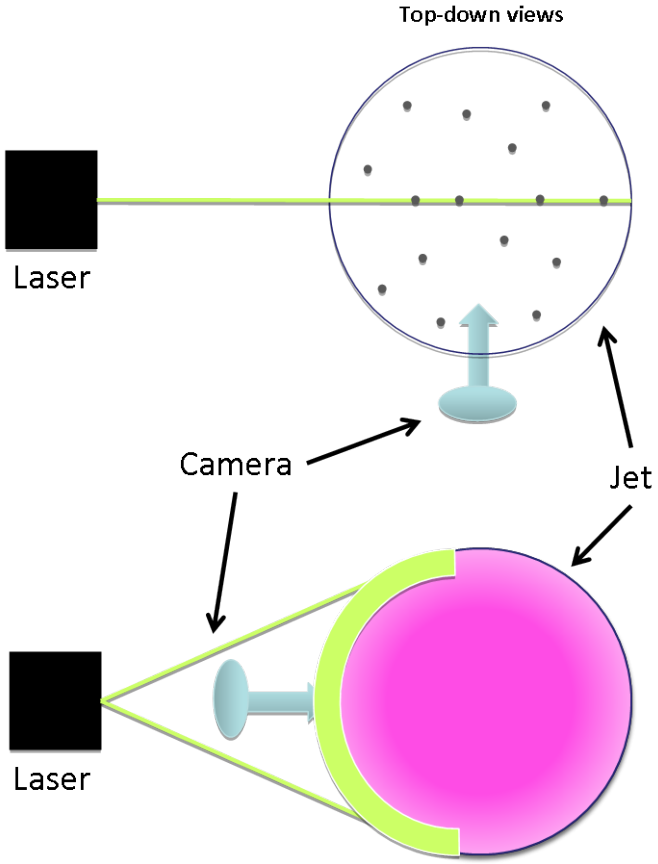

Figure 3.7: Relative positions and configuration of the laser and camera for imaging of the jet interior (top) and exterior (bottom)

resolved measurements between pairs of images. Comparing the laser's characteristic time to that of the (typical) flow,

$$\frac{\tau_L}{\tau_j} = \frac{1/f}{d/U} = \frac{12.6\ m/s}{(0.004\ m)(10Hz)} = 315, \tag{3.6}$$

indicates that the image capturing is a couple of orders of magnitude shy of being able to directly compare pairs of images to each other.

However, we make the assumption that the flow under consideration is statistically stationary; that is, the statistics of the calculated velocity field $\boldsymbol{U}$ are invariant with time (Pope (2000)). While the pairs of images may be recorded relatively sparsely in time, because the

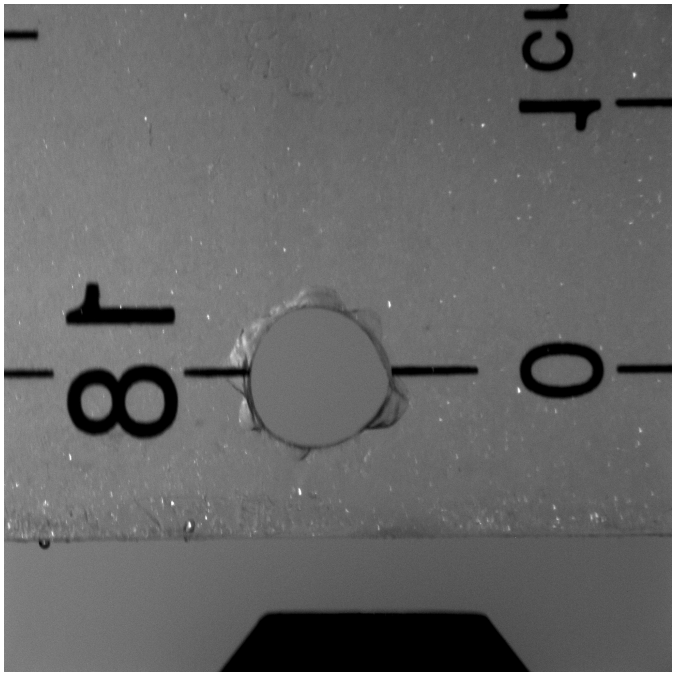

Figure 3.8: Image of the nozzle with the calibrated scale in place

flow is statistically stationary, statistical characteristics can be computed from image pairs collected over relatively long periods of time.

3.3.3 Visualization Techniques

A removable fixture holds a calibration scale above the nozzle, perpendicular to the camera's focal axis, and located across the centerline of the jet. The fixture's weight keeps it stationary during filling; once calibration is complete, it can be pulled up and out of the tank with a rope attached to its top. Figure 3.8 shows a typical calibration picture taken before injection of fluid through the nozzle.

Depending on whether it is desirable to visualize the interior or the exterior of the jet, the jet liquid is prepared with lycopodium particles and Rhodamine-B dye, respectively.

3.3.3.1 Seeded Flow Imaging

For traditional PIV, using seeding particles in an otherwise transparent flow, lycopodium particles were used as tracers. While the dry powder tends to be hydrophobic, once the particles are wetted, they mix well with water and form a relatively stable suspension. The particles are nearly neutrally buoyant (density is within 5% that of water), so settling effects are irrelevant over the course of an experiment.

In order for the particles to be true flow tracers, they must quickly respond to the dynamic flow conditions. The Stokes number is a useful metric for evaluating the response; it is the ratio of the particle relaxation time to the flow relaxation time. If we use the Kolmogorov microscale as the fastest characteristic time for velocity fluctuations that the particles should respond to, we obtain:

$$St = \frac{\tau_p}{\tau_f} \tag{3.7}$$

where the relaxation time of a spherical particle in a fluid is defined as (Kennedy & Moody, 1998):

$$\tau_p = \frac{\rho_p d_p^2}{18 \rho_f \nu_f}. \tag{3.8}$$

If we assume that the lycopodium particles are spherical and less than 30 microns in diameter, and considering their density is 5% greater than that of water (Okubo et al., 2010), then the relaxation time of our PIV seeding particles becomes:

$$\tau_p = 1.05 \frac{(30 \times 10^{-6}\ m)^2}{18\ (10^{-6}\ m^2/s)} = 52.5\ \mu s \tag{3.9}$$

For the fluid relaxation time of turbulent flow, we use the Kolmogorov time scale of the flow (Pope (2000)):

$$\tau_f = \sqrt{\frac{\nu_f}{\epsilon}} \tag{3.10}$$

where ϵ is the turbulent dissipation, and it is assumed that

$$\hat{\epsilon} = \frac{\epsilon r_{1/2}}{U_0^3} = \frac{\epsilon S\,(z - z_0)^4}{(B U_j d)^3} \tag{3.11}$$

is self-similar at large enough distance from the nozzle ($z/d >> 1$) and independent of Reynolds number (Pope, 2000). Note that S, the spreading rate, is taken to be equal to 0.094. As a result, the relaxation time for the fluid can be written as

$$\tau_f = \left(\frac{S\nu_f}{\hat{\epsilon}}\right)^{1/2} \frac{(z-z_0)^2}{(BU_j d)^{3/2}} \tag{3.12}$$

and the Stokes number becomes

$$St = \frac{\tau_p}{\tau_f} = \frac{7}{120}\left(\frac{d_p}{z-z_0}\right)^2 \left(\frac{\hat{\epsilon}}{S}\right)^{1/2} \left(\frac{BU_j d}{\nu_f}\right)^{3/2} = \frac{7}{120}\left(\frac{z^*}{d}\right)^{-2} \left(\frac{\hat{\epsilon}}{S}\frac{d_p}{d}\right)^{1/2} \left(B\frac{U_j d_p}{\nu_f}\right)^{3/2} \tag{3.13}$$

In a round, turbulent jet, the maximum dissipation at a given downstream distance occurs approximately at the centerline (or at least is near maximum at the centerline). If we assume an approximate centerline value of $\hat{\epsilon} = 0.017$ (Panchapakesan & Lumley, 1993a), the maximum dissipation (minimum characteristic fluid time) can be calculated as a function of downstream distance. Note that the expression in equation 3.11 diverges as $(z - z_0) \to 0$. The value of turbulent dissipation is physically bounded, and the smallest time scales in the developing jet are not accurately predicted by their definition in equation 3.12, which would estimate a zero time scale for an infinite value of $\hat{\epsilon}$. Figure 3.9 is a plot of the Stokes number along the centerline as a function of downstream distance, assuming a jet diameter of 4 mm, a jet velocity of 12.6 m/s.

The actual value of the Stokes number below which a particle can be considered a fluid tracer has been suggested in the literature to be $St = 1$ (Kennedy & Moody, 1998); since this seems like a high value ($St = 1$ particles interact strongly with the eddies with size near the Kolmogorov scale and up to the peak of the dissipation spectra), we will conservatively set the threshold at $St < 0.1$. As can be seen in Figure 3.9, this condition is satisfied for all downstream distances greater than $z/d \approx 45$ ($St < 1$ is satisfied past $z/d \approx 15$). Arguably, the lycopodium particles are still adequate tracers upstream of this point, since the values we used to calculate τ_f assume a fully developed flow; in fact, the relevant fluid time scale likely increases significantly closer to the nozzle where turbulence is still developing.

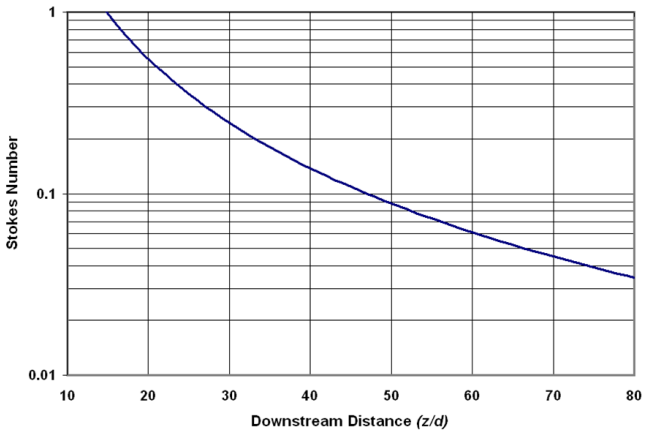

Figure 3.9: Stokes number as a function of downstream distance

3.3.3.2 Rhodamine-B

The major thrust of this investigation is to visualize the turbulent jet exterior. For establishing a baseline, we wanted to inject an opaque liquid with properties essentially identical to water. Many of the liquids we considered to image the jet exterior were not opaque, and they certainly could not reflect/absorb the large energies emitted by the pulsed laser. Additionally, even if a single appropriate liquid were identified, it would likely limit the range of density and viscosity ratios we aim to examine.

Ultimately, we settled on Rhodamine-B as a dye to visualize the exterior surface of the jet. This gives us the flexibility to use many types of liquids (Rhodamine-B is soluble in aqueous solutions). Rhodamine is superior to other types of dye because it fluoresces at the wavelength of the Nd:YAG laser. As a result, a liquid with dissolved Rhodamine does not necessarily need to inhibit transmission of all the light that hits the interface between the injected fluid and the ambient fluid; the Rhodamine on the turbulent/non-turbulent interface of the jet fluoresces strongly and prevents imaging the interior of the jet. Relatively little dry powder needs to be mixed in to the jet (nominally $0.25\,g/L$), and it does not affect the physical properties of the liquid. Figure 3.10 is a picture of a Rhodamine-dyed jet showing how it appears under ordinary fluorescent lighting.

In order to determine the suitability of Rhodamine-B as a dye for inspecting the jet

Figure 3.10: Photograph of a Rhodamine-dyed water jet

surface, the laser penetration depth should be evaluated. The Beer-Lambert Law relates the transmissivity (γ) of a given length (l) within a solution to the molar concentration (c) and molar absorptivity (ϵ_a):

$$\gamma = 10^{-\epsilon_a l c} \tag{3.14}$$

which can be rearranged to solve for l:

$$l = -\frac{1}{\epsilon_a c} log_{10}\, \gamma. \tag{3.15}$$

The value of ϵ_a for Rhodamine-B at our laser wavelength in water is nominally $1{\times}10^5$ L/cm/mol (Ramette & Sandell (1956)). Using this value, in conjunction with the molar concentration used in our experiments ($0.25\, g/L$ yields $5.22 \times 10^{-4}\, mol/L$), we can solve for the thickness of solution required to achieve a desired transmissivity:

$$l = -\frac{1}{\epsilon c} log_{10}\, \gamma. \tag{3.16}$$

For example, at a transmissivity of 50%, the length is calculated to be less than 0.6 mm. In other words, 50% of the laser light has been absorbed (and re-emitted) by the outer 0.6 mm of the jet. We believe this to be sufficiently opaque to allow for PIV measurement of the jet exterior; images from the experiments support this conclusion.

3.3.4 Fluids

3.3.4.1 Water-Water

The best-understood free jet scenario involves a single-component, single-phase flow; thus to set the baseline for the experimental results and analysis, our investigation begins with a water jet (seeded with dye or particles) being injected into quiescent water. Temperatures are typically in the range of 20 $^{\circ}C$ to 25 $^{\circ}C$.

Using water not only eliminates physical disparities between the jet and surroundings that would complicate the flow characteristics, but it also simplifies visualization of the flow interior. For PIV of the jet interior using seeding particles, it is important that the index of refraction is constant throughout the jet flow field.

3.3.4.2 Water-Hot Water

Water, however, does not have universal properties. Specifically, the viscosity of water is a function of temperature. The viscosity changes as a function of temperature according to (Cheng (2008)):

$$\mu_w = 1.790 \exp\left(\frac{(-1230 - T)T}{36100 + 360T}\right) \tag{3.17}$$

where μ_w is in cP and T is in $^{\circ}C$.

The hot water jet is achieved by heating the water in-line as it is injected by the pressurized tank. Two steam-powered heat exchangers are used in series to heat up the injected water to the level needed for the desired viscosity. Thermocouples are placed both in between heat exchangers and slightly upstream of the nozzle to monitor temperatures. The heat exchanger temperature is difficult to control, but temperatures vary by less than 2 $^{\circ}C$ about the mean during an experiment. We believe that our conclusions are valid, but improving the accuracy and precision of the injected water temperature would be an obvious

% Water	% Glycerol	Viscosity (cP)
70	30	2
40	60	10
16	84	100

Table 3.2: Proportions of water and glycerol (by volume) used to achieve various viscosities

possible improvement to our experimental setup.

At a near boiling temperature of 95 $^{\circ}C$, the viscosity is reduced to a value of 0.3 cP. Unfortunately, at temperatures greater than approximately 70 $^{\circ}C$, the injected water is permeated with vapor bubbles. We presume that in order to achieve such high temperatures, there is local boiling in the heat exchanger, and the steam is not reabsorbed before injection. This is another drawback of our current method of heating.

We assume that the effect on density of these temperature changes in the water does not play a significant role in the dynamics of the flow, compared to the effect of viscosity, the variable on which we focus our analysis.

3.3.4.3 Water-Glycerol

Water-glycerol solutions are mixed at different concentrations to produce a liquid of homogeneous properties with varying viscosity (according to standard viscosity tables from Sheely (1932)). Dynamic viscosity values are reported on Table 3.2 together with the water/glycerol ratios (by volume) used to achieve the different viscosities investigated (temperature is nominally 25 $^{\circ}C$).

3.4 Particle Image Velocimetry

3.4.1 PIV Methodology

Particle-Image Velocimetry (PIV) has been developed extensively over the last two decades (Raffel et al., 2007). The cross-correlation technique relies on two images being captured within a relatively short time interval compared to the characteristic time of the turbulence (i.e. $\frac{\delta t}{\tau_f} << 1$) in order to ensure the displacements vary smoothly across the interrogation

sub-windows in which the imaged area is divided for analysis.

Typically, the images used in the correlation to find displacements are of flows that have been seeded with particles and illuminated sufficiently to achieve appropriate levels of exposure for the camera; furthermore, the exposure or illumination must be sufficiently brief to prevent streaking of the particles. The images are taken as pairs (see Figure 3.17), typically with a only a small time delay between the two images in a pair, δt. The first image is subdivided into interrogation areas of size $M \times N$ pixels (where the areas are typically square, $M = N$), and a cross-correlation field is calculated for each one against each possible sub-window of the same size on the second image:

$$C_{II}(x,y) = \sum_{i=1}^{M}\sum_{j=1}^{N} \left[I(i,j) - \mu_I\right]\left[I'(i+x, j+y) - \mu_{I'}(x,y)\right] \tag{3.18}$$

where I and I' correspond to pixel intensity fields of interrogation areas of the first and second images respectively, and μ_I and $\mu_{I'}$ are average pixel intensities for the same interrogation areas:

$$\begin{aligned} \mu_I &= \sum_{i=1}^{M}\sum_{j=1}^{N} \frac{I(i,j)}{MN} \\ \mu_{I'}(x,y) &= \sum_{i=1}^{M}\sum_{j=1}^{N} \frac{I(i+x,j+y)}{MN} \end{aligned} \tag{3.19}$$

Notice that the correlation function is calculated not with the absolute pixel intensities, but with differences from the mean. Improved performance is observed with the normalized correlation function (Raffel et al. (2007)):

$$c_{II}(x,y) = \frac{C_{II}(x,y)}{\sqrt{\sigma_I(x,y)}\sqrt{\sigma_{I'}(x,y)}} \tag{3.20}$$

where σ_I and $\sigma_{I'}$ are the squares of the standard deviations of the intensity fields:

$$\begin{aligned}\sigma_I(x,y) &= \sum_{i=1}^{M}\sum_{j=1}^{N}\left[I(i,j)-\mu_I\right]^2 \\ \sigma_{I'}(x,y) &= \sum_{i=1}^{M}\sum_{j=1}^{N}\left[I'(i,j)-\mu_{I'}(x,y)\right]^2\end{aligned} \tag{3.21}$$

The value of (x, y) at which the value of the correlation function is maximized is taken to represent the displacement of the interrogation area. By repeating the exercise of finding the maximum of the cross-correlation for each interrogation sub-window over the entire image and dividing the displacements given by these maxima by the time between images, δt, the velocity field can be calculated. Further improvements can be made by making multiple passes using various interrogation area sizes, as well as calculating sub-pixel displacement and interrogation area transformations. These sophisticated refinements are outside the scope of this discussion; they are addressed in depth by Raffel et al. (2007) and Adrian & Westerweel (2011).

Figure 3.11 shows two different size of interrogation sub-windows from an image pair. In Figure 3.12, the contour of the covariance function is plotted on top of the second image; an arrow indicates the displacement (ignoring sub-pixel resolution effects) indicated by the calculated peak.

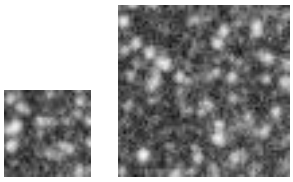

(a) (b)

Figure 3.11: Interrogations areas from a pair of particle-seeded images; (a) M=N=32 pixel square area from first image, (b) 64 pixel square area from second image

To further illustrate the result, Figure 3.13 shows a color contour of the first image plotted on top of the second image, with squares showing both the original location of the first image's interrogation area and the calculated displacement of the area. This displacement,

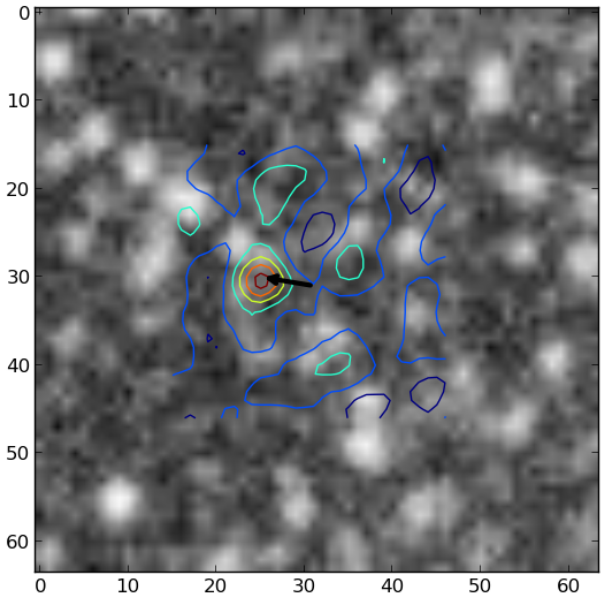

Figure 3.12: Contours of the computed cross-correlation function plotted on the first image from Figure 3.11; arrow indicates displacement of the covariance peak from the image center

used in conjunction with the time between images determines the velocity; the process is repeated for interrogation areas throughout the first image to calculate the velocity field.

Though it was originally intended to work on a flow seeded with particles, here we extend the PIV technique by applying it to the images of the surface of an opaque flow. For the turbulent jet, this surface is equivalent to the viscous superlayer: the interface separating turbulent and non-turbulent flow. Figures 3.14 through 3.16 reproduce the same content as Figures 3.11 through 3.13 but for an image pair taken from an experiment of the jet exterior.

Notice important differences between Figures 3.15 and 3.12. The features of the particle-seeded images are much smaller and more diverse than the dyed-fluid images. This finer patterning presents the opportunity for better correlations for a given window size. Also, the covariance function tends to be more sophisticated, with several local maxima and minima. In both cases, there is a clear maximum value indicating the location of the best correlation.

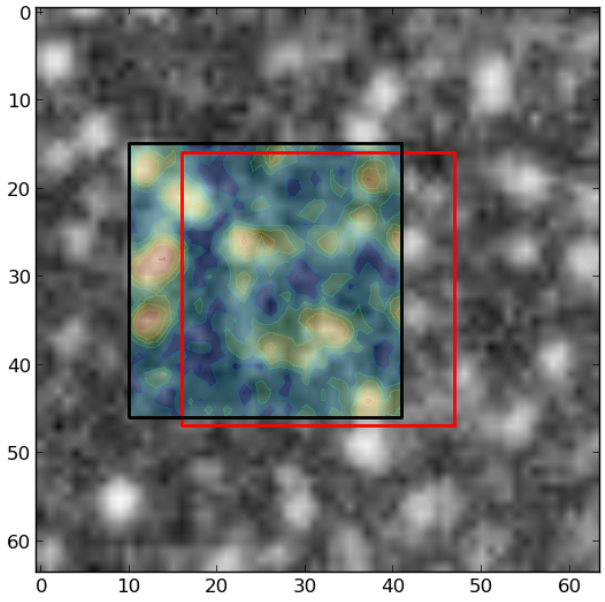

Figure 3.13: Filled contour of the displaced interrogation area (from image 1) plotted on image 2 (see Figure 3.11), with squares showing original and displaced locations

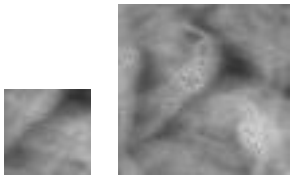

Figure 3.14: Interrogations areas from a pair of opaque turbulent/non-turbulent interface images; (a) M=N=32 pixel square area from the first image, (b) 64 pixel square area from the second image

3.4.2 Image Processing

PIV analysis can be improved by preprocessing the image pair in order to give the algorithm optimum image contrast to calculate the image-correlation and subsequent velocity field. For laser plane imaging of particle-seeded flows, preprocessing the image allows for particles

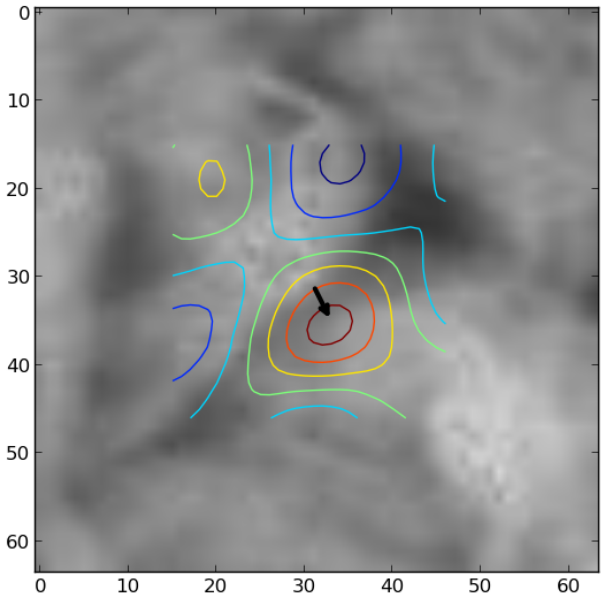

Figure 3.15: Contours of the computed cross-correlation function plotted on the first image from Figure 3.14; arrow indicates displacement of the covariance peak from the image center

(and as a result, particle patterns) to be emphasized, while background noise is suppressed. Furthermore, preprocessing is an especially critical step when examining the jet interfacial velocity using an Nd:YAG laser such as our own; having two laser heads allows for very small time steps between pulses, but also leads to appreciable differences in beam shape and intensity, as noted by Raffel et al. (2007) and Adrian & Westerweel (2011).

Image processing is performed with ImageJ (NIH, Rasband (1997–2011)). Contrast is typically adjusted by performing histogram normalization of the brightness levels. Binning of the images (whereby adjacent pixels are combined with a resulting averaged pixel intensity) helps improve the PIV software's performance; this binning can either be performed on board the camera, increasing the maximum frame rate, or it could be done in post-processing. The resulting images have half of the resolution in each direction (from 2048×2048 down to 1024×1024 pixels). Figure 3.17 shows a pair of images of the particle-seeded flow illuminated by laser planes both before and after the process of image manipulation.

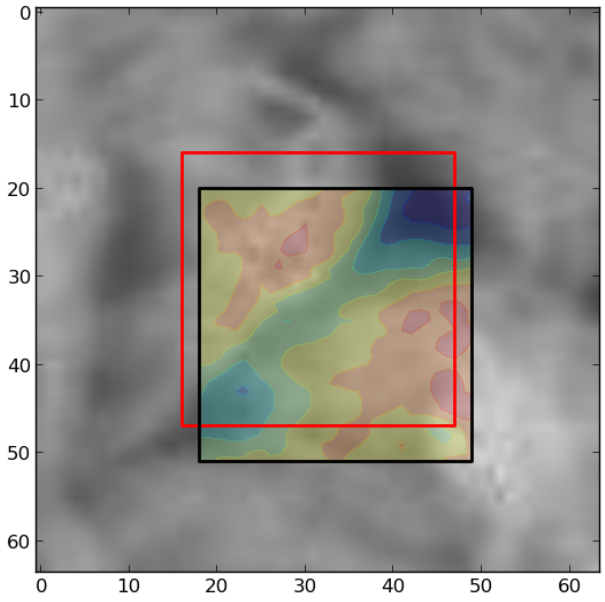

Figure 3.16: Filled contour of the displaced interrogation area (from image 1) plotted on image 2 (see Figure 3.14), with squares showing original and displaced locations

3.4.3 PIV Analysis

We use the open source package `gpiv` (van der Graaf (2012)) for analysis of the image pairs, both of the jet interior with particle seeding and of the jet interface dyed with Rhodamine-B. It uses a multi-pass technique, calculating displacements for progressively smaller interrogation areas. The use of displacement predictions for interrogation area selections is critical in this application, since the jet may contain a wide range of fluid velocities over the imaged area.

The smallest interrogation areas were typically 16×16 pixels (occasionally 32×32 pixels was used, and little difference was noticed). For images with dimensions 1024×1024 pixels, this results in a velocity field with slightly less than 64×64 vectors.

The `gpiv` software includes an image deformation interrogation scheme, which allows for better correlation than simple translation. After each pass, validation is performed on all

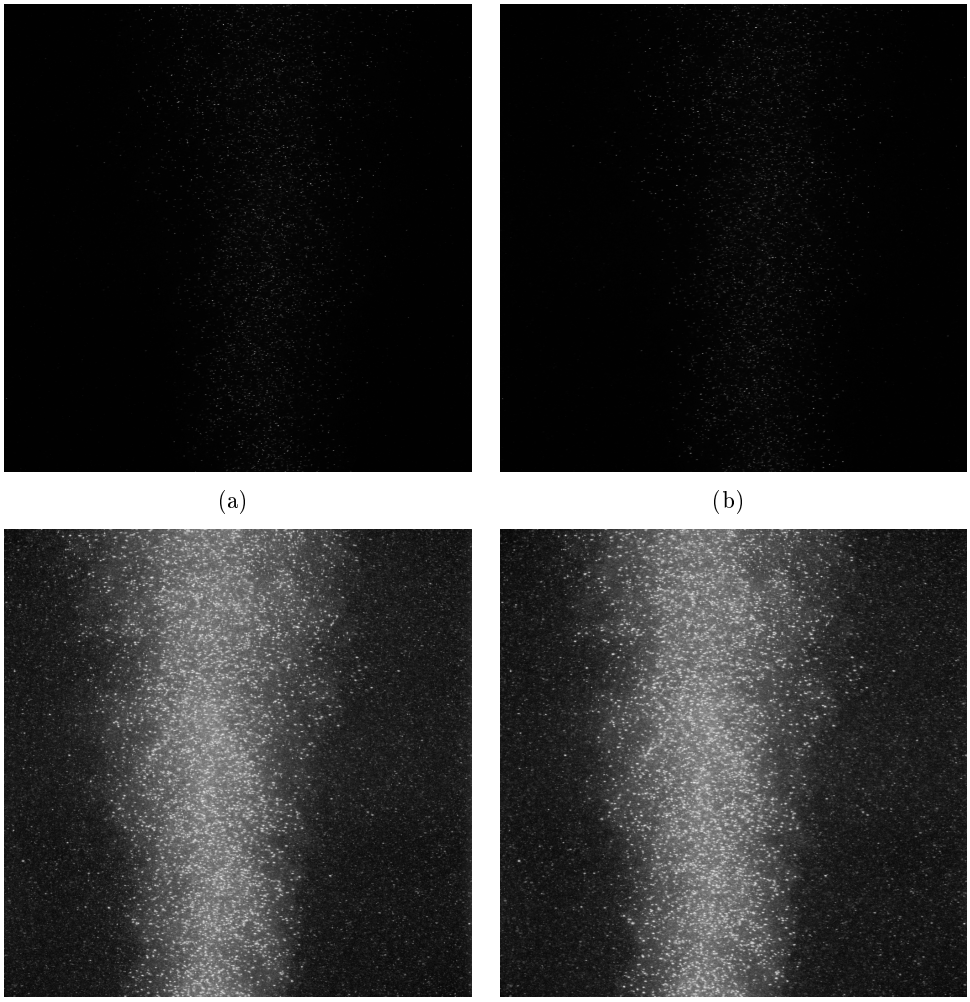

Figure 3.17: Image pairs ($\delta t = 20\ \mu s$) of illuminated lycopodium particles within a water jet ($Re = 25,000$) interior both before (top) and after (bottom) contrast normalization via ImageJ

of the calculated velocity vectors. Each vector is compared with the median of neighboring vectors; if an inappropriate deviation is detected, the offending vector is replaced with the median value of the neighboring vectors. This may improve correlation on subsequent passes with smaller interrogation areas. If, after the final pass, a vector is still determined to be invalid, it is excluded from the analysis. Additional parameters that were used consistently include Gauss weighting of the correlation (in order to suppress spurious peaks near the

boundaries), as well as Gaussian interpolation of sub-pixel displacements. The `gpiv` software is able to increase the performance of the cross-correlation by accounting for rotation of interrogation areas. Sub-pixel interpolation was used in order to further improve accuracy. Figure 3.18 shows the results of PIV analysis of the image pair from Figure 3.17; only one quarter of the calculated vectors are shown in order to de-clutter the image.

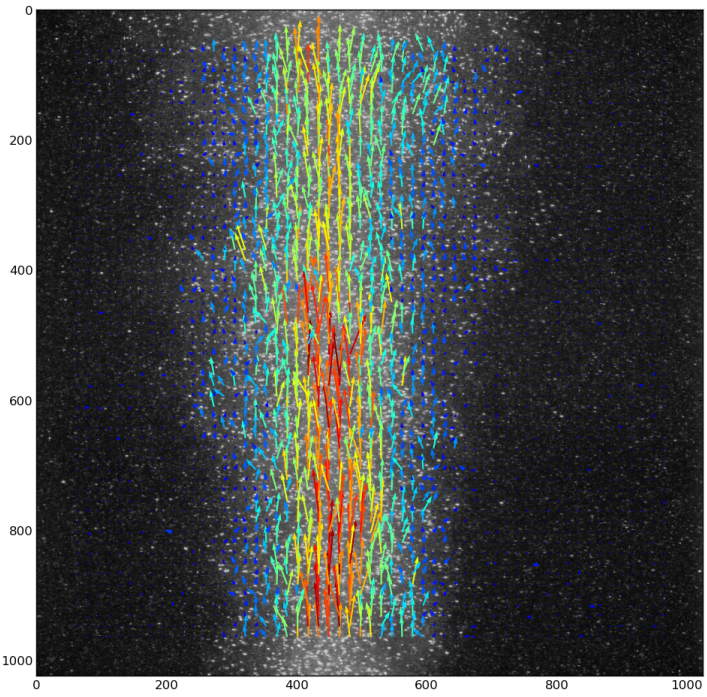

Figure 3.18: Calculated velocity vector field of the image pair from Figure 3.17; vectors are colored by magnitude

3.4.4 Statistical Treatment of the PIV Measurements

The `gpiv` software saves the velocity vector data for each pair of images as a text file. A `python` routine is used to average the velocity information from all pairs of images, as well as to collect statistics on velocity fluctuations. The results can then be saved to another file

and/or plotted. Figure 3.19 shows a typical averaged velocity field where the multitude of turbulent fluctuations have yielded a smoothly varying velocity field. Several hundred pairs of images are used for each averaged experimental velocity field.

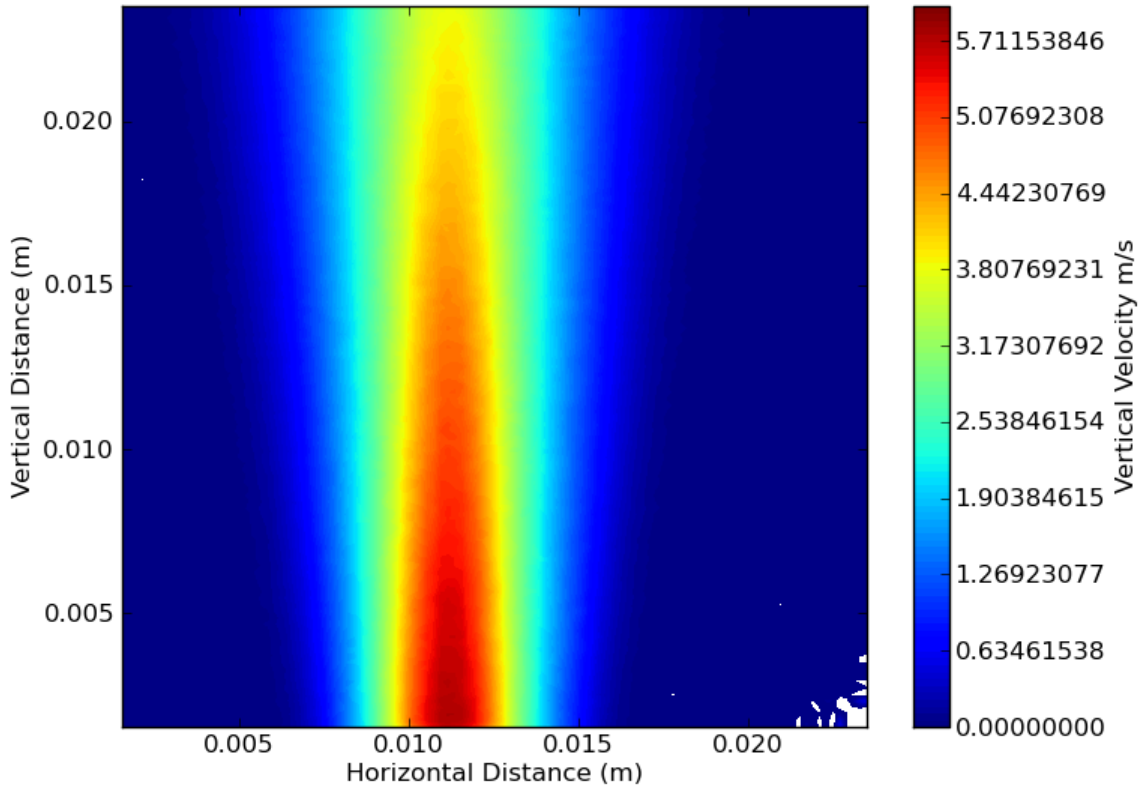

Figure 3.19: Velocity field calculated by averaging 1300+ image pairs from the same experiment as Figure 3.18

3.5 Results

3.5.1 Flow Velocity across the Jet

The first experimental tests and analysis focused on the single-phase turbulent jet flow field, studied with a laser plane cutting along the jet centerline. This simple flow configuration has been one of the most thoroughly studied phenomena in the field of turbulent free-shear flows.

Furthermore, since the exterior jet PIV promised to push the technique beyond its nominal capabilities, it was important to confirm the capabilities of the experimental setup and the `gpiv` analysis for a canonical PIV-seeded flow. Experiments examining the interior of the jet also allowed us to confirm that our turbulent jet was behaving in a manner consistent with classical turbulent jet flows (Wygnanski & Fiedler, 1969; George, 1989; Hussein et al., 1994).

In order to achieve a comprehensive flow field description, several experiments must be conducted for each experimental configuration. The camera field of view (at the magnification needed for detailed PIV analysis), was not adequate to capture the entire flow field of interest. Therefore, the experiment was repeated keeping all aspects of the fluid injection identical, while the camera field of view was translated downstream to examine a different region of the flow field.

Figure 3.20 shows the flow profile as a function of non-dimensional downstream distance, η (not to be confused with the Kolmogorov length scale), for several downstream distances in a number of experiments; they exhibit the same self-similarity found in the classical literature (Wygnanski & Fiedler, 1969), shown in Figure 3.1. Additionally, we calculated the Reynolds stresses (see Figure 3.21), and they also qualitatively, if not fully quantitatively, compare favorably to previous experiments in Figure 3.2. The $z/d = 50$ results more closely match the self-similar data in Figure 3.2. It is widely believed that the self-similar region does not truly begin as early as $z/d = 25$, so the improved agreement between measurements of the Reynolds stresses (a higher order statistic) with increased downstream distance is to be expected.

Finally, the centerline velocity decay is plotted in Figure 3.22, combining results from a range of downstream distances. The behavior matches well quantitatively to equation 3.1, which is also plotted ($B = 5.8$, $z_0 = 4d$ per Hussein et al. (1994)), and to experimental results from Figure 3.3. Note that these favorable comparisons exist despite the fact that experiments from the literature used entirely difference velocity measurement techniques (static/flying hot-wire anemometry, laser Doppler anemometry).

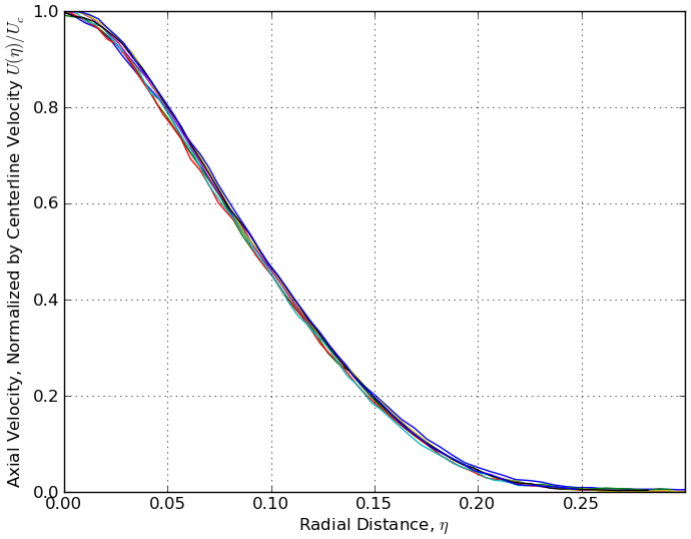

Figure 3.20: Normalized plots of axial velocity profiles, demonstrating the self-similarity of the flow measured with PIV (4 mm nozzle, $Re = 50,000$)

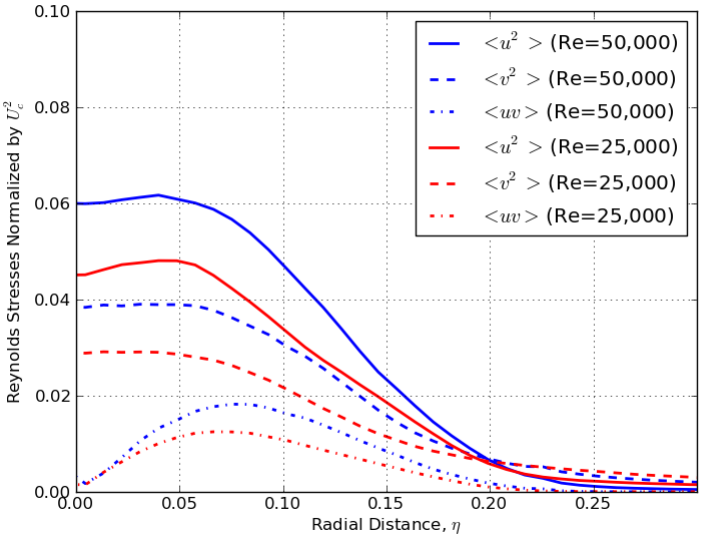

Figure 3.21: Plots of Reynolds stresses measured with PIV for flow through a 4 mm nozzle

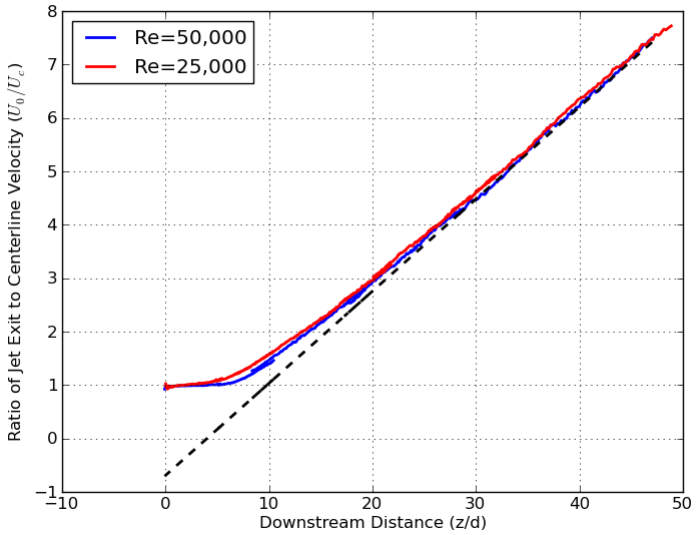

Figure 3.22: PIV results of the centerline velocity ratio decay for flow through a 4 mm nozzle

3.5.2 Flow Turbulent/Non-Turbulent Interface

Analyzing the flow velocity along the jet cross-section utilizes PIV in a conventional way, matching patterns of illuminated seeding particles. When working with the jet turbulent/non-turbulent interface, there are no seeding particle images to correlate, but there may very well be correlatable patterns on the visible superlayer. For the same reasons it is important to condition the images of seeding particles prior to performing PIV, the images of the illuminated jet exterior should also be normalized. Figure 3.23 shows a pair of images before and after image manipulation similar to those from Figure 3.17.

The velocities measured were significantly smaller than the core jet velocities for a given experimental condition. Figure 3.24 is a plot of the flow field calculated from the image pair in Figure 3.23. Because the mean velocity is significantly lower than in the jet velocity field measurements, the degree of variation in velocity vectors is on the same order as their magnitude. Thus, the averaging of long series of image pair calculations is an important step to understanding the general behavior of the flow. Figure 3.25 shows the velocity field obtained after averaging 380 measurements from image pairs; the velocity vectors outside

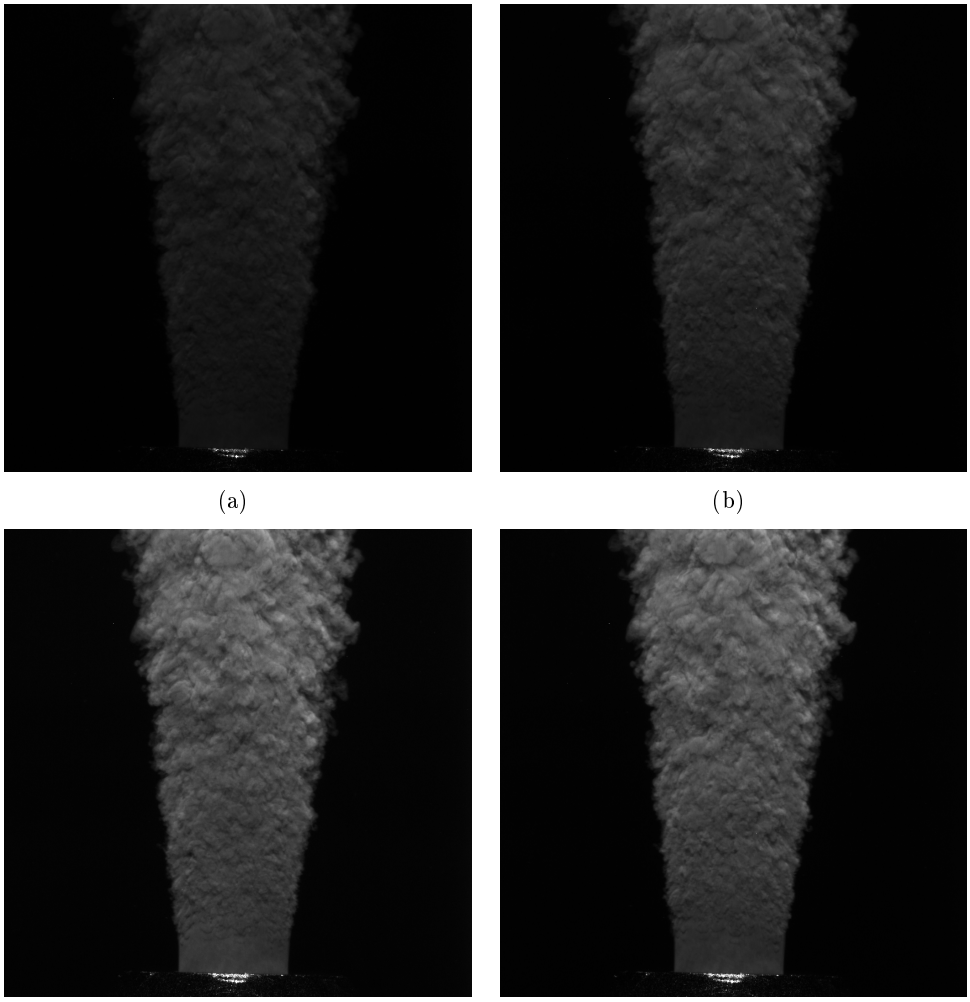

(a) (b)

(c) (d)

Figure 3.23: Image pairs ($\delta t = 120\ \mu s$) of an illuminated Rhodamine-dyed water jet ($Re = 50,000$) interface both before (top) and after (bottom) contrast normalization via ImageJ

the region of interest have largely canceled out, resulting in a coherent picture of the average flow.

Also, it is worth noting some obvious qualitative differences between the averaged turbulent/non-turbulent interface velocity field in Figure 3.25 and the averaged PIV velocity field from Figure 3.19. While the jet PIV velocity field decays smoothly in the radial direction, the interface velocity is uniform across the width of the jet before dropping off abruptly at the jet edges. This is due to the fact that the visualization of the jet exterior surface is es-

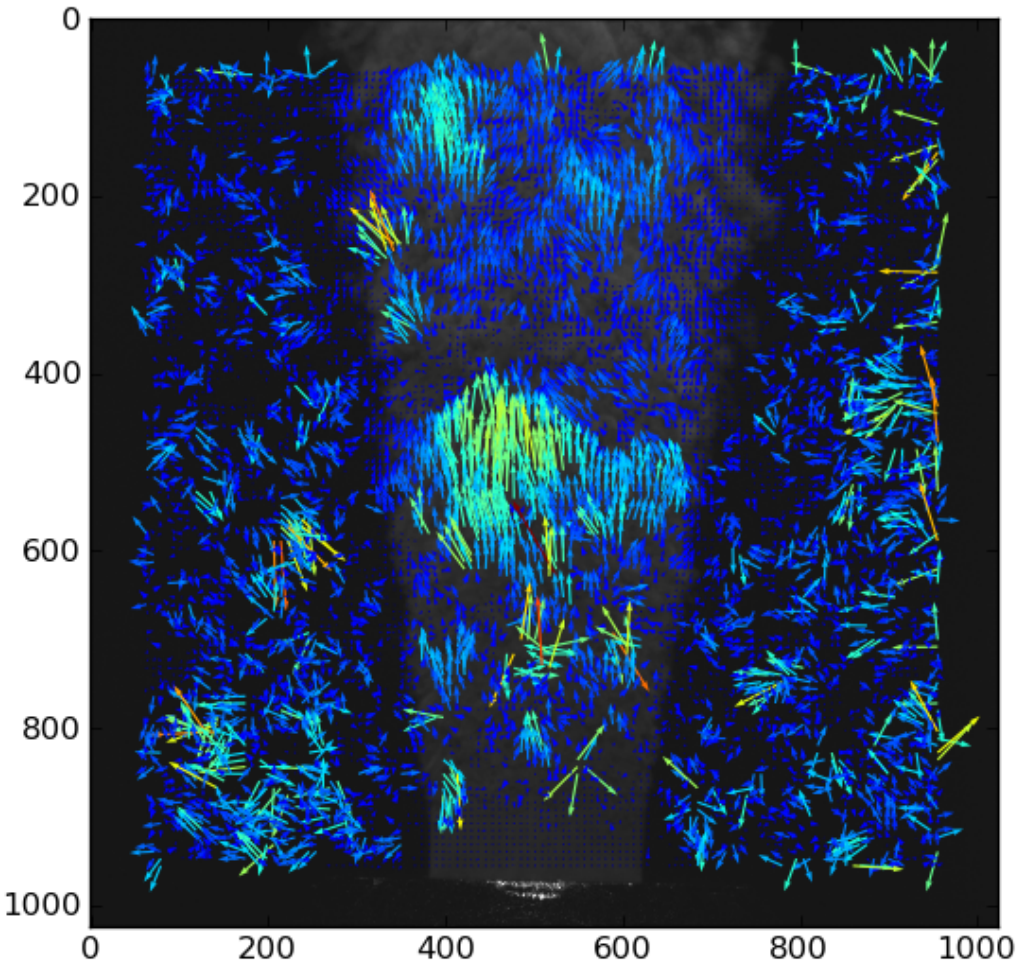

Figure 3.24: Calculated velocity vector field of the image pair from Figure 3.23; vectors are colored by magnitude

sentially of the mixing superlayer. The superlayer's radial distance from the jet's center is approximately axisymmetric, accounting for the uniformity of velocity across the width of the jet in this average field.

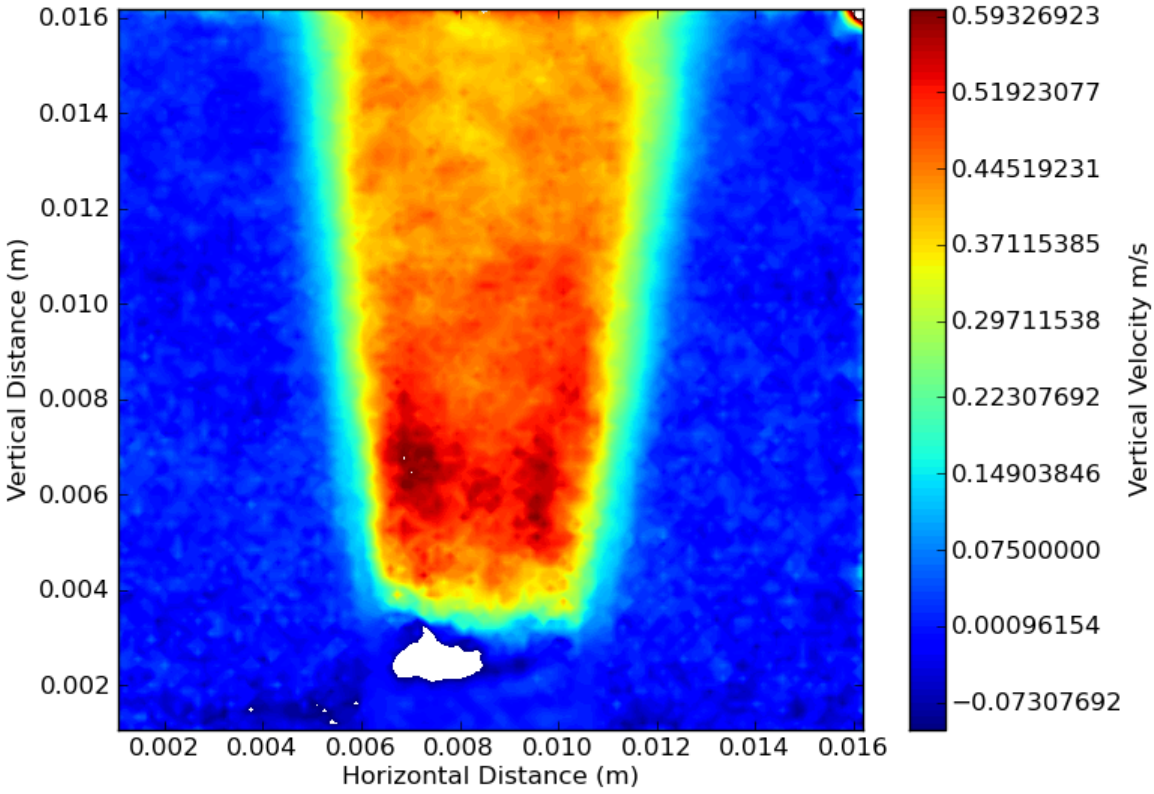

Figure 3.25: Velocity field calculated by averaging 380+ image pairs from the same experiment as Figure 3.24

3.5.2.1 Reynolds Number

We performed experiments for a variety of Reynolds numbers achieved by varying both the nozzle diameter and the exit velocity. Figure 3.26 shows data points for the jet core-to-interface velocity ratio measured at 1.5 diameters downstream distance versus Reynolds number. Except for some outliers in the 50-100 range, the results show no trend with the Reynolds number, as we expect in experiments with jet Reynolds number well above the mixing transition of $10,000$ (see Dimotakis (2005)).

Of course, we do not expect the measured velocity ratios to be random, but a function of another parameter. While the Reynolds number completely defines the characteristics of

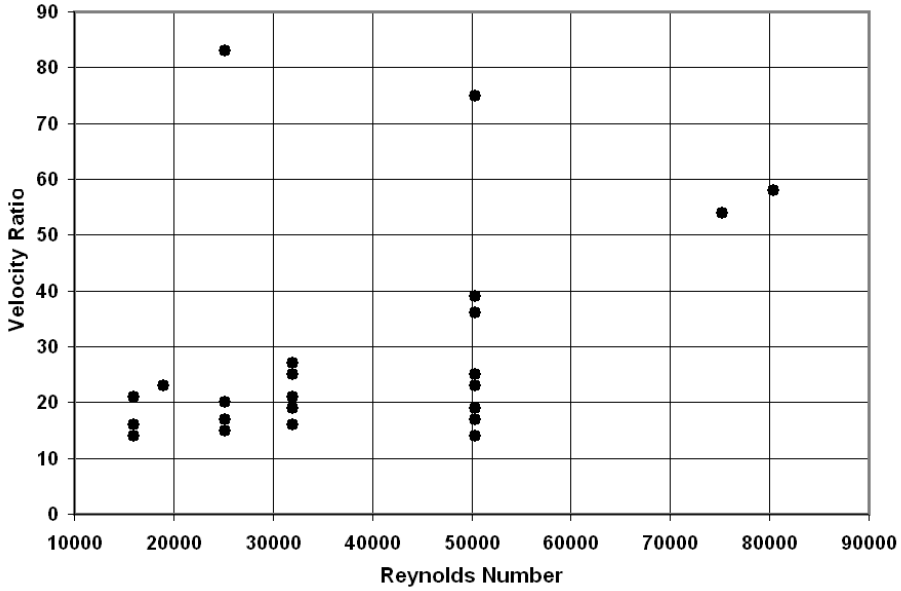

Figure 3.26: Plot of the exterior jet velocity ratio (at $z/d = 1.5$) versus Reynolds number for many experiments (uniform fluid properties)

an axisymmetric, constant viscosity jet, the captured image pair introduces an additional variable. For a constant viscosity jet, dimensional analysis yields a second non-dimensional number that relates the timescale of the image pair with that of the jet:

$$\hat{\tau} = \frac{\delta t}{\frac{d}{U}} = \frac{U \delta t}{d}. \tag{3.22}$$

If we differentiate the points from Figure 3.26 according to this new time ratio, $\hat{\tau}$, we obtain Figure 3.27 which indicates that amongst a fixed value of $\hat{\tau}$, the velocity ratio is indeed independent of Reynolds number. However, the dependency on this new flow-imaging parameter is clear.

3.5.2.2 Inter-Frame Time Delay

Our PIV analysis of particle flow throughout the center-plane of the turbulent jet showed no dependency on the time delay used between pulses (nor would we expect it to, in adequately

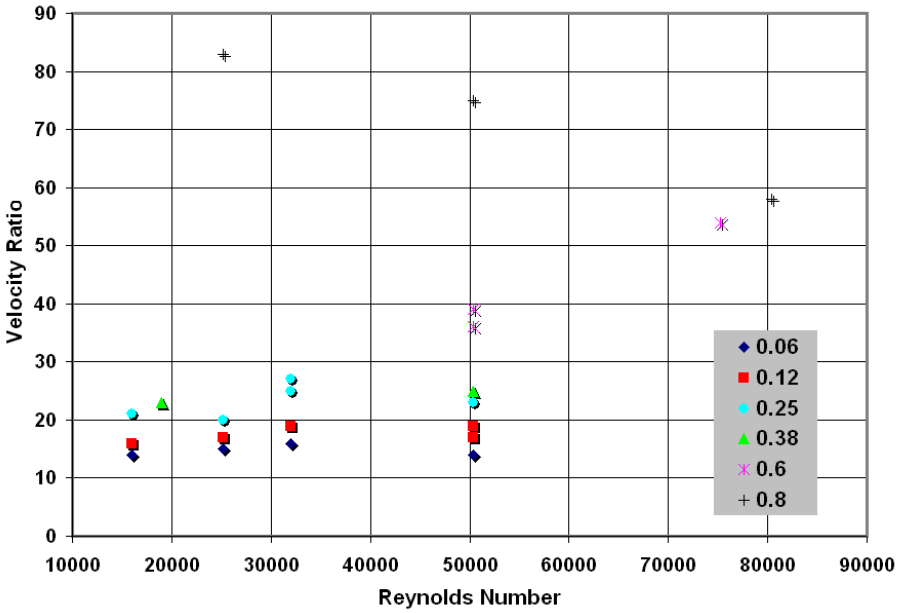

Figure 3.27: Plot of the exterior jet velocity ratio (at $z/d = 1.5$) versus Reynolds number colored by various values of $\hat{\tau}$

performed PIV, subject to certain constraints (Adrian & Westerweel (2011)). However, when examining the jet exterior, we noticed that the measured velocity had a significant dependency on the time between image pairs.

Figure 3.28 shows the results of plotting the velocity ratio, $\hat{U} = \frac{U_j}{U_e}$ measured at a downstream distance of $1.5d$, against $\hat{\tau}$ (defined in equation (3.22)). The data, including results from a range of nozzle diameters, initial velocities, and camera time steps, tends to collapse fairly tightly. We believe this is the first time this effect has been observed and quantified. Although there have been several efforts to use PIV-correlation algorithms on images of flow features collected from naturally occurring flows (Melville & Matusov (2002); Ryu et al. (2005); Kleiss & Melville (2011); Rodriguez-Rodriguez et al. (2011)), this effect has not been reported, most likely because it is not observed for traditional PIV measurements of particle displacements, and the imaging setup in the naturally-occurring flows are heavily constrained, not lending themselves to this type of rigorous study.

The data appears to behave linearly over most of its range. We will see later (section

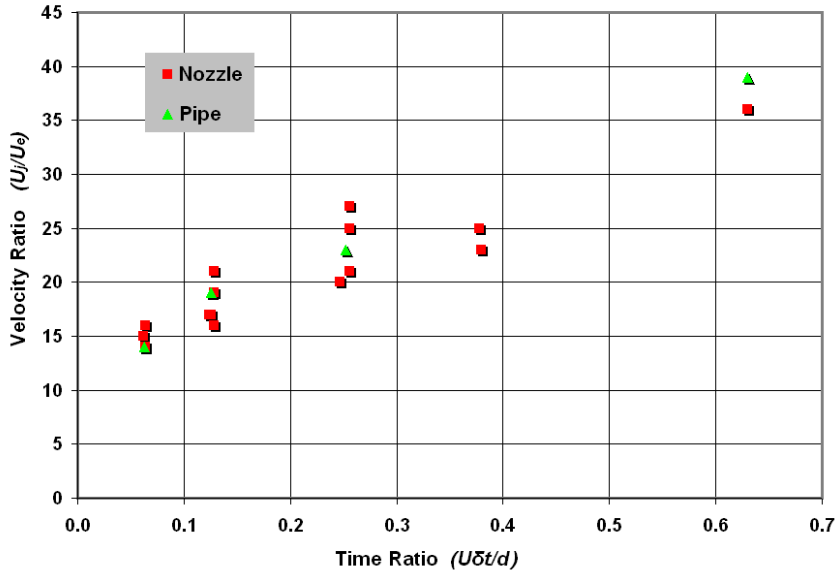

Figure 3.28: Plot of experimental data comparing the effect of $\hat{\tau}$ on $\hat{U}$ at 1.5 diameters downstream distance

3.5.2.5) that similar linear relationships exist for jets with different viscosity ratios.

Clearly, the time delay between the images constituting a pair for PIV analysis must be selected with care. However, the physics that cause this dependency are not entirely understood. Our hypothesis is that the timescales of the vortical features, which are correlated as patterns between two consecutive images by the PIV algorithm, are critically related to the imaging time. Since the PIV algorithm is Gaussian-weighted, it will skew to zero displacement if there is a lack of pattern-matching between images. As δt grows compared to the flow time d/U_j, there will be larger deformation/diffusion of vortical structures between images, resulting in less pattern matching. This will tend to decrease the average calculated displacements, by biasing the field towards zero values.

3.5.2.3 Jet Initial Conditions

The initial jet experiments were all conducted with a cubic spline nozzle (see equation (3.4) and Figure 3.5) which is designed to produce a top hat velocity profile for universality and reproducibility of our results. However, such well-organized flows are not necessarily common

in nature. As such, it is of interest to study a similar flow, a round turbulent jet, starting with non-uniform flow velocity conditions. In the literature, a developed turbulent flow (achieved by flowing through a length of circular pipe) is also a common experimental jet initial condition (e.g. Crow & Champagne (1971), Pitts (1991b), Richards & Pitts (1993), Chhabra et al. (2005)).

We use constant diameter aluminum pipes to provide an inhomogeneous flow in the instantaneous sense, with vortical structures forced by the shear on the pipe wall that make the surface feature-rich so the PIV algorithm can be applied from the very start of the flow at the rim of the nozzle. Our 10.3 and 4.05 mm diameter pipe nozzles had the longest lengths allowed by our injector geometry in order to maximize the development region of the pipe flow before ejection into the tank; 14 and 35 diameters respectively.

Mi et al. (2001b,a) reported how the jet exit conditions affect the development of a turbulent jet, as well as the effect on the distribution of a passive scalar. A major conclusion of their research was that it is inappropriate to treat the free jet as a momentum point source even far downstream; exit conditions should not be ignored. Specifically, concerning scalar distribution, the initially turbulent pipe flow does a much more thorough job of mixing in the near field, creating lasting effects.

Figure 3.29 compares pictures taken of nozzle and pipe flow at $Re = 50,000$, with both outlets being nominally 4 mm in diameter. Very near the outlets, the flows are visibly different. The nozzle jet emerges in what appears to be a laminar fashion until instabilities become appreciable approximately half a diameter downstream. In contrast, the pipe jet shows signs of turbulence on the jet exterior immediately after the nozzle. However, as Figure 3.28 illustrates, the flows' non-dimensional velocities, measured two diameters downstream, plotted against $\hat{\tau}$ are essentially the same.

3.5.2.4 Buoyancy

The buoyancy of the jet is typically of interest when working with multiple fluids of different densities. Lee & Chu (2003) describes a length scale at which the momentum and buoyancy

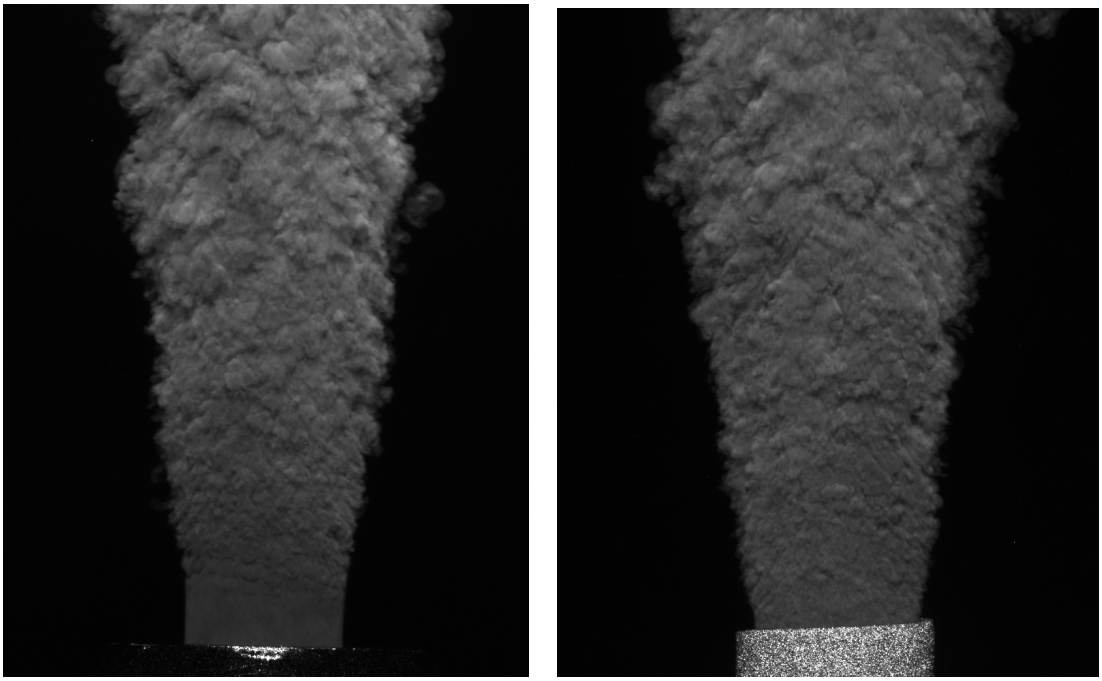

(a) 4 mm nozzle exit (b) 4 mm pipe exit

Figure 3.29: Images of free, turbulent jet exteriors at $Re = 50,000$

forces will be balanced for a free jet:

$$z \approx \frac{M_0^{3/4}}{B_0^{1/2}} \tag{3.23}$$

where M_0 is the specific momentum ($U_j Q_j$) and B_0 is the specific buoyancy ($(\rho_a - \rho_j) g Q_j$) and $Q_j = \frac{1}{4}\pi d^2 U_j$. We will adjust the definition of B_0 to accommodate jets with either negative or positive buoyancy, by taking the absolute value of the density difference. The equation can be rearranged to produce a dimensionless number criterion:

$$1 \approx \left(\frac{4}{\pi}\right)^{1/4} \approx \sqrt{\frac{gd}{U_j^2}\frac{|\rho_a - \rho_j|}{\rho_a}} \cdot \frac{z}{d} = P \tag{3.24}$$

Therefore, we can use P as a threshold criterion for determining whether a jet is dominated by buoyancy or momentum at a downstream position z/d. For a value much above

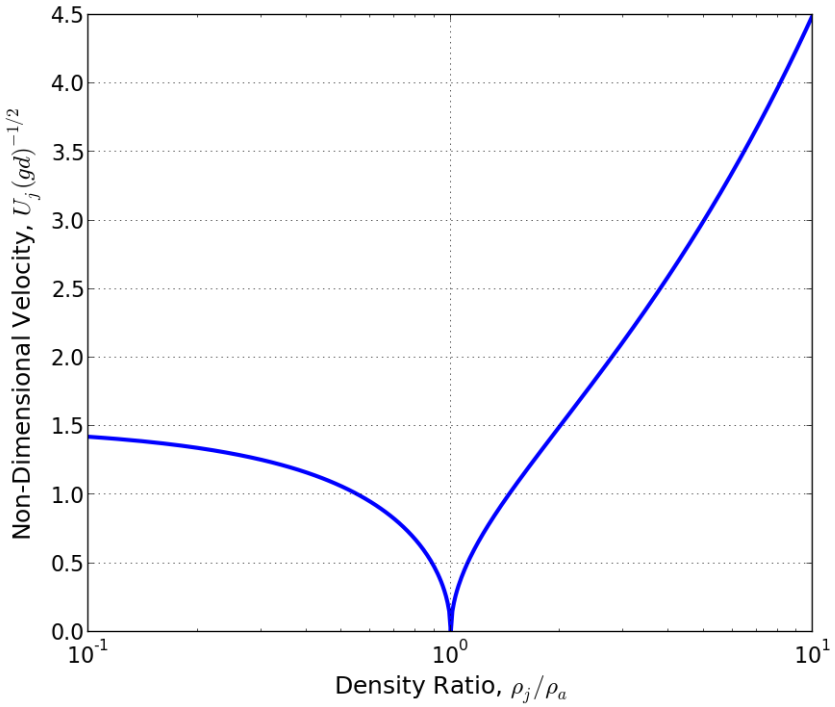

Figure 3.30: Plots the minimum non-dimensional velocity $(U_j(gd)^{-1/2})$ required for $P > 1$ as a function of the jet density ratio (ρ_j/ρ_a)

unity, the jet is considered buoyancy dominated; conversely, a value of P much below unity indicates the jet is momentum dominated. For values in the vicinity of unity, the jet will be significantly affected by both buoyancy and momentum. This criterion appears to be superior to that described by Pasumarthi & Agrawal (2005) which experiences difficulties at either end of the density ratio spectrum (very light jet or a jet with nearly uniform density).

Since we typically evaluate the jet at 1.5 downstream diameters, it is worth exploring the requirements at that distance to avoid buoyancy effects. Figure 3.30 plots the minimum non-dimensional velocity $(U_j(gd)^{-1/2})$ required for $P < 1$ as a function of the jet density ratio (ρ_j/ρ_a). Of course, it is desirable for the velocity to be well in excess of this value in order to minimize the effect of buoyancy.

Our primary concern is that, when experimenting with high viscosity jets, the glycerin-

water solutions are denser than water alone. Experiments of extended duration result in the jet forming a plume downstream (above the nozzle) and falling back down towards the nozzle, obscuring the jet. However, at relatively close distances (i.e. $z/d = 1.5$) we ensure that the jet is indeed momentum dominated.

3.5.2.5 Viscosity

We are interested in investigating the effect of jet fluid viscosity on the turbulent/non-turbulent interface velocity (see Figure 3.31). It is common to have fluid with different viscosities exiting in a jet-like manner into a quiescent fluid, such as volcanic eruption in particle-free, colder air or oil spilling into a body of water. While mean velocities and stresses are insensitive to absolute viscosity at sufficiently high Reynolds numbers, viscosity gradients can play a significant role in modifying free jet development (Chhabra et al., 2005). In the case of a converging nozzle, the laminar flow must first destabilize; Figure 3.32 illustrates that this transition to turbulence is affected by the presence of a viscosity gradient (even for flows with equivalent Reynolds number).

Figure 3.33 shows the effect that varying the jet viscosity has on the relationship between $\hat{\tau}$ and $\hat{U}$. In general, increasing the viscosity difference decreases the velocity ratio (increases the measured velocity of the jet interface) measured at 1.5 diameters downstream.

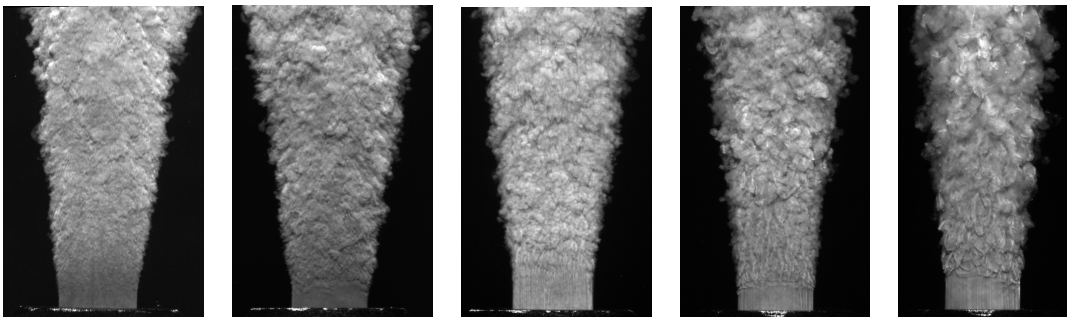

(a) (b) (c) (d) (e)

Figure 3.31: Images of jets issuing from a 4 mm convergent nozzle at 12.6 m/s; the jet viscosity is (left to right) 0.5 cP, 1 cP, 2 cP, 10 cP, 100 cP

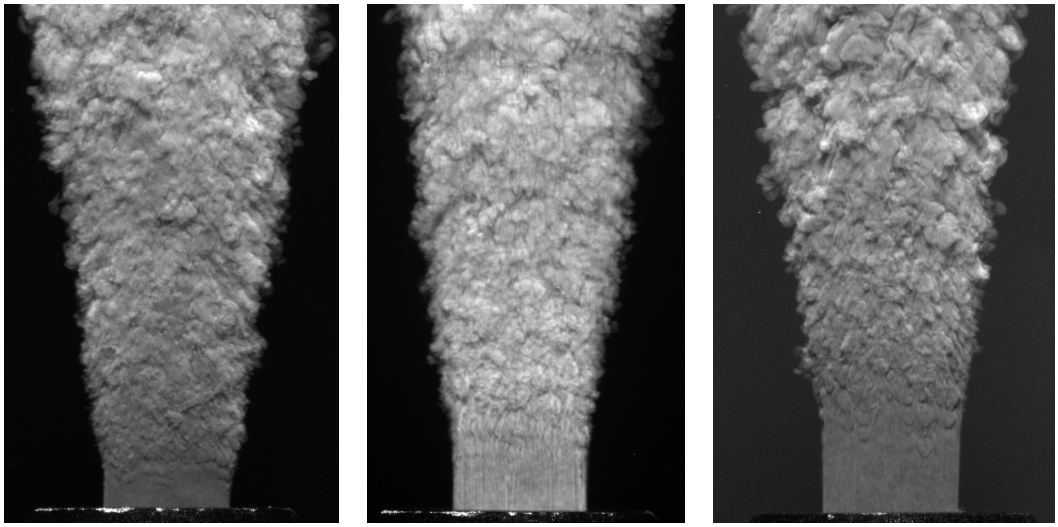

(a) (b) (c)

Figure 3.32: Images of three jets issuing from a 4 mm convergent nozzle; the left-most jet is 1 cP and has a velocity of 12.6 m/s ($Re = 50,000$); the middle jet is 2 cP and has a velocity of 12.6 m/s ($Re = 25,000$); the right-most jet is 1 cP and has a velocity of 6.3 m/s ($Re = 25,000$)

Figure 3.34 is a plot of the velocity ratio versus downstream distance for $\hat{\tau} = 0.25$. The interesting trend shown indicates that, while a higher viscosity universally increases the observed velocity close to the nozzle, the jets tend to revert back to the uniform viscosity case further downstream, presumably due to mixing. Indeed, experiments with a pipe tend to exhibit lower viscosity effects quicker, because the wall-induced turbulence present at the jet exit likely reduces the viscosity gradient closer to the pipe exit. In a later section, we use stability arguments to explain the differences in observed velocities near the nozzle and make predictions about velocity ratios we cannot currently test for.

3.5.3 Signal to Noise Ratio (SNR)

While $\hat{\tau}$ has proven to be an informative and reliable metric for estimating the velocity ratio, its definition relies on the jet velocity. Thus, it is less than ideal for determining a non-laboratory flow's jet velocity. We conjectured in section 3.5.2.2 that the dependence on $\hat{\tau}$ is due to deteriorating correlation as δt grows, driving the velocity to zero (and the

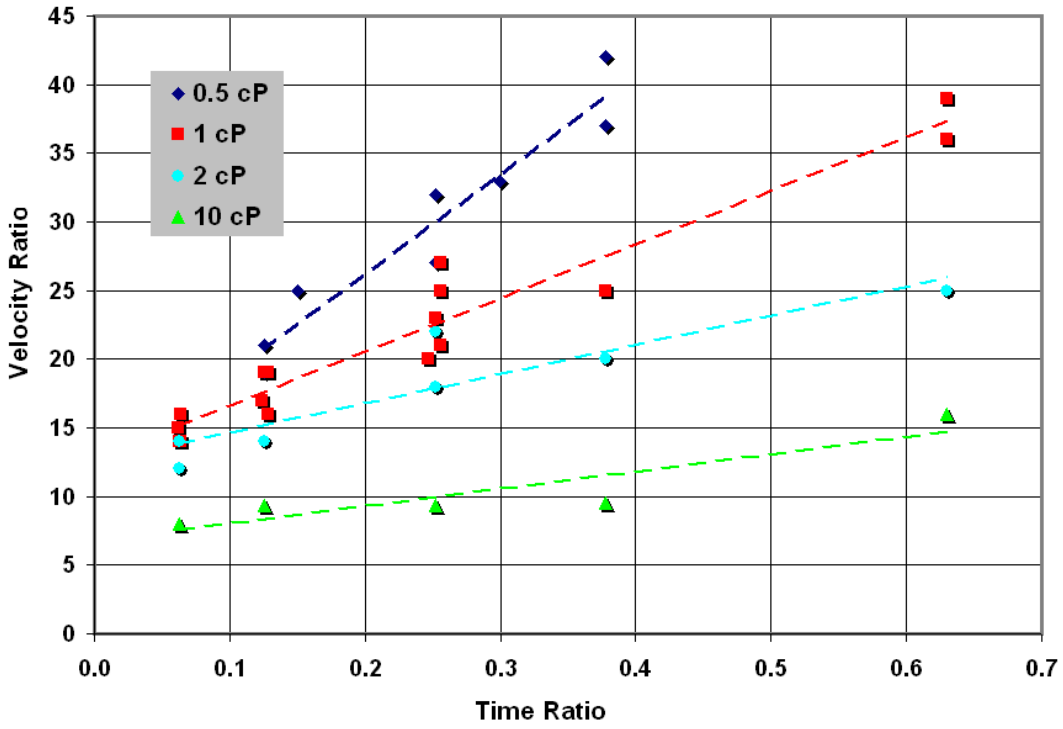

Figure 3.33: Plot of the velocity ratio (U_e/U_J) versus the time ratio ($\hat{\tau}$) measured at $1.5d$ for jets (converging nozzle) of several different viscosities

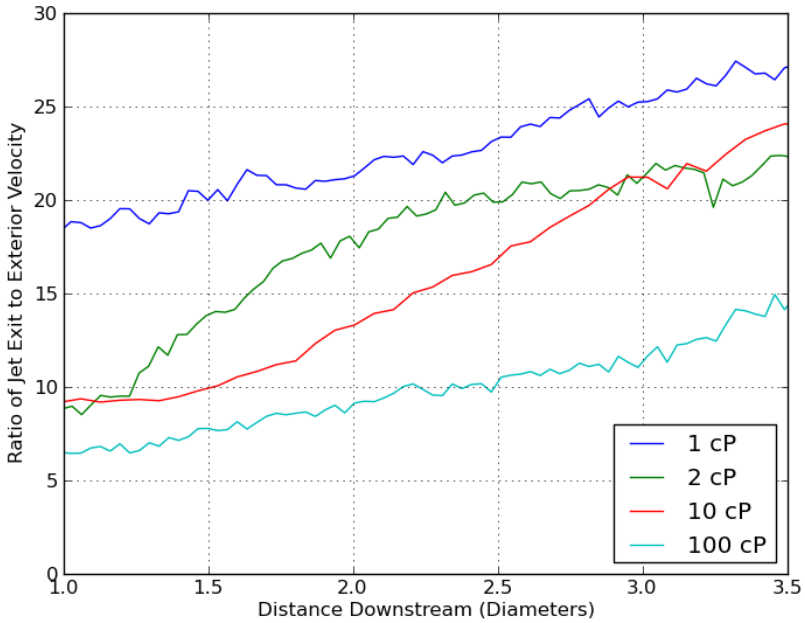

Figure 3.34: Plot of the velocity ratio (U_e/U_J) as a function of downstream distance for jets of several different viscosities ($\hat{\tau} = 0.25$)

velocity ratio higher and higher). If this is true, we should see it manifested in the quality of the PIV, as measured by the signal to noise ratio (SNR) in the image correlation.

The confidence in a calculated displacement value is often measured by the SNR, which is a ratio of the displacements' signal strength to the ambient noise of the covariance function. Defining the "noise" can be done in several ways. When performing PIV on a flow seeded with particles, defining the noise as the second largest peak can be a sensible thing to do. The cross-correlation function plotted in Figure 3.12 shows a sophisticated behavior with a number of local maxima and minima. Such a textured function indicates that there will likely be a second peak against which to compare.

However, when applying these SNR techniques to a naturally-occurring flow, there may be times that there is no usable second peak. Figure 3.15 shows the contour plot of the cross-correlation function for a typical exterior image pair. We have already noted that these contours are much smoother with fewer peaks and valleys. Thus, the occurrence of a second peak is far from guaranteed. As such, we have made use of the average cross-correlation value within the interrogation area to replace the second peak as the reference in the calculation of SNR, modifying the `gpiv` code to produce the desired results. Note, that these trends are qualitatively similar to those of a fellow researcher using a completely different PIV code that uses the second-highest peak to calculate SNR.

If we plot the experimental results of the SNR versus the time ratio, we see the data collapses quite well (Figure 3.35). In fact, the sensitivity to jet viscosity actually diminishes. This supports the idea that calculating the velocity ratio data as a function of PIV-algorithm SNR will result in useful trends, eliminating the need for a priori knowledge of the jet velocity to adjust imaging parameters. A quick set of PIV-algorithm SNR can be calculated from sample videos of the flow under study to determine the ideal imaging conditions, and the resulting jet velocity ratio to apply in order to interpret the results.

Indeed, when we plot our results as a function of the signal to noise ratio, rather than $\hat{\tau}$, we see the points once again organize themselves according to jet viscosity (see Figure 3.36). This is likely much more appropriate for applying to non-laboratory flows when the jet exit velocity is unknown.

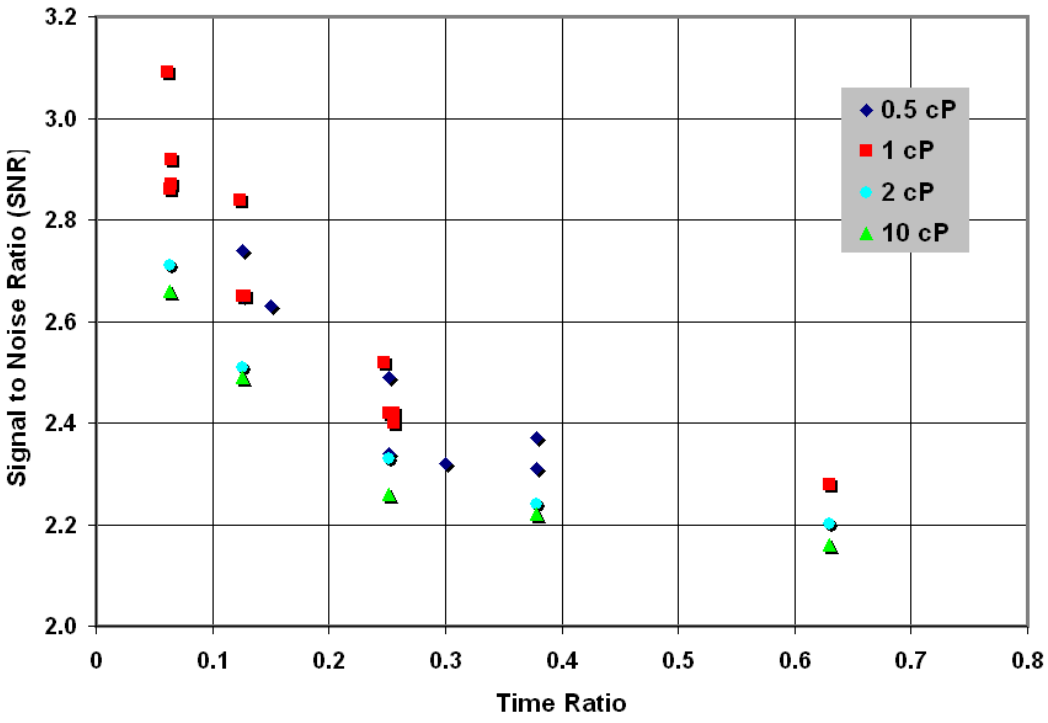

Figure 3.35: Plot of the SNR versus time ratio for several jet viscosities

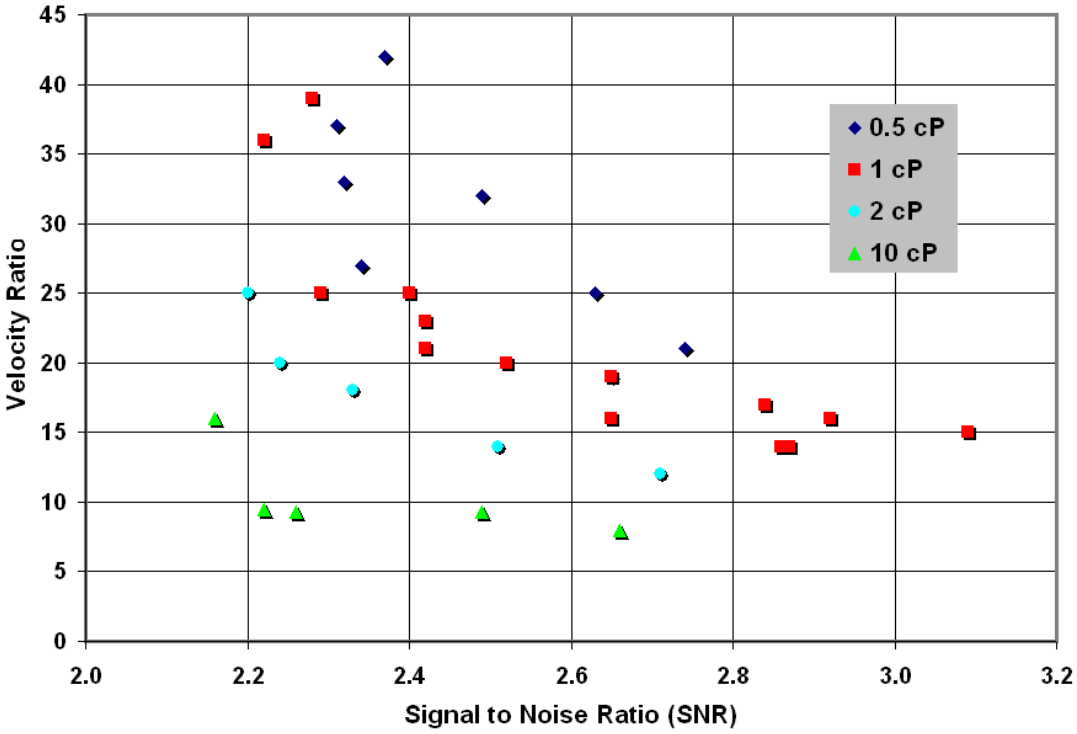

Figure 3.36: Plot of the velocity ratio versus SNR for several jet viscosities

3.6 Conclusions

Our experiments indicate that there is a consistent, predictable relationship between the PIV-calculated velocity of the jet turbulent/non-turbulent interface and the velocity at the jet core, especially for small time ratios ($U_j \delta t/d$) or large signal-to-noise ratios. This relationship is modified, but still tractable when the viscosity of the jet is different than the ambient fluid's.

The signal to noise ratio dependency of the core-to-interface velocity ratio (Figure 3.36) indicates that for sufficiently high signal to noise ratio, the velocity ratio converges to a more or less constant value. Additionally, as the SNR goes up, the scatter of the points also decreases. Thus, not only does the velocity ratio stabilize (not being a strong function of SNR), but there is greater confidence that it is an accurate value. The goal when capturing these flows is to use a sufficiently small δt to maximize the signal to noise ratio. The only conceivable drawback to an ever decreasing δt would be a lack of pixel resolution to determine very small displacements, although we did not encounter such a problem during our investigation. A balance between average convective velocity and spatial coverage of the flow in the image (taking into account pixel resolution in the imaging sensor) can be found to avoid this potential problem in the field.

The various viscosity ratios converge to different values at difference SNR values. For the constant viscosity jet, the velocity ratio appears to converge to 15 at an SNR of approximately 3.0. The 0.5 and 2.0 cP jets appear to exhibit the same converging trends, but they do not decisively converge in our plot. Based on our limited data, the 10 cP viscosity jet appears to converge, at a very low SNR, to a velocity ratio of approximately 8 or 9.

Information can potentially be gleaned at lower signal to noise ratios, below the threshold for constant velocity ratio. As the SNR decreases, however, Figure 3.36 indicates the scatter of the velocity ratio goes up considerably.

It is as yet unclear why the viscosity of the jet affects the behavior of the jet interface, as it relates to scrutiny using PIV. Quite interestingly, if we re-plot the data from Figure 3.33, but multiplying the time ratio by the viscosity ratio, μ_a/μ_j, the curves tend to collapse (see Figure 3.37).

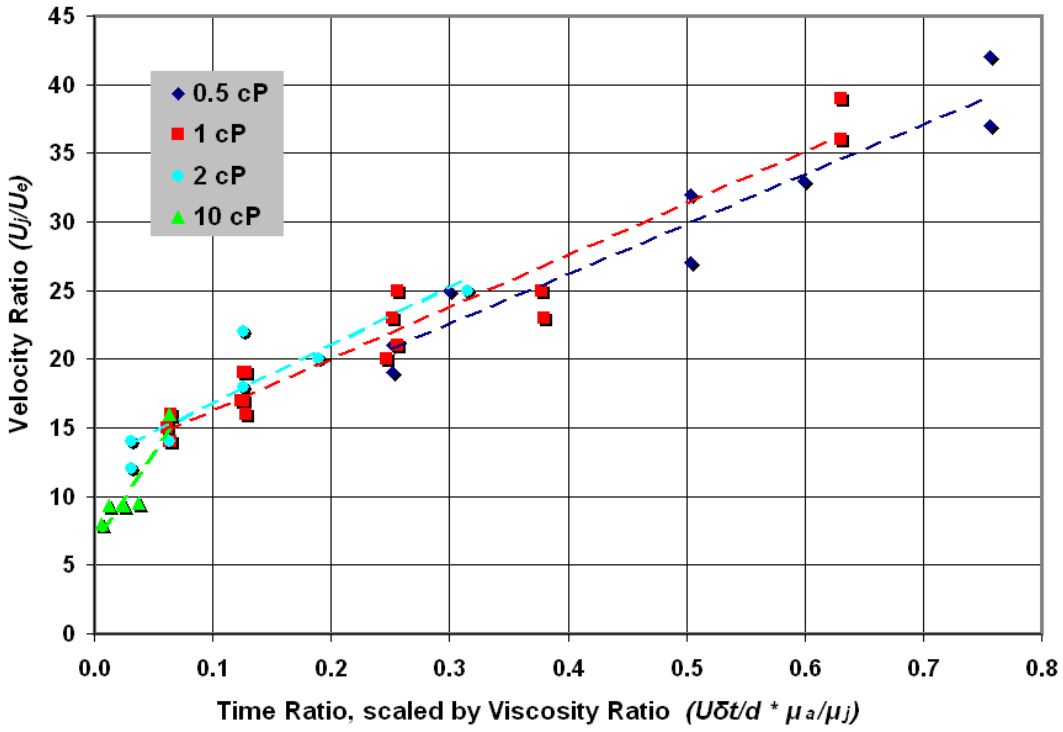

Figure 3.37: Plot of the experimental data velocity ratios versus the time ratio scaled by the viscosity ratio ($\hat{\tau}\mu_r$)

It is not immediately obvious what causes the discrepancy in velocity ratios between jets with different viscosities. It is our hypothesis that the viscosity affects the velocity prediction through modification of the onset of turbulence. In the next chapter, we will examine the effect of viscosity on the stability of the jet as it emerges from the nozzle.

3.7 Future Work

The jet experimental facility we designed is appropriate for a much wider variety of flows than we have addressed thus far. In order to be able to address more complicated naturally-occurring flows, additional variables may be introduced. Experiments can be conducted to study buoyancy driven rather than momentum driven flows. We expect that just as the relationship between the velocity and SNR/time-ratio changes as a function of viscosity, the buoyancy ratio will also have an effect.

In order to produce jets with relatively high Reynolds number, our small scale facility requires large velocities; thus, density ratios must be large to favor buoyancy versus momentum. Heavier fluids, such as glycerin, can be used to study negatively buoyant flows, although any desire to match the jet and ambient fluids' viscosities could be problematic. For a positive buoyancy jet, it may be difficult to secure liquids that are significantly lighter than water. Because of the tank's size, it is infeasible to fill it with a liquid significantly heavier than water and inject water. Alternatively, air may be added to the injected water to produce a multi-phase, buoyant flow. Multi-phase flows are a common occurrence in nature, so investigating them is a natural extension of the work.

We conducted several preliminary tests with water jets using air injected into flowing water well upstream of the nozzle. Though the air significantly reduces the jet's average density, momentum is still an important factor. Figure 3.38 shows the type of image generated with our experimental setup. It appears that the air is distributed in large, continuous pockets as opposed to small, evenly distributed bubbles. We foresee this will result in a poor approximation to the type of continuously variable, low density jet we are interested in. Nevertheless, we plotted the velocity ratio results in Figure 3.39, and they yield a curve not unlike that of the 0.5 cP jet.

Similar to Figure 3.37, we re-plotted the 1 cP and air data from Figure 3.39, scaling

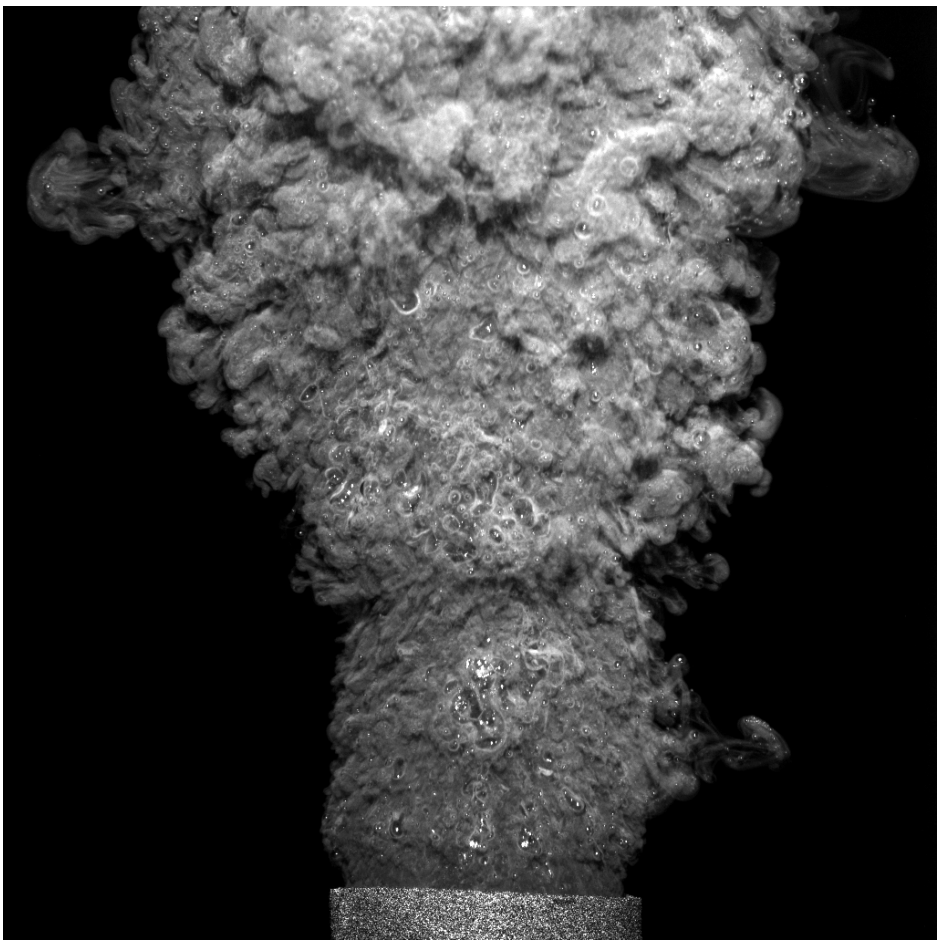

Figure 3.38: Illuminated exterior of a Rhodamine-dyed jet consisting of air and water

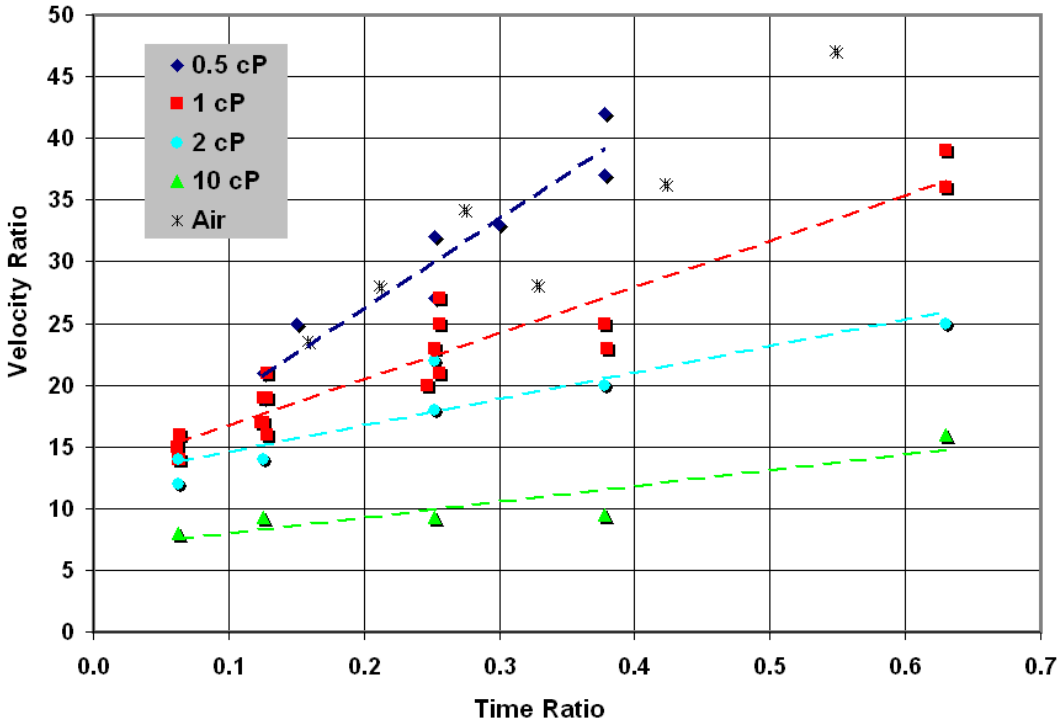

Figure 3.39: Plot of the experimental data velocity ratios versus the time ratio including the jet containing air

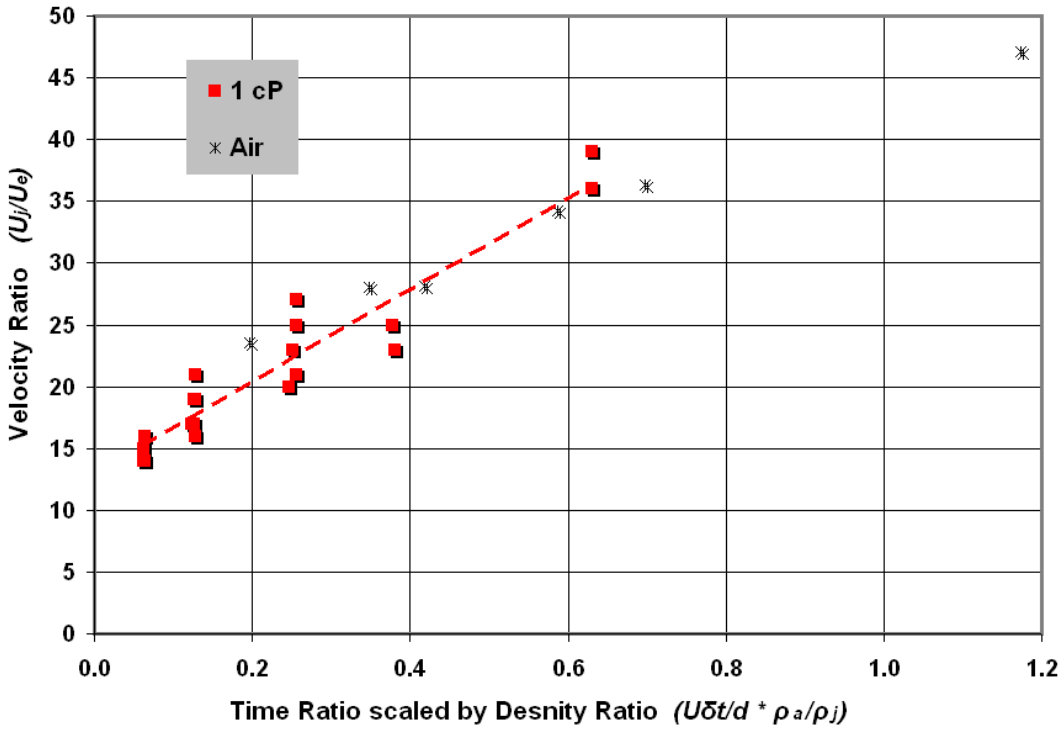

Figure 3.40: Plot of the experimental data velocity ratios versus the time ratio scaled by the viscosity ratio ($\hat{\tau}\mu_r$)

the time ratio by the density ratio, ρ_a/ρ_j. Figure 3.40 indicates that the data may again collapse. However, this deserves additional attention before drawing any strong conclusions. Depending on the exact aim of the research, it may be more appropriate to inject a higher number density of smaller air bubbles if density differences are the primary concern.

Furthermore, other non-laboratory flows of interest may experience cross-flow. Though our current experimental facility is not currently equipped to produce a cross-flow, it is conceivable modifications could be made that would allow for this configuration. Regardless, the effect of cross-flow is likely a configuration worth investigation.

Also, since our investigation primarily focuses on a specific downstream distance ($z/d = 1.5$), there are open questions about the velocity ratio for additional downstream distances. It may be useful to have velocity ratio relationships for locations much farther downstream,

if such relationships meaningfully exist.

Chapter 4

ROUND JET STABILITY

4.1 Nomenclature

$U(r)$	Normalized jet velocity profile
μ	Dynamic viscosity
C	Concentration
δ	Boundary layer thickness (at nozzle exit)
Θ	Parameter used to define momentum thickness of the free boundary shear layer
Θ_c	Parameter used to define thickness of the concentration gradient at the shear layer
μ_r	Viscosity ratio, μ_a/μ_j
C_r	Concentration ratio, C_a/C_j
D	Diffusion coefficient
$(\cdot)_a$	Ambient fluid quantity
$(\cdot)_j$	Jet fluid quantity
u, v, w, p, c	Mean flow variables
$R,\ d$	Jet radius, diameter
R_{out}	Size of computational domain
$Re,\ Re_d$	Reynolds number (defined relative to the jet radius, diameter)
z	Axial coordinate (downstream distance)
r	Radial coordinate
θ	Azimuthal coordinate
n	Azimuthal wavenumber
ω	Frequency
α	Axial (complex) wavenumber
$\hat{(\cdot)}$	Non-dimensionalized value

4.2 Background

In Chapter 3, we reported that velocity measurements for the turbulent/non-turbulent interface on the round jet are a function of the viscosity difference between the jet and the ambient fluid. Qualitative visual observations show differences in the turbulent structures even when several non-dimensional numbers are matched. We investigate the cause of these modified structures that produce the different Feature Image Correlation velocity measurement results. In his paper reviewing jet stability theory, Michalke (1984) notes that "[the] many investigations of jet turbulence have shown that the coherent structures of jet turbulence are a consequence of the instability of the turbulent jet shear layer". George (1989) and Carazzo et al. (2006) both conclude that large coherent structures in the turbulent jet may affect the downstream development of the self-similar profile. Hence, it is appropriate that we examine the characteristics of the shear layer instability in order to better understand the role that the viscosity gradient plays in jet development.

Michalke (1965) was among the first to conduct stability analyses by examining spatial, as opposed to temporal, growth rates of small perturbations. He observed that analysis of spatial perturbations was more appropriate for certain classes of flows, to which our turbulent round jet belongs. He also noted that "experimental investigations of free boundary layers of plane and axisymmetric jets ... have shown that for large Reynolds numbers the instability properties of free boundary layers are not noticeably affected by viscosity". This statement is, however, based on the implicit assumption that the fluid viscosity is constant.

The appendix of Michalke (1965) presents data from a 1965 paper by Freymuth (which was published in German) that compares spatial and temporal stability analysis results with experiments of forced flow. The results from spatial stability show that the wavenumber, phase velocity and spatial growth rates all compare more favorably to experimental results than temporal stability predictions (for small Strouhal numbers). The conclusion supports physical arguments that the flow is best described as spatially rather than temporally evolving.

On the other hand, Crow & Champagne (1971) notes that their experimental results more closely resemble the temporal analysis results from Batchelor & Gill (1962), particularly

when comparing phase velocity to wavenumber. However, the temporal analysis of Batchelor & Gill (1962) assumes inviscid flow with a discontinuous plug velocity profile. In fact, most of the literature on round jet stability since Michalke (1965) has focused on examining the spatial instability. Despite the fact that the temporal stability analysis can be considerably simpler to perform than the spatial counterpart, we will discuss techniques for conducting the spatial analysis, since the consensus is that it is the more relevant approach for the jet.

Yih (1967) was the first to look at the effect of a non-uniform viscosity on flow stability characteristics. His investigations focused on immiscible fluids, where the viscosity varied discontinuously. He found that Couette-Poiseuille flow became unconditionally unstable when such an infinite viscosity gradient was introduced. Oztekin et al. (1999) and Ern et al. (2003) both applied numerical techniques to further investigate the effect of a continuous viscosity gradient on 2-D planar flows. In addition to equations of fluid motion, an equation for viscosity transport was required. Both Oztekin et al. (1999) and Ern et al. (2003) derived equations examining only temporally evolving (as opposed to spatially unstable) flows using assumed relationships between concentration and viscosity.

Selvam et al. (2007) looked at axisymmetric flow with miscible fluids of different viscosities, but also restricted their analysis to examining the temporal instabilities. Because the flow in question was an internal flow, the spatial evolution is arguably not as important as it is for a spatially-evolving free-shear flow. Like most authors, they used an assumed relationship between concentration and viscosity; our analysis accommodates an arbitrary viscosity definition.

In our analysis, we derive the spatial stability equations for a flow for which viscosity varies arbitrarily with scalar concentration. Specifically, the flow of concern is a round free jet where two miscible fluids of different viscosities are interacting; the instabilities themselves are not necessarily axisymmetric.

Due to the complexity of the stability equations, numerical methods are required in order to solve them. A variety of methods have been marshaled to solve the eigenproblem. Finite-difference and spectral methods are often used to approximate the equations, and the resulting, sometimes large, matrices can be inverted numerically. In the past, when computer memory constraints were more pressing, shooting methods were successfully applied (e.g.

Petersen & Samet (1988).

In this chapter, we opted to solve the spectral problem with a Chebyshev method. Not only does it have a good track record for these types of problems (see Orszag (1971), Zebib (1984), Khorrami et al. (1989), Oztekin et al. (1999), Reshotko & Tumin (2001), Boeck & Zaleski (2005), Selvam et al. (2007)), but it also exhibits good accuracy using relatively few modes.

It has been noted that the traditional Orr-Sommerfeld analysis is not always the definite answer for analyzing instability growth in fluid flow problems. Trefethen & Embree (2005) noted that examining only the eigenvalues of the Orr-Sommerfeld equation is unwise for particular classes of confined, laminar flow. Specifically, Poiseuille, Couette and pipe flow were identified as being poor candidates, since algebraic growth is more significant than exponentially growing modes in understanding the instability and transition of these flows. However, it appears that free-shear flows, such as the one we are examining here, are well suited for eigenvalue-based linear stability analysis.

Because the stability analysis starts with a jet velocity profile, those characteristics will be used to define a particular Reynolds number for use with this analysis. Unless otherwise defined, the Reynolds number we use in this section will be defined as:

$$Re = \frac{\rho_j U_j R}{\mu_j} \tag{4.1}$$

where ρ_j is the jet density, U_j is the jet velocity within the potential core, R is the jet half-width (equivalent to the jet radius within the potential core), and μ_j is the jet fluid viscosity.

4.2.1 Velocity Profiles

Michalke (1984) discusses four different normalized velocity profiles for round jets commonly used to study instability behavior:

Profile 1:

$$U = 0.5 \left\{ 1 + tanh \left[b_1 \left(1 - \frac{r}{R} \right) \right] \right\} \tag{4.2}$$

where

$$b_1 = 0.5\frac{R}{\Theta} >> 1 \tag{4.3}$$

Profile 2:

$$U = 0.5\left\{1 + tanh\left[b_2\left(\frac{R}{r} - \frac{r}{R}\right)\right]\right\} \tag{4.4}$$

where

$$b_2 = 0.25\frac{R}{\Theta} \tag{4.5}$$

Profile 3:

$$U = \exp\left\{n\left[b_3\left(\frac{r}{R} - 1\right) + 1\right]^2\right\} \tag{4.6}$$

where

$$\begin{aligned} b_3 &= 0.312\frac{R}{\Theta} \\ n &= \begin{cases} 0, & \frac{r}{R} \leq 1 - \frac{1}{b_3} \\ -\ln 2, & \text{otherwise} \end{cases} \end{aligned} \tag{4.7}$$

Profile 4:

$$U = \left[1 + b_4\left(\frac{r}{R}\right)^2\right]^{-2} \tag{4.8}$$

where

$$\begin{aligned} b_4 &= \sqrt{2} - 1 \\ \frac{R}{\Theta} &= 2.185 \end{aligned} \tag{4.9}$$

In the equations above, R characterizes the jet half-width (i.e. $U(R) = 0.5$), and Θ characterizes the momentum layer thickness; typically it is defined as:

$$\Theta = \int_0^\infty U(r)(1 - U(r))dr \tag{4.10}$$

Figure 4.1 shows the profiles for $\Theta/R = 0.15$. We will concentrate primarily on profile 2; it is meant to approximate the flow in the development region of the jet and has been used by numerous authors (e.g. Morris (1976), Crighton & Gaster (1976), Plaschko (1979),

Michalke & Hermann (1982)). In this case, R is not only the jet half-width, but also the nozzle radius. Profile 4, which represents the velocity profile of a fully developed jet, is also used for validation purposes.

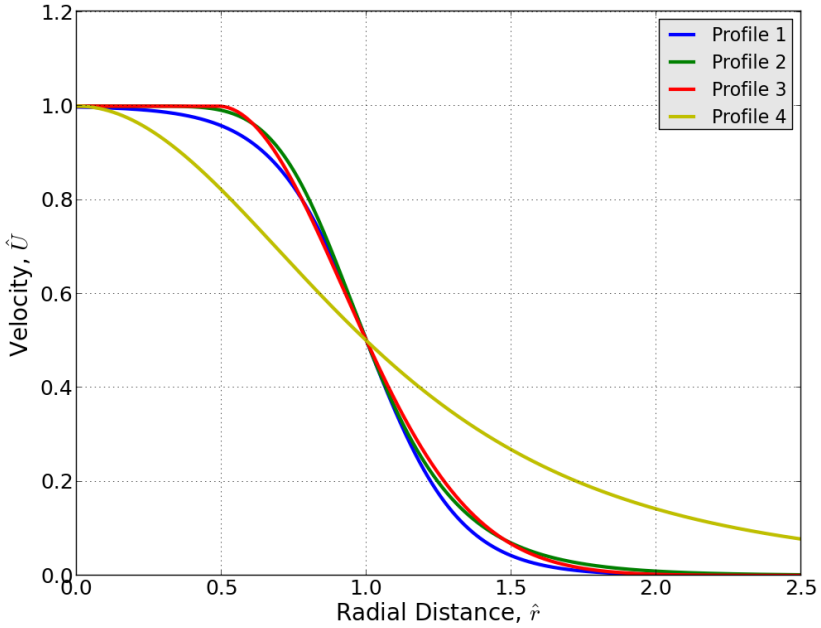

Figure 4.1: Plots of the four velocity profiles outlined by Michalke (1984) ($\Theta/R = 0.16$)

4.3 Derivation

In this section, we will give a brief overview of the stability equations. Appendix A covers their derivation in more depth. See Figure 4.2 for a diagram of geometry used for the stability analysis.

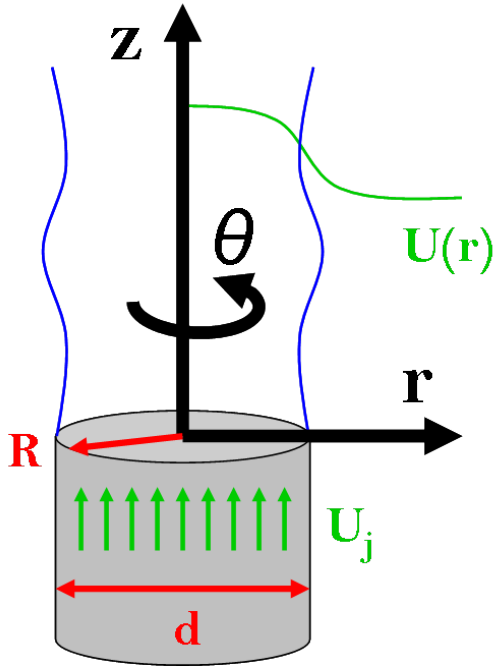

Figure 4.2: Diagram of the coordinate system and geometry of the round jet

First, the flow variables must be decomposed into their mean and fluctuating parts:

$$\begin{aligned} u(z,r,\theta,t) &= U(z,r,\theta) + u'(z,r,\theta,t) \\ v(z,r,\theta,t) &= V(z,r,\theta) + v'(z,r,\theta,t) \\ w(z,r,\theta,t) &= w'(z,r,\theta,t) \\ p(z,r,\theta,t) &= P(z,r,\theta) + p'(z,r,\theta,t) \\ c(z,r,\theta,t) &= C(z,r,\theta) + c'(z,r,\theta,t) \end{aligned} \tag{4.11}$$

and we assume the fluctuation parts have the harmonic form:

$$\begin{aligned} u'(z,r,\theta,t) &= \bar{u}(r)\exp\left\{i\left(\alpha z + n\theta + \omega t\right)\right\} \\ v'(z,r,\theta,t) &= \bar{v}(r)\exp\left\{i\left(\alpha z + n\theta + \omega t\right)\right\} \\ w'(z,r,\theta,t) &= \bar{w}(r)\exp\left\{i\left(\alpha z + n\theta + \omega t\right)\right\} \\ p'(z,r,\theta,t) &= \bar{p}(r)\exp\left\{i\left(\alpha z + n\theta + \omega t\right)\right\} \\ c'(z,r,\theta,t) &= \bar{c}(r)\exp\left\{i\left(\alpha z + n\theta + \omega t\right)\right\} \end{aligned} \tag{4.12}$$

Additionally, there are supplemental equations that allow us to have a linear system of equations:

$$\begin{aligned} \bar{u}_\alpha &= \alpha\bar{u} \\ \bar{v}_\alpha &= \alpha\bar{v} \\ \bar{w}_\alpha &= \alpha\bar{w} \\ \bar{c}_\alpha &= \alpha\bar{c} \end{aligned} \tag{4.13}$$

These additional equations make clear the extra price that spatial stability analysis exacts. Temporal analysis yields terms only linear in ω, requiring only a system of five equations to solve, whereas the supplemental equations needed to make α appear linearly result in a system of nine equations. The remaining five equations consist of three equations for momentum, an equation for scalar concentration advection/diffusion, and finally, the simplified continuity equation (based on the assumption of incompressible, constant density flow). The non-dimensional versions of the equations are as follows:

z-momentum:

$$\begin{aligned} &\left(-\hat{\omega} - i\tfrac{1}{Re}\tfrac{\partial\hat{\mu}}{\partial C}\tfrac{\partial C}{\partial\hat{r}}\tfrac{\partial}{\partial\hat{r}} + i\tfrac{1}{Re}\hat{\mu}(C)\left(\tfrac{n^2}{\hat{r}^2} - \tfrac{1}{\hat{r}}\tfrac{\partial}{\partial\hat{r}} - \tfrac{\partial^2}{\partial\hat{r}^2}\right)\right)\hat{\bar{u}} - \hat{U}\hat{\bar{u}}_\alpha \\ &+ i\tfrac{\partial\hat{U}}{\partial\hat{r}}\bar{v} + i\tfrac{1}{Re}\left(\hat{\mu}(C)\tfrac{\partial}{\partial\hat{r}} + \hat{\mu}(C)\tfrac{1}{\hat{r}} - \tfrac{\partial\hat{\mu}}{\partial C}\tfrac{\partial C}{\partial\hat{r}}\right)\hat{\bar{v}}_\alpha - i\tfrac{\hat{\mu}(C)}{Re}\tfrac{n}{\hat{r}}\hat{\bar{w}}_\alpha \\ &+ i\tfrac{1}{Re}\left(\tfrac{\partial\hat{U}}{\partial\hat{r}}\left.\tfrac{\partial\hat{\mu}}{\partial\hat{c}}\right|_C\tfrac{\partial}{\partial\hat{r}} + \tfrac{\partial^2\hat{U}}{\partial\hat{r}^2}\left.\tfrac{\partial\hat{\mu}}{\partial\hat{c}}\right|_C + \tfrac{1}{\hat{r}}\tfrac{\partial\hat{U}}{\partial\hat{r}}\left.\tfrac{\partial\hat{\mu}}{\partial\hat{c}}\right|_C + \tfrac{\partial\hat{U}}{\partial\hat{r}}\tfrac{\partial}{\partial C}\left(\left.\tfrac{\partial\hat{\mu}}{\partial\hat{c}}\right|_C\right)\tfrac{\partial C}{\partial\hat{r}}\right)\hat{\bar{c}} \\ &= \hat{\alpha}\hat{\bar{p}} \end{aligned} \tag{4.14}$$

r-momentum:

$$\begin{aligned}
&\left(-i\hat{\omega}\tfrac{Re}{\hat{\mu}(C)} - \tfrac{n^2+1}{\hat{r}^2} + \tfrac{1}{\hat{r}}\tfrac{\partial}{\partial\hat{r}} + \tfrac{\partial^2}{\partial\hat{r}^2} + 2\tfrac{1}{\hat{\mu}(C)}\tfrac{\partial\hat{\mu}}{\partial C}\tfrac{\partial C}{\partial\hat{r}}\tfrac{\partial}{\partial\hat{r}}\right)\hat{\bar{v}} \\
&- i\hat{U}\tfrac{Re}{\hat{\mu}(C)}\hat{\bar{v}}_\alpha - 2i\tfrac{n}{\hat{r}^2}\hat{\bar{w}} \\
&+ i\tfrac{1}{\hat{\mu}(C)}\tfrac{\partial\hat{U}}{\partial\hat{r}}\left.\tfrac{\partial\hat{\mu}}{\partial\hat{c}}\right|_C\hat{\bar{c}}_\alpha - \tfrac{Re}{\hat{\mu}(C)}\tfrac{\partial}{\partial\hat{r}}\hat{\bar{p}} \\
&= \hat{\alpha}\hat{\bar{v}}_\alpha
\end{aligned} \tag{4.15}$$

θ-momentum:

$$\begin{aligned}
&i\tfrac{n}{\hat{r}}\left(\tfrac{1}{\hat{\mu}(C)}\tfrac{\partial\hat{\mu}}{\partial C}\tfrac{\partial C}{\partial\hat{r}} + 2\tfrac{1}{\hat{r}}\right)\hat{\bar{v}} \\
&+ \left(-i\hat{\omega}\tfrac{Re}{\hat{\mu}(C)} - \tfrac{n^2+1}{\hat{r}^2} + \tfrac{1}{\hat{r}}\tfrac{\partial}{\partial\hat{r}} + \tfrac{\partial^2}{\partial\hat{r}^2} - \tfrac{1}{\hat{\mu}(C)}\tfrac{\partial\hat{\mu}}{\partial C}\tfrac{\partial C}{\partial\hat{r}}\tfrac{1}{\hat{r}} + \tfrac{1}{\hat{\mu}(C)}\tfrac{\partial\hat{\mu}}{\partial C}\tfrac{\partial C}{\partial\hat{r}}\tfrac{\partial}{\partial\hat{r}}\right)\hat{\bar{w}} \\
&- i\hat{U}\tfrac{Re}{\hat{\mu}(C)}\hat{\bar{w}}_\alpha - i\tfrac{n}{\hat{r}}\tfrac{Re}{\hat{\mu}(C)}\hat{\bar{p}} \\
&= \hat{\alpha}\hat{\bar{w}}_\alpha
\end{aligned} \tag{4.16}$$

Concentration:

$$-Pe\tfrac{\partial C}{\partial\hat{r}}\hat{\bar{v}} - \left[i\hat{\omega}Pe - \left(\tfrac{\partial^2}{\partial\hat{r}^2} + \tfrac{1}{\hat{r}}\tfrac{\partial}{\partial\hat{r}} - \tfrac{n^2}{\hat{r}^2}\right)\right]\bar{c} - iPe\hat{U}\hat{\bar{c}}_\alpha = \hat{\alpha}\hat{\bar{c}}_\alpha \tag{4.17}$$

Continuity:

$$i\tfrac{\partial}{\partial\hat{r}}\hat{\bar{v}}_\alpha + \tfrac{i}{\hat{r}}\hat{\bar{v}}_\alpha - n\tfrac{1}{\hat{r}}\hat{\bar{w}}_\alpha = \hat{\alpha}\hat{\bar{u}}_\alpha \tag{4.18}$$

This system of nine equations can be succinctly written in matrix form:

$$\boldsymbol{A}\boldsymbol{q} = \hat{\alpha}\boldsymbol{B}\boldsymbol{q} \tag{4.19}$$

where, expanded, the matrices are defined as:

$$\hat{\alpha}\boldsymbol{Bq} = \hat{\alpha}\begin{bmatrix} 1 & 0 & 0 & 0 & 0 & 0 & 0 & 0 & 0 \\ 0 & 1 & 0 & 0 & 0 & 0 & 0 & 0 & 0 \\ 0 & 0 & 1 & 0 & 0 & 0 & 0 & 0 & 0 \\ 0 & 0 & 0 & 1 & 0 & 0 & 0 & 0 & 0 \\ 0 & 0 & 0 & 0 & 1 & 0 & 0 & 0 & 0 \\ 0 & 0 & 0 & 0 & 0 & 1 & 0 & 0 & 0 \\ 0 & 0 & 0 & 0 & 0 & 0 & 1 & 0 & 0 \\ 0 & 0 & 0 & 0 & 0 & 0 & 0 & 1 & 0 \\ 0 & 0 & 0 & 0 & 0 & 0 & 0 & 0 & 1 \end{bmatrix} \begin{bmatrix} \hat{\bar{u}} \\ \hat{\bar{u}}_\alpha \\ \hat{\bar{v}} \\ \hat{\bar{v}}_\alpha \\ \hat{\bar{w}} \\ \hat{\bar{w}}_\alpha \\ \hat{\bar{c}} \\ \hat{\bar{c}}_\alpha \\ \hat{\bar{p}} \end{bmatrix} \tag{4.20}$$

and

$$\boldsymbol{Aq} = \begin{bmatrix} 0 & 1 & 0 & 0 & 0 & 0 & 0 & 0 & 0 \\ 0 & 0 & 0 & A_{24} & 0 & A_{26} & 0 & 0 & 0 \\ 0 & 0 & 0 & 1 & 0 & 0 & 0 & 0 & 0 \\ 0 & 0 & A_{43} & A_{44} & A_{45} & 0 & A_{47} & 0 & A_{49} \\ 0 & 0 & 0 & 0 & 0 & 1 & 0 & 0 & 0 \\ 0 & 0 & A_{63} & 0 & A_{65} & A_{66} & 0 & 0 & A_{69} \\ 0 & 0 & 0 & 0 & 0 & 0 & 0 & 1 & 0 \\ 0 & 0 & A_{83} & 0 & 0 & 0 & A_{87} & A_{88} & 0 \\ A_{91} & A_{92} & A_{93} & A_{94} & 0 & 0 & A_{97} & 0 & 0 \end{bmatrix} \begin{bmatrix} \hat{\bar{u}} \\ \hat{\bar{u}}_\alpha \\ \hat{\bar{v}} \\ \hat{\bar{v}}_\alpha \\ \hat{\bar{w}} \\ \hat{\bar{w}}_\alpha \\ \hat{\bar{c}} \\ \hat{\bar{c}}_\alpha \\ \hat{\bar{p}} \end{bmatrix} \tag{4.21}$$

where

$$
\begin{aligned}
A_{24} &= i\tfrac{\partial}{\partial\hat{r}} + i\tfrac{1}{\hat{r}} \\
A_{26} &= -n\tfrac{1}{\hat{r}} \\
A_{43} &= -i\hat{\omega}\tfrac{Re}{\hat{\mu}(C)} - \tfrac{n^2+1}{\hat{r}^2} + \tfrac{1}{\hat{r}}\tfrac{\partial}{\partial\hat{r}} + \tfrac{\partial^2}{\partial\hat{r}^2} + 2\tfrac{1}{\hat{\mu}(C)}\tfrac{\partial\hat{\mu}}{\partial C}\tfrac{\partial C}{\partial\hat{r}}\tfrac{\partial}{\partial\hat{r}} \\
A_{44} &= -i\hat{U}\tfrac{Re}{\hat{\mu}(C)} \\
A_{45} &= -2i\tfrac{n}{\hat{r}^2} \\
A_{48} &= i\tfrac{1}{\hat{\mu}(C)}\tfrac{\partial\hat{U}}{\partial\hat{r}}\ \tfrac{\partial\hat{\mu}}{\partial\hat{c}}\Big|_C \\
A_{49} &= -\tfrac{Re}{\hat{\mu}(C)}\tfrac{\partial}{\partial\hat{r}} \\
A_{63} &= i\tfrac{n}{\hat{r}}\left(\tfrac{1}{\hat{\mu}(C)}\tfrac{\partial\hat{\mu}}{\partial C}\tfrac{\partial C}{\partial\hat{r}} + 2\tfrac{1}{\hat{r}}\right) \\
A_{65} &= -i\hat{\omega}\tfrac{Re}{\hat{\mu}(C)} - \tfrac{n^2+1}{\hat{r}^2} + \tfrac{1}{\hat{r}}\tfrac{\partial}{\partial\hat{r}} + \tfrac{\partial^2}{\partial\hat{r}^2} - \tfrac{1}{\hat{\mu}(C)}\tfrac{\partial\hat{\mu}}{\partial C}\tfrac{\partial C}{\partial\hat{r}}\tfrac{1}{\hat{r}} + \tfrac{1}{\hat{\mu}(C)}\tfrac{\partial\hat{\mu}}{\partial C}\tfrac{\partial C}{\partial\hat{r}}\tfrac{\partial}{\partial\hat{r}} \\
A_{66} &= -i\hat{U}\tfrac{Re}{\hat{\mu}(C)} \\
A_{69} &= -i\tfrac{n}{\hat{r}}\tfrac{Re}{\hat{\mu}(C)} \\
A_{83} &= -Pe\tfrac{\partial C}{\partial\hat{r}} \\
A_{87} &= -i\hat{\omega}Pe + \left(\tfrac{\partial^2}{\partial\hat{r}^2} + \tfrac{1}{\hat{r}}\tfrac{\partial}{\partial\hat{r}} - \tfrac{n^2}{\hat{r}^2}\right) \\
A_{88} &= -iPe\hat{U} \\
A_{91} &= -\hat{\omega} - i\tfrac{1}{Re}\tfrac{\partial\hat{\mu}}{\partial C}\tfrac{\partial C}{\partial\hat{r}}\tfrac{\partial}{\partial\hat{r}} + i\tfrac{1}{Re}\hat{\mu}(C)\left(\tfrac{n^2}{\hat{r}^2} - \tfrac{1}{\hat{r}}\tfrac{\partial}{\partial\hat{r}} - \tfrac{\partial^2}{\partial\hat{r}^2}\right) \\
A_{92} &= -\hat{U} \\
A_{93} &= i\tfrac{\partial\hat{U}}{\partial\hat{r}} \\
A_{94} &= \tfrac{1}{Re}\left(\tfrac{\partial\hat{\mu}}{\partial C}\tfrac{\partial C}{\partial\hat{r}} - \hat{\mu}(C)\tfrac{\partial}{\partial\hat{r}} - \hat{\mu}(C)\tfrac{1}{\hat{r}}\right) \\
A_{96} &= -i\tfrac{\hat{\mu}(C)}{Re}\tfrac{n}{\hat{r}} \\
A_{97} &= i\tfrac{1}{Re}\left(\tfrac{\partial\hat{U}}{\partial\hat{r}}\ \tfrac{\partial\hat{\mu}}{\partial\hat{c}}\Big|_C\tfrac{\partial}{\partial\hat{r}} + \tfrac{\partial^2\hat{U}}{\partial\hat{r}^2}\ \tfrac{\partial\hat{\mu}}{\partial\hat{c}}\Big|_C + \tfrac{1}{\hat{r}}\tfrac{\partial\hat{U}}{\partial\hat{r}}\ \tfrac{\partial\hat{\mu}}{\partial\hat{c}}\Big|_C + \tfrac{\partial\hat{U}}{\partial\hat{r}}\tfrac{\partial}{\partial C}\left(\tfrac{\partial\hat{\mu}}{\partial\hat{c}}\Big|_C\right)\tfrac{\partial C}{\partial\hat{r}}\right)
\end{aligned}
\tag{4.22}
$$

4.3.1 Boundary Conditions

In order to calculate the instability behavior, it is important to properly define the boundary conditions at the extremes of the domain. Our 1-D calculations will be conducted along the r–axis from the axis of symmetry to the outer part of the domain, R_{out}. The following

boundary conditions as $r \to 0$ are driven by the requirements outlined in Khorrami et al. (1989), with the addition of a concentration constraint:

$$\begin{aligned} \lim_{r\to 0} \frac{\partial \boldsymbol{u}}{\partial \theta} &= 0 \\ \lim_{r\to 0} \frac{\partial p}{\partial \theta} &= 0 \\ \lim_{r\to 0} \frac{\partial c}{\partial \theta} &= 0 \end{aligned} \tag{4.23}$$

Looking first at the condition for velocity, we can concentrate on the fluctuating part, since the mean flow has no azimuthal dependence:

$$\frac{\partial \boldsymbol{u'}}{\partial \theta} = \frac{\partial}{\partial \theta}\left(u'\boldsymbol{e_z} + v'\boldsymbol{e_r} + w'\boldsymbol{e_\theta}\right). \tag{4.24}$$

Therefore, by applying the chain rule:

$$\lim_{r\to 0} \frac{\partial \boldsymbol{u'}}{\partial \theta} = \frac{\partial u'}{\partial \theta}\boldsymbol{e_z} + u'\frac{\partial \boldsymbol{e_z}}{\partial \theta} + \frac{\partial v'}{\partial \theta}\boldsymbol{e_r} + v'\frac{\partial \boldsymbol{e_r}}{\partial \theta} + \frac{\partial w'}{\partial \theta}\boldsymbol{e_\theta} + w'\frac{\partial \boldsymbol{e_\theta}}{\partial \theta} = 0. \tag{4.25}$$

Since

$$\frac{\partial \boldsymbol{e_z}}{\partial \theta} = 0, \frac{\partial \boldsymbol{e_r}}{\partial \theta} = \boldsymbol{e_\theta}, \frac{\partial \boldsymbol{e_\theta}}{\partial \theta} = -\boldsymbol{e_r} \tag{4.26}$$

we can write the velocity boundary condition as:

$$\lim_{r\to 0} \frac{\partial \boldsymbol{u'}}{\partial \theta} = \frac{\partial u'}{\partial \theta}\boldsymbol{e_z} + \frac{\partial v'}{\partial \theta}\boldsymbol{e_r} + v'\boldsymbol{e_\theta} + \frac{\partial w'}{\partial \theta}\boldsymbol{e_\theta} - w'\boldsymbol{e_r} = 0. \tag{4.27}$$

Substituting the exponential form from (4.12) and dividing through by the exponential factor yields:

$$\lim_{r\to 0} \frac{\partial \bar{\boldsymbol{u}}}{\partial \theta} = in\bar{u}\boldsymbol{e_z} + in\bar{v}\boldsymbol{e_r} + \bar{v}\boldsymbol{e_\theta} + in\bar{w}\boldsymbol{e_\theta} - \bar{w}\boldsymbol{e_r} = 0. \tag{4.28}$$

Grouping according to components leads to:

$$\lim_{r\to 0} \frac{\partial \bar{\boldsymbol{u}}}{\partial \theta} = in\bar{u}\boldsymbol{e_z} + \left(in\bar{v} - \bar{w}\right)\boldsymbol{e_r} + \left(\bar{v} + in\bar{w}\right)\boldsymbol{e_\theta} = 0. \tag{4.29}$$

As Khorrami et al. (1989) points out, in order to satisfy the equality, each of the components

must equal zero. Similarly, from (4.23), pressure and concentration can be written:

$$\begin{aligned} \lim_{r\to 0} \frac{\partial p}{\partial \theta} &= in\bar{p} = 0 \\ \lim_{r\to 0} \frac{\partial c}{\partial \theta} &= in\bar{c} = 0 \end{aligned} \tag{4.30}$$

Therefore as $r \to 0$:

$$\begin{aligned} in\bar{u} &= 0 \\ in\bar{v} - \bar{w} &= 0 \\ \bar{v} + in\bar{w} &= 0 \\ in\bar{p} &= 0 \\ in\bar{c} &= 0 \end{aligned} \tag{4.31}$$

Because the equations involving v' and w' are linearly dependent when $n = 1$, we will need another boundary condition, generated by enforcing continuity at the centerline:

$$\boldsymbol{\nabla} \cdot \boldsymbol{u'} = \frac{\partial u'}{\partial z} + \frac{\partial v'}{\partial r} + \frac{1}{r} v' + \frac{1}{r} \frac{\partial w'}{\partial \theta} = 0. \tag{4.32}$$

Again, substitution from (4.12) and dividing by the exponential factor, we obtain (keeping $n = 1$):

$$i\alpha\bar{u} + \frac{\partial \bar{v}}{\partial r} + \frac{1}{r}\bar{v} + \frac{i}{r}\bar{w} = 0. \tag{4.33}$$

If we again take the limit as $r \to 0$:

$$\lim_{r\to 0} i\alpha\bar{u}(r) + \frac{\partial \bar{v}}{\partial r} + \frac{1}{r}\bar{v}(r) + \frac{i}{r}\bar{w}(r) = 0. \tag{4.34}$$

Since we are currently limiting ourselves to $n = 1$:

$$\lim_{r\to 0} \bar{u} = 0. \tag{4.35}$$

And recalling $\bar{v}(0) + i\bar{w}(0) = 0$

$$\lim_{r\to 0} \frac{\partial \bar{v}}{\partial r} + \frac{1}{r}\left(\bar{v}(r) - \bar{v}(0) + i\bar{w}(r) - i\bar{w}(0)\right) = 0. \tag{4.36}$$

Formally, the definition of a derivative is:

$$\frac{\partial}{\partial x} f(a) = \lim_{h\to 0} \frac{f(a+h) - f(a)}{h}. \tag{4.37}$$

Therefore the previous condition becomes:

$$2\frac{\partial}{\partial r}\bar{v}(0) + in\frac{\partial}{\partial r}\bar{w}(0) = 0. \tag{4.38}$$

This is the additional boundary equation we must utilize when $n = 1$.

Let us now examine the conditions at $r = 0$ for specific cases of n:

$$\begin{aligned}
n = 0 &\begin{cases} \frac{\partial}{\partial r}\bar{u}(0) = 0 \\ \frac{\partial}{\partial r}\bar{p}(0) = 0 \\ \frac{\partial}{\partial r}\bar{c}(0) = 0 \\ \bar{v}(0) = \bar{w}(0) = 0 \end{cases} \\
n = 1 &\begin{cases} \bar{u}(0) = \bar{p}(0) = \bar{c}(0) = 0 \\ \bar{v}(0) + i\bar{w}(0) = 0 \\ 2\frac{\partial}{\partial r}\bar{v}(0) + i\frac{\partial}{\partial r}\bar{w}(0) = 0 \end{cases} \\
n > 1 &\begin{cases} \bar{u}(0) = \bar{p}(0) = \bar{c}(0) = 0 \\ \bar{v}(0) + in\bar{w}(0) = 0 \\ in\bar{v}(0) - \bar{w}(0) = 0 \end{cases}
\end{aligned} \tag{4.39}$$

Finally, for any value of n, $\bar{u}_\alpha(0) = \alpha\bar{u}(0)$, $\bar{v}_\alpha(0) = \alpha\bar{v}(0)$, $w'_\alpha(0) = \alpha\bar{w}(0)$, and $c'_\alpha(0) = \alpha\bar{c}(0)$.

For the purposes of implementation, it is more useful to state $\bar{v}(0)+i\bar{w}(0) = 0$ as opposed

to $\bar{v}(0) = -i\bar{w}(0)$. We will discuss exactly how to implement these conditions in section 4.3.2.

For all variables, as r approaches ∞:

$$\lim_{r\to\infty} \bar{u}, \bar{u}_\alpha, \bar{v}, \bar{v}_\alpha, \bar{w}, \bar{w}_\alpha, \bar{p}, \bar{c}, \bar{c}_\alpha = 0. \tag{4.40}$$

The condition at the axis of symmetry will mimic the ideal flow, however, our computational domain will prevent us from strictly defining the boundary as $r \to \infty$. For computational purposes, we will enforce the conditions at the outer boundary: $r = R_{out}$.

4.3.2 Method of Solution

The matrix system in the previous section represents only the statement of the problem; a method of solution remains to be determined. The domain requires discretization, and the model equations must be converted to equations in differences at the nodes. As mentioned in the introduction, a Chebyshev method was implemented where domain discretization was performed at the Gauss-Lobatto collocation points (see Trefethen (2000) and an appendix of Schmid & Henningson (2001)), recast from $[-1, 1]$ to $[0, R]$:

$$y_j = \frac{R}{2}\left[cos\left(\frac{j\pi}{N}\right) + 1\right]. \tag{4.41}$$

These collocation points are appropriate for approximating Chebyshev polynomials, and the distribution clusters nodes at the boundaries. This concentration of nodes at the domain edges prevents interpolation errors that would otherwise occur at the boundaries (known as the Runge phenomenon). We will define our desired solution f as a sum of Chebyshev polynomials T_n:

$$f(y) = \sum_{n=0}^{N} a_n T_n(y) \tag{4.42}$$

where the Chebyshev polynomials are mutually orthogonal and make up the basis of our solution:

$$T_n(y) = \frac{1}{2}\left[\left(y + \sqrt{y^2-1}\right)^n + \left(y - \sqrt{y^2-1}\right)^n\right]. \tag{4.43}$$

We can relate the first and second derivatives to $f(y)$ via the differentiation matrix:

$$\begin{aligned}\left[\boldsymbol{Df}\right]_j &= \sum_{n=0}^{N} a_n \tfrac{\partial T_n}{\partial r}(y_j) \\ \left[\boldsymbol{D^2 f}\right]_j &= \sum_{n=0}^{N} a_n \tfrac{\partial^2 T_n}{\partial r^2}(y_j)\end{aligned} \tag{4.44}$$

where $\boldsymbol{f}$ is a vector composed of $f(y_j)$.

Rather than constructing our matrix system with the Chebyshev polynomials and solving for the coefficients a_n, we will use the differentiation matrix $\boldsymbol{D}$ to solve for the unknown variable $\boldsymbol{f}$ directly. Trefethen (2000) defines the differentiation matrix $\boldsymbol{D}$ for discretization of N segments (according to (4.41)) to be of size $(N+1)\times(N+1)$ with the following entries:

$$\begin{aligned}\boldsymbol{D_{00}} &= -\boldsymbol{D_{NN}} = \frac{2N^2+1}{6}, \\ \boldsymbol{D_{jj}} &= -\frac{x_j}{2\left(1-x_j^2\right)}, && j = 1,\ldots,N-1, \\ \boldsymbol{D_{ij}} &= \frac{c_i}{c_j}\frac{(-1)^{i+j}}{x_i - x_j}, && i \neq j, \qquad i,j = 0,\ldots,N, \\ c_i &= \begin{cases} 2, & i = 0 \text{ or } N \\ 1, & \text{otherwise} \end{cases}\end{aligned} \tag{4.45}$$

and additionally,

$$\boldsymbol{D^2} = \boldsymbol{DD}. \tag{4.46}$$

In order to solve the eigenproblem, the Python programming language was used, taking advantage of the `numpy`, `scipy` and `matplotlib` libraries (Jones et al., 2001; Hunter, 2007). The matrices were assembled according to the equations outlined in section 4.3. The first and last row of each matrix block were reserved for the definition of boundary conditions (or the rows/columns were deleted for homogenous Dirichlet conditions). In the case of, for instance $n = 1$, the conditions involving $\bar{v}$ and $\bar{w}$ are implemented on the right hand side of the eigenvalue equation. That is, $\bar{v}(0) + i\bar{w}(0) = 0$ becomes $\alpha\bar{v_\alpha}(0) + i\alpha\bar{w_\alpha}(0) = 0$; in this way, the right-hand side matrix $\boldsymbol{B}$ can remain non-singular, and while $\boldsymbol{A}$ is rendered

singular, $\boldsymbol{B}^{-1}\boldsymbol{A}$ is usually non-singular.

4.3.3 Identifying the Most Unstable Mode

In the case of the one-equation Orr-Sommerfeld analysis, the identification of the most unstable mode is as simple as looking for the eigenvalue which creates the largest real exponent for the fluctuating flow parameters (equations (4.12)). However, as additional equations are incorporated, either to increase the number of spatial dimensions analyzed or increase the factors considered (e.g. density, concentration), the identification becomes more difficult.

Nichols (2005) examined a round jet and noted that there are two main components of the eigenvalue spectrum: the continuous and discrete parts. Because we are approximating an infinite domain with a discretized, finite-sized domain, the continuous part of the spectrum is rendered discrete with a finite number of eigenvalues (the resolution of which will increase with more computational nodes). Additionally, the discrete part of the spectrum is represented by individual eigenvalues that may become more accurate, but not more numerous as the refinement is increased. The discrete modes are typically the ones responsible for instabilities in these flows.

Unfortunately, with increased complexity and computational approximations, spurious modes arise that need to be identified and ignored; see Malik (1990), Zebib (1984), Gottlieb & Orszag (1977).

From the literature, we have identified a set of unstable modes reported for assorted flow conditions. Due to the difficulty of identifying the importance of a particular eigenvalue to the stability problem, we have opted for an iterative technique that relies on marching from known unstable modes to predict new unstable modes at slightly different conditions.

4.3.3.1 Inverse Iteration Method

Rather than calculating the entire set of eigenvalues, it seems sensible to limit our attention to the most unstable value, especially because it saves significant computational time. Furthermore, once the most unstable value for a set of parameters (Reynolds number, vis-

cosity ratio, etc.) has been identified, if we slightly perturb the circumstances, we expect the eigenvalue/vector to change only slightly.

Subject to these considerations, the inverse iteration method is considered an appropriate approach for our analysis.

The method requires an initial guess for the eigenvalue of interest, $\hat{\alpha}$, with a less stringent requirement for the corresponding eigenvector, $\boldsymbol{b}$. The eigenvector is determined via iteration (Bender & Orszag (1999)):

$$\boldsymbol{b_{k+1}} = \frac{(\boldsymbol{A} - \hat{\alpha}\boldsymbol{I})^{-1}\,\boldsymbol{b_k}}{C_k} \tag{4.47}$$

where $C_k = \|(\boldsymbol{A} - \hat{\alpha}\boldsymbol{I})^{-1}\,\boldsymbol{b_k}\|$ and is used for normalization.

Starting from a base state with a known unstable eigenvalue, inverse iteration is seeded with the relevant $\hat{\alpha}$ (note: the algorithm is fairly forgiving when $\boldsymbol{b}$ is unknown). Depending on the parameter space to be explored, any value (e.g. Re, $\hat{\omega}$) can be slightly perturbed. Subsequent calculations are marched out, filling the parameter space, using the previous local value of the eigenvalue/vector to calculate a new value at the desired flow conditions. Trial and error is necessary to determine the biggest steps that can be taken in the parameter space without calculating an undesirable eigenvalue.

4.4 Validation

In order to build confidence in our model, we validate it against existing results published in the literature. Although the spatial stability of the round jet with viscosity gradients has not been specifically solved, there is literature available to compare against for constant viscosity analyses.

One of the earlier papers available for comparison is Morris (1976). Not only is a wide range of results from spatial stability analyses presented, but the parameters of the calculations (e.g. velocity profile) are clear. Furthermore, within this paper results are compared favorably to previous papers, notably Mollendorf & Gebhart (1973). Finally, there are detailed results for eigenvalues that provide for quantitative comparison against the method presented here.

The results from Morris (1976) are for a round jet with constant viscosity. Though a

different numerical scheme was used, we expect our results to match those in the seminal paper, as the underlying physics and assumptions are the same. However, a few important distinctions should be noted. Morris (1976) examines both velocity profiles 2 and 4, though for profile 4, $b_4 = 1$ is used. Furthermore, as noted by Lessen & Singh (1973), some of the non-dimensional numbers differ from traditional definitions; we believe this is a source of some of the minor discrepancies observed in the comparison below.

The plot presented in Morris (1976) of damped modes ($n = 0$, $Re = 80$, $\hat{\omega} = -0.2$) compares favorably with our calculations. Using 400 nodes, and a domain size of $R_{out} = 10R$, Figure 4.3 shows the eigenvectors calculated for the four eigenvalues satisfying $0 \leq \hat{\alpha}_r \leq 1$, $0 \leq \hat{\alpha}_i \leq 2$. These results compare favorably, in a qualitatively sense, with results from several previous studies; Mollendorf & Gebhart (1973) studied the spatial stability characteristics of thermally buoyant jets. Initial results for a uniform density jet at similar Re and ω found an eigenvector that closely resembles the most stable eigenvector from Figure 4.3.

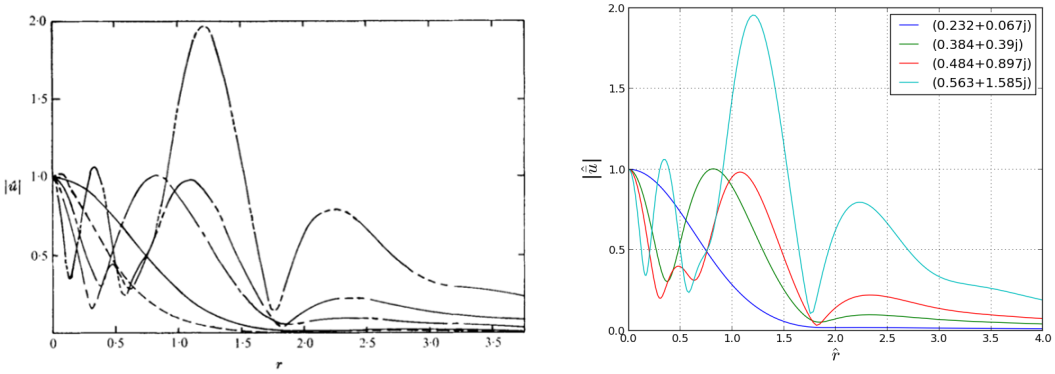

(a) (b)

Figure 4.3: Eigenfunctions corresponding to four eigenvalues identified by Morris (1976) (results are normalized such that function has the value 1 at $\hat{r} = 0$); left: original plot from Morris (1976), right: results from the current study

The eigenvalues that correspond to the eigenvectors shown in Figure 4.3 are displayed in Table 4.1, with the current results side by side with those of Morris (1976).

To provide further validation, we computed the value of the most unstable mode as a

Morris (1976)		Current study	
$\hat{\alpha}_r$	$\hat{\alpha}_i$	$\hat{\alpha}_r$	$\hat{\alpha}_i$
0.2322	0.0666	0.23248366	0.06659581
0.3840	0.3904	0.38379811	0.39048067
0.4842	0.8976	0.48396263	0.89729115
0.5628	1.5850	0.56341682	1.58520790

Table 4.1: Eigenvalues from Morris (1976) compared to those from the current study ($n = 0$, $Re = 80$, $\hat{\omega} = -0.2$, $R_{out} = 10$, 400 nodes)

function of $\hat{\omega}$ at several Reynolds numbers. Figure 4.4 present the results for $n = 0$ and $n = 1$ that we obtained under jet conditions similar to those in Figure 4.3. These plots also compare favorably to comparable plots from Morris (1976).

Figure 4.5 provides a more thorough look at the $n = 1$ results; the contour plot of $-\alpha_i$ over a range of Reynolds numbers and $\hat{\omega}$ once again compares favorably to Morris (1976). It is worth noting that for large Reynolds numbers, the $\hat{\omega}$ corresponding to the maximum value of $-\hat{\alpha}$ remains constant.

Recall that velocity profile 4 (4.8) corresponds to that of a fully developed jet. Perhaps the more pertinent velocity profile is profile 2 (4.4), for which we can also validate our results. Figure 4.6 displays our results for both $n = 0$ and $n = 1$ modes, both of which appear identical to their counterparts from Morris (1976).

4.4.1 Resolution Study

In order to ensure we are using a sufficient number of nodes, we conducted a resolution study of our results. Since the momentum thickness is inversely related to the Reynolds number, it is worth investigating a relatively large Reynolds number. If the resolution is adequate to resolve a very thin boundary layer, it will be adequate for lower Reynolds numbers and thicker boundary layers. This study was conducted using a flow profile with a Θ/R value of approximately 0.04. Figure 4.7 shows the convergence of the value of $-\hat{\omega}$ where the peak $\hat{\alpha}$ occurs for a constant viscosity flow where the domain size $R_{out} = 10R$.

As shown in the figure, 150 nodes can be thought of as the bare minimum to obtain accurate results. At 250 nodes, the results appear to reach a very consistent value. It is

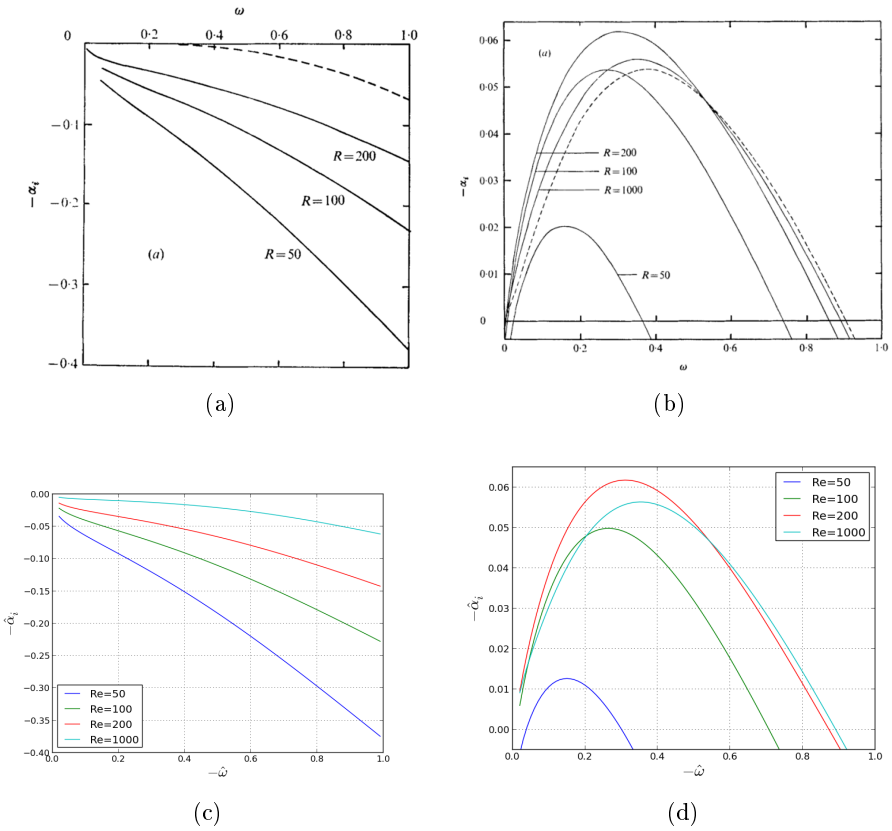

Figure 4.4: Plots of $-\hat{\alpha}_i$ corresponding to the most unstable eigenvalue for four different Reynolds numbers for velocity profile 4 (200 nodes); left: $n = 0$, right: $n = 1$; top: original plots from Morris (1976), bottom: results from the current study

expected that for larger values of Θ/R, fewer nodes may be needed.

4.5 Results

At first glance, the stability problem laid out by the stability equations has a huge number of degrees of freedom. The concentration and velocity profiles each essentially have an infinite number of degrees of freedom. Additionally, there are the non-dimensional numbers describing the flow: the Reynolds number and the Péclet number. Furthermore, there are the two real numbers in the disturbance equations (4.12): the circular frequency, $-\hat{\omega}$, and the azimuthal mode number n. Computationally, we also have the resolution, N and the domain size R_{out}. Finally, there is the relationship between the concentration, c, and the

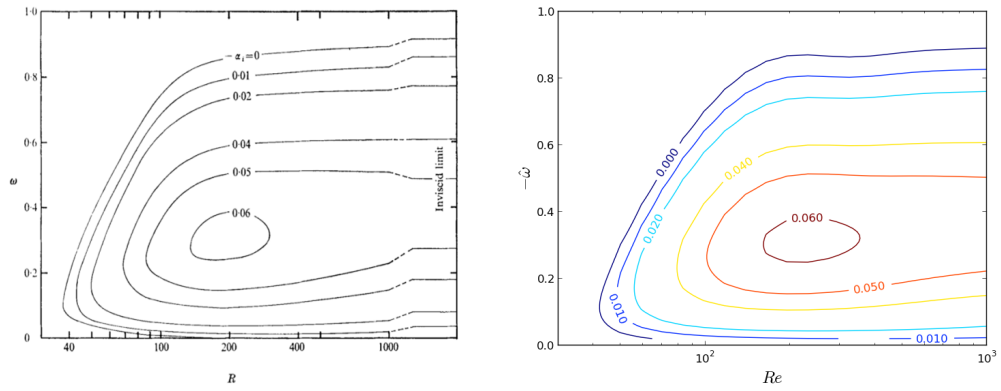

(a) (b)

Figure 4.5: Contour plot of the most unstable $-\hat{\alpha}_i$ versus $-\hat{\omega}$ and Re (200 nodes, $n = 1$); top: original plot from Morris (1976), bottom: results from the current study

viscosity, μ.

Taken together, the parameter space is overwhelmingly extensive. It is necessary to find sensible ways to limit its range to make investigation of this space tractable.

First, we can restrict ourselves to a class of problems looking at large Reynolds numbers. In this case, there is a common velocity profile used by a number of investigators for axisymmetric flows. Recall that Michalke (1984) discusses a "profile 2" that has been used by numerous authors:

$$U = 0.5\left\{1 + tanh\left[b_2\left(\frac{R}{r} - \frac{r}{R}\right)\right]\right\} \tag{4.48}$$

where

$$b_2 = 0.25\frac{R}{\Theta} \tag{4.49}$$

where Θ represents the momentum thickness, which needs to be defined.

Initially, for simplicity, we will define the concentration profile to have the same form as the velocity profile (profile number 2), and we will take the Péclet number equal to the Reynolds number (that is, the Schmidt/Prandtl number is unity). The non-dimensional profile will vary from 1.0 to C_a at the far boundary, and we will investigate the effect of varying C_a. While the viscosity may be an arbitrary function of concentration, our

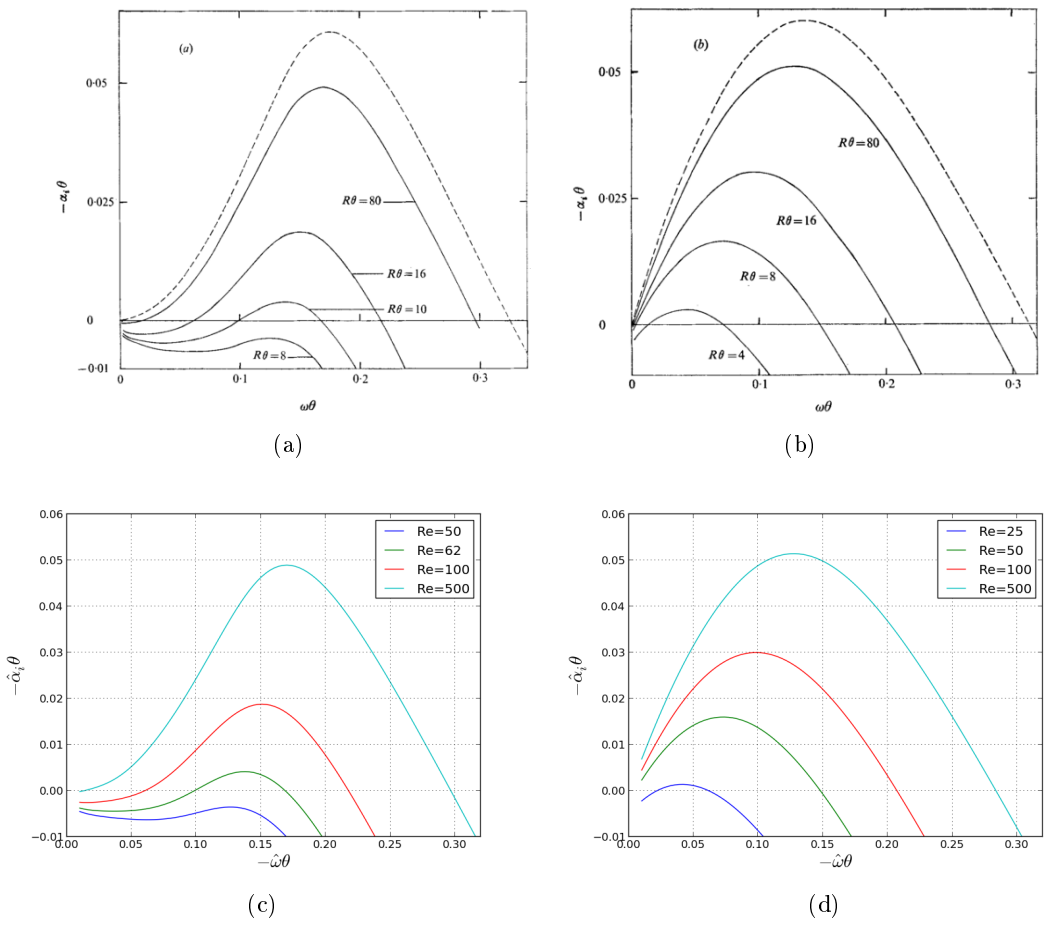

Figure 4.6: Plots of $-\hat{\alpha}_i$ corresponding to the most unstable eigenvalue for four different Reynolds numbers for velocity profile 2, $\Theta/R = 0.16$, (200 nodes); left: $n = 0$, right: $n = 1$; top: original plots from Morris (1976), bottom: results from the current study

investigation will begin by assuming $\hat{\mu} = \hat{c}$.

4.5.1 Concentration Gradient

To this point, we have assumed equivalent thicknesses for both the momentum and concentration gradients, defined by equation (4.52). We want to examine the effect of changing the thickness of the concentration gradient. Figure 4.8 shows the effect of varying Θ_C on the stability characteristics of a flow with $Re_d = 8450$, $C_r = 0.5$. Of course, out of the range of Θ_C investigated, under the jet circumstances, the effect on both the frequency and the

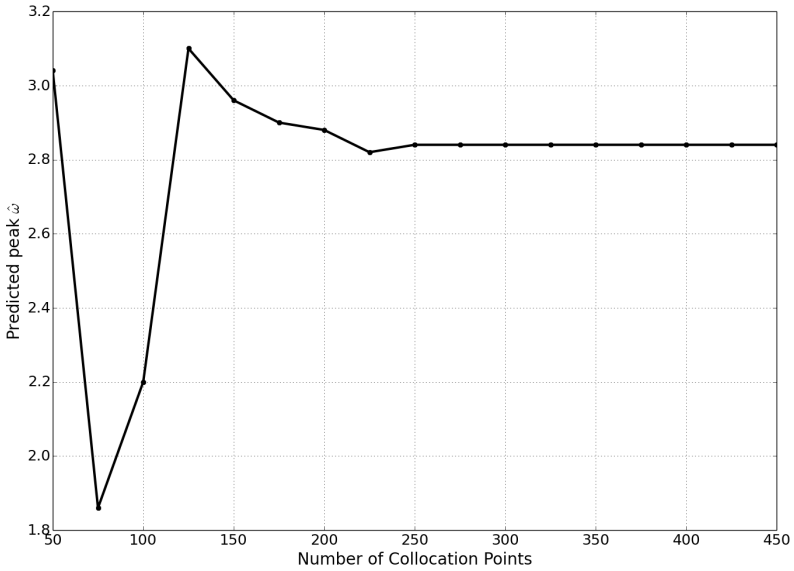

Figure 4.7: Graph of $-\hat{\omega}$ at which the maximum instability occurs versus the number of collocation points ($\Theta/R = 0.04$, $R_{out} = 10R$, $C_r = 1$, $n = 0$)

magnitude of instability appears negligible.

4.5.2 Reynolds Number

Our PIV data in Chapter 3 shows an insensitivity of results versus Reynolds number (for the constant viscosity jet), however this does not in itself imply that the instability will be insensitive to Reynolds number. In fact, comparing the exteriors of different Reynolds number flows (refer back to Figure 3.32), the onset of turbulence at the lower Reynolds number is delayed. We also see the familiar scaling of the turbulent structures, with smaller, finer features corresponding to the high Reynolds number jet. Without the non-dimensional time scaling of the PIV images (see (3.22)), the measured velocities would in fact be dependent on Reynolds number.

Since the velocity profile has an effect on the $-\hat{\omega}$ of maximum instability, it is natural to conclude that Θ should be independent of Re. Indeed, Crighton & Gaster (1976) proposed the following relationship between Θ/R and z/d (subsequently used by Plaschko (1979) and

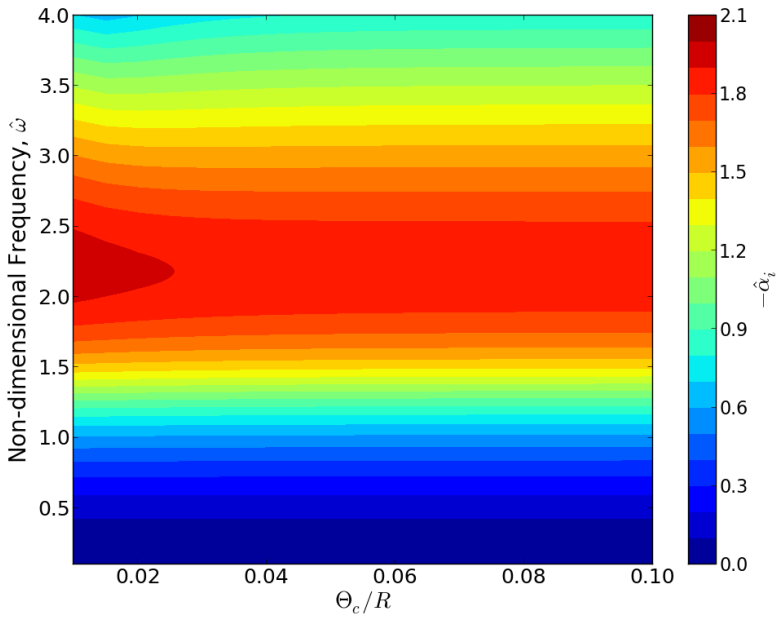

Figure 4.8: Contour plot of the most unstable eigenvalue, $-\hat{\alpha}_i$, as a function of the concentration thickness, Θ_C/R, and the frequency, $-\hat{\omega}$ ($Re_d = 5000$, $C_r = \mu_r = 2.0, \Theta/R = 0.05$)

Michalke & Hermann (1982)), independent of Reynolds number:

$$\frac{\Theta}{R} = 0.06\frac{z}{d} + 0.04 \tag{4.50}$$

However, not only does this relationship generally only hold for $z/d > 1$ (further downstream than we are typically interested in), it does not reduce the degrees of freedom of the problem; it merely substitutes z/d for Θ/R. Indeed, more recent work by Cohen & Wygnanski (1987) found a non-linear relationship upstream of $z/d = 1$, though downstream results still agree with Crighton & Gaster (1976) (see Figure 4.9).

However, our limited experiments indicate a Reynolds number dependence. This seems to agree with observations in Crow & Champagne (1971), which notes that the rippling immediately downstream of the nozzle exit shows a Reynolds number dependence. Also, Hussain & Kaman (1981) noted a dependence of coherent structures on Reynolds numbers

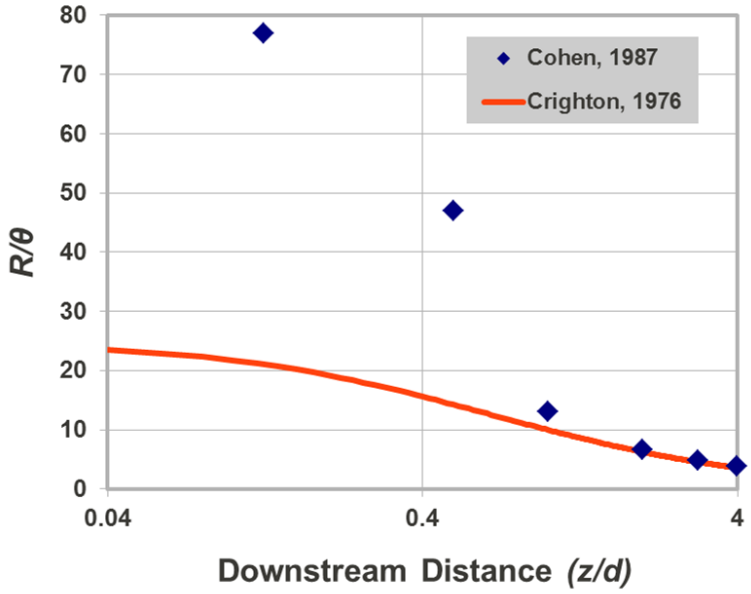

Figure 4.9: Comparison of R/Θ versus downstream distance (z/d) relationships from Crighton & Gaster (1976) and Cohen & Wygnanski (1987)

at higher Re_d flows (55,000). It is generally observed that Reynolds number independence becomes compromised with decreasing Reynolds number, so at our current conditions, certain Reynolds number dependence remains.

Rather than relating the length scale to z/d, Becker & Massaro (1968) presented a correlation between the displacement thickness at inflow, δ and Reynolds number for their converging nozzle (which was designed to produce a top-hat profile):

$$\frac{\delta}{d} = \frac{0.9}{\sqrt{Re_d}}. \tag{4.51}$$

Let us presume that at a given downstream distance, the momentum thickness value Θ is proportional to (4.51). If we take $\Theta \approx 8\delta$ (selected to obtain favorable agreement with experimental results measured at $z/d = 0.5$), the equation becomes:

$$\frac{\Theta}{R} = \frac{14.4}{\sqrt{Re_d}} = \frac{7.2}{\sqrt{2Re}}. \tag{4.52}$$

This allows us to completely define the velocity profile at a given Re, reducing our parameter space. Figure 4.10 shows a subtle dependence of the most unstable $\hat{\omega}$ on Reynolds number, where Re_d is dependent on Θ/R according to (4.52).

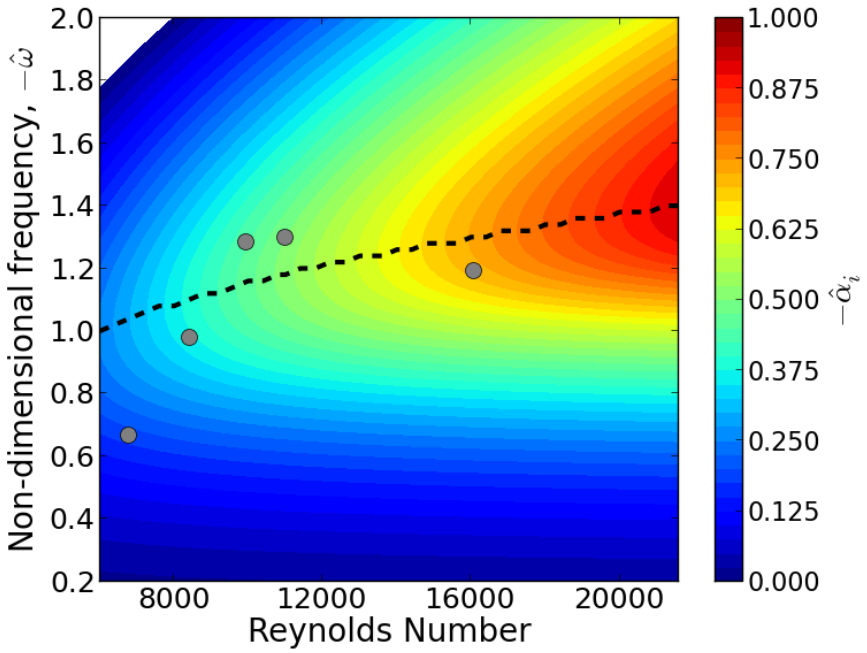

Figure 4.10: Contour plots of the most unstable $-\hat{\alpha}_i$ versus $-\hat{\omega}$ and Re_d; dashed line indicates maximum value of $-\hat{\alpha}_i$ at a given μ_r (with points representing experimental results)

4.5.3 Viscosity Ratio

As a preliminary examination of the effect of viscosity gradients on the stability characteristics of the jet, let us reproduce Figure 4.6 but this time with concentration gradients (both $C_r = 0.5$ and $C_r = 2.0$) present. Note that we mentioned that Θ is a function of Re, but to make the comparison more straight-forward, we will first produce results for $\Theta/R = 0.16$ in Figure 4.11.

We extend the range of concentration ratios to investigate in an attempt to uncover a dependency on the viscosity gradient. Figure 4.12 is a contour plot of $-\hat{\alpha}_i$ over several

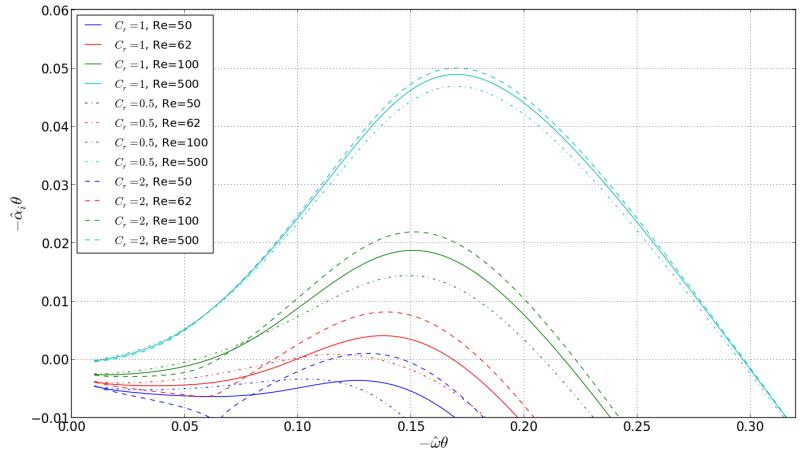

(a)

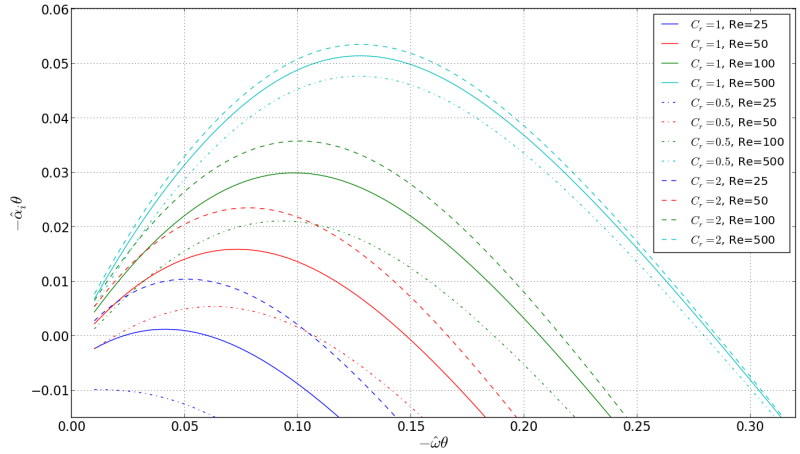

(b)

Figure 4.11: Contour plots of the most unstable $-\hat{\alpha}_i$ versus $-\hat{\omega}$ and Re_d (200 nodes); (a) $n = 0$, (b) $n = 1$

decades of viscosity ratios. Despite the extent of the study, we do not observe a significant trend in either the frequency or the magnitude of the peak instability. Isolated from other variables, varying the concentration gradient alone does not produce the types of behavior we have observed experimentally.

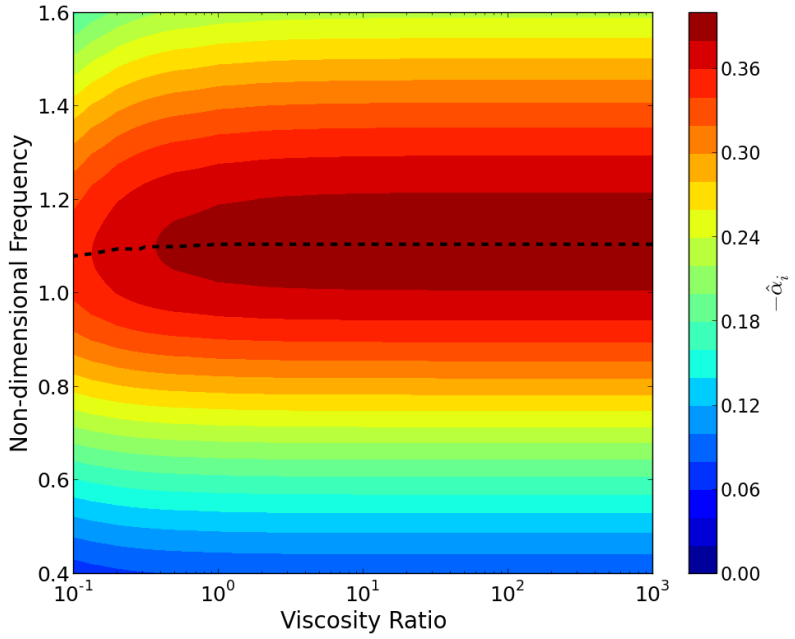

Figure 4.12: Contour plot of $-\hat{\alpha}_i$ versus $-\hat{\omega}$ and μ_r ($Re_d = 8450$, $\Theta_c = \Theta = 0.16R$)

4.5.4 Viscosity/Concentration Relationship

4.5.4.1 High Viscosity Jet

In order to create a jet with a higher viscosity than the ambient water, we used a glycerin/water solution. This high viscosity jet has the advantage of being soluble in the surrounding water. The jet's density, however, is higher than that of the ambient water, due to glycerin's higher density. For instance, a 2 cP jet at 25°C is approximately 7% denser than water.

Sheely (1932) reported the fluid viscosity across the entire range of glycerin/water mixing ratios, from pure water to pure glycerin. This was used as a guide for producing our own liquids at desirable viscosities. A digital viscometer (NDJ-5S, Rinch Industrial Company, Shanghai, China) was used to confirm the viscosity of our glycerin/water solutions prior to injection.

Cheng (2008) developed an equation for viscosity as a function of mass fraction of glycerin (C_m) and temperature (T, in °) that we made use of in our stability code. It is defined as:

$$\mu = \mu_w^{\alpha} \mu_g^{1-\alpha} \tag{4.53}$$

where

$$\begin{aligned} \alpha &= 1 - C_m + \frac{abC_m(1-C_m)}{aC_m + b(1-C_m)} \\ \mu_w &= 1.790 \exp\left(\frac{(-1230-T)T}{36100+360T}\right) \\ \mu_g &= 12100 \exp\left(\frac{(-1233+T)T}{9900+70T}\right) \end{aligned} \tag{4.54}$$

and

$$\begin{aligned} a &= 0.705 - 0.0017T \\ b &= (4.9 + 0.036T)a^{2.5} \end{aligned} \tag{4.55}$$

The validity of this equation compares very favorably to the results from Sheely (1932). Figure 4.13 illustrates the quality of the agreement.

4.5.4.2 Low Viscosity Jet

The experimental setup used heat exchangers to increase the temperature of the water (thereby lowering its viscosity) in a manner identical to that described in section 3.3.4.2. Also described in that section is the equation used to determine water viscosity from Cheng (2008):

$$\mu_w = 1.790 \exp\left(\frac{(-1230-T)T}{36100+360T}\right). \tag{4.56}$$

Armed with the equation for μ_w, the stability equations can be evaluated simply by swapping out concentration (C) for temperature (T).

Figure 4.14 shows the calculated stability over the range of $\mu_r = \mu_a/\mu_j = 0.5$ to 2 using the concentration/temperature relationships for hot water (for $\mu_r > 1$) and glycerin (for $\mu_r < 1$). Still, the stability characteristics appear quite insensitive to μ_r. The behavior is

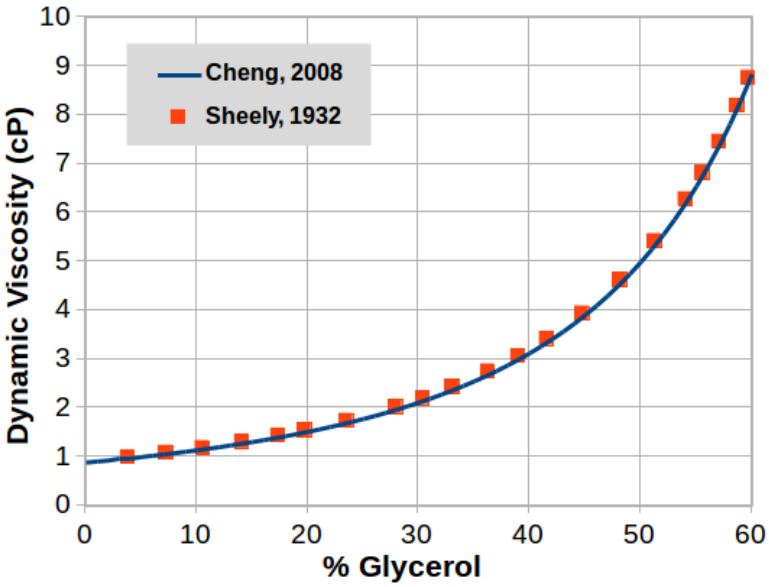

Figure 4.13: Comparison of model prediction from Cheng (2008) and experimental results of Sheely (1932) of glycerin/water mixtures at 25°C

very similar to the stability behavior from Figure 4.12. Again, the effect is not as pronounced as we expected. We must consider other effects that viscosity may have; in the next section we discuss the effect that viscosity has on the velocity profile.

4.5.5 Velocity Profile

Our analyses to this point have not shown much dependence on viscosity gradients. However, this disagrees not only with previous investigators, but also observations from our own experiments. We have to this point ignored the viscosity gradient's effect on the velocity profile, in an attempt to isolate the effect of the concentration fluctuations' influence on the jet's stability. Apparently, the effect is relatively minor. Previous investigators have incorporated the effect of the viscosity gradient on the velocity profile; we must conclude that this is the main driver of stability modification.

Several previous investigators investigating the effect of viscosity on (temporal) instabilities have benefited from a confined flow such that the velocity can be analytically determined

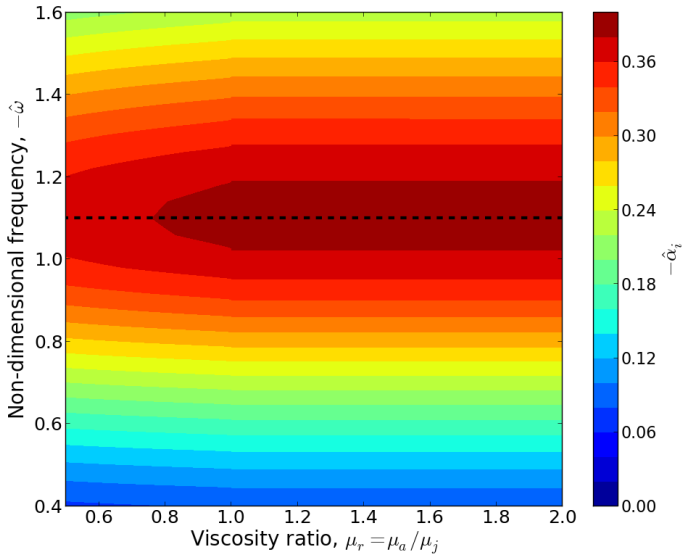

Figure 4.14: Contour plot of $-\hat{\alpha}_i$ versus the frequency and viscosity ratio, where the concentration-viscosity relationship is defined according to equations (4.53) and (4.56)

as a function of the velocity profile (see Yih (1967), Ern et al. (2003), Selvam et al. (2007)). We do not have the benefit of being able to solve for the velocity in our developing free jet problem.

For both temperature and concentration driven viscosity changes, the momentum diffusivity of our problem is approximately an order of magnitude larger than the respective concentration diffusion (e.g. Prandtl number of water is approximately 7). Therefore, let us assume that the concentration profile will be significantly narrower than the velocity profile. For the purpose of calculating the velocity profile, we will simplify the problem by assuming a discontinuous concentration profile where

$$c = \begin{cases} c_j, & r \leq R \\ c_a, & r > R \end{cases} \tag{4.57}$$

As before, we will set $\mu = c$ for simplicity. We will, however, omit the concentration equation from our stability calculations, as we are assuming the instabilities are driven primarily by

the velocity profile. For lack of experimental guidance, we will conceive a velocity profile by modifying profile 2 (equation (4.4)).

Because of our discontinuous concentration profile, we will define the new velocity profile in a piece-wise sense, inside and outside of $r = R$. On either side of R, the velocity profile will be defined by profile 2, with an appropriate value of b_2. We will assume the jet fluid side still has a value of Θ_j defined by the Reynolds number. Considering it is pulling up the ambient fluid, the ambient fluid velocity profile must match both the velocity and the shear stress at $r = R$. The velocity will automatically match, since $U(R) = 0.5$ for any value of b_2. In order to match the shear, we must satisfy, as r approaches R from either direction:

$$\mu_j \frac{dU_j}{dr} = \mu_a \frac{dU_a}{dr}. \tag{4.58}$$

The derivative of the velocity profile with respect to r is

$$\frac{dU}{dr} = -\frac{0.5 b_2 (R^2 + r^2) sech^2\left(\frac{R}{r} - \frac{r}{R}\right)}{r^2 R}. \tag{4.59}$$

Evaluated at the midpoint, $r = R$:

$$\frac{dU}{dr} = -\frac{b_2}{R} = -\frac{1}{4\Theta}. \tag{4.60}$$

Therefore,

$$-\frac{\mu_j}{4\Theta_j} = -\frac{\mu_a}{4\Theta_a} \tag{4.61}$$

or

$$\Theta_a = \frac{\mu_a}{\mu_j}\Theta_j \tag{4.62}$$

Thus, the new, modified velocity profile becomes:

$$U(r) = \begin{cases} 0.5\left\{1 + tanh\left[\frac{R}{4\Theta_j}\left(\frac{R}{r} - \frac{r}{R}\right)\right]\right\}, & r \le R \\ 0.5\left\{1 + tanh\left[\frac{R\mu_j}{4\mu_a\Theta_j}\left(\frac{R}{r} - \frac{r}{R}\right)\right]\right\}, & r > R \end{cases} \tag{4.63}$$

Figure 4.15 shows the velocity profiles for various viscosity ratios.

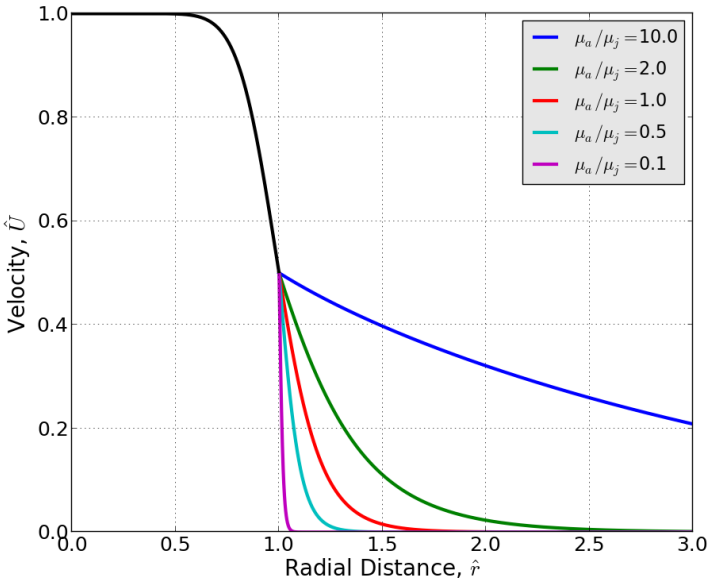

Figure 4.15: Non-dimensional velocity profiles defined by equation (4.63) for various viscosity ratios, $\mu_r = \mu_a/\mu_j$

As we mentioned, due to the small effect observed, we have omitted the equation for the concentration instability, as well as the terms for concentration in the other equations from the following analyses. The viscosity-altered velocity profiles are driving the instabilities. Figure 4.16 first shows the effect varying $\mu_r = \mu_a/\mu_j$ has on the most unstable eigenvalue as a function of $\hat{\omega}$. An interesting behavior emerges. There is a local minimum in the most unstable ω at approximately $\mu_r = 1$.

If we plot the wavenumber, $\hat{\alpha}_r$ instead, we can begin to see the wavenumber associated with the most unstable mode (see Figure 4.17).

Isolating just the most unstable wavenumber at every value of μ_r, Figure 4.18 shows how we expect the disturbances to shrink or grow as a function of the viscosity ratio. Again, there is a minimum (maximum wavelength) at $\mu_r \approx 1$.

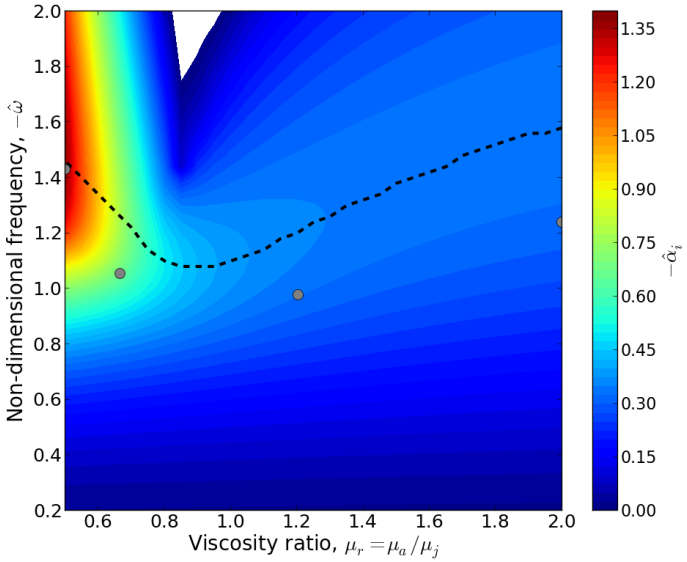

Figure 4.16: Contour plot of $-\hat{\alpha}_i$ as a function of μ_r and $-\hat{\omega}$; dashed line indicates maximum value of $-\hat{\alpha}_i$ at a given μ_r (with points representing experimental results)

4.5.6 Asymmetric Instability Mode

As stated previously, we have primarily concentrated on the axisymmetric mode. This is, in part, simply to limit the scope of our investigation to something manageable, but also, the experiments that follow in section 4.6, exhibit primarily axisymmetric instabilities. In Figure 4.19 we compare the calculated instability of the axisymmetric mode with the first asymmetric mode. Across the range of relevant viscosity ratios, the axisymmetric mode is at least marginally larger.

4.6 Experiments

4.6.1 Experimental Setup

Due to our use of liquids, we made use of dye to visualize the jet cross-section with a high-speed camera that could provide the necessary temporal resolution. PIV did not provide the necessary temporal resolution to make it an effective tool to study the instability devel-

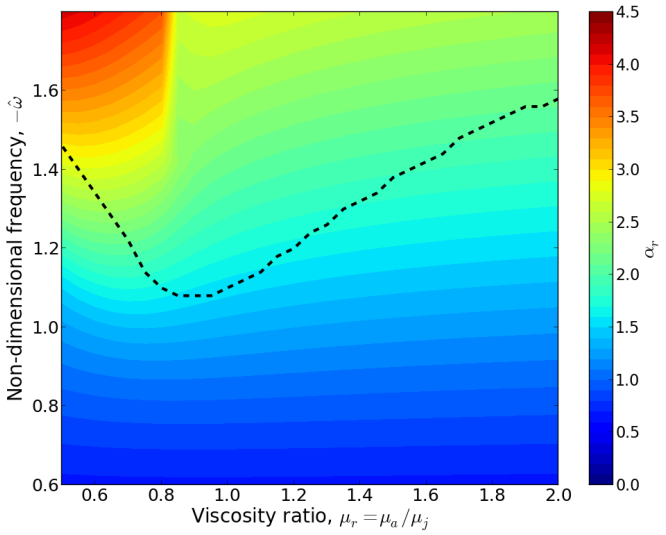

Figure 4.17: Contour plot of $\hat{\alpha}_r$ as a function of μ_r and $-\hat{\omega}$; dashed line indicates maximum value of $-\hat{\alpha}_i$ at a given μ_r

opment, and hot-wire anemometry was not available for use in liquids (hot film) to record the velocity characteristics near the jet interface.

We conducted experiments in the experimental tank which has already been described in detail in 3.3. Specifically, we used a laser plane similar to the more traditional PIV configuration outlined in section 3.3.2. There are, however, a few noteworthy differences in how the experiments were conducted. Whereas in PIV tests, we wanted the jet to be essentially opaque to the laser light, we now desire uniform illumination of the jet interior. Therefore we used significantly lower Rhodamine concentration to dye the injected fluid. Furthermore, rather than illuminating with a pulsed laser, synchronized with the MegaPlus camera, we used a 514.5 nm continuous laser (Stabilite 2017 Ion Laser, Spectra-Physics, Santa Clara, CA) that was manipulated to become a laser sheet co-planar with the jet centerline. Figure 4.20 is a photograph of the laser plane illuminating Rhodamine-dyed high-viscosity fluid above the 10 mm nozzle.

Video of the flow was captured with a high-speed camera (Phantom V12, Vision Research, Trenton, N.J.) that allowed us to record the continuous evolution of the flow. Our

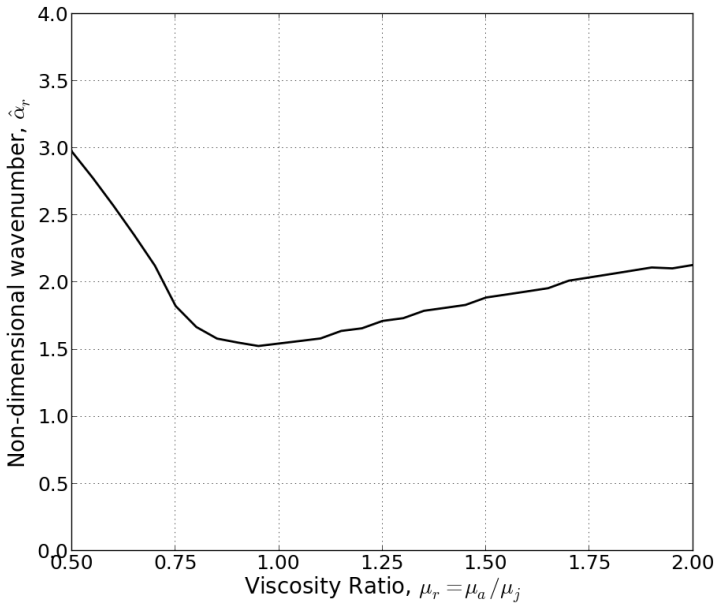

Figure 4.18: Plot of most unstable $\hat{\alpha}_r$ as a function of μ_r

experiments were imaged at between 1000 and 5000 frames per second, which provided acceptable temporal resolution for the flow rates considered.

In order to observe the frequency of the instability, we analyzed the images extracted from the high-speed video in `ImageJ`, creating individual TIFF images for each video frame. A vertical line of pixels is taken from a number of consecutive images; these columns are stacked horizontally along a time axis at a particular downstream location. Figure 4.21 shows both an example source image, as well as the result from compiling columns of pixels from approximately 500 consecutive images. The columns of the image each represent the same downstream location at successive frames from the video. Taken at, say 2000 frames per second, two adjacent pixels represent the change at the location one half millisecond apart in time. An image 500 pixels wide therefore spans 250 milliseconds of video. By counting the number of peaks or valleys at the jet edge (interface fluctuations) – in this case, approximately 38 – and dividing by the timespan, we can determine the frequency of the dominant instability to be $38/0.25\ sec = 152\ Hz$. Calculation of the non-dimensional

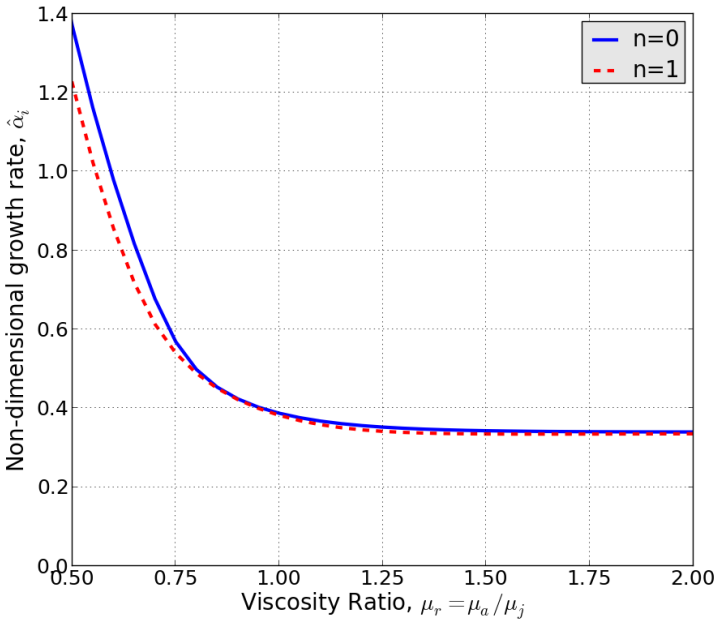

Figure 4.19: Plot of $\hat{\alpha}_i$ versus μ_r for both $n = 0$ and $n = 1$ modes ($Re_d = 8450, \Theta/R = 0.16$)

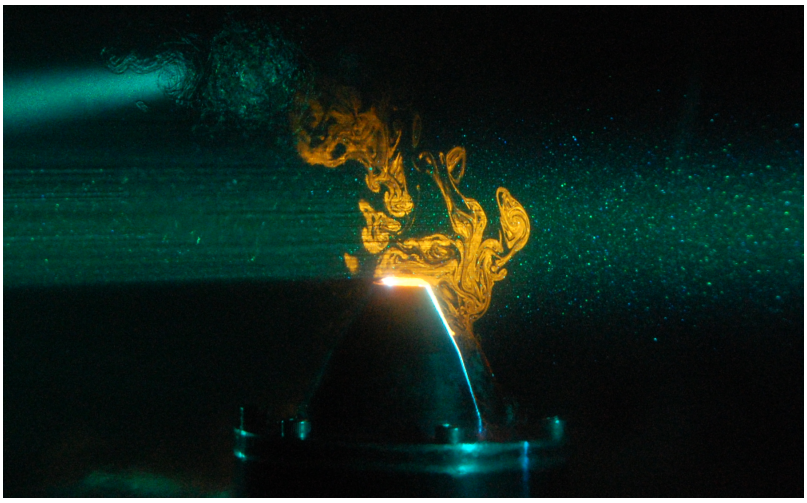

Figure 4.20: Photograph of the laser plane generated by the continuous laser illuminating Rhodamine-dyed high-viscsity fluid above the 10 mm nozzle

frequency can be made given U_j and R:

$$\hat{\omega} = \frac{\omega R}{U_j} = \frac{(152\ Hz)(0.00475m)}{0.74m/s} = 0.98 \tag{4.64}$$

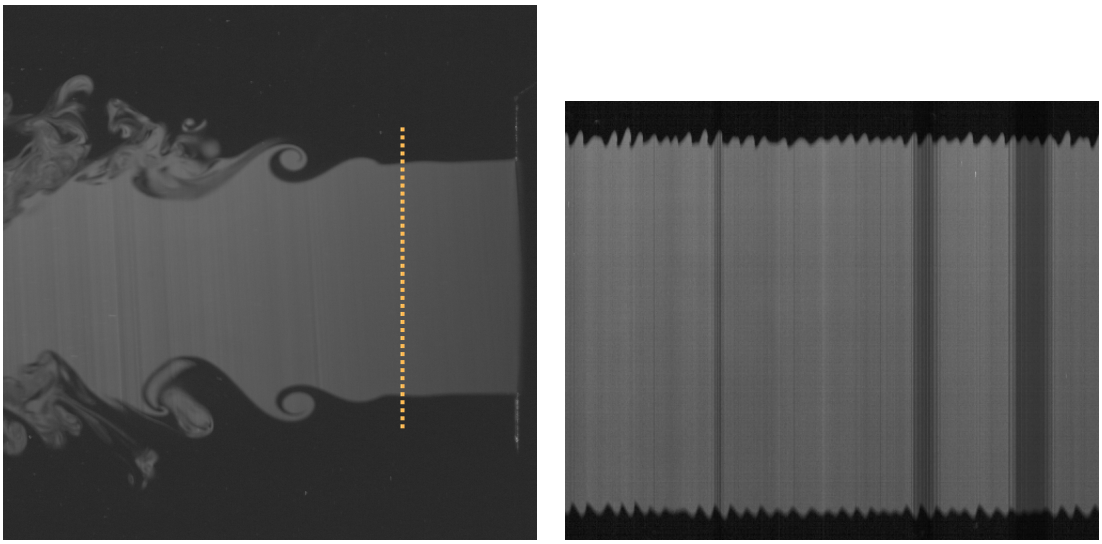

(a) (b)

Figure 4.21: (a) Single frame from the high-speed video of a stability experiment ($Re_d = 8450$, $C_r = 1$), showing $z/d \approx 0.5$, (b) Columns of pixels from 500 consecutive images grabbed from the indicated position from image (a)

Additionally, since peaks and valleys in the top of the image roughly correspond to the same phase peaks and valleys in the bottom of the image, we can conclude that the dominant disturbance is indeed axisymmetric. As Figure 4.21 makes clear, individual images from the video confirm that the instability is axisymmetric.

We conducted experiments in two main directions. First, we tested uniform viscosity jet flows at several Reynolds numbers. Then, we held the jet Reynolds number fixed ($Re_d = 8450$) and varied the viscosity ratio, $\mu_r = \mu_a/\mu_j$. The ratio was controlled by leaving the ambient fluid as water ($\sim 1\ cP$) and adjusting the viscosity of the jet. As discussed previously, low viscosity jets were achieved by heating the water, and high viscosity jets were produced by mixing the water with an appropriate amount of glycerin.

4.6.2 Reynolds Number Variation

In section 4.5.2, we discussed a likely effect of Reynolds number of the velocity profile of the jet. We have largely used equation (4.52) to define the constant-viscosity jet profile as a function of Reynolds number.

Figure 4.10 includes experimental points generated from analysis of the constant-viscosity jets. The experiments have quite a bit of scatter, but generally adhere to the magnitude and trend of the predictions. One source of uncertainty is that our frequency analysis focuses on $z/d = 0.5$, but the location of the initial instability growth may be sensitive the Reynolds number.

4.6.3 Viscosity Ratio Variation

As we mentioned, the viscosity of the jet is varied to achieve different viscosity ratios. Specifically, we heated the jet water to $\sim 55\ ^{\circ}C$ to drive the viscosity down to $0.5\ cP$ (while the density remains essentially unchanged). As interesting as it would be to explore even lower viscosities, it is difficult to achieve higher temperatures with this setup without having localized boiling, which generates many small bubbles that affect the flow stability.

On the other side, we are able to mix in glycerin to increase the viscosity to $2\ cP$. This is accompanied by a mild increase in the jet density ($\sim 6\%$ higher), which we anticipate will have little effect on stability. Higher viscosities are easy to achieve by mixing in a larger proportion of glycerin, however the density starts to be noticeably affected.

In order to maintain a constant jet Reynolds number of $Re_d = 8450$, the jet velocity is adjusted accordingly; for the lower viscosity jet, the velocity was halved, and for the higher viscosity jet, the velocity was doubled.

Figure 4.22 includes still images from the video of each jet. There are a few different observations we can make right away. First, the jet disturbances are much smaller for the high viscosity jet than either of the other jets. These disturbances do not appear to grow into vortices of the same size as both of the other jets do. The wavelength of the low viscosity jet is comparable, but slightly shorter than the jet with nearly uniform viscosity ($\mu_r = 1.2$). Second, the onset of the instability occurs further upstream for higher viscosity

jets (corresponding to lower viscosity ratios).

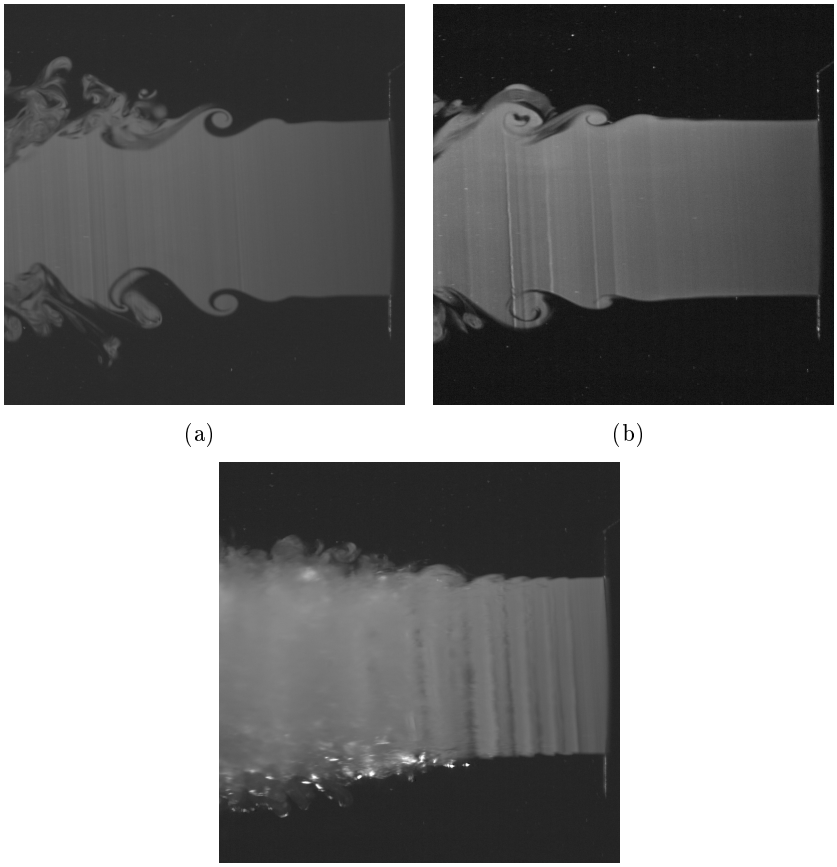

(a) (b)

(c)

Figure 4.22: Images of jets with various viscosities having Reynolds number $Re_d = 8450$; (a) $\mu_j = 0.8\ cP$ ($\mu_r = 1.2$), (b) $\mu_j = 0.5\ cP$ ($\mu_r = 2$), (c) $\mu_j = 2\ cP$ ($\mu_r = 0.5$)

Both of these observations agree with the predictions from section 4.5.5. Figure 4.16 suggests that instability growth rate increases with decreasing μ_r, consistent with our experimental findings. Figure 4.18 predicts that the most unstable wavenumber will grow (wavelength will shrink) as μ_r increases or decreases; however, it is appreciably larger for $\mu_r = 0.5$ than $\mu_r = 2$ as is the case in our experiments. Furthermore, the wavelengths for $\mu_r = 1.2$ and $\mu_r = 2.0$ are comparable in both the experiments and stability predictions.

Additionally, we took several hundred images from each video and used `ImageJ` to plot the standard deviation of the collection, based on pixel intensity. The resulting gray-scale

plot has pixel intensities corresponding to the magnitude of the standard deviations. Figure 4.23 shows the results for the three jets. It is clear that the jet with the uniform viscosity expands more quickly, and entrains more ambient fluid, than either the high or low viscosity jet.

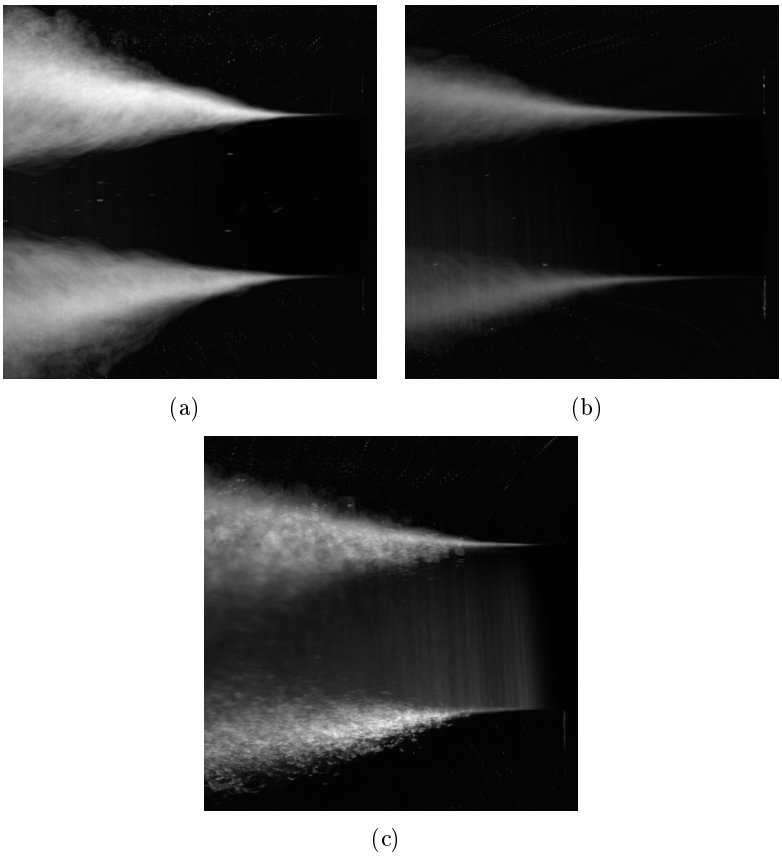

Figure 4.23: Standard deviation plot of jets with various viscosities having Reynolds number $Re_d = 8450$; (a) $\mu_j = 0.8\ cP$ ($\mu_r = 1.2$), (b) $\mu_j = 0.5\ cP$ ($\mu_r = 2$), (c) $\mu_j = 2\ cP$ ($\mu_r = 0.5$)

This behavior is consistent with previous investigators when initial engulfment is inhibited. Buratinni & Djenidi (2004) used a grid to enhance turbulence at the jet origin. The effect is to inhibit the organization of coherent structures caused by instability near the jet exit. The reduction in these coherent structures corresponds to a reduced entrainment, centerline jet decay, and radial spreading. The increase in the jet viscosity accomplishes much the same thing, because the initial disturbances are reduced in size.

4.7 Discussion

Our investigation of the viscosity gradient's role on jet stability led us to incorporate equations for the concentration distribution throughout the domain and account for its relationship to viscosity. However, by examining each parameter's effect on the stability space while holding other parameters constant, we are led to conclude that the mere presence of a viscosity/concentration gradient is not sufficient to alter the stability behavior. Rather, it is the modification of the velocity profile by the viscosity gradient that must be responsible for observed changes in the stability. Having made this observation, we can omit the concentration equations from our eigenvalue analysis, saving computational time.

The experiments and stability analysis both indicate that the modification of stability behavior on jet entrainment is at least partly responsible for the PIV behavior seen in Figure 3.36. Our analysis indicated that as the viscosity ratio is modified in either direction from (approximately) unity, the frequency and wavenumber of the initial instability both increase (see Figures 4.16 and 4.18). We hypothesize that the reduced entrainment by higher viscosity jets not only allows the centerline velocity to decay more slowly, but the surrounding fluid offers less shear resistance to the jet superlayer than equal viscosity ambient fluid in a similar Reynolds number jet. These factors contribute to the higher measured velocity of the jet turbulent/non-turbulent interface, relative to the jet core velocity.

The lower viscosity jet also exhibits reduced entrainment. Campbell & Turner (1985), concerned with naturally-occurring magma flows, conducted experiments of a low-viscosity fluid injected into a chamber of higher-viscosity fluid. Consistent with our results in Figure 4.23, they also concluded that entrainment is inhibited. However, the mixing thresholds they calculated were for much lower Reynolds numbers than the current study, and buoyancy was a significant effect.

Chhabra et al. (2005) conducted jet experiments with the ambient fluid having a viscosity 6 to 45 times greater than that of the jet. They saw reduced entrainment, also leading to elevated centerline velocities relative to the constant viscosity counterparts. From their plots of the axial velocity profiles, it appears that the velocity of the jet boundaries may decay more quickly than in the constant viscosity case. However, without knowing the position

of the turbulent/non-turbulent interface of the jet, it is impossible to tell exactly what the velocity of the jet interfacial surface is. We suggest that, it is the elevated viscous stress provided by the surrounding high viscosity fluid that causes the lower velocity to be measured by the Feature Image Correlation in Chapter 3.

4.8 Future Work

This analysis would benefit greatly from more detailed and abundant experimental data. Specifically, rather than making assumptions about the velocity profile, experiments and numerical investigations could provide more concrete guidance on the conditions to model. Without experiments, there are additional estimations for the velocity profile that can be tried. For instance, the approximations we have made for the viscosity-altered velocity profiles (section 4.5.5) do not preserve the momentum injected at the jet nozzle. While we match the shear force and velocity at the fluid interface (at $r = R$), we do not take measures to ensure that momentum is consistent among the profiles. Figure 4.24 shows profiles resulting from adjusting the interface velocity in order to conserve the flow momentum. As a result of the momentum conservation, the interface velocity increases for lower viscosity ratios, and decreases for higher viscosity ratios. This trend is consistent with the PIV observations qualitatively if not quantitatively.

Accurate velocity measurements may require experimenting with gases rather than liquids. That would open up the opportunity to use hot-wire anemometry. Alternatively, hot-film measurements could be conducted at the liquid jet edge with very high spatial resolution (the boundary layer thickness of a few hundred microns needs to be resolved with ~ 10 data points). Liquids with different viscosities typically have sufficiently different indices of refraction that PIV experiments are not accurate.

Similarly, corresponding experimentally-measured concentration profiles would also add certainty to the analyses.

The experimental setup may benefit from vibration dampening measures such as isolating the table from the ground. While it is not obvious that the experimental results were affected, our laboratory is clearly subject to vibrations from nearby traffic and heavy equipment.

Furthermore, covering a wider range of Reynolds numbers is desirable. It would be

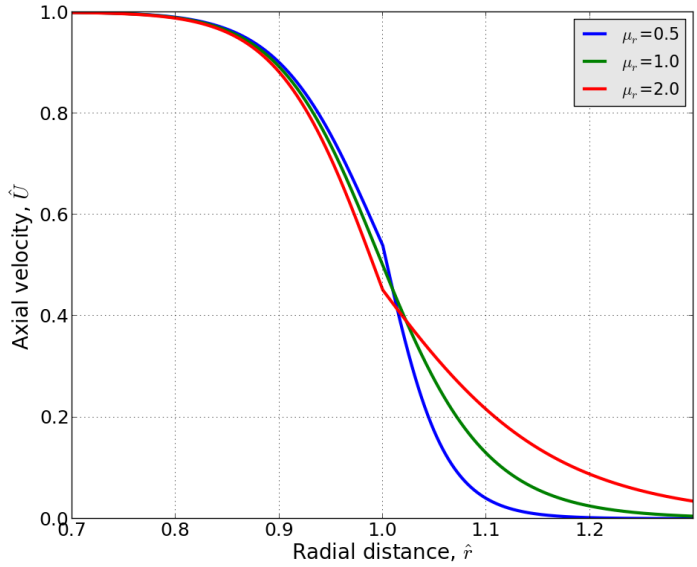

Figure 4.24: Plot of momentum-conserving velocity profiles for various viscosity ratios ($\Theta_j/R \approx 0.1$)

interesting to have results for both lower Reynolds numbers where the onset of instability is delayed, and higher Reynolds numbers where asymmetric modes may become dominant.

While engulfment is an important feature of turbulent jet flow, the downstream, smaller scale "nibbling" is seen to play a large role in entrainment (Westerweel et al., 2005). For the flows in our experiment, at large downstream distances the viscosity will homogenize due to diffusion. However, if wishing to analyze immiscible fluids with the Feature Image Correlation velocity measurement technique developed in this thesis, turbulent features farther downstream may be an important consideration. Such analyses may demand a different approximation of the velocity profile; additionally, the assumption of an axisymmetric velocity profile would likely need to be re-examined for downstream locations.

Chapter 5

CONDENSATION AT THE EDGE OF A TURBULENT JET

5.1 Nomenclature

η	Non-dimensional radius $(r/(z - z_0))$
z	Distance downstream from the nozzle
z_0	Downstream distance of virtual origin
z^*	Virtual downstream distance $(z - z_0)$
d	Nozzle diameter
U_j	Jet exit velocity
$\hat{z}$, $\hat{z}^*$	Dimensionless downstream distances $(z/d, z^*/d)$
$f(\hat{z}^*, \eta)$	Scalar value, eq. (5.3)
$f_c(\hat{z}^*)$	Scalar value along jet centerline
f_j	Scalar value at jet exit, assumed to be unity
$F(\eta)$	Dimensionless scalar value, eq. (5.1)
$\langle \cdot \rangle$	R.M.S variation of turbulent quantity
P_v	Vapor pressure
P_{sat}	Saturation pressure
Γ	Turbulent transport coefficient, eq. (5.14)
σ	Schmidt number
h_p	Specific enthalpy of a computational particle, eq. (5.18)
h_{we}	Latent heat of evaporation for water
c_{pa}	Specific heat capacity of air at constant pressure
c_{pw}	Specific heat for water vapor at constant pressure
c_w	Specific heat capacity of water
x	Mass fraction of the water (liquid and vapor)
x_l	Mass fraction of liquid water (with respect to the total particle mass)

5.2 Background

Growth of liquid droplets by condensation is an important phenomenon in many environmental and industrial applications. In a homogeneous environment, condensation will tend to narrow the diameter distribution of a poly-disperse collection of droplets. This is because, in the most basic analysis, droplet growth is proportional to the inverse of the drop radius (Squires, 1952).

The mixing driven by a turbulent flow will, however, entrain additional aerosols that will play the role of condensation nuclei, which can broaden the droplet diameter distribution. Furthermore, turbulence can have the effect of subjecting droplets in close proximity to very different local conditions leading to a different growth rate based on different histories of sampling an intermittent supersaturation field. This type of droplet size distribution broadening is critical to understanding many vapor deposition processes, including rain formation in clouds.

In order to properly understand the condensation behavior of water droplets in a turbulent flow, it is crucial to understand the dispersion of a passive scalar (e.g. temperature, water vapor), as well as that of small inertial particles. This scalar dispersion is important to understand how water vapor and temperature are dispersed, the combination of which dictates supersaturation, the main driver of droplet condensational growth or evaporation.

5.2.1 Momentum-Dominated Turbulent Jet

We have already discussed velocity statistics in section 3.2; just as Hussein et al. (1994) observed self-similarity in the velocity field, a passive scalar being emitted by the jet exhibits a self-similar nature in the developed region of the turbulent jet. Thus, the average and root mean squared (R.M.S.) of the distribution of a passive scalar, f, can be predicted at any downstream distance and radial position (Panchapakesan & Lumley, 1993b). The normalized, self-similar mean profile is typically approximated by a Gaussian function,

$$F(\eta) = \exp\left(-A\eta^2\right) \tag{5.1}$$

where we will select $A = 59$ based on Richards & Pitts (1993). We assume the centerline value, f_c, will be defined as a function of downstream distance, $\hat{z}^* = \frac{z - z_0}{d}$:

$$f_c(\hat{z}^*) = f_0 \frac{B}{\hat{z}^*} = \frac{B}{\hat{z}^*} \tag{5.2}$$

where Richards & Pitts (1993) observed B to be 4.76. In this way, the mean value of the scalar f, which has a value of unity at the jet exit and zero in the ambient environment, can be defined for any $(\hat{z}^*, \eta)$ position:

$$f(\hat{z}^*, \eta) = F(\eta) f_c(\hat{z}^*). \tag{5.3}$$

Scalar quantities with different values at the boundaries, such as ω (water vapor concentration) and T (temperature), can be related to f:

$$f(\hat{z}^*, \eta) = \frac{\omega(\hat{z}^*, \eta) - \omega_\infty}{\omega_c(\hat{z}^*) - \omega_\infty} = \frac{T(\hat{z}^*, \eta) - T_\infty}{T_c(\hat{z}^*) - T_\infty} \tag{5.4}$$

where quantities with the subscript c represent centerline values. This definition is similar to that used by Strum & Toor (1992).

While the radial variation of concentration fluctuation intensity, $\frac{\langle f \rangle}{f}$, typically is not described by an equation, it also exhibits self-similarity. We will look to the literature and interpolate quantities from Figure 5.1 provided by Panchapakesan & Lumley (1993b).

5.2.2 Condensation Mixing Model

The literature is relatively sparse regarding attempts to model the condensation and evaporation of a liquid-vapor system inside of a turbulent jet.

A notable example of modeling the condensation problem in a turbulent jet can be found in Strum & Toor (1992). The model is based on the concept of a series of ever larger continuously stirred-tank reactors (CSTR), which are a commonly used analytic tool in chemical engineering (see Figure 5.2). The jet is discretized into CSTRs in the axial, but not the radial direction. As a result, within a CSTR, the fluid conditions (e.g. particle distribution, water vapor partial pressure) are assumed to be homogeneous, though the

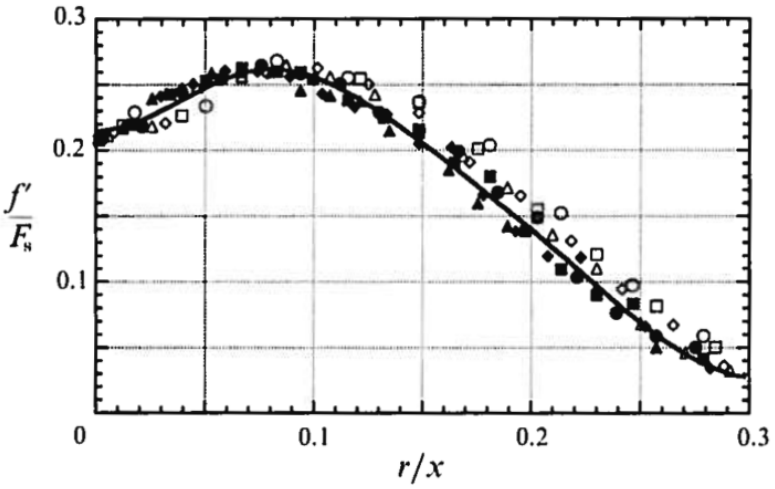

Figure 5.1: Graph of the radial variation concentration fluctuation intensity from Panchapakesan & Lumley (1993b)

contained droplets will not necessarily all have the same size. The droplet size distribution evolves with axial distance but does not depend on the radial location, a clearly incorrect assumption that implies mixing is infinitely fast and the supersaturation statistics are the same at the centerline of the jet and at the edge, for a given distance downstream from the nozzle. However oversimplified, this represented an superior use of the CSTR model compared to Friedlander (2000), which neglected even the axial dependence.

At each axial position, there are two important steps in computing with this model. The droplet population is grown (or shrunk) based on the (uniform) conditions in the CSTR section. Additionally, "dry," ambient air is entrained along with the condensation nuclei it contains. Once these tasks are performed, the entire mass is convected into the next downstream CSTR. One would expect non-uniform droplet profiles to develop due to the entrainment.

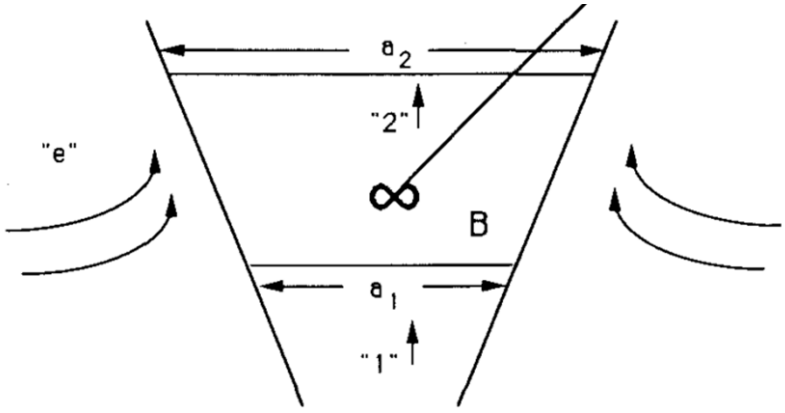

FIGURE 22. Condensation mixing model.

Figure 5.2: Figure from Strum & Toor (1992) illustrating the continual stirred-tank reactor used in the condensation mixing model

5.3 An Improved Axisymmetric, Two-Dimensional CSTR Model

5.3.1 Description

The previous CSTR-based model from the literature, with a dependence only on axial distance, represents a first step in including differential jet velocities and entrainment dependency in the mixing and condensation. A more complete model of condensation in a turbulent jet should include the radial dependence both because the mixing of droplets and entrained nuclei is not instantaneous across the jet width, and the droplets themselves are advected in the axial direction at different speeds as a function of their position along the jet radius (in the average sense).

Mixing in the free turbulent jet is dominated by eddies which intersperse fluid from otherwise disparate regions. The stretching creates elongated sheets and filaments of the fluid regions, increasing the surface area of the boundary between the regions, which allows molecular diffusion to mix more effectively. The distribution of the iso-concentration regions throughout the jet is independent of the jet Reynolds number (see Figure 5.3 from Villermaux & Innocenti (1999)). This is a necessary condition in order for self-similar profiles of mean and R.M.S. scalar values to exist independent of downstream distance and Reynolds number.

Therefore, when variations in a passive scalar in the flow are observed, it is because otherwise homogeneous regions are being increasingly subdivided and interspersed. Diffusion takes hold as the interfacial surface area is ever-increased, resulting in the continuous distribution of scalar values described by the self-similar mean and R.M.S. profiles.

As such, when discretizing the jet at a given downstream distance, it is more meaningful to discretize based on intervals in the value of the passive scalar, rather than on radial location. Indeed, the scalar at a given downstream distance and radius should not be described by a single value; there will be a distribution of values due to the nature of turbulence. Knowing the properties of each scalar region, we should be able to reconstruct the jet behavior as a function of radius, based on the self-similar mean and R.M.S. behavior of the scalar.

Based on the number density and size distribution of the droplets in a region of constant F, we can calculate the actual water vapor content and temperature based on the depletion of water vapor and release of latent heat.

We will rely on several assumptions in order to develop our model. The self-similar nature of a turbulent jet is presumed to extend upstream throughout the development region. Any negative effects due to this assumption are mitigated by the small volume and high velocity of the region. The self-similarity also holds downstream as far as the model considers active mixing and supersaturation in the axial direction along the jet; also, the buoyancy force is neglected. Knowledge about the mean value and standard deviation of F allows us to calculate the relative proportions of any number of discretized F regions at an arbitrary radius η.

An additional assumption is that droplet number density is constant throughout the field. Assuming the jet's particle concentration is approximately equal to the ambient's, then according to Friedlander (2000):

$$\frac{\partial N_\infty}{\partial t} = I_d + \left[\frac{\partial N_\infty}{\partial t}\right]_{coag}. \tag{5.5}$$

Since we are ignoring coagulation (droplets' Stokes numbers are small), and homogeneous

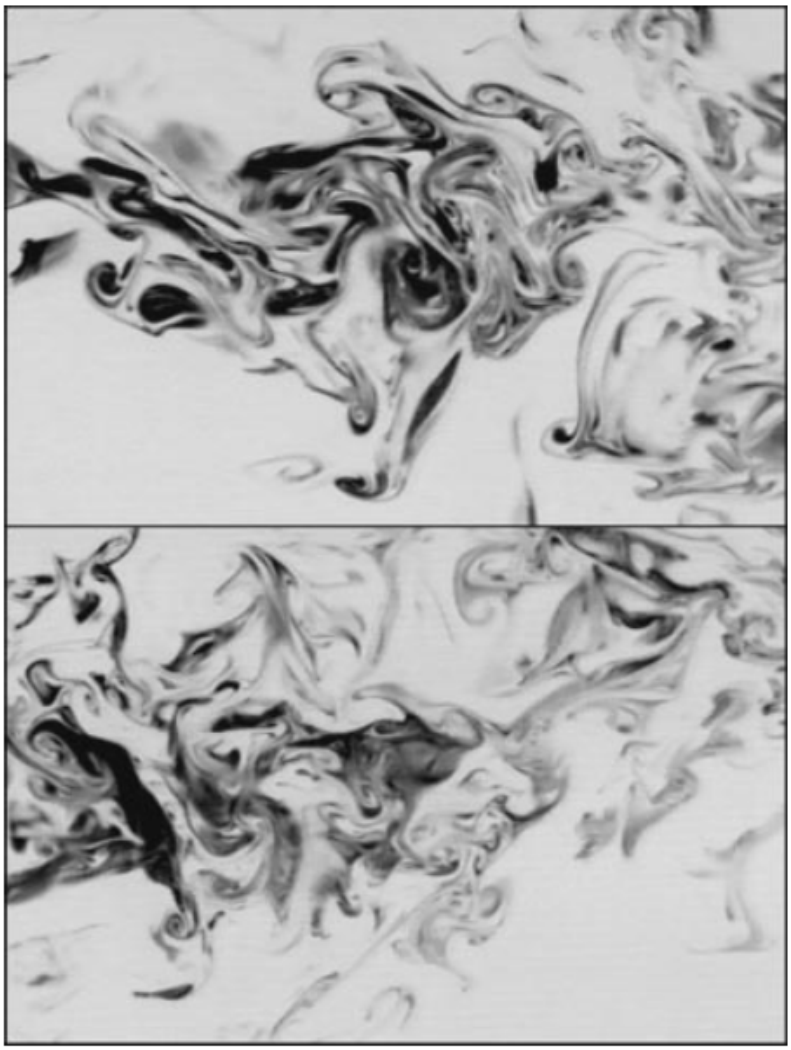

Figure 5.3: Figure from Villermaux & Innocenti (1999) illustrating Reynolds number independence of iso-concentration regions; the upper image is of a jet with half the Reynolds number of the jet in the lower image

nucleation is absent ($I_d = 0$), the result is

$$\frac{\partial N_\infty}{\partial t} = 0. \tag{5.6}$$

That is, the total number concentration is constant in time.

5.3.2 Implementation

First, at each downstream location, the jet must be discretized into regions based on their non-dimensional scalar value, each with size dF. This may represent widely difference radial width of the spatial discretization, but equal "width" in scalar value, which guarantees similar resolution of the scalar gradients, the important metric to resolve the supersaturation field accurately (equivalent to grid refinement based on the local gradient).

We know the value of the mean and R.M.S. of $F(\eta)$, but we do not necessarily know the distribution of F that yields the behavior. In order to move forward, we will assume a normal Gaussian distribution of the fluid across F at each η, given self-similar values of the mean, $F_\mu(\eta)$ and the standard deviation, $F_\sigma(\eta)$. Thus, the specific volume of a range of F, $F_2 - F_1 = dF$, is defined as

$$\nu = \int_{F_1}^{F_2} \frac{1}{\sigma\sqrt{2\pi}} e^{-\frac{(F-F_\mu)^2}{2F_\sigma^2}} dF. \tag{5.7}$$

Dividing the F domain into bins of dF, the size of each bin can be computed as a function of η. Figure 5.4 is a representation of the F distribution that can be used throughout the succeeding calculations.

The jet is discretized in the radial direction by the common non-dimensional variable $\eta = r/(z - z_0)$. This provides for a well-defined computational domain, rather than allowing the jet radius to grow without bound as downstream distances increase. Similarly, scalar discretization will proceed on the variable F. At each discretized span of η, the normalized mean value of $F(\eta)$ and its standard deviation are known a priori (as described in the previous section). Each of these annular sections in the value of F are well-mixed CSTR regions similar to the regions described by Strum & Toor (1992) (see Figure 5.2).

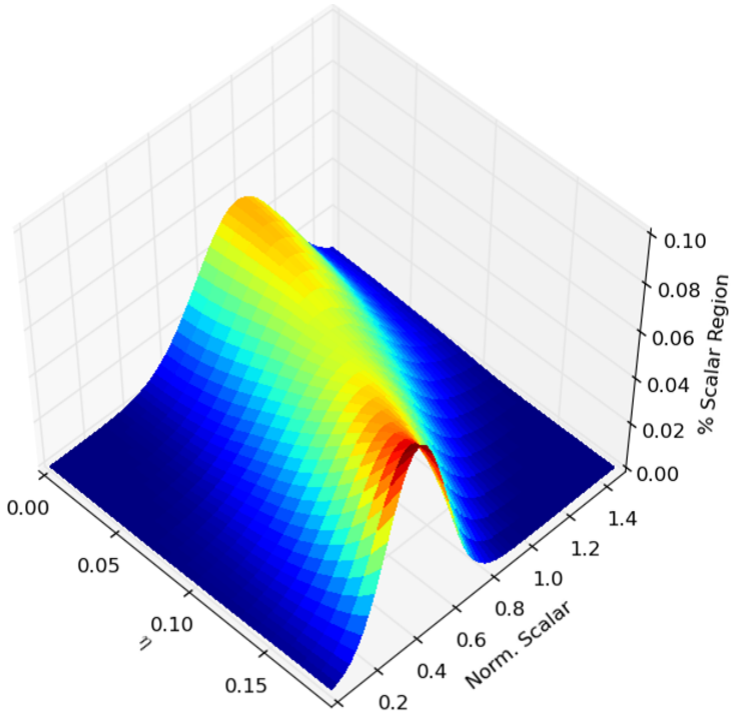

Figure 5.4: Graph of normalized proportion of scalar bin $dF = 0.03$ as a function of F value and η

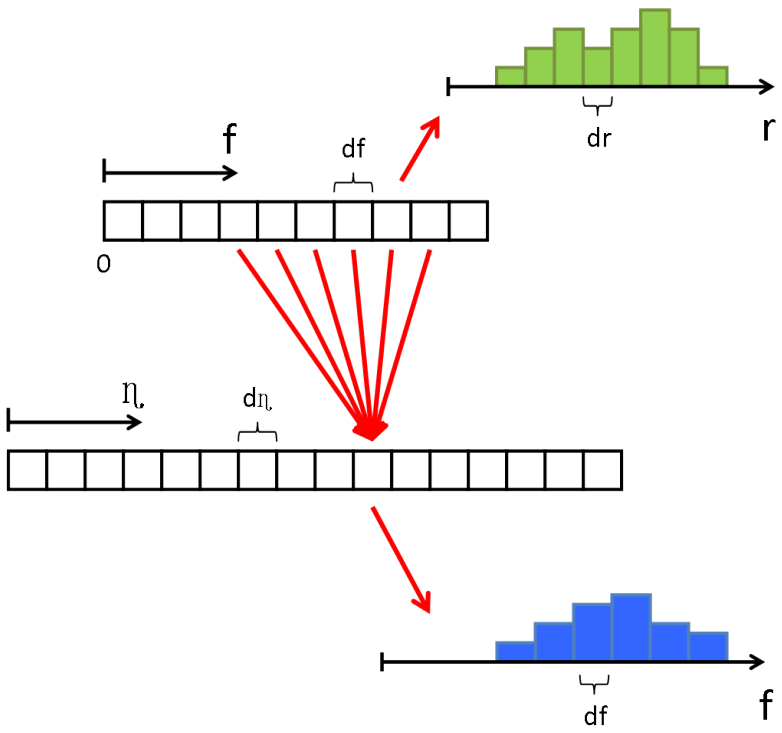

Figure 5.5: Illustration of the computational domain decomposition

Garmory & Mastorakos (2008) noted in their work studying condensation in a turbulent jet that modeling droplet diameter distribution with only a few moments may be inadequate. Therefore each discretized region dF is further discretized into droplet radius bins, dr, rather than assuming a Weibull (or other) distribution. Figure 5.5 illustrates the decomposition of the domain at each downstream distance (as opposed to Figure 5.2) where the entire axial slice is considered well-mixed and therefore described by a single scalar concentration value.

Note that each F bin exists independent of the η discretization. It is knowledge of the distribution of F (see Figure 5.4) that allows for reconstruction of the droplet distribution at each η location. That is, we assume that the droplet size distribution within a given dF bin is the same regardless of the radial position. This allows for a significant savings in computational storage and time. It can be justified by arguing that regions with similar values of F have undergone similar histories regardless of their η location.

The downstream fluid conditions in each dF bin are calculated using equations 5.3 and

5.4. The droplet diameter distributions are advanced from the previous axial position and their effect on the region's temperature (through latent heat release) and water vapor content (reduction in water vapor) is calculated. This, in turn, is used to calculate the region's local water vapor pressure using Antoine's equation:

$$log_{10}P_{sat} = A - \frac{B}{C+T} \tag{5.8}$$

where A, B and C are constants tailored to the particular gas and temperature range of concern. In the case of water vapor (Albright, 2008):

$$\begin{aligned} A &= 8.07131 \\ B &= 1730.63 \\ C &= 233.426 \end{aligned} \tag{5.9}$$

which yield P_{sat} in units of mm Hg. The vapor pressure, P_v, must be determined from the local conditions of the dF bin.

This is sufficient information to calculate the supersaturation, which is used to simultaneously integrate the system of ordinary differential equations:

$$\frac{dr_b}{dt} = \gamma \frac{ss}{r_b} \tag{5.10}$$

where

$$ss = \frac{P_v}{P_{sat}} - 1 \tag{5.11}$$

and the subscript b is the diameter bin index. In this analysis, we assume that the droplet growth will not have a significant influence on the local supersaturation conditions over the interval of time integration, dt. The time over which the integration occurs will depend on the F bin's approximate mean axial velocity, by determining $U(\hat{z}^*, \eta_1)$ given $F = F(\eta_1)$. That is, the value of dt is calculated for each dF bin:

$$dt = \frac{dz}{U(\hat{z}^*, \eta)}. \tag{5.12}$$

Once the growth of each droplet bin diameter has been determined, the new droplet distribution among the bins will be determined by interpolation, ensuring conservation of liquid water mass.

As a consequence of the jet expansion, although the $d\eta$ values will remain constant as the simulation progresses downstream, the actual volume of each discretization will continue to grow. In order for the N concentration to remain constant (see equation 5.6), droplets must be added to each $d\eta$ region. Beginning with the centerline $d\eta$, the appropriate number of droplets are moved from each dF bin contained in the next outermost $d\eta$ inward to maintain N.

The outermost $d\eta$ bin will mix in the same type of aerosol "droplets" present at the inlet. These nuclei are assumed to behave as very small particles, and they are given a nominally small, uniform diameter; in our case they are 0.1 μm. As such, we do not let drops evaporate below that threshold diameter, at which point they are assumed to have completely evaporated. This obviously ignores any effects specific to nucleation.

The values ω and T can be computed from equation 5.4. Time is marched forward by advancing in increments of axial distance, $\hat{z}$. Rather than fit a Weibull distribution, we discretize the droplet diameter distribution, organizing droplet populations into diameter bins. These will be tracked as a function of axial distance ($\hat{z}$) and radial distance (η).

The described algorithm is implemented with the Python programming language. We leveraged routines from `numpy`, `scipy` and `matplotlib` libraries (Jones et al., 2001; Hunter, 2007) to streamline the coding process.

5.3.3 Comparison with Experiments from Literature

In order to justify the model's added complexity, it was important that the model worked to adequately predict not only the diameter distribution as a function of axial distance (already well-captured the original one-dimensional model of Strum & Toor (1992)), but also to provide accurate predictions as a function of radial distance from the jet centerline.

The experiments consisted of air saturated with water vapor being injected into the ambient environment using a 1.1 cm diameter nozzle at a Reynolds number of ~ 2000. The

jet inflow in the case considered here was free of droplets and nuclei (we will look at jets seeded with droplets in section 5.4). A PDPA was used to measure the particle sizes and velocities at various radial and axial locations.

To validate the two-dimensional model, we first compared the one-dimensional evolution of the average diameter along the centerline, for increasing distance downstream of the nozzle, to the experimental measurements provided in Strum & Toor (1992). Figures 5.6 and 5.7 show the volume-averaged droplet diameter, D_{30}, as a function of axial distance, z/d, for 62 and 85 $^{\circ}C$ saturated jets. Note D_{30} is a volume-averaged diameter, while D_{10} is a simple arithmetic average of the recorded droplet diameters. The model correctly predicts the trend for the growth of particles in the unseeded case (noted as u62 and u85 in the legend of the plots). For the 62 $^{\circ}C$ jet, it provides quantitatively-accurate measures of the maximum value of the average diameter, $\sim$ 4.5 μm, and the location of this maximum, between 15 and 25 diameters downstream. It correctly captures, although exaggerating the magnitude, the decrease of the droplet size due to evaporation as the supersaturation decays with entrainment of more dry ambient air beyond an axial distance of about 25 diameters. In the 85 $^{\circ}C$ jet, the model correctly predicts the growth of droplets to a maximum of $\sim$ 7 μm, but it delays the position of this maximum to about 25 diameters downstream, rather than the 15 diameters observed in the experiments.

The next step in the validation of the model is the comparison of actual droplet size distributions, rather than the first moments, the average diameter. Figures 5.8 and 5.9 show comparisons of the droplet diameter distributions in the model (right) versus experiments (left) for downstream locations, over a wide range from $\sim 2d$ to $\sim 40d$. Both the 62 and 85 $^{\circ}C$ jets show a monotonic decrease of the percentage of small droplets and an increase in the larger droplets along the jet centerline from the nozzle to a distance of $\sim 15d$, in good agreement with the experiments. At $z/d \approx 25$, the diameter distribution shows significant flattening. The distribution of relatively large and small droplets both increase, exhibiting a bimodal behavior, while the mean droplet diameter decreases very slowly (as noted in Figures 5.6 and 5.7).

Finally, modeled droplet size distributions at various radial locations are compared side-by-side with the experimental results in Figures 5.10 and 5.11. This is the novel contribution

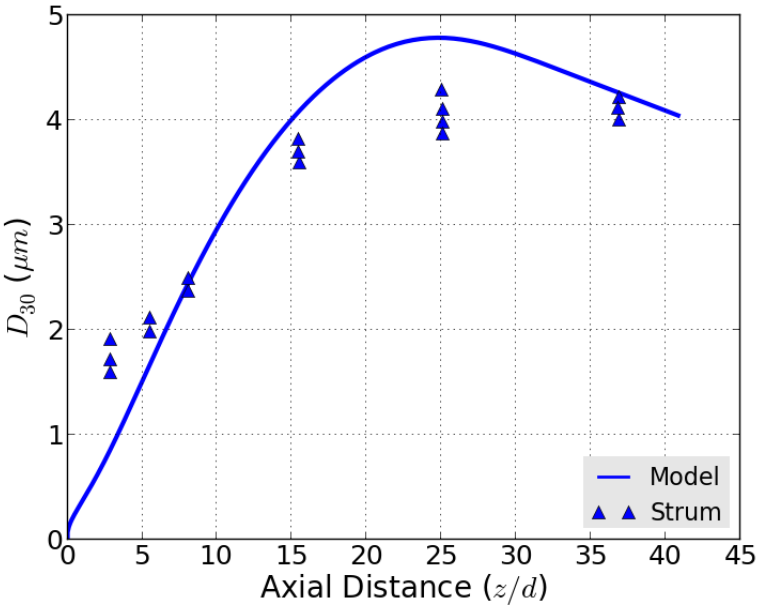

Figure 5.6: Comparison of experimental and model results of droplet diameter, D_{30}, at the jet centerline as a function of downstream distance for a saturated 62 $°C$ jet

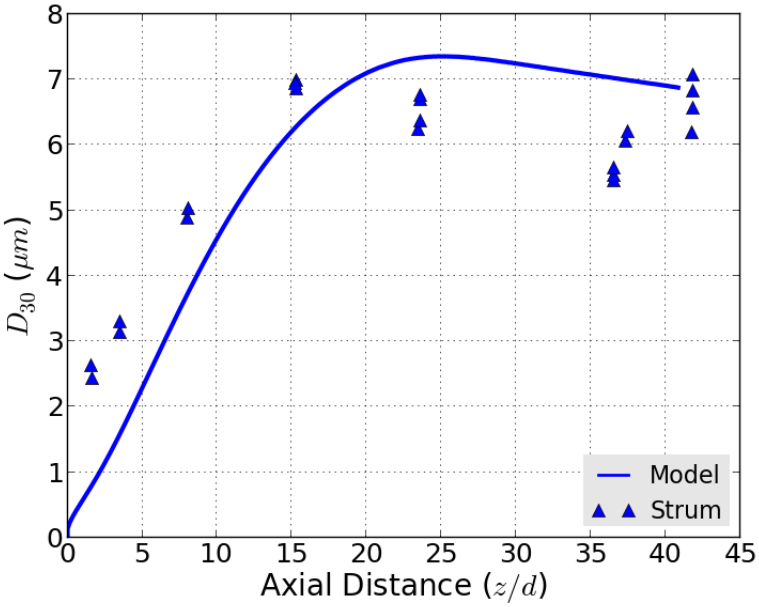

Figure 5.7: Comparison of experimental and model results of droplet diameter, D_{30}, at the jet centerline as a function of downstream distance for a saturated 85 $°C$ jet

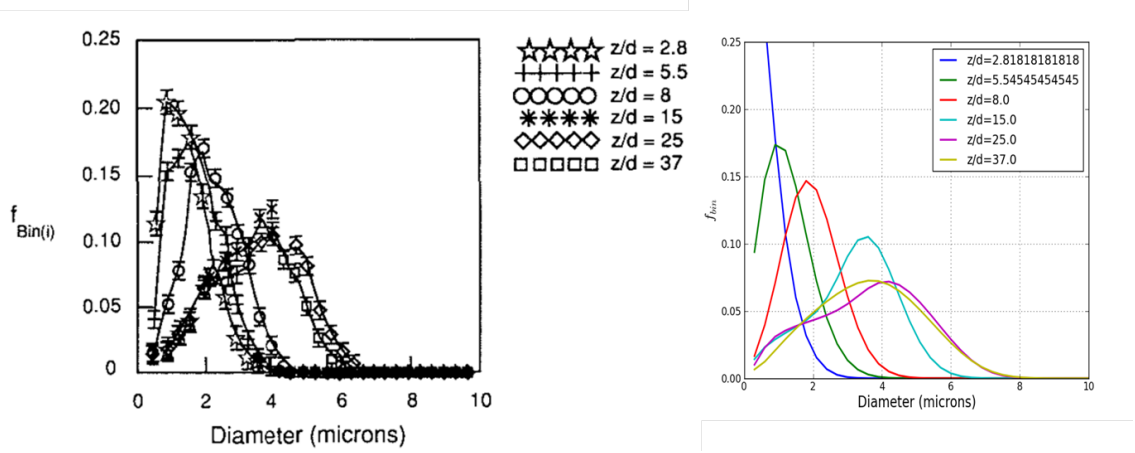

Figure 5.8: Comparison of experimental and model results of droplet diameter distribution at the jet centerline for various downstream positions for a saturated 62 $^{\circ}C$ jet

of this two-dimensional model, as the axial-only model did not discriminate between radial positions and considered the size distribution uniform along these axial slices. The results at $z/d = 1.7$ show a small inhomogeneity of the size distribution within the jet, with good qualitative agreement with the experiments. Because the measurement locations are largely within the potential core, the number of droplets being measured is quite low. Furthermore, the accuracy of the PDPA is suspect for such small droplet diameters. The plots in Figure 5.11 present a much richer behavior in which the outskirts of the jet ($r/d = 4$) have a decrease in the mode droplet number but an increase in the larger ($\sim 10\ \mu m$) and smaller ($\sim 2\ \mu m$) droplets, due to the inhomogeneity of the mixing in that region. This is similar to the behavior of the droplets near the centerline observed in Figures 5.8 and 5.9, but for much larger distances downstream ($z/d \approx 25 - 35$) where the inhomogeneity in supersaturation reaches the centerline fluid.

Thus, this two-dimensional model captures the transition from a unimodal near the jet centerline to a bimodal distribution near the mixing layer by capturing the radial distribution of supersaturation and the distinct evolution of the droplets near the edges. Both of these phenomena are important for large scale flows in which the mixing-induced inhomogeneities significantly contribute to condensation/evaporation dynamics.

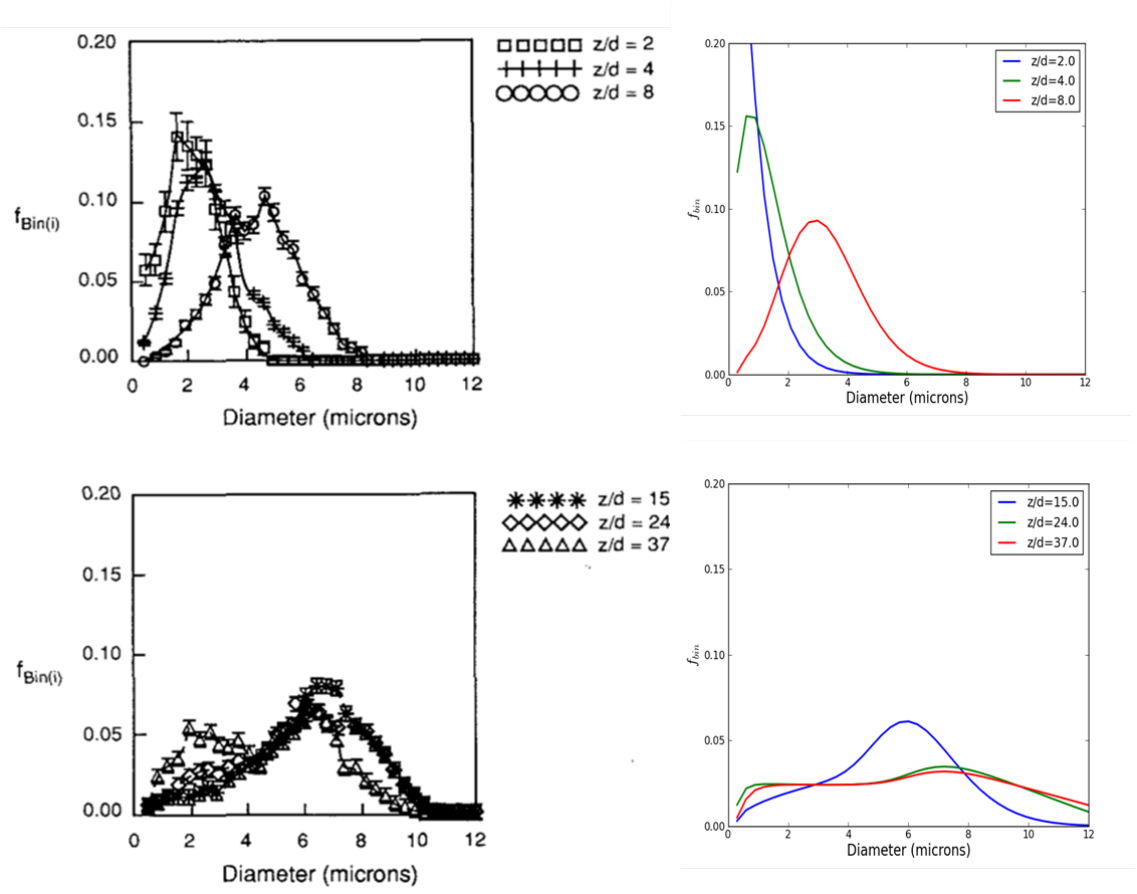

Figure 5.9: Comparison of experimental and model results of droplet diameter distribution at the jet centerline for various downstream positions for a saturated 85 $^{\circ}C$ jet

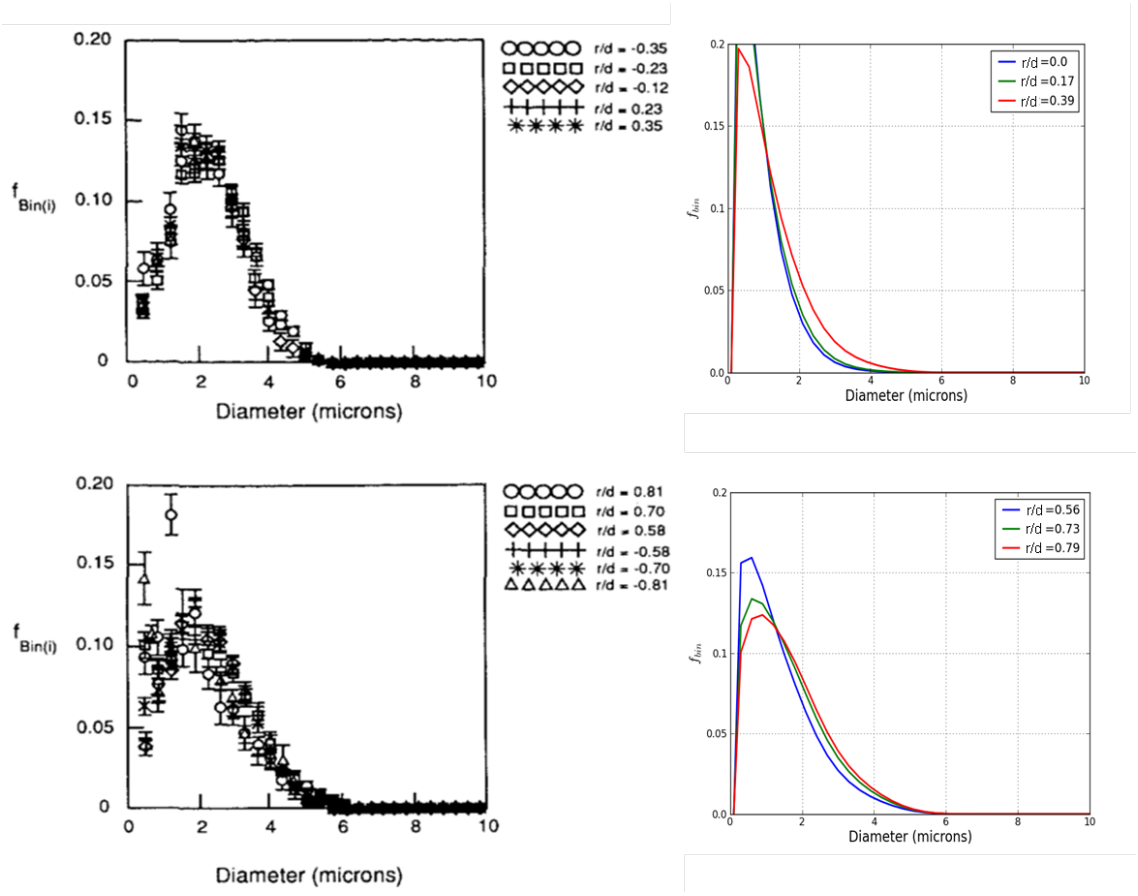

Figure 5.10: Comparison of experimental and model results of droplet diameter distribution at various radial positions at a downstream distance of $z/d = 1.7$ for a saturated 85 $^{\circ}C$ jet

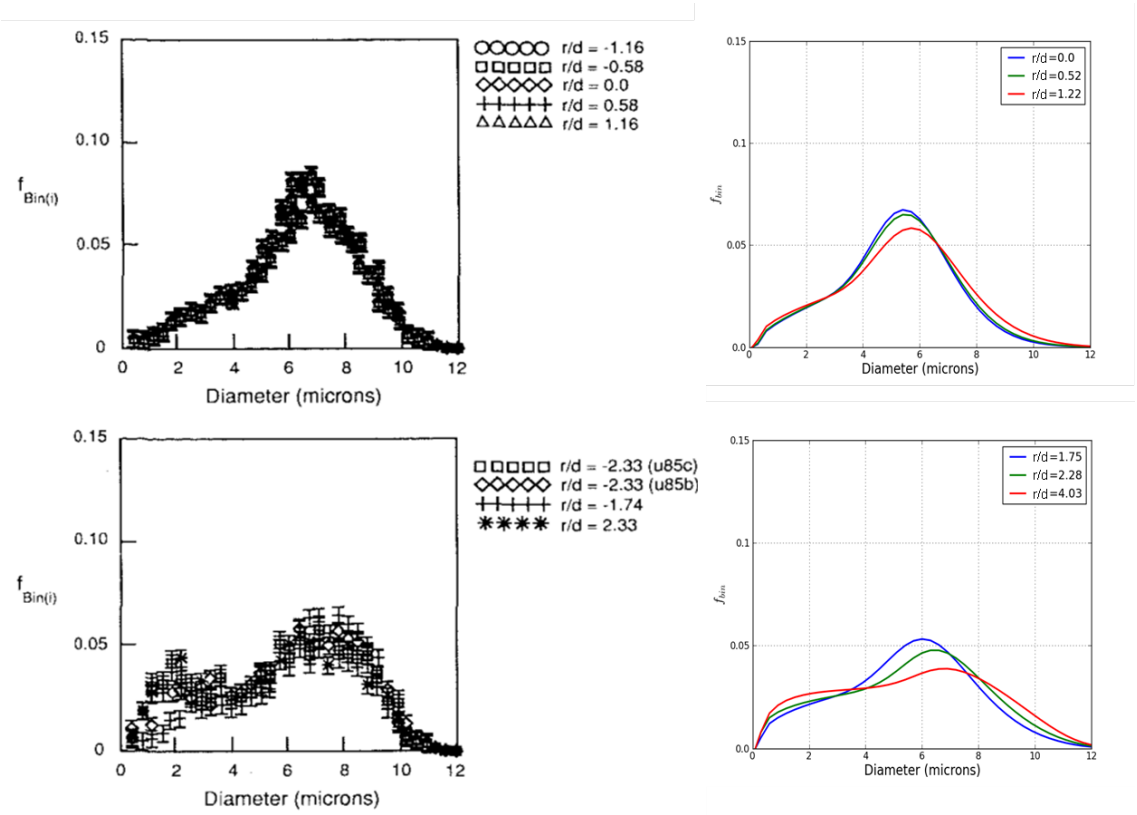

Figure 5.11: Comparison of experimental and model results of droplet diameter distribution at various radial positions at a downstream distance of $z/d = 15$ for a saturated 85 $^{\circ}C$ jet

5.4 PDF-Based Model

The two-dimensional analytic model developed in the previous section exhibits an ability to predict droplet distributions throughout the domain (both in the radial and axial directions). However, due to the numerous assumptions made, it is heavily dependent on the knowledge of the scalar concentration and velocity self-similar fields, a priori, and therefore it cannot be easily expanded to other more realistic flow configurations beyond the turbulent jet. Hence, we develop a more general model that would be flexible enough to compute droplet growth in a much wider variety of turbulent flows. We will, however, validate it using the same turbulent jet experimental data from Strum & Toor (1992) used in section 5.3.

Turbulence modeling has been a subject of great interest within the fluid dynamics community since the inception of numerical simulations. Numerical models range from fully resolving the turbulence with direct numerical simulation (DNS) to Reynolds-Averaged Navier-Stokes (RANS) models that simply calculate a few moments of the mean velocity field.

DNS models have resolution demands (in both space and time) that make moderate and high Reynolds number flows inaccessible to solve in a timely manner. In fact, when considering the mixing of particulate flows (e.g. smoke or small water droplets), the computations become even more demanding. The Schmidt numbers of such flows tend to be in the $10^5 - 10^6$ range (Dimotakis, 2005). The associated steep gradients can dramatically drive up spatial requirements, as well as the associated computational demands.

RANS models solve the closure problem by using averaged versions of the Navier-Stokes equations and utilizing models of varying complexity for the Reynolds stresses, $\overline{u_i' u_j'}$. The RANS models can make modeling efforts of high Reynolds number flows tractable, but the instantaneous fluctuations of velocities (and subsequently, any advected scalars) are omitted. When modeling non-linear behavior such as condensation or combustion, scalar averages are insufficient; the fluctuations of scalars are critically important to track.

Large-Eddy Simulations (LES) tend to serve as a compromise in both computational demands and accuracy of the two previous methods, but consequently, it suffers from both sets of drawbacks: large computational requirements and significant modeling sensitivity.

Probability density function (PDF) methods have been proposed as an alternative approach to addressing the closure problem in turbulence modeling. While it enjoys some use for velocity joint PDF modeling, it has found greater utility modeling scalar transport and chemical reactions.

Pope (1985) made a seminal contribution in proposing and discussing a solution algorithm for a composition-velocity joint PDF method. Given a velocity field with information about the turbulence characteristics, stochastic particles were evolved during each time step over a sequence of fractional steps. These fractional steps included a reaction model (for combustion, condensation, etc.), a mixing model, and finally displacement (advection/diffusion).

Muradoglu et al. (1999) formalized a hybrid Lagrangian particle/Eulerian carrier-fluid method. Like other investigators, their aim was to take advantage of the best aspects of the finite volume and stochastic particle methods while minimizing their weaknesses. In their method, the finite volume code is used to calculate the mean velocity and pressure fields. The stochastic computational particles account for the turbulent velocity fluctuations and the chemical reactions.

Veroli & Rigopoulos (2010) also tackles the condensation problem using a hybrid method. However, rather than treating the PDF of velocity fluctuations, they use the turbulence model in their CFD code to calculate turbulent quantities such as turbulent viscosity. This, in turn, is used to calculate appropriately random velocity vectors by which to advect the computational particles. The stochastic particle properties are only species concentrations, particle/droplet size and mass.

They test their code against experimental results of $BaSO_4$ precipitation. The $BaSO_4$ droplet/particle population distribution is heavily dependent on the nucleation rate which is very sensitive to supersaturation. The evolution of the precipitation is not believed to have a significant impact on the flow dynamics, so their Monte Carlo code is one-way coupled to the CFD results. As is the case with our approach, they chose to model the droplet population by discretizing the size domain into diameter bins. Typically, researchers have modeled the droplet/particle population using (relatively few) moments as a computational compromise. As computing resources have become more accessible, full size distribution binning discretization has become more feasible.

We adopt an approach similar to Veroli & Rigopoulos (2010), utilizing a finite-volume code (`OpenFOAM`) to calculate the underlying velocity field. The CFD simulation uses a traditional turbulence model (e.g. $k - \epsilon$) to compute the free-shear turbulent flow field. A particle-mesh Monte Carlo method utilizes a large number of stochastic particles throughout the domain to resolve the PDF of the water vapor and droplets. Haworth (2010) provides a comprehensive overview of PDF methodology for reactive flows, on which we relied heavily when developing the code for this thesis.

To the computational strategy of Veroli & Rigopoulos (2010), we are adding a thermodynamic model that tracks enthalpy to calculate temperature which, combined with the water vapor partial pressure, defines supersaturation. Furthermore, we incorporate a relatively new computing method that offers valuable simulation speed-up.

The advent of graphical processing units (GPU) for numerical calculations provides new, affordable opportunities for such a Monte Carlo approach. The acceleration afforded by utilizing hundreds or thousands of GPU cores per processor (as opposed to tens of CPU cores) allows for the computation of larger domains, more chemical species, and finer discretization of the population.

The gaming industry has been driving design and cost improvements of GPU hardware since the 1980s. In the past decade, researchers have begun to co-opt the processing power of graphics hardware to assist with scientific computing. Platforms such as nVidia's CUDA and OpenGL has begun to make non-graphics uses more mainstream. Owens et al. (2008) lists characteristics that make a given application particularly well-suited to be solved using a GPU:

- Computational requirements are large
- Parallelism is substantial
- Throughput is more important than latency

Our Lagrangian Monte Carlo particle code satisfies all three requirements, so it is sensible to proceed with programming to take advantage of GPU hardware.

The PDF method is implemented with parallelization based on GPU hardware. GPUs have traditionally been used to speed up graphics calculations by leveraging specialized parallel cores to compute ray tracing and shading, for example. However, as the cores have become more sophisticated, densely packed, and cheaper, they have increasingly been used for other types of parallel computations. Specifically, companies such as nVidia have developed software tools to more easily use the hardware for generic computational engineering problems. We used `Eclipse`, nVidia's integrated development environment, to program our C++ based code.

The overhead involved in utilizing the GPU consists mostly of copying data between the CPU's and the GPU's memory. nVidia's parallel GPU architecture, called CUDA, handles much of the memory management on the GPU. Once the data is copied to the GPU, it is further distributed to the various cores, which share a limited amount of memory in blocks, as well as each core having a small amount of easily accessible memory. The CUDA architecture ensures efficient parallel computation (maximizing throughput) by running computational threads on cores as they become available, so that the typical idle time occupied by memory access is minimized.

5.4.1 Model Overview

5.4.1.1 Computational Domain

Unlike the CFD simulation, the PDF model does not use the computational grid to discretize governing equations. It merely serves as an organizing system for the averaging, mixing, etc. of the computational particles.

Because we are limiting our studies to the turbulent jet, where the flow statistics are axisymmetric, we create a rectangular, two-dimensional axisymmetric domain. The grid spacing is uniform in both the radial and axial directions, though the grid spacing in each direction is not necessarily equal. Typically, the radial direction was afforded more resolution in order to provide adequate refinement at the mixing interface. Though the spacing is equal, due to the nature of cylindrical coordinates, the volumes in the radial direction are unequal, particularly near the axis of symmetry.

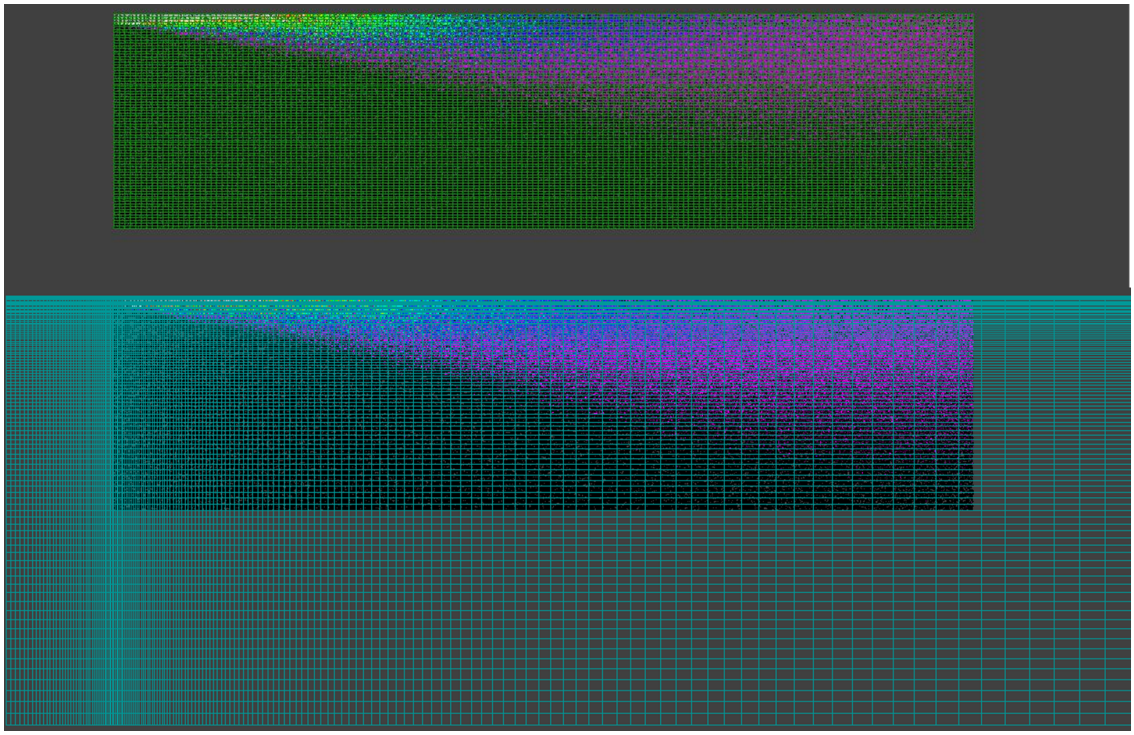

Figure 5.12: PDF particle field (particles colored by passive scalar) overlaid with the PDF computational grid (top) and CFD computational grid (bottom)

Of course, the rectangular grid and regular cell resolution are not necessary features of this computational approach. However, body-fitting or gradient-tracking grid refinement requires additional computational overhead that is not justified in this case, as will be shown later in the presentation of the composition PDF calculations.

The spatial discretization for the PDF is constructed to be completely encompassed by the CFD domain. This is because the CFD domain needs to extend further in all directions to accurately calculate the flow field in the core of the domain where mixing s taking place. In the case of this simulation, the PDF calculations can exist solely in the region of interest and produce satisfactory results. See Figure 5.12 for a comparison of the particle fields (colored by passive scalar value) over-set by both the PDF and CFD grids.

The domain of PDF particles is typically subdivided into the same cells as the CFD computational grid Haworth (2010). However, the demands of the CFD grid do not neces-

sarily align with those of the PDF grid. In this particular case, the CFD grid resolution calls for fine resolution near the jet's axis of symmetry. The wedge cell volumes are necessarily smaller even with constant spacing; clustered spacing near the axis would exacerbate the problem. Since cell balancing requires comparable numbers of particles in all cells, the particles near the jet axis will have significantly smaller masses than those at the fringes. This can cause undesirable issues with mixing, and cell/mass balancing. For a typical simulation, we used a resolution of 80 radial and 160 axial cells. With an average of 20 computational particles per cell, there are approximately 250,000 particles to track.

5.4.1.2 Initial Conditions

The domain is initially seeded such that each cell has a number of computational particles equal to the desired average (i.e. 20 for the baseline case). They are seeded uniformly, at the center of each mesh cell, but random velocity fluctuations cause them to disperse. The particles are all assigned similar scalar values representing ambient temperature/water vapor conditions. The simulation must be run out, allowing the jet to propagate through the domain, before the flow becomes statistically stationary and the results can be averaged.

5.4.1.3 Boundary Conditions

Based on the velocity information provided by the CFD results, particles were added and subtracted from each of the PDF model's boundary cells, such that the mass fluxes matched. Concerning cells with a net outflow, particles are subtracted at each time step until the appropriate amount of mass is removed. New computational particles are created within cells at inflow boundaries at each time step. Each new particle is given a mass corresponding to the cell's mass divided by the average (or desired) number of particles. If a particle is to otherwise cross one of the domain's boundaries, it is reflected back into the domain as if it were a symmetry boundary. This is based on the assumption that if particles leave the domain in excess of what the CFD results describe (due to inherent random motion), they would be offset by comparable particles randomly moving into the domain.

Newly created particles at the boundary are given a scalar value corresponding to the

region from which they originate. Particles inside the jet radius are given a scalar value of unity and the appropriate initial distribution of droplets/nuclei (if the jet is seeded). Other particles are given a scalar value of zero and seeded with an amount of nuclei to correspond to their mass.

5.4.2 Model Time Stepping

The code advances all the particles in the entire domain using discrete time steps; during each time step, the following fractional steps are performed on all computational particles/cells.

5.4.2.1 Advection Model

Each particle is translated during each time step based on the following equation:

$$dx_i = u_i dt + \frac{1}{\langle\rho\rangle}\frac{\partial\Gamma}{\partial x}dt + \left(\frac{1}{\langle\rho\rangle}\Gamma\right)^{0.5} dW_i. \tag{5.13}$$

where Γ is the turbulent transport coefficient, defined as (Haworth (2010)):

$$\Gamma = \frac{\mu}{\sigma} = \frac{\nu}{\rho\sigma} \tag{5.14}$$

where σ is the Schmidt number. The values for u_i, ρ, $\frac{\partial\Gamma}{\partial x}$ and Γ are interpolated based on the particle's position within the overlapping CFD cell. Additionally, dW_i is a Wiener process proportional to $\delta t^{0.5}$.

5.4.2.2 Cell Balancing

The PDF method relies on modeling stochastic particles that are tracked throughout the domain. In order to collect proper statistics, an appropriate number of particles must be maintained in each cell, regardless of the cell size (Haworth, 2010). If a cell contains less than the threshold number of required particles, existing computational particles are selected and divided to make two particles, each with half the mass of the original particle, and identical properties otherwise. In the case of too many particles, particles are randomly selected to be combined, and their properties are mass-averaged to create a single particle while preserving

all of the appropriate quantities.

5.4.2.3 Reaction Model

The reaction model is not specific to the PDF method itself, but instead directly relates to the particular problem being studied. In the case of the condensing jet, the thermodynamic processes of condensation, evaporation, and the associated latent heat exchange must be accounted for within each fluid particle of the PDF model.

In non-reacting flow, the best quantity to track is enthalpy, since it is a conserved scalar:

$$H = U + pV. \tag{5.15}$$

In a closed, constant pressure system such as our computational particles (we make the assumption that the static pressure is homogeneous throughout the domain), the enthalpy is constant. This of course breaks down when mixing between particles occurs. The new (specific) enthalpy can be calculated from the particle's scalar value:

$$h_p = ch_j + (1 - c)h_a. \tag{5.16}$$

The scalar values are assigned such that particles emanating from the jet are designated with the value of unity, and particles from the ambient are given a zero value. Intermediate values occur when particles interact through mixing (see section 5.4.2.4).

For an adiabatic particle, the process of droplet condensation/evaporation does not affect its enthalpy:

$$h_p = h_{air} + h_{vapor} + h_{liquid}. \tag{5.17}$$

Our enthalpy calculations will rely on use of a reference temperature (i.e. $h = 0$ when $T = 0\ ^\circ C$). Over the small range of temperatures we are considering, it is reasonable to assume that the enthalpy components have a linear dependence on temperature. Thus, rather than using tables, we can rewrite equation (5.17) as

$$h_p = (1 - x)\, c_{pa} T + (x - x_l)\, (c_{pw} T + h_{we}) + x_l c_w T \tag{5.18}$$

where h_p is the computational particle's specific enthalpy, c_{pa} is the specific heat capacity of air at constant pressure (1.006 $kJ/kg\ ^\circ C$), x_l is the mass fraction of the liquid water to the total particle mass (kg/kg), c_{pw} is the specific heat of water vapor at constant pressure (1.84 $kJ/kg\ ^\circ C$), h_{we} is the evaporation heat of water vapor at 0 $^\circ C$ (2501 kJ/kg), x is the mass fraction of all of the water (kg/kg), and c_w is the specific heat capacity of water (4.19 $kJ/kg\ ^\circ C$).

For a computational particle with a given water content and droplet distribution, all values in the above equation are known, except for the temperature. Rearranging, we can solve for temperature:

$$T = \frac{h_p - (x - x_l)\, h_{we}}{(1 - x)\, c_{pa} + (x - x_l)\, c_{pw} + x_l c_w}. \tag{5.19}$$

The computational particle's temperature is needed to calculate the local saturated water vapor pressure using Antoine's equation (see equation 5.8). The particle's actual water vapor pressure can be computed, assuming that all particles are at the local atmospheric pressure:

$$P_w = P_{atm}\left(1 - \frac{(1 - x)}{(1 - x) + (x - x_l)M_{air}/M_w}\right). \tag{5.20}$$

As was the case with the 2-D CSTR model from section 5.3, the local supersaturation is simply a function of the calculated water vapor pressure and the stochastic fluid particle's water vapor partial pressure:

$$ss = \frac{P_w}{P_{sat}} - 1 \tag{5.21}$$

and again, this supersaturation is used to calculate the growth/evaporation of the droplet diameter bins local to the fluid particle:

$$\frac{dr_b}{dt} = \gamma \frac{ss}{r_b}. \tag{5.22}$$

5.4.2.4 Mixing Model

Haworth (2010) describes two main classes of particle mixing methods. There are methods that involve individual particle compositions interacting weakly with the neighboring particles. The interaction by exchange with the mean (IEM) model is perhaps the best-

known of this type. The other class of methods involves direct particle-particle interaction. This is sometimes called a coalescence-dispersion model. Perhaps the oldest and most well-known of this class of methods is described in Curl (1963). The probability of two particles in a computational cell mixing directly during a time step (i.e. both assuming the same mass-weighted average composition) is described by the following equation:

$$C_\phi N \omega dt \tag{5.23}$$

where N is the number of particles in the cell, and C_ϕ has been reported to be a range of values from 1 to 4 according to Haworth (2010).

The work of Dopazo (1979) and Janicka et al. (1979), suggested a modification to Curl's model that not only randomizes the occurrence of particle mixing, but also the degree to which the particles are mixed. Pope (1982) defines it as:

$$\begin{aligned} \phi_a^* &= (1-\alpha)\phi_a + \tfrac{1}{2}\alpha\left(\phi_a + \phi_b\right) \\ \phi_b^* &= (1-\alpha)\phi_b + \tfrac{1}{2}\alpha\left(\phi_a + \phi_b\right) \end{aligned} \tag{5.24}$$

In these equations, α is a random number, with a uniform distribution from 0 to 1. Since our particles do not have identical masses, we take ϕ to represent the particle mass. In order to completely define the new particles, the associated scalars are weight-averaged according to the degree of mass mixing, such that all quantities are conserved. Pope (1982) determined that C_{phi} should be taken to be 3 when α is evenly distributed.

Furthermore, Pope (1982) extended this to an "improved" mixing model which takes the particle age into account when predicting the occurrence of mixing. However, this has been shown by Chen & Kollmann (1991) to not improve significantly the results for the scalar statistics we are concerned with.

5.4.3 RANS Simulation

Because we are limiting ourselves to modeling the joint-composition of two scalars (as opposed to joint-composition-velocity), a CFD code must be used to calculate the appropri-

ate velocity field, as well as the turbulent kinetic energy and dissipation fields. We used `OpenFOAM`, a flexible, open-source solver (ope (2012)) for our RANS computations. The current implementation uses one-way coupling, where the CFD results inform the PDF model, similar to Veroli & Rigopoulos (2010).

We have first evaluated `OpenFOAM` using a $k-\epsilon$ turbulence model for a canonical, turbulent jet (no heating or species reactions). Aside from the density differences, the jet mimics the 85 $^{\circ}C$ jet from Strum & Toor (1992). The jet nozzle has a 1.1 cm diameter with a top-hat flow profile with a velocity of 4.57 m/s. Because of the axisymmetric nature of the problem, the simulation is two-dimensional using cylindrical symmetry; the plane of cells creates a 20 radii wide (100 cells) wedge that extends 10 radii upstream and 100 radii downstream (160 cells), for a total of $16,000$ computational cells. Figure 5.13 shows a contour plot of the z-velocity across the entire computational domain. Figure 5.14 plots the non-dimensional velocity against non-dimensional radial distance at various downstream distances, a dozen locations spanning approximately $z/d = 30$ to 50. The curves are nearly indistinguishable, conforming to the self-similarity principle of a turbulent jet (see Figure 3.1). Furthermore, Figures 5.16 and 5.15 show the comparison of CFD results (centerline velocity ratio and jet half width) against analytic solutions. Equation 3.1 is plotted with coefficients $B = 4.7$ and $z_0 = 2d$; the equation for the jet half-width is (Pope, 2000):

$$r_{1/2} = S(z - z_0) \tag{5.25}$$

where $S = 0.105$ and $z_0 = 2d$. This level of agreement across these metrics is judged to be adequate to use the flow field data as the basis for the PDF section of this analysis.

Most of our interest is in warm, humid jets, so before selecting a solver, it is important to evaluate the relative important of buoyancy and momentum. Lee & Chu (2003) describes a length scale at which the momentum and buoyancy forces will be balanced for a free jet:

$$z \approx \frac{M_0^{3/4}}{B_0^{1/2}} \tag{5.26}$$

where M_0 is the specific momentum ($U_j Q_j$) and B_0 is the specific buoyancy ($(\rho_\infty - \rho_j) g Q_j$).

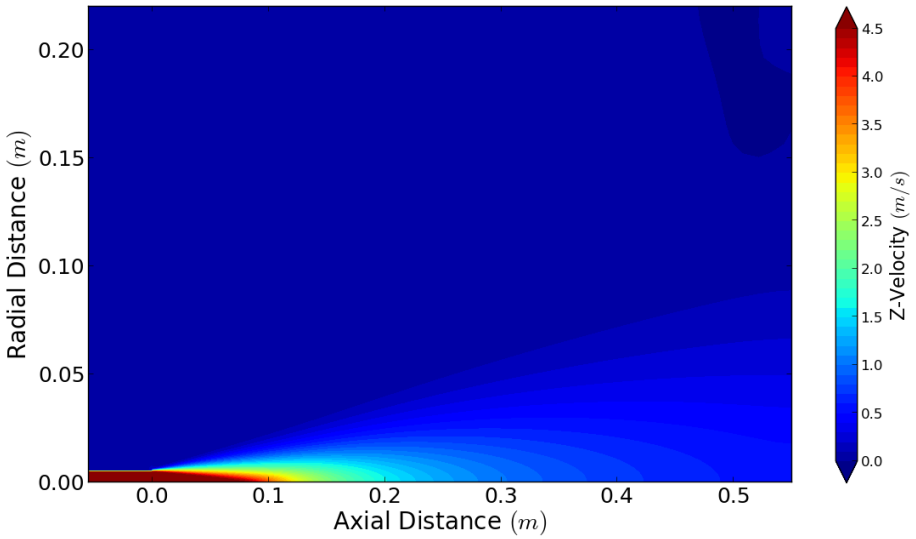

Figure 5.13: CFD results from `OpenFOAM` showing velocity contours

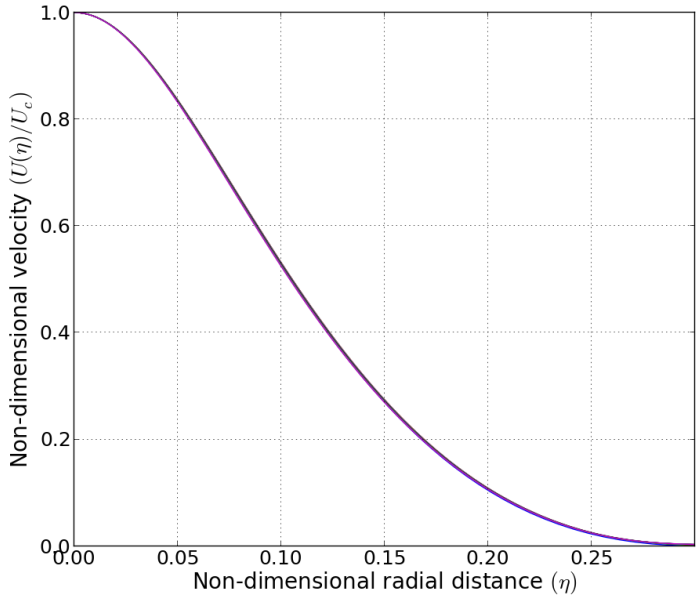

Figure 5.14: Plot of normalized jet velocity as a function of η at various downstream distances

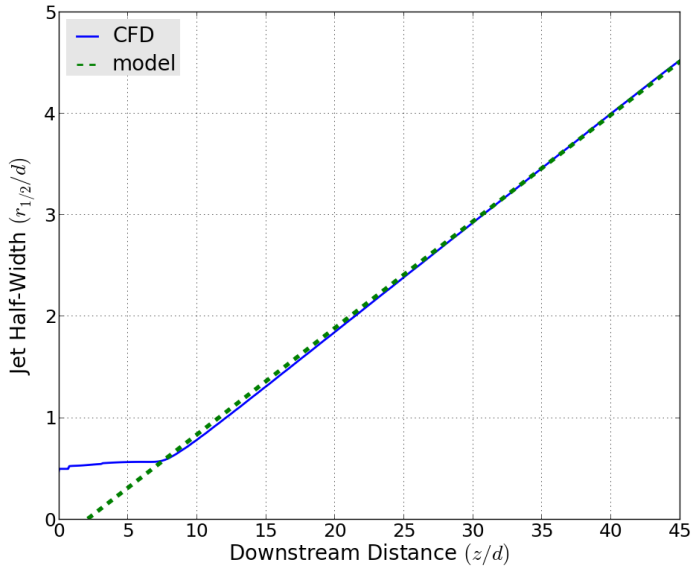

Figure 5.15: Plot of the jet half-width as a function of downstream distance

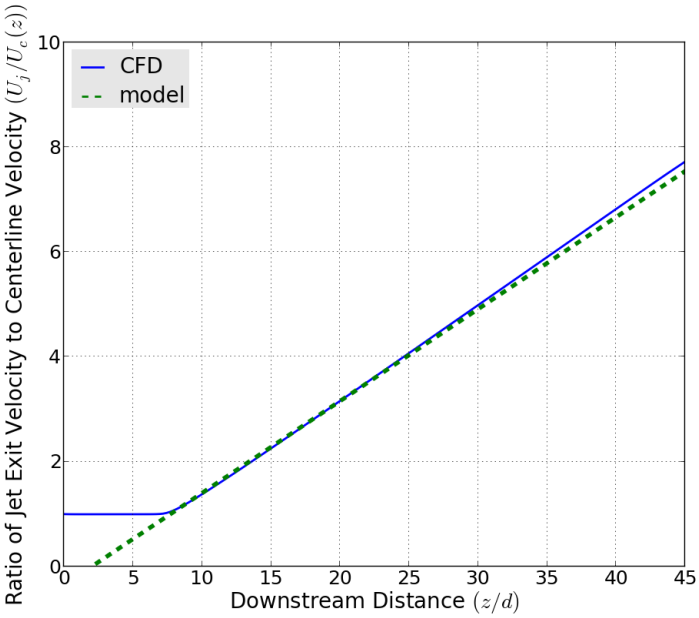

Figure 5.16: Plot of the jet centerline velocity ratio ($U_j/U_c(z)$) as a function of non-dimensional downstream distance (z/d)

This equation can be rearranged:

$$\sqrt{\frac{gd}{U_j^2}\frac{\rho_\infty - \rho_j}{\rho_\infty}} \cdot \frac{z}{d} = \left(\frac{4}{\pi}\right)^{1/4} \approx 1 \tag{5.27}$$

If we define a new variable P:

$$P = \sqrt{\frac{gd}{U_j^2}\frac{\rho_\infty - \rho_j}{\rho_\infty}} \cdot \frac{z}{d} \tag{5.28}$$

we can use P as a threshold criteria for determining buoyancy versus momentum dominated at a downstream position z/d. For a value much above unity, the jet is considered buoyancy dominated; conversely, a value of P much below unity indicates the jet is momentum dominated. For values in the vicinity of unity, the jet will be significantly affected by buoyancy and momentum. This criteria appears to be superior to that described by Pasumarthi & Agrawal (2005) which experiences difficulties for either very light jets or jets with nearly uniform densities.

For the experiments in Strum & Toor (1992) that we use for comparison, the values of P are for the 62 $^\circ C$ jet:

$$P = \sqrt{\frac{(9.81\ m/s^2)(0.011\ m)}{(4.1\ m/s)^2}(1 - 0.81)} \cdot \frac{z}{d} = 0.035\frac{z}{d} \tag{5.29}$$

and for the 85 $^\circ C$ jet:

$$P = \sqrt{\frac{(9.81\ m/s^2)(0.011\ m)}{(4.57\ m/s)^2}(1 - 0.65)} \cdot \frac{z}{d} = 0.042\frac{z}{d}. \tag{5.30}$$

For both jets, buoyancy effects begin to equal momentum forces around $\frac{z}{d} = 30$. We examine our jets to $\frac{z}{d} = 40$, so buoyancy forces may indeed play a role. Based on these results, although we ran the simulations using a buoyancy model in `buoyantSimpleFoam`, we expect its effect to be negligible in the development of the jet in the area of interest for droplet condensation. Additionally, even absent buoyancy forces, it is important to account for the lower density of the jet in the momentum dynamics and mixing.

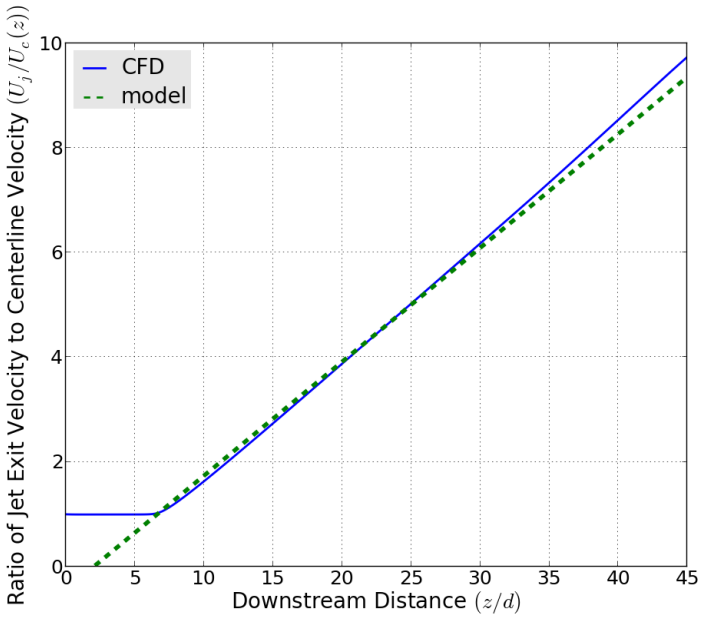

Figure 5.17: Plot of the jet centerline velocity ratio ($U_j/U_c(z)$) as a function of non-dimensional downstream distance (z/d) for the low-density, 85 $°C$ jet

Panchapakesan & Lumley (1993b) modified the decay equation, 3.1, with an effective diameter, $d_e = \left(\frac{\rho_j}{\rho_a}\right)^{1/2} d$, that accounts for density differences between the jet and ambient:

$$\frac{U_c(z)}{U_j} = \left(\frac{\rho_j}{\rho_a}\right)^{0.5} \frac{Bd}{z - z_0} = \left(\frac{\rho_j}{\rho_a}\right)^{0.5} \frac{Bd}{\bar{z}} \tag{5.31}$$

We ran simulations with jet densities of $\rho_j/\rho_a = 0.65$ and 0.81 to match experimental conditions from the 85 $°C$ and 62 $°C$ jets respectively. Figure 5.17 shows the comparison of equation (5.31) (featuring the same coefficients as Figure 5.16) with the CFD results.

5.4.4 PDF Implementation

Using CUDA, the PDF solver software is written in C++, which handles the particle array bookkeeping, as well as the sequential execution of the model steps from 5.4.2.

5.4.4.1 Time-Stepping

In our PDF simulations, the grid spacing in the z-direction is uniform. The velocity is obviously largest near the nozzle exit, therefore, we set our time step such that particles near the nozzle do not travel further than one cell in a single time step (i.e. $\Delta t < \frac{U_j \delta t}{\Delta z}$).

5.4.4.2 Diameter Distribution

Rather than using only a few "moments" to represent the droplets' diameter distribution, we have subdivided the diameter continuum into a finite number of bins, similar to section 5.3. In these simulations, each bin increments the droplet diameter by 0.3 μm over the previous bin. Rather than tracking a droplet concentration within each bin, the actual number of droplets in the computational particle is accounted for within each droplet diameter bin.

A typical simulation used 50 diameter bins spanning a total of $15\mu m$ to resolve the droplet size distribution. For a computation with a quarter million particles, doing a number of Runge-Kutta time steps to grow each diameter bin can begin to become very expensive computationally; hence the need for parallelization. The GPU computations allow us to compute the diameter distribution using this more detailed approach.

After each simulation time step, each bin has been calculated to grow or shrink to a new diameter. These new droplets are redistributed between the bracketing diameter bins such that the total droplet number is preserved. The values tracked in each represent the predicted number of droplets in the computational particle (fractional values are allowed).

5.4.4.3 Reaction Model

Because every particle requires thermodynamic calculations at each time step, and the thermodynamics calculations are the most numerically intense, parallelization of this step is critical for efficiency and speed. Fortunately, there is no particle communication necessary for this step, so the parallelization is quite effective (serialization in fact).

A fourth order Runge-Kutta algorithm is used to calculate the condensation/evaporation of the water droplets. All of the particle bins must be done simultaneously, in order for the particle's new supersaturation to be computed correctly within the Runge-Kutta algorithm.

Typically, the time-step over which the droplet growth calculations are computed must be smaller than the time-step needed for particle advection/mixing (especially for the smallest droplets). In our case, we use 10 smaller time steps for the reaction model at each model time step.

Speaking to the efficiency (and necessity) of the GPU implementation, we focused on evaluating the "reaction" subroutine, which calculates the droplet growth rate and associated thermodynamics of the computational particles. As part of the software execution, the reaction portion takes a majority of the run time during each time step (about 80%). In real-time on our computer's GeForce GT 730M, this accounts for just over one second of clock time. Upon serialization of the routine, the same routine, running on the laptop's 2.5 GHz i5 Intel processor takes nearly a minute to complete during each time step.

5.4.4.4 Boundary Conditions

By definition, the boundary conditions only need to be examined and updated in a limited number of cells. Furthermore, the particles involved are limited only to those incoming and outgoing which, because of the small time step, are typically only a fraction of those particles present. Therefore, in order to simplify the programming and bookkeeping, the boundary conditions are handled at each time step by a serial routine.

5.4.4.5 Cell Balancing

Because cell balancing necessarily involves all of the cells in the domain, we elected to use the CUDA platform and do the particle subtraction/addition in parallel. Of course, since the CUDA threads have very limited communication, certain care must be taken. There are "atomic" functions available in CUDA that prevent other threads from progressing if the array of particles needs to be manipulated (addition or subtraction of particles). That ensures that no other threads modify the array before becoming aware of the current array changes.

5.4.4.6 Cell Integration and Advection

Simulations with wide variations in element volumes (as is the case for our cylindrical geometry) are known to promote discrepancies in the mass distribution (Zhang & Haworth, 2004). In order to mitigate the negative effects of mass accumulation, we have implemented a velocity correction algorithm. Particle velocities are modified to move them in the direction opposite the local gradient of the density error. Figure 5.18 shows the effect of the velocity correction on a uniform density flow. Without velocity correction, it is clear the domain has density discrepancies of nearly 10% throughout the domain, and well over 10% near the jet axis along the length of the domain. However, the velocity correction restores the vast majority of the domain to a density nearly identical to that of the CFD simulation. Near the jet axis, the density is less than 10% off; furthermore, the volumes near the axis are so small that the actual mass imbalance is negligible. Only near the nozzle exit, where velocity gradients are quite high, do the density inhomogeneities persist.

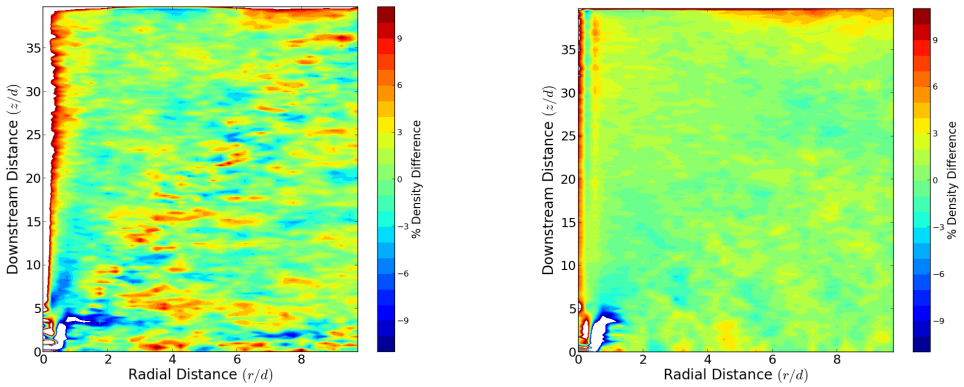

(a) (b)

Figure 5.18: Plot the density discrepancies between the PDF and CFD simulations both (a) with and (b) without velocity corrections

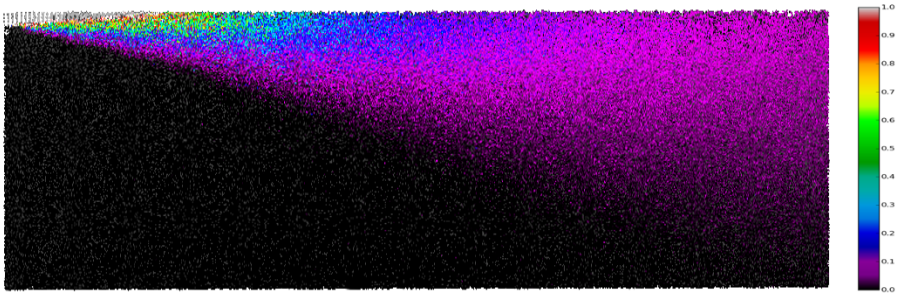

Figure 5.19: Plot of computational particles colored with scalar value

5.4.5 Validation

Before looking at the more interesting condensation results, validating the code for a passive scalar is a useful exercise. Our initial PDF simulations do not model any chemical reactions; our goal is to match the scalar distribution and variance for the well-studied problem of passive scalar mixing in a turbulent jet. Comparisons can be directly made against other investigators experimental and computational results to ensure the scalar in our code is being dispersed correctly. Figure 5.19 shows all of the stochastic particles at several times during the PDF simulation plotted together and colored by the scalar value.

The statistics of scalar distribution in a momentum-dominated turbulent jet have been investigated by a number of authors. Section 5.2.1 provides some results for both average scalar and its R.M.S. by Richards & Pitts (1993).

An obvious point of validation is the centerline decay of a passive scalar. Like the decay of the velocity, the inverse of the non-dimensional value assumes a linear profile. We compare our results against two studies in Figure 5.20. In the first study, Pitts (1991a) examined the concentration decay of an injected low-density gas. His derived expression can be simplified by assuming $\rho_j = \rho_a$ (as is the case in our validation simulation):

$$\frac{C_j}{C_c} = 0.114\frac{z}{r}. \tag{5.32}$$

Additional results appeared in Lubbers et al. (2001); they completed a Direct Numerical Simulation (DNS) of a passive scalar in a round, axisymmetric jet and compared their results

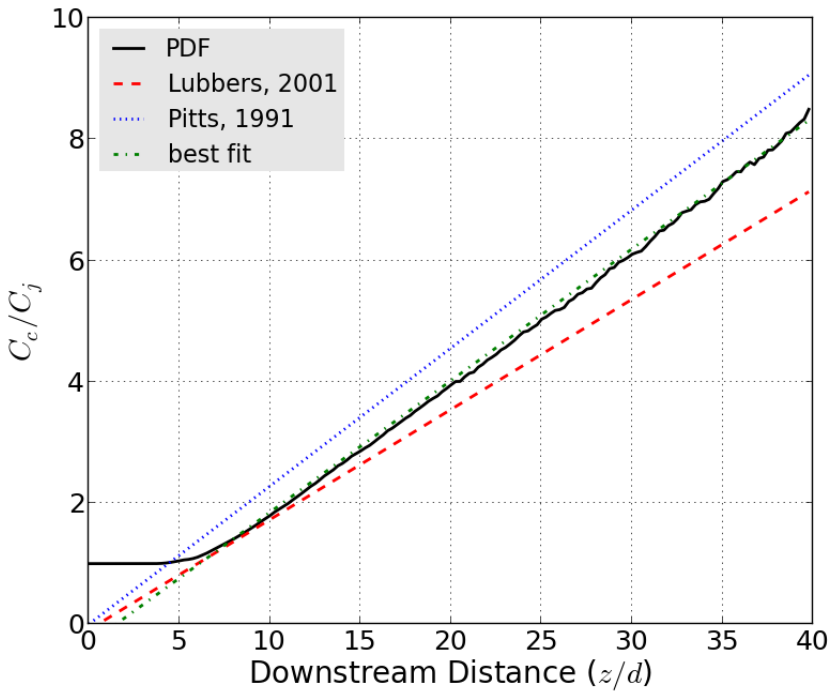

Figure 5.20: Plot of the non-dimensionalized centerline concentration decay

to Dowling & Dimotakis (1990) as well as several other investigators. It is believed that at a sufficiently high Reynolds number (they used 2000), the distribution characteristics of a passive scalar are independent of Reynolds number. They described the centerline decay of the mean concentration value:

$$\frac{C_j}{C_c} = \frac{z - z_0}{\kappa_c d} \tag{5.33}$$

where $z_0 = 0.5$ and $\kappa_c = 5.5$. Figure 5.20 displays these results with our own best fit line where $z_0 = 1.5$ and $\kappa_c = 4.7$. Lubbers et al. (2001) makes a survey of previous literature and finds values of κ_c between 4 and 6, so our value falls comfortably within that range.

Another well-established property of the round, turbulent jet is its self-similarity. In addition to the velocity profile being self-similar, investigators have found the concentration profile to also be self-similar (e.g. Dowling & Dimotakis (1990)). Figure 5.21 shows over a dozen profiles from $z/d = 20$ to $z/d = 40$. It is apparent that they collapse onto each other.

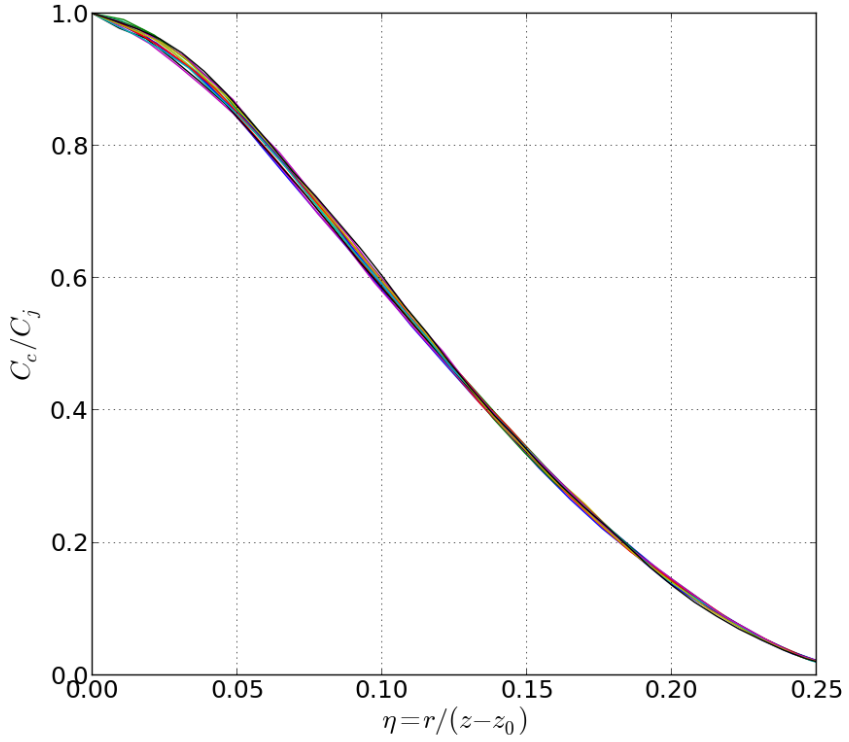

Figure 5.21: Plot of the non-dimensionalized concentration profiles

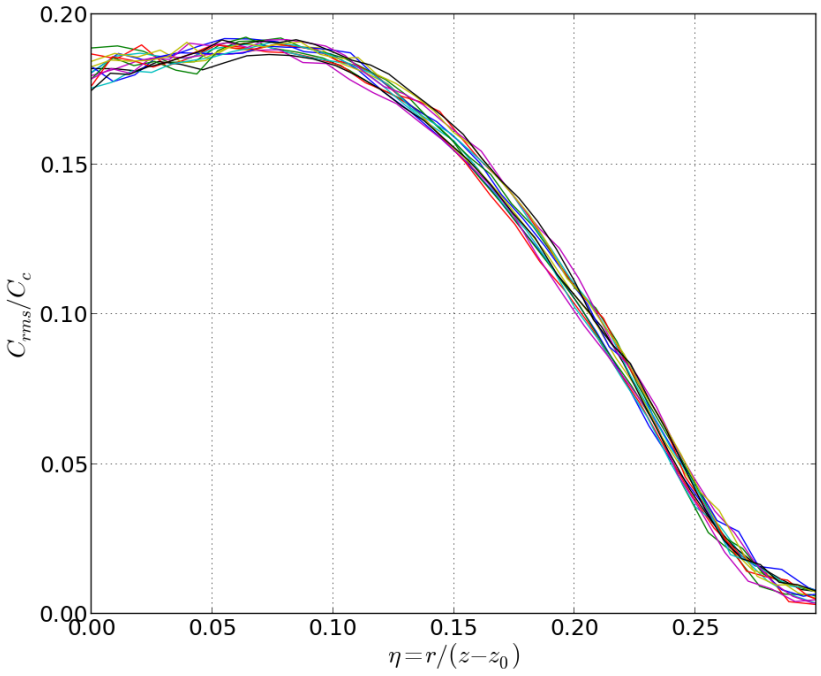

Figure 5.22: Plot of the non-dimensionalized concentration profiles

Of course, if the particle velocity field is properly defined, the mean concentration profile will be predicted correctly regardless of how the particles are mixed (i.e. exchange of mass and associated properties). The R.M.S. on the other hand, strongly depends on the way the particles have been mixed to that point. The resulting profile should be self-similar, as mentioned by Panchapakesan & Lumley (1993b) (see section 5.2.1). Lubbers et al. (2001), Babu & Mahesh (2005) and Dowling & Dimotakis (1990) made similar observations. The results from the PDF code (again from $z/d = 20$ to $z/d = 40$) are plotted in Figure 5.22. They qualitative and quantitative agree with the literature, giving us confidence in our mixing algorithm, described in section 5.4.2.4.

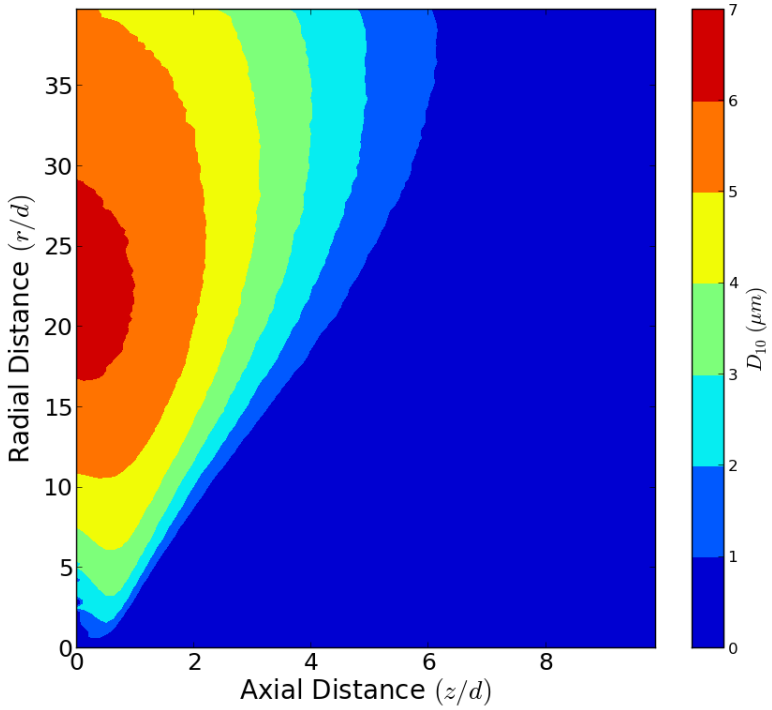

Figure 5.23: Contour plot of D_{10} values predicted by PDF for the 85 $^{\circ}C$ jet

5.4.6 Comparison to Experiments from Literature

As done earlier with the simplified analytic two-dimensional radial-axial CSTR model, we compare our model results against the experiments of Strum & Toor (1992). To present an overview of our 2-D flow, Figure 5.23 shows the flow field with contours of average diameter (D_{10}). An interesting effect observed is the development in the near nozzle field where drops form on the jet border but are absent from the (potential) core. In early attempts at experiments we undertook, this effect was also quite clear when the water-vapor-saturated jet was illuminated by a laser plane (see Figure 5.24).

We present our model results side-by-side with the experimental results for comparison. Figure 5.25 shows the diameter distributions along the jet centerline for the unseeded 62 $^{\circ}C$ jet. Figure 5.26 shows the same comparison with experimental data, in this case for the

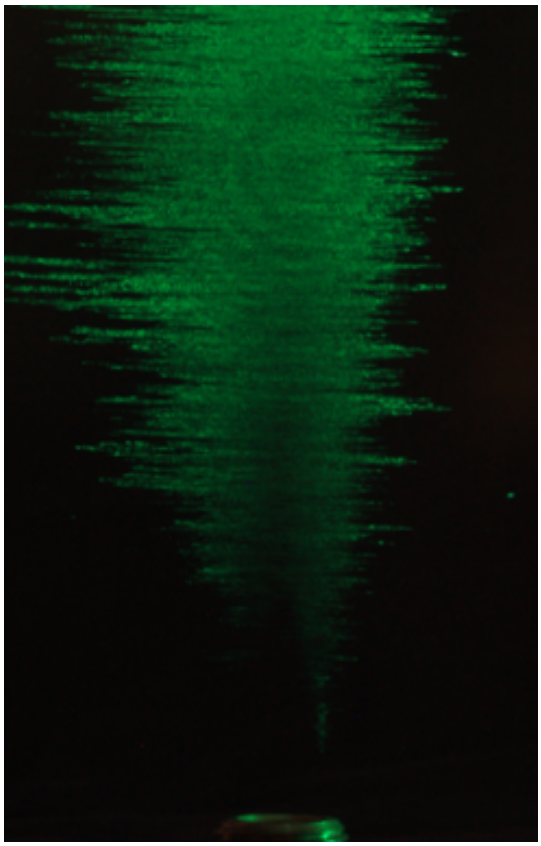

Figure 5.24: Time-lapse photo of a condensing jet illuminated by a laser sweeping along the jet axis

unseeded 85 $^{\circ}C$ jet.

The model captures well the rate of droplet growth, in number density and diameter, until modes of about $5-7\ \mu m$ are reached at $z/d = 25$. The flattening of the size distribution that occurs after $z/d = 25$, particularly in the 85 $^{\circ}C$ data, is also correctly predicted by the model. Increases in probability for the smallest and largest droplets, and a marked decrease in the probability of median droplets, can be observed in the simulations of both the 62 $^{\circ}C$ and 85 $^{\circ}C$ jets. The mixing of ambient dry air makes the probability of droplets encountering a region of supersaturation decrease with distance downstream (after an initial increase due to the nonlinearity in the supersaturation with temperature and vapor mixing). Because droplet growth depends non-linearly on diameter, and supersaturation depends also non-linearly on mixing, the smallest and largest droplets are more sensitive to the inhomogeneities in the supersaturation field. As droplets evaporate, the larger droplets do it slower and their weight in the total distribution increases. Small droplets evaporate quickly back to the nuclei size ($0.1\ \mu m$) but can also grow quickly into $1-2\ \mu m$ droplets as they visit an improbable supersaturated region, an asymmetric behavior that will bias the distribution towards having more of them. The most numerous droplets will evaporate with the decrease in supersaturated with a rate that is best represented by the average properties. A bimodal distribution is established by this non-linear response, as shown in Figure 5.26(c), and this complex behavior is well captured by the model, as seen in Figure 5.26(d). A potential additional source of disparities between the measurements and the model is the limitations of the PDPA experimental technique, especially circa 1990 when the data was collected, to fully account for the number of droplets with diameters below $2\ \mu m$. This explains the extremely low percentage of droplets detected below $1\ \mu m$ and the relatively low probability of droplets in the $1-2\ \mu m$ range detected, versus predicted from basic nucleation statistics.

Notice that in both 5.25 and 5.26 our model omits curves for distributions closest to the nozzle ($z/d \approx 2$). This is because at a location so far upstream, the velocity field is well within the potential core, there is no active mixing, and not only is super-saturation less than or equal to unity, but also no nuclei have been entrained yet into the jet centerline. As a result, our PDF model does not have any droplets to report. In fact, while Strum & Toor (1992) did report a droplet distribution at that location, other data in the paper indicate an

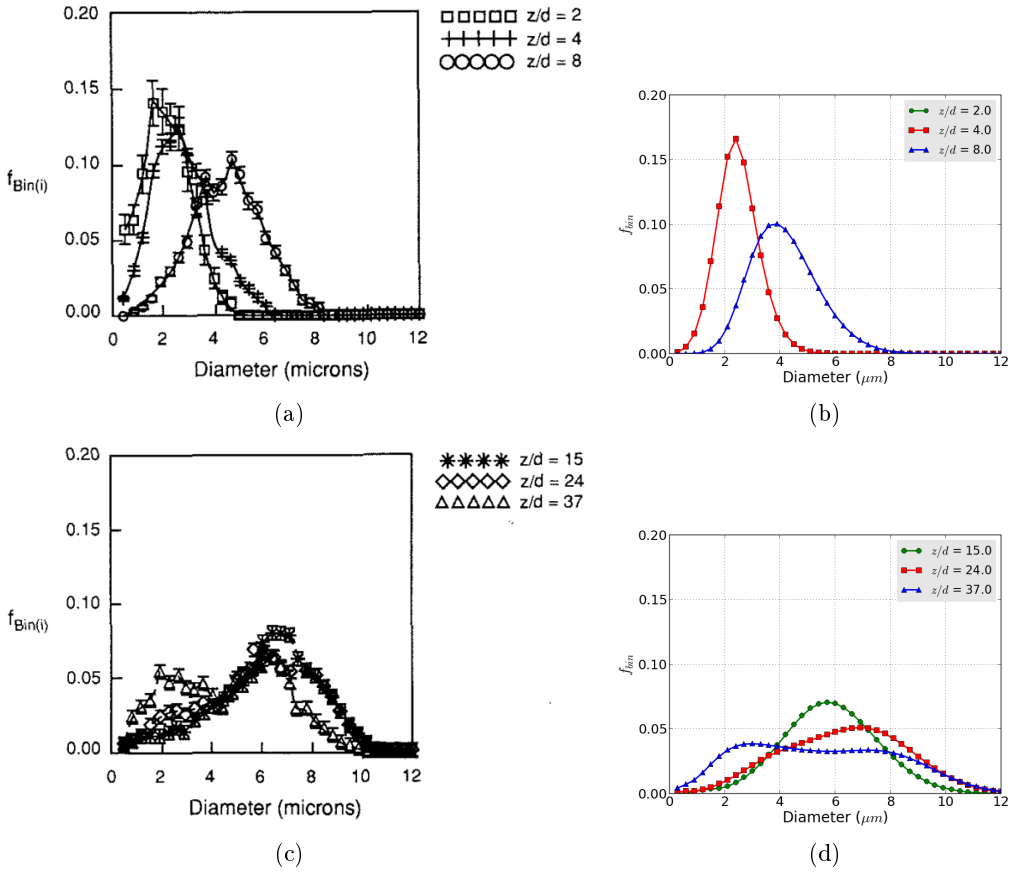

Figure 5.25: Plot of the diameter distribution of the centerline of the 85 $°C$ jet at various downstream distances

extremely low droplet concentration; the droplets that were recorded/reported are almost incidental.

Figure 5.27 shows experimental and modeled diameter distributions at various radial locations for the unseeded 85 $°C$ jet at $z/d = 15$. Our model does a fairly good job of reproducing both the diameter and relative distribution of the droplets. Similar physics as discussed in the evolution of the droplet size distribution along the centerline at late stages in the jet ($z/d > 25$) control the condensation and evaporation of droplets in jet outskirts ($r/d \approx 2$) for this intermediate downstream stage ($z/d = 15$). A bimodal distribution of droplets is also observed to occur in Figure 5.27(c) for the measurements at $r/d = 2.25$ and it is successfully predicted by the model, as shown in Figure 5.27(d).

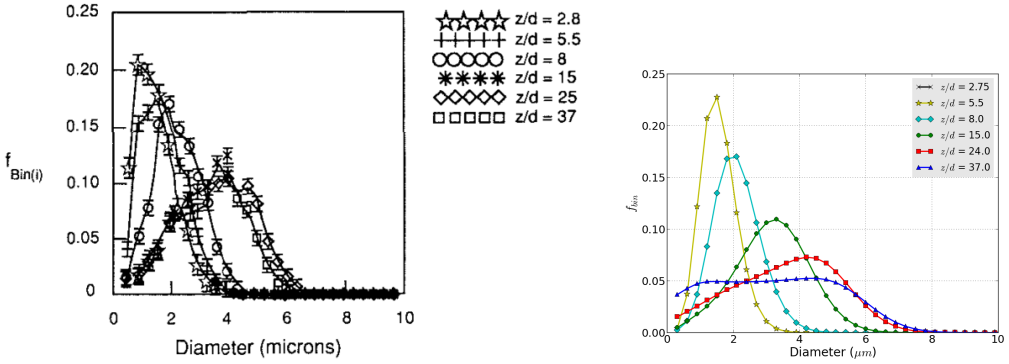

(a) (b)

Figure 5.26: Plot of the diameter distribution of the centerline of the 62 $^{\circ}C$ jet at various downstream distances

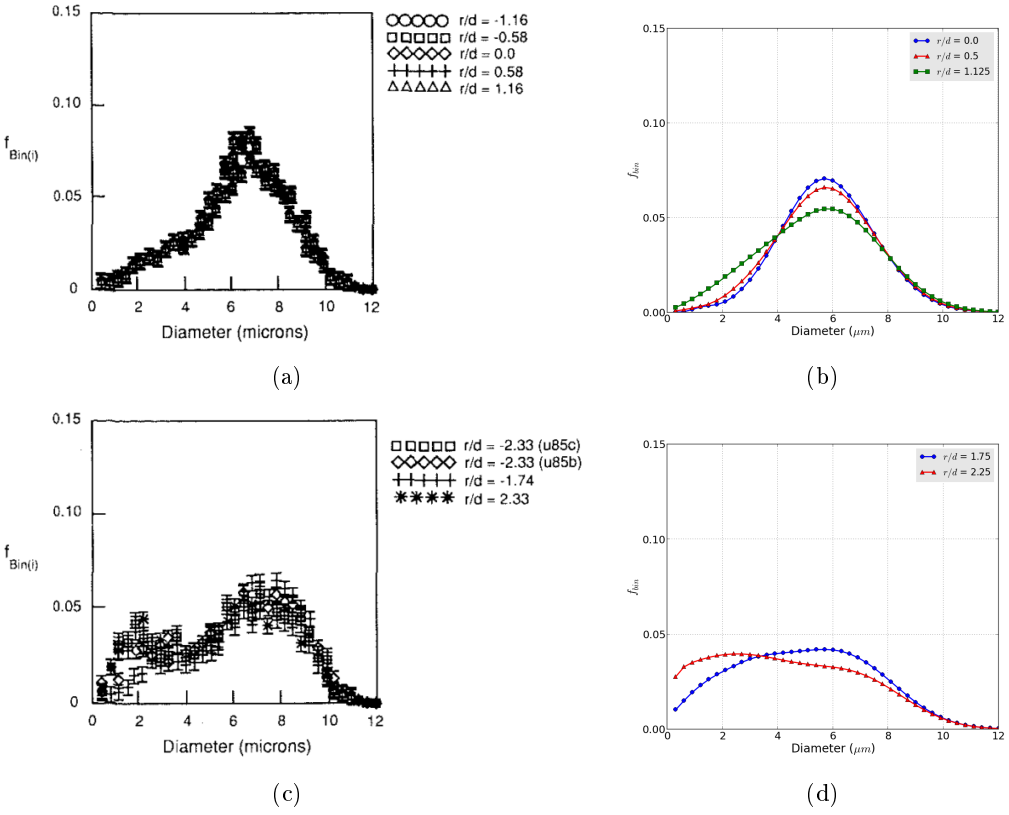

(a) (b)

(c) (d)

Figure 5.27: Plot of the diameter distribution for the 85 $^{\circ}C$ jet at $z/d = 15$ at various radial distances

In addition to the humid, unseeded jets, Strum & Toor (1992) also ran experiments with jets seeded with water droplets generated with an atomizer, at the same temperatures and humidities. These droplets were reported to have a D_{30} value of 2 μm at initial injection into the jet, so we simply added droplets with uniform 2 μm diameters to the injected computational particles. The experimental measurements for the seeded jets are plotted as D_{30} data along with the unseeded jets in Figures 5.28 and 5.29. These figures show the PDF-model data seeded with a uniform distribution of small, 2 μm diameter, water droplets plotted alongside the experimental data reproduced from Strum & Toor (1992). The blue dotted line in this figure shows the evolution of the droplet volume-averaged diameter in the jet. The abundance of condensation nuclei limits the availability of supersaturation, reducing the growth rate well below the unseeded case. The distribution reaches a maximum diameter of about 4.5 μm at about the same location as in the unseeded case ($z/d \approx 25$) and begins to evaporate, although slower than in the unseeded case. The abundance of small droplets that have grown from the condensation nuclei represents a source of quickly accessible water vapor, as the small droplets will be the first to evaporate. The larger droplets that dominate the volume-averaged statistics will therefore suffer the decrease of the saturation less acutely than in the unseeded case, where more of the water vapor had been locked in large droplets, slower to return to the vapor field.

5.4.6.1 Effect of Aerosol/Droplet Concentration

Pruppacher & Klett (1997) estimated a nuclei concentration of 10^3 to 10^5 cc^{-1} (over land), and perhaps as high as 10^6 in urban areas. For their unseeded experiments, Strum & Toor (1992) assumed an ambient concentration of condensation nuclei in the range of 20×10^3 to 65×10^3. We use 40×10^3 cc^{-1} and achieve very comparable results. Strum & Toor (1992) reported their seeded jet to have a droplet concentration of 10^5 cc^{-1}. However, they acknowledged that the precision of the PDPA's droplet counting for this size range $diameter < 2$ μm is uncertain. We found successful comparisons by seeding the jet in the PDF simulation with 5×10^5 droplets. This is actually more consistent with the atomizer specifications from Strum (1990) that list a number concentration of 2×10^6 cc^{-1}.

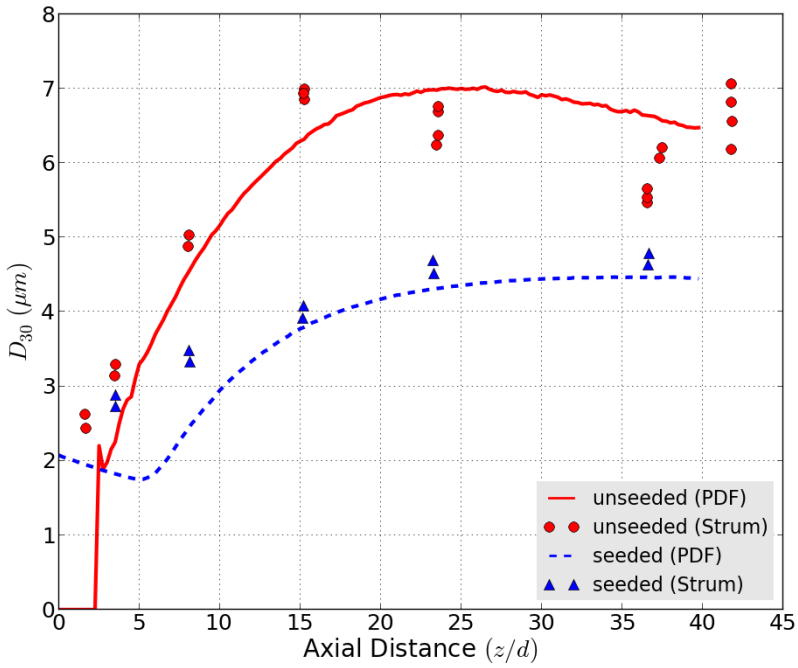

Figure 5.28: Comparison plot of D_{30} versus downstream distance for the 85 $^{\circ}C$ jet, both seeded and unseeded

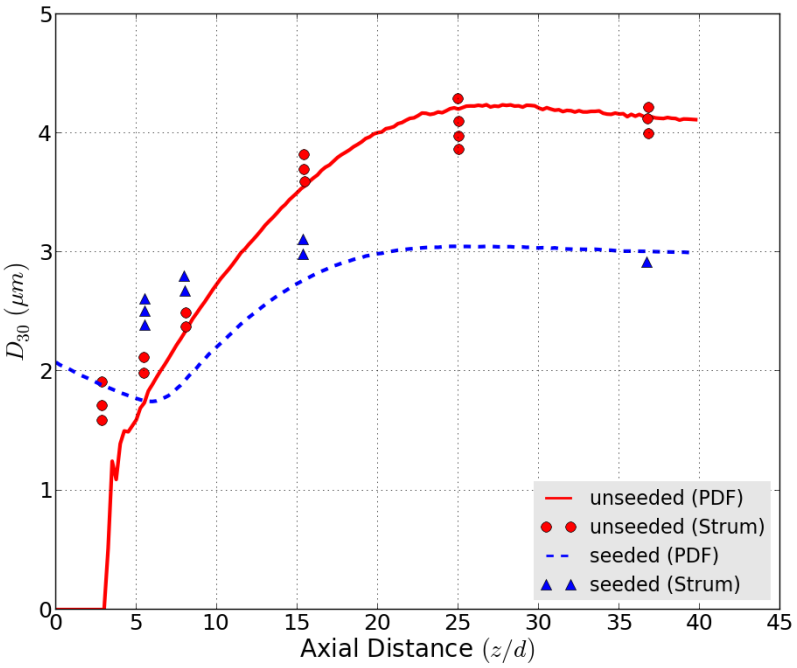

Figure 5.29: Comparison plot of D_{30} versus downstream distance for the 62 $^{\circ}C$ jet, both seeded and unseeded

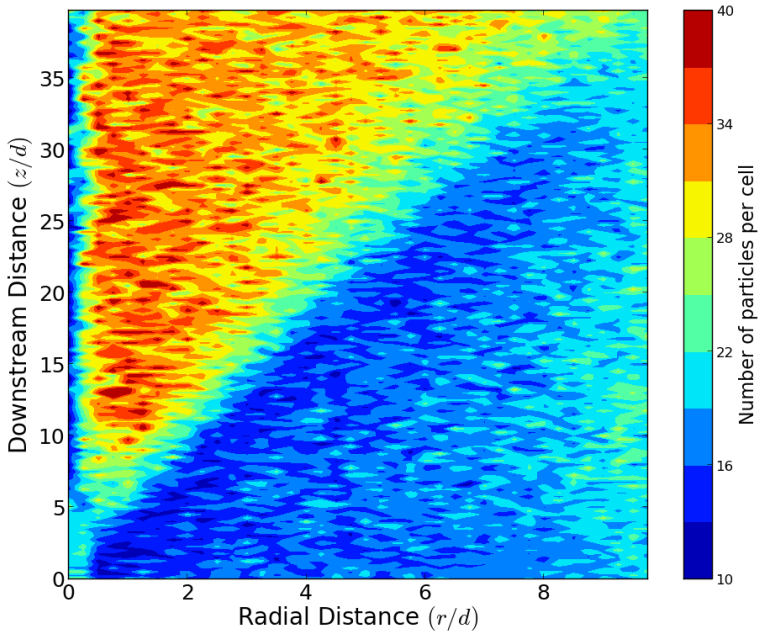

Figure 5.30: Plot of the typical particle concentration throughout the domain

5.4.6.2 Effect of Computational Particle Concentration

The computational particle concentration we used was typically an average of 20 particles/cell, with a minimum of 10 and maximum of 40. Figure 5.30 shows the particle density throughout the domain for a typical simulation. The low concentration near the jet axis is a persistent problem caused by the relatively small volumes. There is no good solution to prevent the volume disparity in a cylindrical mesh without compromising radial resolution near the axis. An alternative would be to use a Cartesian mesh with equal size/volume cells everywhere (which could still utilize quarter-symmetry).

The behavior of the scalar fields indicate this is adequate for the scalar distribution, but we also conducted simulations with more particles. Figure 5.31 shows the D_{30} results along the centerline for the baseline case as well as a simulation with an average of 40 particles/cell with a minimum of 20 and maximum of 60. The negligible difference indicates that our baseline concentration is adequate.

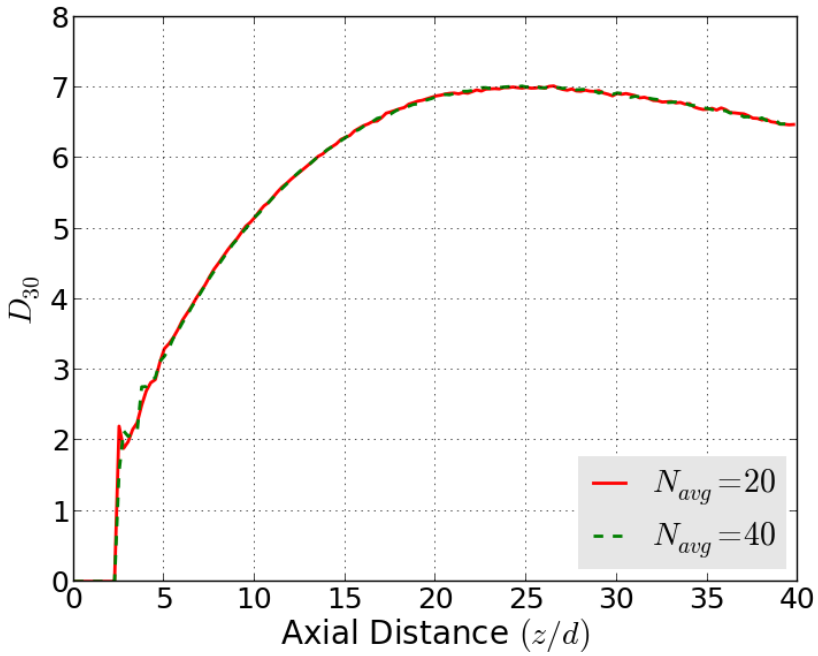

Figure 5.31: Plot of D_{30} along the jet centerline for two particle density cases

5.4.6.3 Effect of Diameter Bin Size

We conducted another refinement study to examine the effect of the discretization size of the droplet diameter distribution. Our baseline case uses 50 0.3 μm diameter bins to resolve droplet sizes over the range of the nuclei stage to 15 μm in diameter. Again, the comparison of D_{30} for the baseline and refined values shows insensitivity to this parameter of the PDF discretization, as seen in Figure 5.32.

These results, in conjunction with the previous sensitivity study, looking at the effect of computational particle concentration, not only illustrate the insensitivity with regards to the simulation parameters, but also exemplify the reproducibility of our Monte Carlo results given sufficient averaging. Typically, the results presented are composed of 2000 time steps (not counting the time needed to initialize the simulation).

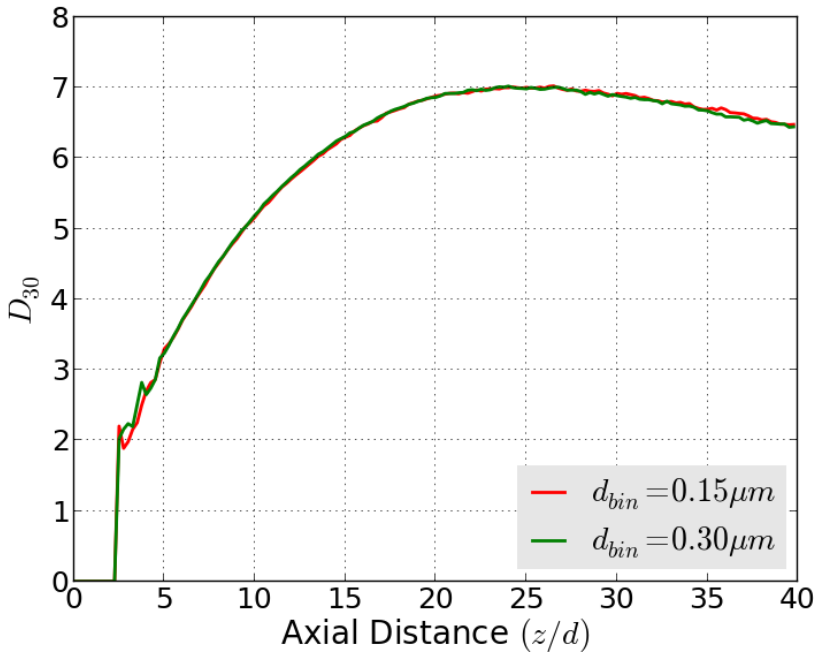

Figure 5.32: Plot of D_{30} along the jet centerline for two diameter bin discretizations

5.5 Conclusions

Our hybrid stochastic computational particle/finite volume method accurately reproduces the experimental results from Strum & Toor (1992) for a condensing water-vapor-saturated jet. The particle size distribution agrees with the measurements both as it evolves downstream and radially. The stochastic particles satisfactorily reproduce the scalar distribution, and as a result they are able to predict the bimodal behavior observed in some locations in the experiments.

The GPU hardware is well-suited to parallelize this type of problem. The thermodynamic calculations are isolated within each computational particle during a time step, and therefore they are readily parallelized. The calculations of the supersaturation, droplet growth, and population balance within each thermodynamic step are among the most time-consuming operations within the code. On the computer used for this study, we observed approximately between one and two orders of magnitude speed-up: month-long simulations

become day-long simulations; day-long simulations are completed in a half-hour. This type of acceleration traditionally requires parallel execution on high-end, expensive CPUs with many cores, or a computational cluster. The GPU approach opens up the possibility of undertaking problems with far greater scope using more sophisticated GPUs, or combining traditional parallelization strategies to utilize arrays of GPUs.

5.6 Future Work

Due to the model's satisfactory comparison with experiments, as well as the relatively mild effect condensation has on buoyancy (esp. relative to combustion), it is unlikely that coupling of the CFD to the PDF code would dramatically change the results. However, if the scale of the problem is increased (e.g. atmospheric simulations), it is easy to imagine that even a few degrees of temperature difference could lead to density changes that would cumulatively have a large impact on a buoyancy-driven, slowly-developing flow. Therefore, in order to apply this technique to a wider range of problems, it would be necessary to implement two-way coupling between the PDF code and `OpenFOAM`. It is not clear, however, how tight the coupling needs to be. That is, do the codes need to run alongside each other for each time step, or does the coupling only need to take place periodically? This decision will drive the architecture of the programming. It may very well be compatible to continue a CFD calculation, which is perhaps already designed to be parallelized across multiple processors, alongside a PDF simulation which takes advantage of GPU hardware.

The code may also require additional features to tackle other classes of flow scenarios. For instance, in the case of a flow featuring homogeneous nucleation, the thermodynamic routine would need the relevant thermodynamic model. If the super-saturation field is sufficiently expansive, or residence times are prolonged, the droplets would cease to behave as Stokes particles. A collision kernel could be incorporated to account for the redistribution of droplet sizes.

We confined ourselves to studying a statistically stationary flow, but it is not difficult to imagine extending this methodology to time-dependent flows. In order to collect sufficient data for averaging, one would either need to use many more particles per cell, or run the simulation multiple times.

Appendix A

DERIVATION OF VISCOSITY-DEPENDENT STABILITY EQUATIONS

A.1 Navier-Stokes (Cylindrical Coordinates)

A general form of the Navier-Stokes equation is presented as

$$\rho \frac{D\boldsymbol{u}}{Dt} = \boldsymbol{f} + \boldsymbol{\nabla} \cdot \boldsymbol{\tau}, \tag{A.1}$$

as well as equations for continuity,

$$\frac{D\rho}{Dt} + \rho \boldsymbol{\nabla} \cdot \boldsymbol{u} = 0 \tag{A.2}$$

and concentration,

$$\frac{Dc}{Dt} + (\boldsymbol{\nabla} \cdot \boldsymbol{u})c = \boldsymbol{\nabla} \cdot (D\boldsymbol{\nabla} c) + R \tag{A.3}$$

where for cylindrical coordinates:

$$\boldsymbol{u} = (u_z, u_r, u_\theta) = (u, v, w) \tag{A.4}$$

and

$$\frac{D}{Dt} \equiv \frac{\partial}{\partial t} + \boldsymbol{u} \cdot \boldsymbol{\nabla} \equiv \frac{\partial}{\partial t} + u\frac{\partial}{\partial z} + v\frac{\partial}{\partial r} + w\frac{1}{r}\frac{\partial}{\partial \theta} \tag{A.5}$$

These can be expanded to

$$\rho \left[\frac{\partial \boldsymbol{u}}{\partial t} + (\boldsymbol{u} \cdot \boldsymbol{\nabla})\boldsymbol{u} \right] = \boldsymbol{f} + \boldsymbol{\nabla} \cdot \boldsymbol{\tau} \tag{A.6}$$

Continuity:

$$\frac{\partial \rho}{\partial t} + u\frac{\partial \rho}{\partial z} + v\frac{\partial \rho}{\partial r} + \frac{1}{r}w\frac{\partial \rho}{\partial \theta} + \rho\frac{\partial u}{\partial z} + \frac{1}{r}\rho\frac{\partial (rv)}{\partial r} + \frac{1}{r}\rho\frac{\partial w}{\partial \theta} = 0 \tag{A.7}$$

Concentration:

$$\begin{aligned}\frac{\partial c}{\partial t}+u\frac{\partial c}{\partial z}+v\frac{\partial c}{\partial r}+\frac{1}{r}w\frac{\partial c}{\partial \theta}+(\boldsymbol{\nabla}\cdot\boldsymbol{u})c=\\ \frac{\partial}{\partial z}\left(D\frac{\partial c}{\partial z}\right)+\frac{1}{r}\frac{\partial}{\partial r}\left(rD\frac{\partial c}{\partial r}\right)+\frac{1}{r}\frac{\partial}{\partial \theta}\left(\frac{D}{r}\frac{\partial c}{\partial \theta}\right)+R\end{aligned} \tag{A.8}$$

We will assume uniform density, incompressible flow, meaning $\frac{\partial \rho}{\partial t}=\frac{\partial \rho}{\partial z}=\frac{\partial \rho}{\partial r}=\frac{\partial \rho}{\partial \theta}=0$ (by extension, continuity implies $\boldsymbol{\nabla}\cdot\boldsymbol{u}=0$), and constant diffusive coefficient D, so the components of the Navier-Stokes equation can be written as:

z-momentum:

$$\begin{aligned}\rho\left(\frac{Du}{Dt}\right)=&\rho\left(\frac{\partial u}{\partial t}+u\frac{\partial u}{\partial z}+v\frac{\partial u}{\partial r}+\frac{w}{r}\frac{\partial u}{\partial \theta}\right)\\ =&f_z+\frac{\partial \tau_{rz}}{\partial r}+\frac{1}{r}\left[\frac{\partial \tau_{\theta z}}{\partial \theta}+\tau_{rz}\right]+\frac{\partial \tau_{zz}}{\partial z}\end{aligned} \tag{A.9}$$

r-momentum:

$$\begin{aligned}\rho\left(\frac{Dv}{Dt}-\frac{w^2}{r}\right)=&\rho\left(\frac{\partial v}{\partial t}+u\frac{\partial v}{\partial z}+v\frac{\partial v}{\partial r}+\frac{w}{r}\frac{\partial v}{\partial \theta}-\frac{w^2}{r}\right)\\ =&f_r+\frac{\partial \tau_{rr}}{\partial r}+\frac{1}{r}\left[\frac{\partial \tau_{\theta r}}{\partial \theta}+(\tau_{rr}-\tau_{\theta\theta})\right]+\frac{\partial \tau_{zr}}{\partial z}\end{aligned} \tag{A.10}$$

θ-momentum:

$$\begin{aligned}\rho\left(\frac{Dw}{Dt}-\frac{vw}{r}\right)=&\rho\left(\frac{\partial w}{\partial t}+u\frac{\partial w}{\partial z}+v\frac{\partial w}{\partial r}+\frac{w}{r}\frac{\partial w}{\partial \theta}-\frac{vw}{r}\right)\\ =&f_\theta+\frac{\partial \tau_{r\theta}}{\partial r}+\frac{1}{r}\left[\frac{\partial \tau_{\theta\theta}}{\partial \theta}+(\tau_{r\theta}+\tau_{\theta r})\right]+\frac{\partial \tau_{z\theta}}{\partial z}\end{aligned} \tag{A.11}$$

For cylindrical coordinates, the symmetric stress tensor $\boldsymbol{\tau}$ is defined as:

$$\begin{aligned}
\tau_{zz} &= -p + 2\mu\frac{\partial u}{\partial z} + \kappa\boldsymbol{\nabla}\cdot\boldsymbol{u} \\
\tau_{rr} &= -p + 2\mu\frac{\partial v}{\partial r} + \kappa\boldsymbol{\nabla}\cdot\boldsymbol{u} \\
\tau_{\theta\theta} &= -p + 2\mu\left(\frac{1}{r}\frac{\partial w}{\partial \theta} + \frac{v}{r}\right) + \kappa\boldsymbol{\nabla}\cdot\boldsymbol{u} \\
\tau_{zr} &= \tau_{rz} = \mu\left(\frac{\partial u}{\partial r} + \frac{\partial v}{\partial z}\right) \\
\tau_{r\theta} &= \tau_{\theta r} = \mu\left(\frac{1}{r}\frac{\partial v}{\partial \theta} + \frac{\partial w}{\partial r} - \frac{w}{r}\right) \\
\tau_{\theta z} &= \tau_{z\theta} = \mu\left(\frac{\partial w}{\partial z} + \frac{1}{r}\frac{\partial u}{\partial \theta}\right)
\end{aligned} \tag{A.12}$$

where κ is the bulk viscosity. We have already stated the assumption of incompressible flow which makes $\kappa\boldsymbol{\nabla}\cdot\boldsymbol{u} = 0$. Substituting:

z-momentum:

$$\begin{aligned}
\rho\left(\frac{Du}{Dt}\right) =& \rho\left(\frac{\partial u}{\partial t} + u\frac{\partial u}{\partial z} + v\frac{\partial u}{\partial r} + \frac{w}{r}\frac{\partial u}{\partial \theta}\right) \\
=& f_z - \frac{\partial p}{\partial z} + \frac{\partial}{\partial z}\left[2\mu\frac{\partial u}{\partial z}\right] + \frac{1}{r}\frac{\partial}{\partial r}\left[\mu r\left(\frac{\partial v}{\partial z} + \frac{\partial u}{\partial r}\right)\right] \\
&+ \frac{1}{r}\frac{\partial}{\partial \theta}\left[\mu\left(\frac{1}{r}\frac{\partial u}{\partial \theta} + \frac{\partial w}{\partial z}\right)\right]
\end{aligned} \tag{A.13}$$

r-momentum:

$$\begin{aligned}
\rho\left(\frac{Dv}{Dt} - \frac{w^2}{r}\right) =& \rho\left(\frac{\partial v}{\partial t} + u\frac{\partial v}{\partial z} + v\frac{\partial v}{\partial r} + \frac{w}{r}\frac{\partial v}{\partial \theta} - \frac{w^2}{r}\right) \\
=& f_r - \frac{\partial p}{\partial r} + \frac{\partial}{\partial z}\left[\mu\left(\frac{\partial v}{\partial z} + \frac{\partial u}{\partial r}\right)\right] + \frac{\partial}{\partial r}\left[2\mu\frac{\partial v}{\partial r}\right] \\
&+ \frac{1}{r}\frac{\partial}{\partial \theta}\left[\mu\left(\frac{1}{r}\frac{\partial v}{\partial \theta} + \frac{\partial w}{\partial r} - \frac{w}{r}\right)\right] + \frac{2\mu}{r}\left[\frac{\partial v}{\partial r} - \frac{1}{r}\frac{\partial w}{\partial \theta} - \frac{v}{r}\right]
\end{aligned} \tag{A.14}$$

θ-momentum:

$$\begin{aligned}\rho\left(\frac{Dw}{Dt}-\frac{vw}{r}\right) =&\rho\left(\frac{\partial w}{\partial t}+u\frac{\partial w}{\partial z}+v\frac{\partial w}{\partial r}+\frac{w}{r}\frac{\partial w}{\partial \theta}-\frac{vw}{r}\right)\\ =&f_\theta-\frac{1}{r}\frac{\partial p}{\partial \theta}+\frac{\partial}{\partial z}\left[\mu\left(\frac{1}{r}\frac{\partial u}{\partial \theta}+\frac{\partial w}{\partial z}\right)\right]+\frac{\partial}{\partial r}\left[\mu\left(\frac{1}{r}\frac{\partial v}{\partial \theta}+\frac{\partial w}{\partial r}-\frac{w}{r}\right)\right]\\ &+\frac{1}{r}\frac{\partial}{\partial \theta}\left[\frac{2\mu}{r}\left(\frac{\partial w}{\partial \theta}+v\right)\right]+\frac{2\mu}{r}\left[\frac{1}{r}\frac{\partial v}{\partial \theta}+\frac{\partial w}{\partial r}-\frac{w}{r}\right]\end{aligned} \tag{A.15}$$

Our simplified equations for continuity and concentration become:

Continuity:

$$\rho\frac{\partial u}{\partial z}+\rho\frac{\partial v}{\partial r}+\frac{1}{r}\rho v+\frac{1}{r}\rho\frac{\partial w}{\partial \theta}=0 \tag{A.16}$$

Concentration:

$$\frac{\partial c}{\partial t}+u\frac{\partial c}{\partial z}+v\frac{\partial c}{\partial r}+\frac{1}{r}w\frac{\partial c}{\partial \theta}=D\left(\frac{\partial^2 c}{\partial z^2}+\frac{\partial^2 c}{\partial r^2}+\frac{1}{r}\frac{\partial c}{\partial r}+\frac{1}{r^2}\frac{\partial^2 c}{\partial \theta^2}\right)+R \tag{A.17}$$

A.2 Decomposition (Mean and Fluctuating Parts)

We will decompose the terms into their mean and fluctuating parts, assuming that the flow is axisymmetric ($\frac{\partial U}{\partial \theta}=\frac{\partial V}{\partial \theta}=\frac{\partial P}{\partial \theta}=\frac{\partial C}{\partial \theta}=0$ and the mean flow in the θ direction is zero ($W(z,r,\theta)=0$):

$$\begin{aligned}u(z,r,\theta,t)&=U(z,r)+u'(z,r,\theta,t)\\ v(z,r,\theta,t)&=V(z,r)+v'(z,r,\theta,t)\\ w(z,r,\theta,t)&=w'(z,r,\theta,t)\\ p(z,r,\theta,t)&=P(z,r)+p'(z,r,\theta,t)\\ c(z,r,\theta,t)&=C(z,r)+c'(z,r,\theta,t)\end{aligned} \tag{A.18}$$

Furthemore, we will assume μ is an arbitrary function of c that is continuously differentiable over the range of c of interest. For instance, if c represents temperature in units of

Kelvin, the viscosity of water can be approximated as Korson et al. (1969)

$$\mu(c) = X \cdot 10^{\frac{Y}{T-Z}} \tag{A.19}$$

where $X = 2.414 \times 10^{-5}$ Pa sec, $Y = 247.8$ K, and $Z = 140$ K.

We will express μ as a Taylor series expanded about C. Since c' is assumed small, we will drop the terms non-linear in c', yielding:

$$\mu(C + c') = \mu(C) + \left.\frac{\partial \mu}{\partial c}\right|_C c' \tag{A.20}$$

z-momentum:

$$\begin{aligned}
&\rho\left(\frac{\partial}{\partial t}(U+u') + (U+u')\frac{\partial}{\partial z}(U+u') + (V+v')\frac{\partial}{\partial r}(U+u') + \frac{w'}{r}\frac{\partial}{\partial \theta}(U+u')\right) \\
=&f_z - \frac{\partial}{\partial z}(P+p') + \frac{\partial}{\partial z}\left[2\left(\mu(C) + \left.\frac{\partial \mu}{\partial c}\right|_C c'\right)\frac{\partial}{\partial z}(U+u')\right] \\
&+ \frac{1}{r}\frac{\partial}{\partial r}\left[r\left(\mu(C) + \left.\frac{\partial \mu}{\partial c}\right|_C c'\right)\left(\frac{\partial}{\partial z}(V+v') + \frac{\partial}{\partial r}(U+u')\right)\right] \\
&+ \frac{1}{r}\frac{\partial}{\partial \theta}\left[\left(\mu(C) + \left.\frac{\partial \mu}{\partial c}\right|_C c'\right)\left(\frac{1}{r}\frac{\partial}{\partial \theta}(U+u') + \frac{\partial w'}{\partial z}\right)\right]
\end{aligned} \tag{A.21}$$

r-momentum:

$$\begin{aligned}
&\rho\left(\frac{\partial}{\partial t}(V+v') + (U+u')\frac{\partial}{\partial z}(V+v') + (V+v')\frac{\partial}{\partial r}(V+v') + \frac{w'}{r}\frac{\partial}{\partial \theta}(V+v') - \frac{w'^2}{r}\right) \\
=&f_r - \frac{\partial}{\partial r}(P+p') + \frac{\partial}{\partial z}\left[\left(\mu(C) + \left.\frac{\partial \mu}{\partial c}\right|_C c'\right)\left(\frac{\partial}{\partial z}(V+v') + \frac{\partial}{\partial r}(U+u')\right)\right] \\
&+ \frac{\partial}{\partial r}\left[2\left(\mu(C) + \left.\frac{\partial \mu}{\partial c}\right|_C c'\right)\frac{\partial}{\partial r}(V+v')\right] \\
&+ \frac{1}{r}\frac{\partial}{\partial \theta}\left[\left(\mu(C) + \left.\frac{\partial \mu}{\partial c}\right|_C c'\right)\left(\frac{1}{r}\frac{\partial}{\partial \theta}(V+v') + \frac{\partial w'}{\partial r} - \frac{w'}{r}\right)\right] \\
&+ \frac{2}{r}\left(\mu(C) + \left.\frac{\partial \mu}{\partial c}\right|_C c'\right)\left[\frac{\partial}{\partial r}(V+v') - \frac{1}{r}\frac{\partial w'}{\partial \theta} - \frac{V+v'}{r}\right]
\end{aligned} \tag{A.22}$$

θ-momentum:

$$\begin{aligned}
&\rho\left(\frac{\partial w'}{\partial t}+(U+u')\frac{\partial w'}{\partial z}+(V+v')\frac{\partial w'}{\partial r}+\frac{w'}{r}\frac{\partial w'}{\partial \theta}-(V+v')\frac{w'}{r}\right)\\
=&f_\theta-\frac{1}{r}\frac{\partial}{\partial\theta}(P+p')+\frac{\partial}{\partial z}\left[\left(\mu(C)+\left.\tfrac{\partial\mu}{\partial c}\right|_C c'\right)\left(\frac{1}{r}\frac{\partial}{\partial\theta}(U+u')+\frac{\partial w'}{\partial z}\right)\right]\\
&+\frac{\partial}{\partial r}\left[\left(\mu(C)+\left.\tfrac{\partial\mu}{\partial c}\right|_C c'\right)\left(\frac{1}{r}\frac{\partial}{\partial\theta}(V+v')+\frac{\partial w'}{\partial r}-\frac{w'}{r}\right)\right]\\
&+\frac{1}{r}\frac{\partial}{\partial\theta}\left[\frac{2}{r}\left(\mu(C)+\left.\tfrac{\partial\mu}{\partial c}\right|_C c'\right)\left(\frac{\partial w'}{\partial\theta}+V+v'\right)\right]\\
&+\frac{2}{r}\left(\mu(C)+\left.\tfrac{\partial\mu}{\partial c}\right|_C c'\right)\left[\frac{1}{r}\frac{\partial}{\partial\theta}(V+v')+\frac{\partial w'}{\partial r}-\frac{w'}{r}\right]
\end{aligned}\tag{A.23}$$

Continuity:

$$\frac{\partial}{\partial z}\left(U+u'\right)+\frac{\partial}{\partial r}\left(V+v'\right)+\frac{1}{r}\left(V+v'\right)+\frac{1}{r}\frac{\partial}{\partial\theta}w'=0\tag{A.24}$$

Concentration:

$$\begin{aligned}
&\frac{\partial}{\partial t}\left(C+c'\right)+\left(U+u'\right)\frac{\partial}{\partial z}\left(C+c'\right)+\left(V+v'\right)\frac{\partial}{\partial r}\left(C+c'\right)+\frac{1}{r}w'\frac{\partial}{\partial\theta}\left(C+c'\right)\\
&=D\left(\frac{\partial^2}{\partial z^2}\left(C+c'\right)+\frac{\partial^2}{\partial r^2}\left(C+c'\right)+\frac{1}{r}\frac{\partial}{\partial r}\left(C+c'\right)+\frac{1}{r^2}\frac{\partial^2}{\partial\theta^2}\left(C+c'\right)\right)+R
\end{aligned}\tag{A.25}$$

A.3 Free Shear Approximation

Because we are concerned with free shear flows, we will the drop forcing terms $\boldsymbol{f}$ and R. As done in most investigations of free shear stability, we will simplify the calculations by assuming the flow is locally parallel. This is a justifiable assumption in the region we are looking at, near the nozzle exit, before the instability has grown to produce significant radial and azimuthal flows (Cohen & Wygnanski (1987)). The assumption leads to the following simplifications: $\partial U/\partial z = 0$, $\partial\mu/\partial z = 0$, $\partial C/\partial z = 0$, $V = 0$.

z-momentum:

$$\begin{aligned}
&\rho\left(\frac{\partial U}{\partial t}+\frac{\partial u'}{\partial t}+U\frac{\partial u'}{\partial z}+u'\frac{\partial u'}{\partial z}+v'\frac{\partial U}{\partial r}+v'\frac{\partial u'}{\partial r}+\frac{w'}{r}\frac{\partial u'}{\partial \theta}\right)\\
=&-\frac{\partial p'}{\partial z}+2\frac{\partial u'}{\partial z}\frac{\partial}{\partial z}\left(\mu(C)+\left.\tfrac{\partial \mu}{\partial c}\right|_C c'\right)+2\left(\mu(C)+\left.\tfrac{\partial \mu}{\partial c}\right|_C c'\right)\frac{\partial^2 u'}{\partial z^2}\\
&+\frac{1}{r}\left(\mu(C)+\left.\tfrac{\partial \mu}{\partial c}\right|_C c'\right)\left(\frac{\partial v'}{\partial z}+\frac{\partial U}{\partial r}+\frac{\partial u'}{\partial r}\right)\\
&+\left(\frac{\partial v'}{\partial z}+\frac{\partial U}{\partial r}+\frac{\partial u'}{\partial r}\right)\frac{\partial}{\partial r}\left(\mu(C)+\left.\tfrac{\partial \mu}{\partial c}\right|_C c'\right)\\
&+\left(\mu(C)+\left.\tfrac{\partial \mu}{\partial c}\right|_C c'\right)\left(\frac{\partial^2 v'}{\partial z\partial r}+\frac{\partial^2 U}{\partial r^2}+\frac{\partial^2 u'}{\partial r^2}\right)\\
&+\frac{1}{r}\left(\frac{1}{r}\frac{\partial u'}{\partial \theta}+\frac{\partial w'}{\partial z}\right)\frac{\partial}{\partial \theta}\left(\mu(C)+\left.\tfrac{\partial \mu}{\partial c}\right|_C c'\right)\\
&+\frac{1}{r}\left(\mu(C)+\left.\tfrac{\partial \mu}{\partial c}\right|_C c'\right)\left(\frac{1}{r}\frac{\partial^2 u'}{\partial \theta^2}+\frac{\partial^2 w'}{\partial z\partial \theta}\right)
\end{aligned}\tag{A.26}$$

r-momentum:

$$\begin{aligned}
&\rho\left(\frac{\partial v'}{\partial t}+U\frac{\partial v'}{\partial z}+u'\frac{\partial v'}{\partial z}+v'\frac{\partial v'}{\partial r}+\frac{w'}{r}\frac{\partial v'}{\partial \theta}-\frac{w'^2}{r}\right)\\
=&-\frac{\partial P}{\partial r}-\frac{\partial p'}{\partial r}+\left(\frac{\partial v'}{\partial z}+\frac{\partial U}{\partial r}+\frac{\partial u'}{\partial r}\right)\frac{\partial}{\partial z}\left(\mu(C)+\left.\tfrac{\partial \mu}{\partial c}\right|_C c'\right)\\
&+\left(\mu(C)+\left.\tfrac{\partial \mu}{\partial c}\right|_C c'\right)\left(\frac{\partial^2 v'}{\partial z^2}+\frac{\partial^2 u'}{\partial r\partial z}\right)\\
&+2\frac{\partial v'}{\partial r}\frac{\partial}{\partial r}\left(\mu(C)+\left.\tfrac{\partial \mu}{\partial c}\right|_C c'\right)+2\left(\mu(C)+\left.\tfrac{\partial \mu}{\partial c}\right|_C c'\right)\frac{\partial^2 v'}{\partial r^2}\\
&+\frac{1}{r}\left(\frac{1}{r}\frac{\partial v'}{\partial \theta}+\frac{\partial w'}{\partial r}-\frac{w'}{r}\right)\frac{\partial}{\partial \theta}\left(\mu(C)+\left.\tfrac{\partial \mu}{\partial c}\right|_C c'\right)\\
&+\frac{1}{r}\left(\mu(C)+\left.\tfrac{\partial \mu}{\partial c}\right|_C c'\right)\left(\frac{1}{r}\frac{\partial^2 v'}{\partial \theta^2}+\frac{\partial^2 w'}{\partial r\partial \theta}-\frac{1}{r}\frac{\partial w'}{\partial \theta}\right)\\
&+\frac{2}{r}\left(\mu(C)+\left.\tfrac{\partial \mu}{\partial c}\right|_C c'\right)\left[\frac{\partial v'}{\partial r}-\frac{1}{r}\frac{\partial w'}{\partial \theta}-\frac{v'}{r}\right]
\end{aligned}\tag{A.27}$$

θ-momentum:

$$\begin{aligned}
&\rho\left(\frac{\partial w'}{\partial t}+U\frac{\partial w'}{\partial z}+u'\frac{\partial w'}{\partial z}+v'\frac{\partial w'}{\partial r}+\frac{w'}{r}\frac{\partial w'}{\partial \theta}-v'\frac{w'}{r}\right)\\
=&-\frac{1}{r}\frac{\partial}{\partial\theta}p'+\left(\frac{1}{r}\frac{\partial u'}{\partial\theta}+\frac{\partial w'}{\partial z}\right)\frac{\partial}{\partial z}\left(\mu(C)+\left.\tfrac{\partial\mu}{\partial c}\right|_C c'\right)\\
&+\left(\mu(C)+\left.\tfrac{\partial\mu}{\partial c}\right|_C c'\right)\left(\frac{1}{r}\frac{\partial^2 u'}{\partial\theta\partial z}+\frac{\partial^2 w'}{\partial z^2}\right)\\
&+\left(\frac{1}{r}\frac{\partial v'}{\partial\theta}+\frac{\partial w'}{\partial r}-\frac{w'}{r}\right)\frac{\partial}{\partial r}\left(\mu(C)+\left.\tfrac{\partial\mu}{\partial c}\right|_C c'\right)\\
&+\left(\mu(C)+\left.\tfrac{\partial\mu}{\partial c}\right|_C c'\right)\left(\frac{1}{r}\frac{\partial^2 v'}{\partial\theta\partial r}-\frac{1}{r^2}\frac{\partial v'}{\partial\theta}+\frac{\partial^2 w'}{\partial r^2}-\frac{1}{r}\frac{\partial w'}{\partial r}+\frac{w'}{r^2}\right)\\
&+\frac{2}{r^2}\left(\frac{\partial w'}{\partial\theta}+v'\right)\frac{\partial}{\partial\theta}\left(\mu(C)+\left.\tfrac{\partial\mu}{\partial c}\right|_C c'\right)+\frac{2}{r^2}\left(\mu(C)+\left.\tfrac{\partial\mu}{\partial c}\right|_C c'\right)\left(\frac{\partial^2 w'}{\partial\theta^2}+\frac{\partial v'}{\partial\theta}\right)\\
&+\frac{2}{r}\left(\mu(C)+\left.\tfrac{\partial\mu}{\partial c}\right|_C c'\right)\left[\frac{1}{r}\frac{\partial v'}{\partial\theta}+\frac{\partial w'}{\partial r}-\frac{w'}{r}\right]
\end{aligned}\tag{A.28}$$

Continuity:

$$\frac{\partial u'}{\partial z}+\frac{\partial v'}{\partial r}+\frac{1}{r}v'+\frac{1}{r}\frac{\partial w'}{\partial\theta}=0\tag{A.29}$$

Concentration:

$$\frac{\partial C}{\partial t}+\frac{\partial c'}{\partial t}+U\frac{\partial c'}{\partial z}+u'\frac{\partial c'}{\partial z}+v'\frac{\partial C}{\partial r}+v'\frac{\partial c'}{\partial r}+\frac{1}{r}w'\frac{\partial c'}{\partial\theta}=D\left(\frac{\partial^2 c'}{\partial z^2}+\frac{\partial^2 C}{\partial r^2}+\frac{\partial^2 c'}{\partial r^2}+\frac{1}{r}\frac{\partial C}{\partial r}+\frac{1}{r}\frac{\partial c'}{\partial r}+\frac{1}{r^2}\frac{\partial^2 c'}{\partial\theta^2}\right)\tag{A.30}$$

Note that the r derivative of the μ terms can be expanded as follows:

$$\begin{aligned}
\frac{\partial}{\partial r}\left(\mu(C)+\left.\tfrac{\partial\mu}{\partial c}\right|_C c'\right)&=\frac{\partial}{\partial r}\mu(C)+\frac{\partial}{\partial r}\left(\left.\tfrac{\partial\mu}{\partial c}\right|_C c'\right)\\
&=\frac{\partial}{\partial r}\mu(C)+\left.\tfrac{\partial\mu}{\partial c}\right|_C\frac{\partial c'}{\partial r}+c'\frac{\partial}{\partial r}\left(\left.\tfrac{\partial\mu}{\partial c}\right|_C\right)\\
&=\frac{\partial\mu}{\partial C}\frac{\partial C}{\partial r}+\left.\tfrac{\partial\mu}{\partial c}\right|_C\frac{\partial c'}{\partial r}+c'\frac{\partial}{\partial C}\left(\left.\tfrac{\partial\mu}{\partial c}\right|_C\right)\frac{\partial C}{\partial r}
\end{aligned}\tag{A.31}$$

Similarly, the derivatives with respect to z and θ are:

$$\begin{aligned}
\frac{\partial}{\partial\theta}\left(\mu(C)+\left.\tfrac{\partial\mu}{\partial c}\right|_C c'\right)&=\frac{\partial\mu}{\partial C}\frac{\partial \cancel{C}}{\partial\theta}+\left.\tfrac{\partial\mu}{\partial c}\right|_C\frac{\partial c'}{\partial\theta}+c'\frac{\partial}{\partial C}\left(\left.\tfrac{\partial\mu}{\partial c}\right|_C\right)\frac{\partial \cancel{C}}{\partial\theta}\\
\frac{\partial}{\partial z}\left(\mu(C)+\left.\tfrac{\partial\mu}{\partial c}\right|_C c'\right)&=\frac{\partial\mu}{\partial C}\frac{\partial \cancel{C}}{\partial z}+\left.\tfrac{\partial\mu}{\partial c}\right|_C\frac{\partial c'}{\partial z}+c'\frac{\partial}{\partial C}\left(\left.\tfrac{\partial\mu}{\partial c}\right|_C\right)\frac{\partial \cancel{C}}{\partial z}
\end{aligned}\tag{A.32}$$

Since we are assuming small fluctuations, we drop the higher order fluctuating terms. Additionally, we subtract the equations for mean flow, yielding

z-momentum:

$$\begin{aligned}
&\rho\left(\frac{\partial u'}{\partial t}+U\frac{\partial u'}{\partial z}+v'\frac{\partial U}{\partial r}\right)\\
=&-\frac{\partial p'}{\partial z}+2\mu(C)\frac{\partial^2 u'}{\partial z^2}\\
&+\frac{1}{r}\left(\mu(C)\frac{\partial v'}{\partial z}+\frac{\partial U}{\partial r}\left.\frac{\partial\mu}{\partial c}\right|_C c'+\mu(C)\frac{\partial u'}{\partial r}\right)\\
&+\frac{\partial\mu}{\partial C}\frac{\partial C}{\partial r}\frac{\partial v'}{\partial z}+\frac{\partial\mu}{\partial C}\frac{\partial C}{\partial r}\frac{\partial u'}{\partial r}+\frac{\partial U}{\partial r}\left.\frac{\partial\mu}{\partial c}\right|_C\frac{\partial c'}{\partial r}+\frac{\partial U}{\partial r}\frac{\partial}{\partial C}\left(\left.\frac{\partial\mu}{\partial c}\right|_C\right)\frac{\partial C}{\partial r}c'\\
&+\mu(C)\frac{\partial^2 v'}{\partial z\partial r}+\frac{\partial^2 U}{\partial r^2}\left.\frac{\partial\mu}{\partial c}\right|_C c'+\mu(C)\frac{\partial^2 u'}{\partial r^2}\\
&+\frac{1}{r}\left(\frac{1}{r}\mu(C)\frac{\partial^2 u'}{\partial\theta^2}+\mu(C)\frac{\partial^2 w'}{\partial z\partial\theta}\right)
\end{aligned}\tag{A.33}$$

r-momentum:

$$\begin{aligned}
&\rho\left(\frac{\partial v'}{\partial t}+U\frac{\partial v'}{\partial z}\right)\\
=&-\frac{\partial p'}{\partial r}+\frac{\partial U}{\partial r}\left.\frac{\partial\mu}{\partial c}\right|_C\frac{\partial c'}{\partial z}+\mu(C)\frac{\partial^2 v'}{\partial z^2}+\mu(C)\frac{\partial^2 u'}{\partial r\partial z}\\
&+2\frac{\partial\mu}{\partial C}\frac{\partial C}{\partial r}\frac{\partial v'}{\partial r}+2\mu(C)\frac{\partial^2 v'}{\partial r^2}\\
&+\frac{1}{r}\left(\frac{1}{r}\mu(C)\frac{\partial^2 v'}{\partial\theta^2}+\mu(C)\frac{\partial^2 w'}{\partial r\partial\theta}-\frac{1}{r}\mu(C)\frac{\partial w'}{\partial\theta}\right)\\
&+\frac{2}{r}\left(\mu(C)\frac{\partial v'}{\partial r}-\frac{1}{r}\mu(C)\frac{\partial w'}{\partial\theta}-\mu(C)\frac{v'}{r}\right)
\end{aligned}\tag{A.34}$$

θ-momentum:

$$\begin{aligned}
&\rho\left(\frac{\partial w'}{\partial t}+U\frac{\partial w'}{\partial z}\right)\\
=&-\frac{1}{r}\frac{\partial}{\partial\theta}p'+\frac{1}{r}\mu(C)\frac{\partial^2 u'}{\partial\theta\partial z}+\mu(C)\frac{\partial^2 w'}{\partial z^2}\\
&+\frac{\partial\mu}{\partial C}\frac{\partial C}{\partial r}\left(\frac{1}{r}\frac{\partial v'}{\partial\theta}+\frac{\partial w'}{\partial r}-\frac{w'}{r}\right)\\
&+\mu(C)\left(\frac{1}{r}\frac{\partial^2 v'}{\partial\theta\partial r}-\frac{1}{r^2}\frac{\partial v'}{\partial\theta}+\frac{\partial^2 w'}{\partial r^2}-\frac{1}{r}\frac{\partial w'}{\partial r}+\frac{w'}{r^2}\right)\\
&+\frac{2}{r^2}\mu(C)\left(\frac{\partial^2 w'}{\partial\theta^2}+\frac{\partial v'}{\partial\theta}\right)+\frac{2}{r}\mu(C)\left(\frac{1}{r}\frac{\partial v'}{\partial\theta}+\frac{\partial w'}{\partial r}-\frac{w'}{r}\right)
\end{aligned}\tag{A.35}$$

Continuity:

$$\frac{\partial u'}{\partial z}+\frac{\partial v'}{\partial r}+\frac{1}{r}v'+\frac{1}{r}\frac{\partial w'}{\partial\theta}=0\tag{A.36}$$

Concentration:

$$\frac{\partial c'}{\partial t}+U\frac{\partial c'}{\partial z}+v'\frac{\partial C}{\partial r}=D\left(\frac{\partial^2 c'}{\partial z^2}+\frac{\partial^2 c'}{\partial r^2}+\frac{1}{r}\frac{\partial c'}{\partial r}+\frac{1}{r^2}\frac{\partial^2 c'}{\partial\theta^2}\right)\tag{A.37}$$

By rearranging the terms of each momentum equation, we can group terms such that the continuity equation allows us to eliminate them.

z-momentum:

$$\begin{aligned}
&\rho\left(\frac{\partial u'}{\partial t}+U\frac{\partial u'}{\partial z}+v'\frac{\partial U}{\partial r}\right)\\
=&-\frac{\partial p'}{\partial z}+\frac{1}{r}\left(\frac{\partial U}{\partial r}\left.\frac{\partial\mu}{\partial c}\right|_C c'+\mu(C)\frac{\partial u'}{\partial r}\right)+\frac{\partial^2 U}{\partial r^2}\left.\frac{\partial\mu}{\partial c}\right|_C c'\\
&+\frac{\partial\mu}{\partial C}\frac{\partial C}{\partial r}\left(\frac{\partial v'}{\partial z}+\frac{\partial u'}{\partial r}\right)+\frac{\partial U}{\partial r}\left.\frac{\partial\mu}{\partial c}\right|_C\frac{\partial c'}{\partial r}+\frac{\partial U}{\partial r}\frac{\partial}{\partial C}\left(\left.\frac{\partial\mu}{\partial c}\right|_C\right)\frac{\partial C}{\partial r}c'\\
&+\mu(C)\left(\frac{\partial^2 u'}{\partial z^2}+\frac{\partial^2 u'}{\partial r^2}+\frac{1}{r^2}\frac{\partial^2 u'}{\partial\theta^2}\right)+\mu(C)\frac{\partial}{\partial z}\cancel{\left(\frac{\partial u'}{\partial z}+\frac{\partial v'}{\partial r}+\frac{1}{r}v'+\frac{1}{r}\frac{\partial w'}{\partial\theta}\right)}
\end{aligned}\tag{A.38}$$

r-momentum:

$$\begin{aligned}
&\rho\left(\frac{\partial v'}{\partial t}+U\frac{\partial v'}{\partial z}\right)\\
=&-\frac{\partial p'}{\partial r}+\frac{\partial U}{\partial r}\left.\frac{\frac{\partial \mu}{\partial c}}{}\right|_C\frac{\partial c'}{\partial z}+2\frac{\partial \mu}{\partial C}\frac{\partial C}{\partial r}\frac{\partial v'}{\partial r}\\
&+\mu(C)\left(\frac{\partial^2 v'}{\partial z^2}+\frac{\partial^2 v'}{\partial r^2}+\frac{1}{r^2}\frac{\partial^2 v'}{\partial \theta^2}-\frac{2}{r^2}\frac{\partial w'}{\partial \theta}-\frac{v'}{r^2}+\frac{1}{r}\frac{\partial v'}{\partial r}\right)\\
&+\mu(C)\frac{\partial}{\partial r}\cancel{\left(\frac{\partial u'}{\partial z}+\frac{\partial v'}{\partial r}+\frac{1}{r}v'+\frac{1}{r}\frac{\partial w'}{\partial \theta}\right)}
\end{aligned}\tag{A.39}$$

θ-momentum:

$$\begin{aligned}
&\rho\left(\frac{\partial w'}{\partial t}+U\frac{\partial w'}{\partial z}\right)\\
=&-\frac{1}{r}\frac{\partial}{\partial \theta}p'+\frac{\partial \mu}{\partial C}\frac{\partial C}{\partial r}\left(\frac{1}{r}\frac{\partial v'}{\partial \theta}+\frac{\partial w'}{\partial r}-\frac{w'}{r}\right)\\
&+\mu(C)\left(\frac{\partial^2 w'}{\partial z^2}+\frac{\partial^2 w'}{\partial r^2}+\frac{1}{r^2}\frac{\partial^2 w'}{\partial \theta^2}+\frac{2}{r^2}\frac{\partial v'}{\partial \theta}+\frac{1}{r}\frac{\partial w'}{\partial r}-\frac{w'}{r^2}\right)\\
&+\frac{\mu(C)}{r}\frac{\partial}{\partial \theta}\cancel{\left(\frac{\partial u'}{\partial z}+\frac{\partial v'}{\partial r}+\frac{1}{r}v'+\frac{1}{r}\frac{\partial w'}{\partial \theta}\right)}
\end{aligned}\tag{A.40}$$

A.4 Assumed Form of Fluctuating Parts

We will represent the fluctuating components as wavelike solutions of the form

$$u'(z,r,\theta,t)=\bar{u}(r)\exp\left\{i\left(\alpha z+n\theta+\omega t\right)\right\}\tag{A.41a}$$

$$v'(z,r,\theta,t)=\bar{v}(r)\exp\left\{i\left(\alpha z+n\theta+\omega t\right)\right\}\tag{A.41b}$$

$$w'(z,r,\theta,t)=\bar{w}(r)\exp\left\{i\left(\alpha z+n\theta+\omega t\right)\right\}\tag{A.41c}$$

$$p'(z,r,\theta,t)=\bar{p}(r)\exp\left\{i\left(\alpha z+n\theta+\omega t\right)\right\}\tag{A.41d}$$

$$c'(z,r,\theta,t)=\bar{c}(r)\exp\left\{i\left(\alpha z+n\theta+\omega t\right)\right\}\tag{A.41e}$$

After substituting, the equations are simplified by dividing by $\exp\left\{i\left(\alpha z+n\theta+\omega t\right)\right\}$, which is common to every term. The resulting equations are:

z-momentum:

$$\begin{aligned}
&\rho\left(i\omega\bar{u}+i\alpha U\bar{u}+\tfrac{\partial U}{\partial r}\bar{v}\right)\\
&=-i\alpha\bar{p}+\mu(C)\left(\tfrac{\partial^2\bar{u}}{\partial r^2}+\tfrac{1}{r}\tfrac{\partial\bar{u}}{\partial r}-\alpha^2\bar{u}-\tfrac{n^2}{r^2}\bar{u}\right)+\tfrac{\partial\mu}{\partial C}\tfrac{\partial C}{\partial r}\left(i\alpha\bar{v}+\tfrac{\partial\bar{u}}{\partial r}\right)\\
&+\tfrac{\partial U}{\partial r}\left.\tfrac{\partial\mu}{\partial c}\right|_C\tfrac{\partial\bar{c}}{\partial r}+\tfrac{\partial U}{\partial r}\tfrac{\partial}{\partial C}\left(\left.\tfrac{\partial\mu}{\partial c}\right|_C\right)\tfrac{\partial C}{\partial r}\bar{c}+\tfrac{\partial^2 U}{\partial r^2}\left.\tfrac{\partial\mu}{\partial c}\right|_C\bar{c}+\tfrac{1}{r}\tfrac{\partial U}{\partial r}\left.\tfrac{\partial\mu}{\partial c}\right|_C\bar{c}
\end{aligned}\tag{A.42}$$

r-momentum:

$$\begin{aligned}
&\rho\left(i\omega\bar{v}+i\alpha U\bar{v}\right)\\
&=-\tfrac{\partial\bar{p}}{\partial r}+i\alpha\tfrac{\partial U}{\partial r}\left.\tfrac{\partial\mu}{\partial c}\right|_C\bar{c}+2\tfrac{\partial\mu}{\partial C}\tfrac{\partial C}{\partial r}\tfrac{\partial\bar{v}}{\partial r}\\
&\mu(C)\left(-\alpha^2\bar{v}+\tfrac{\partial^2\bar{v}}{\partial r^2}-\tfrac{n^2}{r^2}\bar{v}-2i\tfrac{n}{r^2}\bar{w}-\tfrac{1}{r^2}\bar{v}+\tfrac{1}{r}\tfrac{\partial\bar{v}}{\partial r}\right)
\end{aligned}\tag{A.43}$$

θ-momentum:

$$\begin{aligned}
&\rho\left(i\omega\bar{w}+i\alpha U\bar{w}\right)\\
&=-i\tfrac{n}{r}\bar{p}+\tfrac{\partial\mu}{\partial C}\tfrac{\partial C}{\partial r}\left(i\tfrac{n}{r}\bar{v}+\tfrac{\partial\bar{w}}{\partial r}-\tfrac{\bar{w}}{r}\right)\\
&+\mu(C)\left(-\alpha^2\bar{w}+\tfrac{\partial^2\bar{w}}{\partial r^2}-\tfrac{n^2}{r^2}\bar{w}+2i\tfrac{n}{r^2}\bar{v}+\tfrac{1}{r}\tfrac{\partial\bar{w}}{\partial r}-\tfrac{1}{r^2}\bar{w}\right)
\end{aligned}\tag{A.44}$$

Continuity:

$$i\alpha\bar{u}+\tfrac{\partial\bar{v}}{\partial r}+\tfrac{1}{r}\bar{v}+in\tfrac{1}{r}\bar{w}=0\tag{A.45}$$

Concentration:

$$i\omega\bar{c}+i\alpha U\bar{c}+\bar{v}\tfrac{\partial C}{\partial r}=D\left(-\alpha^2\bar{c}+\tfrac{\partial^2\bar{c}}{\partial r^2}+\tfrac{1}{r}\tfrac{\partial\bar{c}}{\partial r}-\tfrac{1}{r^2}n^2\bar{c}\right)\tag{A.46}$$

A.5 Linearization in α

In order to remove the nonlinearity in α^2, we will define new variables:

$$\bar{u_\alpha} = \alpha\bar{u} \tag{A.47a}$$

$$\bar{v_\alpha} = \alpha\bar{v} \tag{A.47b}$$

$$\bar{w_\alpha} = \alpha\bar{w} \tag{A.47c}$$

$$\bar{c_\alpha} = \alpha\bar{c} \tag{A.47d}$$

Substitute $\bar{u_\alpha}$, etc:

z-momentum:

$$\begin{aligned}
&\rho\left(i\omega\bar{u} + iU\bar{u}_\alpha + \tfrac{\partial U}{\partial r}\bar{v}\right) \\
=&-i\alpha\bar{p} + \mu(C)\left(\tfrac{\partial^2\bar{u}}{\partial r^2} + \tfrac{1}{r}\tfrac{\partial\bar{u}}{\partial r} - \alpha\bar{u}_\alpha - \tfrac{n^2}{r^2}\bar{u}\right) + \tfrac{\partial\mu}{\partial C}\tfrac{\partial C}{\partial r}\left(i\bar{v}_\alpha + \tfrac{\partial\bar{u}}{\partial r}\right) \\
&+ \tfrac{\partial U}{\partial r}\left.\tfrac{\partial\mu}{\partial c}\right|_C \tfrac{\partial\bar{c}}{\partial r} + \tfrac{\partial U}{\partial r}\tfrac{\partial}{\partial C}\left(\left.\tfrac{\partial\mu}{\partial c}\right|_C\right)\tfrac{\partial C}{\partial r}\bar{c} + \tfrac{\partial^2 U}{\partial r^2}\left.\tfrac{\partial\mu}{\partial c}\right|_C\bar{c} + \tfrac{1}{r}\tfrac{\partial U}{\partial r}\left.\tfrac{\partial\mu}{\partial c}\right|_C\bar{c}
\end{aligned} \tag{A.48}$$

r-momentum:

$$\begin{aligned}
&\rho\left(i\omega\bar{v} + iU\bar{v}_\alpha\right) \\
&= -\tfrac{\partial\bar{p}}{\partial r} + i\tfrac{\partial U}{\partial r}\left.\tfrac{\partial\mu}{\partial c}\right|_C\bar{c}_\alpha + 2\tfrac{\partial\mu}{\partial C}\tfrac{\partial C}{\partial r}\tfrac{\partial\bar{v}}{\partial r} \\
&\mu(C)\left(-\alpha\bar{v}_\alpha + \tfrac{\partial^2\bar{v}}{\partial r^2} - \tfrac{n^2}{r^2}\bar{v} - 2i\tfrac{n}{r^2}\bar{w} - \tfrac{1}{r^2}\bar{v} + \tfrac{1}{r}\tfrac{\partial\bar{v}}{\partial r}\right)
\end{aligned} \tag{A.49}$$

θ-momentum:

$$\begin{aligned}
&\rho\left(i\omega\bar{w} + iU\bar{w}_\alpha\right) \\
=&-i\tfrac{n}{r}\bar{p} + \tfrac{\partial\mu}{\partial C}\tfrac{\partial C}{\partial r}\left(i\tfrac{n}{r}\bar{v} + \tfrac{\partial\bar{w}}{\partial r} - \tfrac{\bar{w}}{r}\right) \\
&+ \mu(C)\left(-\alpha\bar{w}_\alpha + \tfrac{\partial^2\bar{w}}{\partial r^2} - \tfrac{n^2}{r^2}\bar{w} + 2i\tfrac{n}{r^2}\bar{v} + \tfrac{1}{r}\tfrac{\partial\bar{w}}{\partial r} - \tfrac{1}{r^2}\bar{w}\right)
\end{aligned} \tag{A.50}$$

For convenience, we will multiply the continuity equation by $i\alpha$:

$$i\tfrac{\partial\bar{v_\alpha}}{\partial r} + i\tfrac{1}{r}\bar{v_\alpha} - n\tfrac{1}{r}\bar{w_\alpha} = \alpha\bar{u_\alpha} \tag{A.51}$$

Concentration:

$$i\omega\bar{c} + iU\bar{c_\alpha} + i\bar{v}\frac{\partial C}{\partial r} = D\left(-\alpha\bar{c_\alpha} + \frac{\partial^2\bar{c}}{\partial r^2} + \frac{1}{r}\frac{\partial\bar{c}}{\partial r} - \frac{1}{r^2}n^2\bar{c}\right) \tag{A.52}$$

Future matrix definitions and calculations will be simplified if each equation has only a single term containing α. The z-momentum equation needs to be modified to have only the pressure term multiplied by α. The αu_α term can be eliminated by substituting the continuity equation, making the z-momentum equation:

$$\begin{aligned}
&\rho\left(i\omega\bar{u} + iU\bar{u}_\alpha + \frac{\partial U}{\partial r}\bar{v}\right) \\
=&-i\alpha\bar{p} + \mu(C)\left(\frac{\partial^2\bar{u}}{\partial r^2} + \frac{1}{r}\frac{\partial\bar{u}}{\partial r} - i\frac{\partial}{\partial r}\bar{v}_\alpha - i\frac{1}{r}\bar{v}_\alpha + \frac{n}{r}\bar{w}_\alpha - \frac{n^2}{r^2}\bar{u}\right) + \frac{\partial\mu}{\partial C}\frac{\partial C}{\partial r}\left(i\bar{v}_\alpha + \frac{\partial\bar{u}}{\partial r}\right) \\
&+\frac{\partial U}{\partial r}\left.\frac{\partial\mu}{\partial c}\right|_C\frac{\partial\bar{c}}{\partial r} + \frac{\partial U}{\partial r}\frac{\partial}{\partial C}\left(\left.\frac{\partial\mu}{\partial c}\right|_C\right)\frac{\partial C}{\partial r}\bar{c} + \frac{\partial^2 U}{\partial r^2}\left.\frac{\partial\mu}{\partial c}\right|_C\bar{c} + \frac{1}{r}\frac{\partial U}{\partial r}\left.\frac{\partial\mu}{\partial c}\right|_C\bar{c}
\end{aligned} \tag{A.53}$$

We will rearrange all the equations, such that the lone term multiplied by α appears along on the right hand side of the equation. This yields:

z-momentum:

$$\begin{aligned}
&\left(i\omega\rho + \mu(C)\frac{n^2}{r^2} - \mu(C)\frac{1}{r}\frac{\partial}{\partial r} - \mu(C)\frac{\partial^2}{\partial r^2} - \frac{\partial\mu}{\partial C}\frac{\partial C}{\partial r}\frac{\partial}{\partial r}\right)\bar{u} + i\rho U\bar{u}_\alpha \\
&+\rho\frac{\partial U}{\partial r}\bar{v} + \left(i\mu(C)\frac{\partial}{\partial r} + i\mu(C)\frac{1}{r} - i\frac{\partial\mu}{\partial C}\frac{\partial C}{\partial r}\right)\bar{v}_\alpha - \mu(C)\frac{n}{r}\bar{w}_\alpha \\
&-\left(\frac{\partial U}{\partial r}\left.\frac{\partial\mu}{\partial c}\right|_C\frac{\partial}{\partial r} + \frac{\partial U}{\partial r}\frac{\partial}{\partial C}\left(\left.\frac{\partial\mu}{\partial c}\right|_C\right)\frac{\partial C}{\partial r} + \frac{\partial^2 U}{\partial r^2}\left.\frac{\partial\mu}{\partial c}\right|_C + \frac{1}{r}\frac{\partial U}{\partial r}\left.\frac{\partial\mu}{\partial c}\right|_C\right)\bar{c} \\
=&-i\alpha\bar{p}
\end{aligned} \tag{A.54}$$

r-momentum:

$$\begin{aligned}
&\left(i\omega\rho + \mu(C)\frac{n^2+1}{r^2} - \mu(C)\frac{1}{r}\frac{\partial}{\partial r} - \mu(C)\frac{\partial^2}{\partial r^2} - 2\frac{\partial\mu}{\partial C}\frac{\partial C}{\partial r}\frac{\partial}{\partial r}\right)\bar{v} + i\rho U\bar{v}_\alpha \\
&+2i\mu(C)\frac{n}{r^2}\bar{w} - i\left.\frac{\partial U}{\partial r}\frac{\partial\mu}{\partial c}\right|_C\bar{c}_\alpha + \frac{\partial}{\partial r}\bar{p} \\
&=-\mu(C)\alpha\bar{v}_\alpha
\end{aligned} \tag{A.55}$$

θ-momentum:

$$\begin{aligned}&\left(-i\tfrac{n}{r}\tfrac{\partial\mu}{\partial C}\tfrac{\partial C}{\partial r}-2i\mu(C)\tfrac{n}{r^2}\right)\bar{v}+i\tfrac{n}{r}\bar{p}\\&+\left(i\omega\rho+\tfrac{\partial\mu}{\partial C}\tfrac{\partial C}{\partial r}\tfrac{1}{r}-\tfrac{\partial\mu}{\partial C}\tfrac{\partial C}{\partial r}\tfrac{\partial}{\partial r}-\mu(C)\tfrac{\partial^2}{\partial r^2}+\mu(C)\tfrac{n^2+1}{r^2}-\mu(C)\tfrac{1}{r}\tfrac{\partial}{\partial r}\right)\bar{w}+i\rho U\bar{w}_\alpha\\&=-\mu(C)\alpha\bar{w}_\alpha\end{aligned}\tag{A.56}$$

Concentration:

$$\tfrac{\partial C}{\partial r}\bar{v}+\left[i\omega-D\left(\tfrac{\partial^2}{\partial r^2}+\tfrac{1}{r}\tfrac{\partial}{\partial r}-\tfrac{n^2}{r^2}\right)\right]\bar{c}+iU\bar{c_\alpha}=-\alpha D\bar{c_\alpha}\tag{A.57}$$

To be consistent with the right hand sides of the previous equations, we will multiply the continuity equation by $i\alpha$. This allows us to have $\alpha\bar{u_\alpha}$ as the only term in α after converting all of the other terms to their $\bar{u_\alpha}$, $\bar{v_\alpha}$, $\bar{w_\alpha}$ counterparts:

$$i\tfrac{\partial}{\partial r}\bar{v_\alpha}+i\tfrac{1}{r}\bar{v_\alpha}-n\tfrac{1}{r}\bar{w_\alpha}=\alpha\bar{u_\alpha}\tag{A.58}$$

A.6 Non-dimensionalization

Before continuing, we will non-dimensionalize the equations. Non-dimensionalized values will be represented with (ˆ); definitions are:

$$
\begin{aligned}
&\hat{U} = \tfrac{U}{U_j} \\
&\hat{r} = \tfrac{r}{R} \\
&\hat{C} = \tfrac{C}{C_j} \\
&\hat{\mu} = \tfrac{\mu}{\mu_j} \\
&\hat{\alpha} = \alpha R \\
&\hat{\omega} = \tfrac{\omega R}{U_j} \\
&\hat{\bar{u}} = \tfrac{\bar{u}}{U_j}, \hat{\bar{u}}_\alpha = \tfrac{\bar{u}_\alpha R}{U_j} \\
&\hat{\bar{v}} = \tfrac{\bar{v}}{U_j}, \hat{\bar{v}}_\alpha = \tfrac{\bar{v}_\alpha R}{U_j} \\
&\hat{\bar{w}} = \tfrac{\bar{w}}{U_j}, \hat{\bar{w}}_\alpha = \tfrac{\bar{w}_\alpha R}{U_j} \\
&\hat{\bar{c}} = \tfrac{\bar{c}}{C_j}, \hat{\bar{c}}_\alpha = \tfrac{\bar{c}_\alpha}{C_j} \\
&\hat{\bar{p}} = \tfrac{\bar{p}}{\rho U_j^2} \\
&Re = \tfrac{\rho U_j R}{\mu_j} \\
&Sc = \tfrac{\mu_j}{D}
\end{aligned}
\tag{A.59}
$$

We will non-dimensionalize the momentum equations by multiplying all terms by $\frac{R}{\rho U_j^2}$:

$$
\begin{aligned}
&\left(i\hat{\omega} - \tfrac{1}{Re}\tfrac{\partial\hat{\mu}}{\partial C}\tfrac{\partial C}{\partial\hat{r}}\tfrac{\partial}{\partial\hat{r}} + \tfrac{1}{Re}\hat{\mu}(C)\left(\tfrac{n^2}{\hat{r}^2} - \tfrac{1}{\hat{r}}\tfrac{\partial}{\partial\hat{r}} - \tfrac{\partial^2}{\partial\hat{r}^2}\right)\right)\hat{\bar{u}} + i\hat{U}\hat{\bar{u}}_\alpha \\
&+ \tfrac{\partial\hat{U}}{\partial\hat{r}}\hat{\bar{v}} + \tfrac{1}{Re}\left(i\hat{\mu}(C)\tfrac{\partial}{\partial\hat{r}} + i\hat{\mu}(C)\tfrac{1}{\hat{r}} - i\tfrac{\partial\hat{\mu}}{\partial C}\tfrac{\partial C}{\partial\hat{r}}\right)\hat{\bar{v}}_\alpha - \tfrac{1}{Re}\hat{\mu}(C)\tfrac{n}{\hat{r}}\hat{\bar{w}}_\alpha \\
&- \tfrac{1}{Re}\left(\tfrac{\partial\hat{U}}{\partial\hat{r}}\ \tfrac{\partial\hat{\mu}}{\partial\hat{c}}\Big|_C\tfrac{\partial}{\partial\hat{r}} + \tfrac{\partial\hat{U}}{\partial\hat{r}}\tfrac{\partial}{\partial C}\left(\tfrac{\partial\hat{\mu}}{\partial\hat{c}}\Big|_C\right)\tfrac{\partial C}{\partial\hat{r}} + \tfrac{\partial^2\hat{U}}{\partial\hat{r}^2}\ \tfrac{\partial\hat{\mu}}{\partial\hat{c}}\Big|_C + \tfrac{1}{\hat{r}}\tfrac{\partial\hat{U}}{\partial\hat{r}}\ \tfrac{\partial\hat{\mu}}{\partial\hat{c}}\Big|_C\right)\hat{\bar{c}} \\
&= -i\hat{\alpha}\hat{\bar{p}}
\end{aligned}
\tag{A.60}
$$

$$\begin{aligned}
&\left(i\hat{\omega}+\tfrac{1}{Re}\hat{\mu}(C)\left(\tfrac{n^2+1}{\hat{r}^2}-\tfrac{1}{\hat{r}}\tfrac{\partial}{\partial\hat{r}}-\tfrac{\partial^2}{\partial\hat{r}^2}\right)-2\tfrac{1}{Re}\tfrac{\partial\hat{\mu}}{\partial C}\tfrac{\partial C}{\partial\hat{r}}\tfrac{\partial}{\partial\hat{r}}\right)\hat{\hat{v}}\\
&+i\hat{U}\hat{\hat{v}}_\alpha+2i\tfrac{1}{Re}\hat{\mu}(C)\tfrac{n}{\hat{r}^2}\hat{\hat{w}}\\
&-i\tfrac{1}{Re}\tfrac{\partial\hat{U}}{\partial\hat{r}}\left.\tfrac{\partial\hat{\mu}}{\partial\hat{c}}\right|_C\hat{\hat{c}}_\alpha+\tfrac{\partial}{\partial\hat{r}}\hat{\hat{p}}\\
&=-\tfrac{1}{Re}\hat{\mu}(C)\hat{\alpha}\hat{\hat{v}}_\alpha
\end{aligned}\tag{A.61}$$

$$\begin{aligned}
&-i\tfrac{1}{Re}\tfrac{n}{\hat{r}}\left(\tfrac{\partial\hat{\mu}}{\partial C}\tfrac{\partial C}{\partial\hat{r}}+2\hat{\mu}(C)\tfrac{1}{\hat{r}}\right)\hat{\hat{v}}\\
&+\left(i\hat{\omega}+\tfrac{1}{Re}\hat{\mu}(C)\left(\tfrac{n^2+1}{\hat{r}^2}-\tfrac{1}{\hat{r}}\tfrac{\partial}{\partial\hat{r}}-\tfrac{\partial^2}{\partial\hat{r}^2}\right)+\tfrac{1}{Re}\tfrac{\partial\hat{\mu}}{\partial C}\tfrac{\partial C}{\partial\hat{r}}\tfrac{1}{\hat{r}}-\tfrac{1}{Re}\tfrac{\partial\hat{\mu}}{\partial C}\tfrac{\partial C}{\partial\hat{r}}\tfrac{\partial}{\partial\hat{r}}\right)\hat{\hat{w}}\\
&+i\hat{U}\hat{\hat{w}}_\alpha+i\tfrac{n}{\hat{r}}\hat{\hat{p}}\\
&=-\tfrac{1}{Re}\hat{\mu}(C)\hat{\alpha}\hat{\hat{w}}_\alpha
\end{aligned}\tag{A.62}$$

We will non-dimensionalize by multiplying both sides of the concentration equation by $\frac{R}{U_jC_j}$:

$$\tfrac{\partial\hat{C}}{\partial\hat{r}}\hat{\hat{v}}+\left[i\hat{\omega}-\tfrac{1}{Sc}\tfrac{1}{Re}\left(\tfrac{\partial^2}{\partial\hat{r}^2}+\tfrac{1}{\hat{r}}\tfrac{\partial}{\partial\hat{r}}-\tfrac{n^2}{\hat{r}^2}\right)\right]\hat{\hat{c}}+i\hat{U}\hat{\hat{c}}_\alpha=-\tfrac{1}{Sc}\tfrac{1}{Re}\hat{\alpha}\hat{\hat{c}}_\alpha\tag{A.63}$$

We will non-dimensionalize the continuity equation by multiplying both sides with $\frac{R^2}{U_j}$:

$$i\tfrac{\partial}{\partial\hat{r}}\hat{v_\alpha}+i\tfrac{1}{\hat{r}}\hat{v_\alpha}-n\tfrac{1}{\hat{r}}\hat{w_\alpha}=\hat{\alpha}\hat{u_\alpha}\tag{A.64}$$

Our last set of operations aim to isolate the right hand sides as simply α times the relevant fluctuating part. Our final system of equations (sans equations (A.47a)-(A.47d)) is as follows:

z-momentum:

$$\begin{aligned}
&\left(-\hat{\omega} - i\tfrac{1}{Re}\tfrac{\partial\hat{\mu}}{\partial C}\tfrac{\partial C}{\partial\hat{r}}\tfrac{\partial}{\partial\hat{r}} + i\tfrac{1}{Re}\hat{\mu}(C)\left(\tfrac{n^2}{\hat{r}^2} - \tfrac{1}{\hat{r}}\tfrac{\partial}{\partial\hat{r}} - \tfrac{\partial^2}{\partial\hat{r}^2}\right)\right)\hat{\bar{u}} - \hat{U}\hat{\bar{u}}_\alpha \\
&+ i\tfrac{\partial\hat{U}}{\partial\hat{r}}\bar{v} + i\tfrac{1}{Re}\left(\hat{\mu}(C)\tfrac{\partial}{\partial\hat{r}} + \hat{\mu}(C)\tfrac{1}{\hat{r}} - \tfrac{\partial\hat{\mu}}{\partial C}\tfrac{\partial C}{\partial\hat{r}}\right)\hat{\bar{v}}_\alpha - i\tfrac{\hat{\mu}(C)}{Re}\tfrac{n}{\hat{r}}\hat{\bar{w}}_\alpha \\
&+ i\tfrac{1}{Re}\left(\tfrac{\partial\hat{U}}{\partial\hat{r}}\left.\tfrac{\partial\hat{\mu}}{\partial\hat{c}}\right|_C\tfrac{\partial}{\partial\hat{r}} + \tfrac{\partial^2\hat{U}}{\partial\hat{r}^2}\left.\tfrac{\partial\hat{\mu}}{\partial\hat{c}}\right|_C + \tfrac{1}{\hat{r}}\tfrac{\partial\hat{U}}{\partial\hat{r}}\left.\tfrac{\partial\hat{\mu}}{\partial\hat{c}}\right|_C + \tfrac{\partial\hat{U}}{\partial\hat{r}}\tfrac{\partial}{\partial C}\left(\left.\tfrac{\partial\hat{\mu}}{\partial\hat{c}}\right|_C\right)\tfrac{\partial C}{\partial\hat{r}}\right)\hat{\bar{c}} \\
&= \hat{\alpha}\hat{\bar{p}}
\end{aligned} \tag{A.65}$$

r-momentum:

$$\begin{aligned}
&\left(-i\hat{\omega}\tfrac{Re}{\hat{\mu}(C)} - \tfrac{n^2+1}{\hat{r}^2} + \tfrac{1}{\hat{r}}\tfrac{\partial}{\partial\hat{r}} + \tfrac{\partial^2}{\partial\hat{r}^2} + 2\tfrac{1}{\hat{\mu}(C)}\tfrac{\partial\hat{\mu}}{\partial C}\tfrac{\partial C}{\partial\hat{r}}\tfrac{\partial}{\partial\hat{r}}\right)\hat{\bar{v}} \\
&- i\hat{U}\tfrac{Re}{\hat{\mu}(C)}\hat{\bar{v}}_\alpha - 2i\tfrac{n}{\hat{r}^2}\hat{\bar{w}} \\
&+ i\tfrac{1}{\hat{\mu}(C)}\tfrac{\partial\hat{U}}{\partial\hat{r}}\left.\tfrac{\partial\hat{\mu}}{\partial\hat{c}}\right|_C\hat{\bar{c}}_\alpha - \tfrac{Re}{\hat{\mu}(C)}\tfrac{\partial}{\partial\hat{r}}\hat{\bar{p}} \\
&= \hat{\alpha}\hat{\bar{v}}_\alpha
\end{aligned} \tag{A.66}$$

θ-momentum:

$$\begin{aligned}
&i\tfrac{n}{\hat{r}}\left(\tfrac{1}{\hat{\mu}(C)}\tfrac{\partial\hat{\mu}}{\partial C}\tfrac{\partial C}{\partial\hat{r}} + 2\tfrac{1}{\hat{r}}\right)\hat{\bar{v}} \\
&+ \left(-i\hat{\omega}\tfrac{Re}{\hat{\mu}(C)} - \tfrac{n^2+1}{\hat{r}^2} + \tfrac{1}{\hat{r}}\tfrac{\partial}{\partial\hat{r}} + \tfrac{\partial^2}{\partial\hat{r}^2} - \tfrac{1}{\hat{\mu}(C)}\tfrac{\partial\hat{\mu}}{\partial C}\tfrac{\partial C}{\partial\hat{r}}\tfrac{1}{\hat{r}} + \tfrac{1}{\hat{\mu}(C)}\tfrac{\partial\hat{\mu}}{\partial C}\tfrac{\partial C}{\partial\hat{r}}\tfrac{\partial}{\partial\hat{r}}\right)\hat{\bar{w}} \\
&- i\hat{U}\tfrac{Re}{\hat{\mu}(C)}\hat{\bar{w}}_\alpha - i\tfrac{n}{\hat{r}}\tfrac{Re}{\hat{\mu}(C)}\hat{\bar{p}} \\
&= \hat{\alpha}\hat{\bar{w}}_\alpha
\end{aligned} \tag{A.67}$$

Concentration:

$$-Pe\tfrac{\partial\hat{C}}{\partial\hat{r}}\hat{\bar{v}} - \left[i\hat{\omega}Pe - \left(\tfrac{\partial^2}{\partial\hat{r}^2} + \tfrac{1}{\hat{r}}\tfrac{\partial}{\partial\hat{r}} - \tfrac{n^2}{\hat{r}^2}\right)\right]\hat{\bar{c}} - iPe\hat{U}\hat{\bar{c}}_\alpha = \hat{\alpha}\hat{\bar{c}}_\alpha \tag{A.68}$$

Continuity:

$$i\tfrac{\partial}{\partial\hat{r}}\hat{\bar{v}}_\alpha + \tfrac{i}{\hat{r}}\hat{\bar{v}}_\alpha - n\tfrac{1}{\hat{r}}\hat{\bar{w}}_\alpha = \hat{\alpha}\hat{\bar{u}}_\alpha \tag{A.69}$$

A.7 Matrix Form

In order to begin to tackle the problem computationally, it behooves us to rewrite the system of equations as a matrix system, now with equations (A.47a) through (A.47d) included, in

the form:

$$\boldsymbol{A}\boldsymbol{x} = \hat{\alpha}\boldsymbol{B}\boldsymbol{x} \tag{A.70}$$

The matrices are defined as follows. The right hand side is simpler and expands as:

$$\hat{\alpha}\boldsymbol{B}\boldsymbol{x} = \hat{\alpha}\begin{bmatrix} 1 & 0 & 0 & 0 & 0 & 0 & 0 & 0 & 0 \\ 0 & 1 & 0 & 0 & 0 & 0 & 0 & 0 & 0 \\ 0 & 0 & 1 & 0 & 0 & 0 & 0 & 0 & 0 \\ 0 & 0 & 0 & 1 & 0 & 0 & 0 & 0 & 0 \\ 0 & 0 & 0 & 0 & 1 & 0 & 0 & 0 & 0 \\ 0 & 0 & 0 & 0 & 0 & 1 & 0 & 0 & 0 \\ 0 & 0 & 0 & 0 & 0 & 0 & 1 & 0 & 0 \\ 0 & 0 & 0 & 0 & 0 & 0 & 0 & 1 & 0 \\ 0 & 0 & 0 & 0 & 0 & 0 & 0 & 0 & 1 \end{bmatrix} \begin{bmatrix} \hat{\tilde{u}} \\ \hat{\tilde{u}}_\alpha \\ \hat{\tilde{v}} \\ \hat{\tilde{v}}_\alpha \\ \hat{\tilde{w}} \\ \hat{\tilde{w}}_\alpha \\ \hat{\tilde{c}} \\ \hat{\tilde{c}}_\alpha \\ \hat{\tilde{p}} \end{bmatrix} \tag{A.71}$$

The matrix $\boldsymbol{A}$ on the left hand side is considerably more complicated. Its definition is:

$$\boldsymbol{A}\boldsymbol{x} = \begin{bmatrix} 0 & 1 & 0 & 0 & 0 & 0 & 0 & 0 & 0 \\ 0 & 0 & 0 & A_{24} & 0 & A_{26} & 0 & 0 & 0 \\ 0 & 0 & 0 & 1 & 0 & 0 & 0 & 0 & 0 \\ 0 & 0 & A_{43} & A_{44} & A_{45} & 0 & A_{47} & 0 & A_{49} \\ 0 & 0 & 0 & 0 & 0 & 1 & 0 & 0 & 0 \\ 0 & 0 & A_{63} & 0 & A_{65} & A_{66} & 0 & 0 & A_{69} \\ 0 & 0 & 0 & 0 & 0 & 0 & 0 & 1 & 0 \\ 0 & 0 & A_{83} & 0 & 0 & 0 & A_{87} & A_{88} & 0 \\ A_{91} & A_{92} & A_{93} & A_{94} & 0 & A_{96} & A_{97} & 0 & 0 \end{bmatrix} \begin{bmatrix} \hat{\tilde{u}} \\ \hat{\tilde{u}}_\alpha \\ \hat{\tilde{v}} \\ \hat{\tilde{v}}_\alpha \\ \hat{\tilde{w}} \\ \hat{\tilde{w}}_\alpha \\ \hat{\tilde{c}} \\ \hat{\tilde{c}}_\alpha \\ \hat{\tilde{p}} \end{bmatrix} \tag{A.72}$$

where

$$
\begin{aligned}
A_{24} &= i\tfrac{\partial}{\partial\hat{r}} + i\tfrac{1}{\hat{r}} \\
A_{26} &= -n\tfrac{1}{\hat{r}} \\
A_{43} &= -i\hat{\omega}\tfrac{Re}{\hat{\mu}(C)} - \tfrac{n^2+1}{\hat{r}^2} + \tfrac{1}{\hat{r}}\tfrac{\partial}{\partial\hat{r}} + \tfrac{\partial^2}{\partial\hat{r}^2} + 2\tfrac{1}{\hat{\mu}(C)}\tfrac{\partial\hat{\mu}}{\partial C}\tfrac{\partial C}{\partial\hat{r}}\tfrac{\partial}{\partial\hat{r}} \\
A_{44} &= -i\hat{U}\tfrac{Re}{\hat{\mu}(C)} \\
A_{45} &= -2i\tfrac{n}{\hat{r}^2} \\
A_{48} &= i\tfrac{1}{\hat{\mu}(C)}\tfrac{\partial\hat{U}}{\partial\hat{r}}\ \tfrac{\partial\hat{\mu}}{\partial\hat{c}}\Big|_C \\
A_{49} &= -\tfrac{Re}{\hat{\mu}(C)}\tfrac{\partial}{\partial\hat{r}} \\
A_{63} &= i\tfrac{n}{\hat{r}}\left(\tfrac{1}{\hat{\mu}(C)}\tfrac{\partial\hat{\mu}}{\partial C}\tfrac{\partial C}{\partial\hat{r}} + 2\tfrac{1}{\hat{r}}\right) \\
A_{65} &= -i\hat{\omega}\tfrac{Re}{\hat{\mu}(C)} - \tfrac{n^2+1}{\hat{r}^2} + \tfrac{1}{\hat{r}}\tfrac{\partial}{\partial\hat{r}} + \tfrac{\partial^2}{\partial\hat{r}^2} - \tfrac{1}{\hat{\mu}(C)}\tfrac{\partial\hat{\mu}}{\partial C}\tfrac{\partial C}{\partial\hat{r}}\tfrac{1}{\hat{r}} + \tfrac{1}{\hat{\mu}(C)}\tfrac{\partial\hat{\mu}}{\partial C}\tfrac{\partial C}{\partial\hat{r}}\tfrac{\partial}{\partial\hat{r}} \\
A_{66} &= -i\hat{U}\tfrac{Re}{\hat{\mu}(C)} \\
A_{69} &= -i\tfrac{n}{\hat{r}}\tfrac{Re}{\hat{\mu}(C)} \\
A_{83} &= -Pe\tfrac{\partial C}{\partial\hat{r}} \\
A_{87} &= -i\hat{\omega}Pe + \left(\tfrac{\partial^2}{\partial\hat{r}^2} + \tfrac{1}{\hat{r}}\tfrac{\partial}{\partial\hat{r}} - \tfrac{n^2}{\hat{r}^2}\right) \\
A_{88} &= -iPe\hat{U} \\
A_{91} &= -\hat{\omega} - i\tfrac{1}{Re}\tfrac{\partial\hat{\mu}}{\partial C}\tfrac{\partial C}{\partial\hat{r}}\tfrac{\partial}{\partial\hat{r}} + i\tfrac{1}{Re}\hat{\mu}(C)\left(\tfrac{n^2}{\hat{r}^2} - \tfrac{1}{\hat{r}}\tfrac{\partial}{\partial\hat{r}} - \tfrac{\partial^2}{\partial\hat{r}^2}\right) \\
A_{92} &= -\hat{U} \\
A_{93} &= i\tfrac{\partial\hat{U}}{\partial\hat{r}} \\
A_{94} &= \tfrac{1}{Re}\left(\tfrac{\partial\hat{\mu}}{\partial C}\tfrac{\partial C}{\partial\hat{r}} - \hat{\mu}(C)\tfrac{\partial}{\partial\hat{r}} - \hat{\mu}(C)\tfrac{1}{\hat{r}}\right) \\
A_{96} &= -i\tfrac{\hat{\mu}(C)}{Re}\tfrac{n}{\hat{r}} \\
A_{97} &= i\tfrac{1}{Re}\left(\tfrac{\partial\hat{U}}{\partial\hat{r}}\ \tfrac{\partial\hat{\mu}}{\partial\hat{c}}\Big|_C\tfrac{\partial}{\partial\hat{r}} + \tfrac{\partial^2\hat{U}}{\partial\hat{r}^2}\ \tfrac{\partial\hat{\mu}}{\partial\hat{c}}\Big|_C + \tfrac{1}{\hat{r}}\tfrac{\partial\hat{U}}{\partial\hat{r}}\ \tfrac{\partial\hat{\mu}}{\partial\hat{c}}\Big|_C + \tfrac{\partial\hat{U}}{\partial\hat{r}}\tfrac{\partial}{\partial C}\left(\tfrac{\partial\hat{\mu}}{\partial\hat{c}}\Big|_C\right)\tfrac{\partial C}{\partial\hat{r}}\right)
\end{aligned}
\tag{A.73}
$$

BIBLIOGRAPHY

(2004). *Committee on the review of existing and potential standoff explosives detection techniques*. National Research Council, Washington, D.C.: The National Academies Press.

(2012). OpenFOAM: The open source CFD toolbox.
URL `http://www.openfoam.net/`

Adrian, R., & Westerweel, J. (2011). *Particle image velocimetry*. Cambridge University Press.

Albright, L. (2008). *Albright's chemical engineering handbook*. CRC Press.

Babu, P., & Mahesh, K. (2005). Direct numerical simulation of passive scalar mixing in spatially evolving turbulent round jets. In *43rd AIAA Aerospace Sciences Meeting*.

Batchelor, G. K., & Gill, A. E. (1962). Analysis of the stability of axisymmetric jets. *Journal of Fluid Mechanics*, *14*(04), 529–551.

Becker, H., & Massaro, T. (1968). Vortex evolution in a round jet. *Journal of Fluid Mechanics*, *31*, 435–448.

Bender, C. M., & Orszag, S. A. (1999). *Advanced mathematical methods for scientists and engineers I Asymptotic methods and perturbation theory*, vol. 1. Springer.

Bender, E., Hogan, A., Leggett, D., Miskolczy, G., & MacDonald, S. (1992). Surface contamination by TNT. *Journal of Forensic Sciences*, *37*, 1673–1678.

Bhattacharya, S., & Mittal, K. (1978). Mechanics of removing glass particulates from a solid surface. *Surface Technology*, *7*(5), 413–425.

Birch, A., Hughes, D., & Swaffield, F. (1987). Velocity decay of high pressure jets. *Combustion Science and Technology*, *52*, 161–171.

Boeck, T., & Zaleski, S. (2005). Viscous versus inviscid instability of two-phase mixing layers with continuous velocity profile. *Physics of Fluids*, *17*(3).

Buratinni, P., & Djenidi, L. (2004). Velocity and passive scalar characteristics in a round jet with grids at the nozzle exit. *Flow, Turbulence and Combustion*, *72*, 199–218.

Campbell, I., & Turner, J. (1985). Turbulent mixing between fluids with different viscosities.

Carazzo, G., Kaminski, E., & Tait, S. (2006). The route to self-similarity in turbulent jets and plumes. *Journal of Fluid Mechanics*, *547*, 137–148.

Chamberlain, R. (2002). Dry transfer method for the preparation of explosives test samples. U.S. Patent No. 6,470,730.

Chen, J.-Y., & Kollmann, W. (1991). Mixing models for turbulent flows with exothermic reactions. In F. Durst, B. Launder, W. Reynolds, F. Schmidt, & J. Whitelaw (Eds.) *Turbulent Shear Flows 7*, (pp. 277–292). Springer-Verlag.

Cheng, N. S. (2008). Formula for the viscosity of a glycerol–water mixture. *Industrial and Engineering Chemistry Research*, *47*, 3285–3288.

Chhabra, S., Shipman, T. N., & Prasad, A. K. (2005). The entrainment behavior of a turbulent axisymmetric jet in a viscous host fluid. *Experiments in Fluids*, *38*(1), 70–79.

Cohen, J., & Wygnanski, I. (1987). The evolution of instabilities in the axisymmetric jet. Part 1. The linear growth of disturbances near the nozzle. *Journal of Fluid Mechanics*, *176*, 191–219.

Corn, M., & Stein, F. (1965). Re-entrainment of particles from a plane surface. *American Industrial Hygiene Association Journal*, *26*(4), 325–336.

Crighton, D., & Gaster, M. (1976). Stability of slowly diverging jet flow. *Journal of Fluid Mechanics*, *77*(2), 397–413.

Crow, S. C., & Champagne, F. H. (1971). Orderly structure in jet turbulence. *Journal of Fluid Mechanics*, *48*(3), 547–591.

Curl, R. (1963). Dispersed phase mixing: I. Theory and effects in simple reactors. *AIChE Journal*, *9*(2), 175–181.

Davidson, W., & Scott, W. (2002). Vapor and particle sampling in the detection of terrorists explosives. *Proceedings - 50th ASMS Conference on Mass Spectrometry and Allied Topics*, (pp. 697–698).

Dimotakis, P. (2005). Turbulent mixing. *Annual Review of Fluid Mechanics*, *37*, 329–356.

Dopazo, C. (1979). Relaxation of initial probability density functions in the turbulent convection of scalar fields. *Physics of Fluids*, *22*, 20–30.

Dowling, D., & Dimotakis, P. (1990). Similarity of the concentration field of gas-phase turbulent jets. *Journal of Fluid Mechanics*, *218*, 109–141.

Ern, P., Charru, F., & Luchini, P. (2003). Stability analysis of a shear flow with strongly stratified viscosity. *Journal of Fluid Mechanics*, *496*, 295–312.

Fletcher, R., Briggs, N., & Ferguson, E. (2008). Measurements of air jet removal efficiencies of spherical particles from cloth and planar surfaces. *Aerosol Science and Techonology*, *42*(12), 1052–1061.

Friedlander, S. K. (2000). *Smoke, dust, and haze: Fundamentals of aerosol dynamics*. Oxford University Press, second ed.

Garmory, a., & Mastorakos, E. (2008). Aerosol nucleation and growth in a turbulent jet using the Stochastic Fields method. *Chemical Engineering Science*, *63*(16), 4078–4089.

George, W. (1989). The self-preservation of turbulent flows and its relation to initial conditions and coherent structures. *Advances in Turbulence*, (pp. 39–72).

Gottlieb, D., & Orszag, S. A. (1977). *Numerical analysis of spectral methods*, vol. 2. SIAM.

Haworth, D. (2010). Progress in probability density function methods for turbulent reacting flows. *Progress in Energy and Combustion Science*, *36*(2), 168–259.

Hunter, J. D. (2007). Matplotlib: A 2d graphics environment. *Computing In Science and Engineering*, *9*(3), 90–95.

Hussain, A., & Kaman, K. (1981). The 'preferred mode' of the axisymmetric jet. *Journal of Fluid Mechanics*, *110*, 39–71.

Hussain, A., & Ramjee, V. (1976). Effects of the axisymmetric contraction shape on incompressible turbulent flow. *Journal of Fluids Engineering*, (March), 58–68.

Hussein, H., Capp, S., & George, W. (1994). Velocity measurements in a high-Reynolds-number, momentum-conserving, axisymmetric, turbulent jet. *Journal of Fluid Mechanics*, *258*(1), 31–75.

Ibrahim, A., Dunn, P., & Brach, R. (2003). Microparticle detachment from surfaces exposed to turbulent air flow: controlled experiments and modeling. *Journal of Aerosol Science*, *34*, 765 – 782.

Janicka, J., Kolbe, W., & Kollmann, W. (1979). Closure of the transport equation for the probability density function of turbulent scalar fields. *Journal of Non-Equilibrium Thermodynamics*, *4*, 47–66.

Jones, E., Oliphant, T., Peterson, P., et al. (2001). SciPy: Open source scientific tools for Python.
URL `http://www.scipy.org/`

Keedy, R., Dengler, E., Ariessohn, P., Novosselov, I., & Aliseda, A. (2012). Removal rates of explosive particles from a surface by impingement of a gas jet. *Aerosol Science and Technology*, *46*, 148–155.

Kennedy, I., & Moody, M. (1998). Particle dispersion in a turbulent round jet. *Experimental Thermal and Fluid Science*, *18*, 11–26.

Khorrami, M. R., Malik, M. R., & Ash, R. L. (1989). Application of spectral collocation techniques to the stability of swirling flows. *Journal of Computational Physics*, *81*(1), 206–229.

Kleiss, J., & Melville, W. (2011). The analysis of sea surface imagery for whitecap kinematics. *Journal of Atmospheric Oceanic Technology*, *28*, 219–243.

Korson, L., Drost-Hansen, W., & Millero, F. J. (1969). Viscosity of water at various temperatures. *The Journal of Physical Chemistry*, *73*(1), 34–39.

Lee, J., & Chu, V. (2003). *Turbulent jets and plumes: A Lagrangian approach*. Springer, illustrated ed.

Lessen, M., & Singh, P. (1973). The stability of axisymmetric free shear layers. *Journal of Fluid Mechanics*, *60*, 433–457.

Lubbers, C. L., Brethouwer, G., & Boersma, B. J. (2001). Simulation of the mixing of a passive scalar in a round turbulent jet. *Fluid Dynamics Research*, *28*(3), 189–208.

Malik, M. (1990). Numerical methods for hypersonic boundary layer stability. *Journal of Computational Physics*, *86*(2), 376–413.

Masuda, H., Gotoh, K., Fukada, H., & Banba, Y. (1994). The removal of particles from flat surfaces using a high-speed air jet. *Advanced Powder Technology*, *5*(2), 205–217.

Melville, W., & Matusov, P. (2002). Distribution of breaking waves at the ocean surface. *Nature*, *417*, 58–63.

Mi, J., Nathan, G., & Nobes, D. (2001a). Mixing characteristics of axisymmetric free jets from a contoured nozzle, an orifice plate, and a pipe. *Journal of Fluids Engineering*, *123*, 878–883.

Mi, J., Nobes, D., & Nathan, G. (2001b). Influence of jet exit conditions on the passive scalar field of an axisymmetric free jet. *Journal of Fluid Mechanics*, *432*, 91–125.

Michalke, A. (1965). On spatially growing disturbances in an inviscid shear layer. *J. Fluid Mech*, *23*(3), 521–544.

Michalke, A. (1984). Survey on jet instability theory. *Progress in Aerospace Sciences*, *21*, 159–199.

Michalke, A., & Hermann, G. (1982). On the inviscid instability of a circular jet with external flow. *Journal of Fluid Mechanics*, *114*, 343–359.

Mollendorf, J. C., & Gebhart, B. (1973). An experimental and numerical study of the viscous stability of a round laminar vertical jet with and without thermal buoyancy for symmetric and asymmetric disturbances. *Journal of Fluid Mechanics*, *61*(2), 367–399.

Morris, P. J. (1976). The spatial viscous instability of axisymmetric jets. *Journal of Fluid Mechanics*, *77*(03), 511.

Muradoglu, M., Jenny, P., Pope, S., & Caughey, D. (1999). A consistent hybrid finite-volume/particle method for the PDF equations of turbulent reactive flows. *Journal of Computational Physics*, *154*(2), 342–371.

Nichols, J. (2005). Simulation and stability analysis of jet diffusion flames.

Okubo, T., Kokufuta, E., Nakamuro, M., Yoshinaga, K., Mizutani, M., & Tsuchida, A. (2010). Drying dissipative structures of lycopodium spore particles in aqueous dispersion. *Colloids and SUrfaces B: Biointerfaces*, *80*, 193–199.

Orszag, S. a. (1971). Accurate solution of the Orr–Sommerfeld stability equation. *Journal of Fluid Mechanics*, *50*(4), 689–703.

Otani, Y., Namiki, N., & Emi, H. (1995). Removal of Fine Particles from Smooth Flat Surfaces by Consecutive Pulse Air Jets. *Aerosol Science and Technology*, *23*(4), 665–673.

Owens, J. D., Houston, M., Luebke, D., Green, S., Stone, J. E., & Phillips, J. C. (2008). GPU computing. *Proceedings of the IEEE*, *96*(5), 879–899.

Oztekin, A., Cumbo, L. J., & Liakopoulos, A. (1999). Temporal stability of boundary-free shear flows: The effects of diffusion. *13*, 77–90.

Panchapakesan, N., & Lumley, J. (1993a). Turbulence measurements in axisymmetric jets of air and helium. Part 1. Air jet. *Journal of Fluid Mechanics*, *246*, 197–223.

Panchapakesan, N., & Lumley, J. (1993b). Turbulence measurements in axisymmetric jets of air and helium. Part 2. Helium jet. *Journal of Fluid Mechanics*, *246*, 225–247.

Pasumarthi, K., & Agrawal, A. (2005). Particle dispersion in a turbulent round jet. *Experimentals in Fluids*, *38*, 541–544.

Petersen, R. a., & Samet, M. M. (1988). On the preferred mode of jet instability. *Journal of Fluid Mechanics*, *194*, 153–173.

Phares, D., Smedley, G., & Flagan, R. (2000a). Effect of particle size and material properties on aerodynamic resuspension from surfaces. *Journal of Aerosol Science*, *31*(11), 1335–1353.

Phares, D., Smedley, G., & Flagan, R. (2000b). The wall shear stress produced by the normal impingement of a jet on a flat surface. *Journal of Fluid Mechanics*, *418*, 351–375.

Phares, D. J., Holt, J. K., Smedley, G. T., & Flagan, R. C. (2000c). Method for characterization of adhesion properties of trace explosives in fingerprints and fingerprint simulations. *Journal of Forensic Sciences*, *45*(4), 774–84.

Pitts, W. (1991a). Effects of global density ratio on the centerline mixing behavior of axisymmetric turbulent jets. *Experiments in Fluids*, *11*, 125–134.

Pitts, W. (1991b). Reynolds number effects on the mixing behavior of axisymmetric turbulent jets. *Experiments in Fluids*, *11*, 135–141.

Plaschko, P. (1979). Helical instabilities of slowly divergent jets. *Journal of Fluid Mechanics*, *92*(2), 209–215.

Pope, S. (1982). An improved turbulent mixing model. *Combustion Science and Technology*, *28*, 131–135.

Pope, S. (1985). PDF methods for turbulent reactive flows. *Progress in Energy and Combustion Science*, *11*, 119–192.

Pope, S. B. (2000). *Turbulent flows*. Cambridge University Press.

Pruppacher, H., & Klett, J. (1997). *Microphysics of clouds and precipitation*. Springer.

Raffel, M., Willert, C., Wereley, S., & Kompenhans, J. (2007). *Particle image velocimetry: A practical guide*. Springer, second ed.

Ramette, R., & Sandell, E. (1956). Rhodamine B equilibria. *Journal of the American Chemical Society*, *78*(19).

Ranade, M. (1987). Adhesion and removal of fine particles on surfaces. *Aerosol Science and Technology*, *7*(2), 161–176.

Rasband, W. (1997–2011). ImageJ. U.S. National Institutes of Health.

Reshotko, E., & Tumin, A. (2001). Spatial theory of optimal disturbances in a circular pipe flow. *Physics of Fluids*, *13*(4), 991.

Richards, C., & Pitts, W. (1993). Global density effects on the self-preservation behaviour of turbulent free jets. *Journal of Fluid Mechanics*, *254*, 417–435.

Rimai, D., DeMejo, L., & Bowen, R. (1990). Surface-force-induced deformations of monodisperse polystyrene spheres on planar silicon substrates. *Journal of Applied Physics*, *68*(12), 6234–6240.

Rodriguez-Rodriguez, J., Marugan-Cruz, C., Aliseda, A., & Lasheras, J. (2011). Dynamics of large turbulent structures in a steady breaker. *Experimental Thermal and Fluid Science*, *35*, 301–310.

Ryu, Y., Chang, K., & Lim, H. (2005). Use of bubble image velocimetry for measurement of plunging wave impinging on structure and associated greenwater. *Measurement Science and Technology*, *16*, 1945–1953.

Schmid, P. J., & Henningson, D. S. (2001). *Stability and transistion in shear flows*. Springer-Verlag.

Selvam, B., Merk, S., Govindarajan, R., & Meiburg, E. (2007). Stability of miscible core–annular flows with viscosity stratification. *Journal of Fluid Mechanics*, *592*, 23–49.

Sheely, M. (1932). Glycerol viscosity tables. *Industrial and Engineering Chemistry*, *24*(9), 1060–1064.

Squires, P. (1952). The growth of cloud drops by condensation I. General considerations. *Aust. J. Sci. Res.*

Strum, M. L. (1990). *Fog formation in a turbulent jet*. Ph.D. thesis, Carnagie Mellon University.

Strum, M. L., & Toor, H. L. (1992). Microphysical measurements of fog formed in a turbulent jet. *Aerosol Science and Technology*, *16*(3), 151–165.

Tokumaru, P., & Dimotakis, P. (1995). Image correlation velocimetry. *Experiments in Fluids*, *19*(1).

Trefethen, L. (2000). *Spectral methods in MATLAB*. Society for Industrial and Applied Mathematics.

Trefethen, L., & Embree, M. (2005). *Spectra and pseudospectra: The behavior of nonnormal matrices and operators*. Princeton University Press.

van der Graaf, G. (2012). Gpiv, open source software for particle image velocimetry. URL `http://gpiv.sourceforge.net/`

Verkouteren, J. (2007). Particle characteristics of trace high explosives: RDX and PETN. *Journal of Forensic Sciences*, *52*(2), 335–340.

Veroli, G., & Rigopoulos, S. (2010). Modeling of turbulent precipitation : A transported population balance-PDF method. *56*(4).

Villermaux, E., & Innocenti, C. (1999). On the geometry of turbulent mixing. *Journal of Fluid Mechanics*, *393*, 123–147.

Wang, H.-C. (1990). Effects of inceptive motion on particle detachment from surfaces. *Aerosol Science and Technology*, *13*(3), 386–393.

Westerweel, J., Fukushima, C., Pedersen, J., & Hunt, J. (2005). Mechanics of the turbulent-nonturbulent interface of a jet. *Physical Review Letters*, *95*(17), 1–4.

Wygnanski, I., & Fiedler, H. (1969). Some measurements in the self-preserving jet. *Journal of Fluid Mechanics*, *38*(3), 577–612.

Yih, C.-s. (1967). Instability due to viscosity stratification. *Journal of Fluid Mechanics*, *27*(2), 337–352.

Zebib, A. (1984). A Chebyshev method for the solution of boundary value problems. *Journal of Computational Physics*, *455*, 443–455.

Zhang, Y., & Haworth, D. (2004). A general mass consistency algorithm for hybrid particle/finite-volume PDF methods. *Journal of Computational Physics*, *194*(1), 156–193.